Title
Improvements to the On-Line Mass Separator, RAMA< the Beta-Delayed Charged-Particle Emission of Proton-Rich sd Shell Nuclei

Author
Ognibene, T.J.

Publication Date
1996-03-01

LBNL-38848
UC-413

ERNEST ORLANDO LAWRENCE
BERKELEY NATIONAL LABORATORY

Improvements to the On-Line Mass Separator, RAMA, and the Beta-Delayed Charged-Particle Emission of Proton-Rich sd Shell Nuclei

T.J. Ognibene
Nuclear Sciences Division

March 1996
Ph.D. Thesis

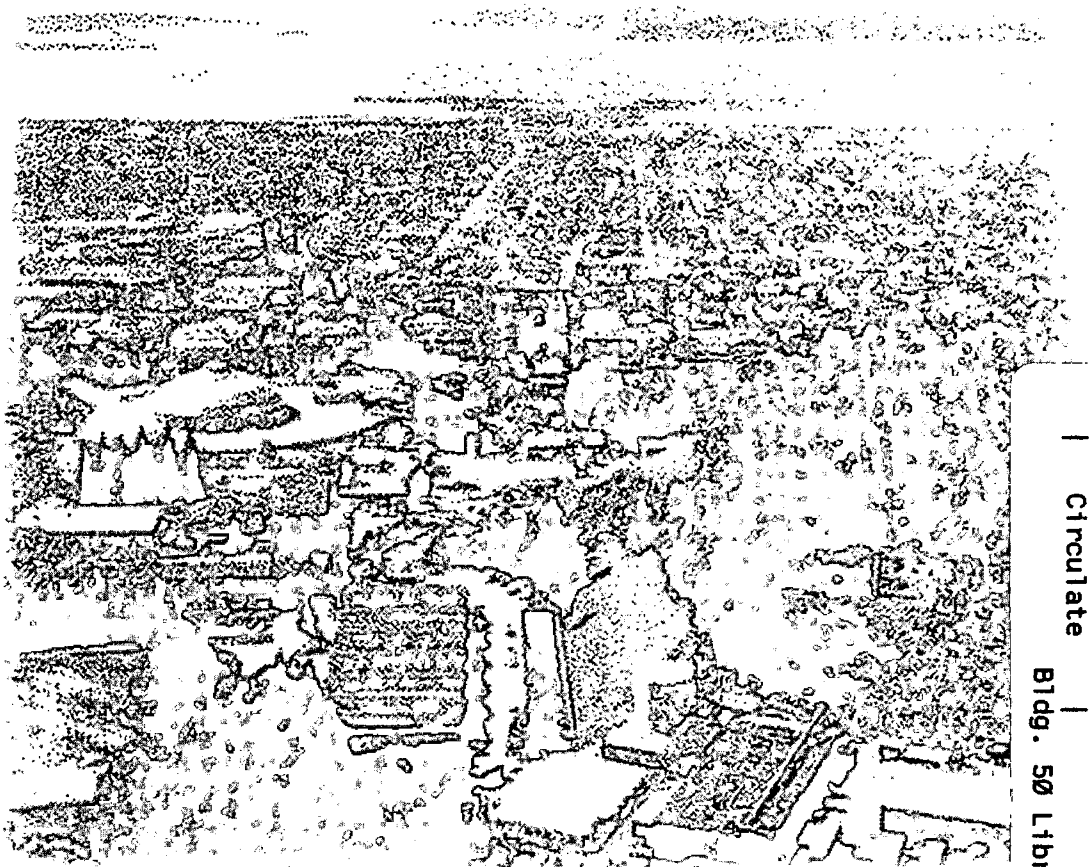

LBNL-38848
UC-413

Improvements to the On-Line Mass Separator, RAMA, and the Beta-Delayed Charged-Particle Emission of Proton-Rich sd Shell Nuclei

Theodore Joseph Ognibene
Ph.D. Thesis

Nuclear Science Division
Ernest Orlando Lawrence Berkeley National Laboratory
University of California
Berkeley, CA 94720

March 1996

This work was supported by the Director, Office of Energy Research, Office of High Energy and Nuclear Physics, Division of Nuclear Physics, of the U.S. Department of Energy under Contract No. DE-AC03-76SF00098.

Improvements to the On-Line Mass Separator, RAMA
and
the Beta-Delayed Charged-Particle Emission of Proton-Rich sd Shell Nuclei

by

Theodore Joseph Ognibene

B.S. (Rensselaer Polytechnic Institute) 1987

A dissertation submitted in partial satisfaction of the
requirements for the degree of
Doctor of Philosophy
in
Chemistry
in the
GRADUATE DIVISION
of the
UNIVERSITY of CALIFORNIA at BERKELEY

Committee in charge:

Professor Joseph Cerny, Chair
Professor Darleane C. Hoffman
Professor P. Buford Price

1996

Abstract

Improvements to the On-Line Mass Separator, RAMA, and the Beta-Delayed Charged-Particle Emission of Proton-Rich sd Shell Nuclei

by

Theodore Joseph Ognibene

Doctor of Philosophy in Chemistry

University of California at Berkeley

Professor Joseph Cerny, Chair

To overcome the extreme difficulties encountered in the experimental decay studies of proton drip line nuclei, several techniques have been utilized, including a helium-jet transport system, particle identification detectors and mass separation. Improvements to the ion source/extraction region of the He-jet coupled on-line Recoil Atom Mass Analyzer (RAMA) and its target/ion source coupling resulted in significant increases in RAMA efficiencies and its mass resolution, as well as reductions in the overall transit time.

At the 88-Inch Cyclotron at LBNL, the decays of ^{31}Cl, ^{27}P and ^{28}P, with half-lives of 150 msec, 260 msec and 270.3 msec, respectively, were examined using a He-jet and low-energy gas ΔE-gas ΔE-silicon E detector telescopes. Total beta-delayed proton branches of 0.3% and 0.07% in ^{31}Cl and ^{27}P, respectively, were estimated. Several proton peaks that had been previously assigned to the decay of ^{31}Cl were shown to be from the decay of ^{25}Si. In ^{27}P, two proton groups at 459±14 keV and 610±11 keV, with intensities of 7±3% and 92±4% relative to the main (100%) group were discovered. The Gamow-Teller component of the preceding beta-decay of each observed proton transition was compared to results from shell model calculations. Finally, a new proton transition was identified, following the β-decay of ^{28}P, at 1444±12 keV with a 1.7±0.5% relative intensity to the 100% group.

Several experiments were attempted, using heavy ion fusion-evaporation reactions, to extend the T_z=-3/2, A=4n+1 series of beta-delayed proton emitters to ^{77}Zr. However, the unambiguous identification of beta-delayed protons from ^{77}Zr was not achieved.

Using similar low-energy detector telescopes and the mass separator TISOL at TRIUMF, the 109 msec and 173 msec activities, ^{17}Ne and ^{33}Ar, were studied. A new proton group with energy 729±15 keV was observed following the beta-decay of ^{17}Ne. Several discrepancies between earlier works as to the energies, intensities and assignments of several proton transitions from ^{17}Ne and ^{33}Ar were resolved.

Table of Contents

Acknowledgments

I am indebted to many people who helped me make this thesis possible. I wish to thank my research director, Professor Joseph Cerny for his guidance and support and Dr. Dennis Moltz for his suggestions and encouragements. In addition, I wish to thank the rest of the RAMA group I have worked with during my graduate school years at Berkeley: Mike Rowe, James Powell, Drew Rice, Jon Batchelder, Rich Tighe, Tom Lang, Jay Reiff, Scott Rippetoe, Steve Thompson, Eric Wang and Celine Detraz.

None of the work described in this thesis could have been possible without the help of the support staff at the 88-Inch Cyclotron, in particular, the operators for their fine beams and the machine shop personnel (Ed, John, Fred and Don) for doing many excellent jobs, often at a moments notice.

I wish to extend to my family my gratitude for everything they have done for me. I want to thank the many friends I have made in Berkeley, including my housemates and the Chem Keg regulars.

And, finally, a special thank you to Kirsten for encouraging me, listening to me, and for just being there when I needed her. Thank you.

I. Introduction

The experimental investigations of exotic nuclei (defined as those nuclei near either the proton drip line or the neutron drip line) serve as a useful means for examining many problems in nuclear physics. These include such fundamental topics as the understanding of the nature of nuclear stability and radioactive decay processes, as well as the elucidation of the motion of nucleons and the structure of the atomic nucleus. These studies provide a stringent test of nuclear models that are often developed based on observations of nuclei that lie closer to the valley of beta stability. There have been several recent articles [Dé 89], [Ro 92] and [Mu 93] that have reviewed the general decay properties of drip-line nuclei and the experimental techniques involved in their studies.

Due to the Coulomb repulsion between protons, the proton drip line lies closer to the valley of beta stability than the neutron drip line and, therefore, is easier to reach experimentally. Additionally, as a result of the Coulomb force, the decay energy rapidly increases as one approaches the proton drip line, opening up such exotic decay modes as beta-delayed proton and alpha emission, beta-delayed two proton emission and direct ground state proton emission. As the following thesis is limited in its discussion of beta-delayed charged-particle emission, the reader is directed to several more detailed reviews [Äy 89], [Ha 88a], [Ho 88] and [Mo 88] that survey these modes of radioactive decay.

Beta-delayed proton or alpha emission is a two step process, in which the precursor nucleus first beta decays to an excited state in the beta daughter (defined as the emitter) which is unbound with respect to either proton and/or alpha emission. If the energy of the isobaric analog state in the beta daughter (defined as the lowest state whose isospin quantum number is the same as the ground state of the parent) is open to proton emission, then the precursor is referred to as a strong beta-delayed proton emitter. The $A = 4n+1$, $T_z = -3/2$ series of nuclei, from ^{17}Ne to ^{61}Ge [Ha 88a], including the recently discovered members ^{65}Se [Ba 93a] and ^{73}Sr [Ba 93c], are all strong βp emitters. The factors governing the emission of the particle are the decay energy available, the height of the Coulomb and centrifugal barrier that the particle must tunnel through and the degree of overlap between the initial and final wavefunctions. The emission of the charged particle is extremely fast so that the observed half-life is the half-life of the preceding beta decay.

The experimental investigation of proton drip-line nuclei is extremely difficult to conduct--as one moves away from the valley of beta-stable nuclides towards the proton drip line, half-lives and production cross sections rapidly decrease. As a result, in order to study the decay properties of the nuclide of interest, it often must be extracted and examined independently from the decays of other nuclei lying closer to stability that were simultaneously and more copiously produced during the bombardment.

The He-jet recoil technique has proven to be a fast and effective method for transporting radioactivity away from the production target chamber to lower background environments. Radioactive recoils, upon exiting the target, are thermalized and attached to potassium chloride aerosols in a helium support gas. They are then transported away from the target chamber via a small diameter (0.5-2 mm i.d.) capillary tube. As the helium is pumped away, the radioactive nuclides-KCl clusters are deposited onto the edge of a wheel where their decays can then be observed by detector telescopes. The detector systems used take advantage of the beta-delayed charged-particle decay characteristics of these proton drip-line nuclei. They have the unique feature of being capable of detecting and identifying low-energy protons (down to ~200 keV) and alpha particles (down to ~400 keV) on an event-by-event basis. These detector telescopes consist of two gas ΔE detectors followed by a silicon E detector. Particle identification is achieved by comparing the differential energy loss in each ΔE gas detector with the total energy deposited in the silicon E detector.

Often identification through delayed proton or alpha decay branches is not sufficient and it is desirable to have a means of mass selection for further verification. Such is the case for the Recoil Atom Mass Analyzer, or RAMA, which is a He-jet coupled on-line mass separator located at the 88-Inch Cyclotron at LBNL. Using a He-jet, the thermalized radioactivity is transported from the target chamber to a differentially pumped skimmer chamber. The excess helium is pumped off and the heavier mass aerosols, which contain the artificially produced radioactivity, enter the ion source, are subsequently broken up and ionized. The ion source consists of a helium-supported arc-discharge plasma which is generated by the thermionic emission of electrons from a hot cathode filament. The primarily +1 charge state ion beam is extracted, accelerated (to energies up to 30 keV), and focused through the main analyzing magnet. The main RAMA dipole is a homogeneous dipole magnet with 13° entrance and exit angles that bends the beam 75.5°. The mass separated radioactive nuclides are then directed and focused to a low background counting station in which their decays are experimentally measured. RAMA was initially developed and successfully used to study the $A = 4n$, $T_Z = -2$ series of beta-delayed proton emitters [Mo 79b]. However, further experiments, although completed, were severely limited by low ion source efficiency and by the long transit time from the target chamber to the ion source. A series of upgrades to RAMA were initiated and completed to increase the ion source efficiency and to reduce the transit time.

This thesis is broken down into five main sections. The second section (the first being this introduction) is a description of isospin and several nuclear mass models, followed by a discussion of the radioactive decay processes undergone by proton drip-line nuclei. Included in this section is a short treatment of the principles of charged-particle ion optics, which are necessary for understanding the underlying features of the RAMA upgrade.

The third section consists of a series of descriptions of the experimental apparatus employed in the study of proton drip-line nuclei examined in this thesis. These, as mentioned above, are the He-jet recoil transport method and the detectors used for the identification of charged particles, as well as details concerning the series of RAMA upgrades. In addition, a brief description is given of the mass separator, TISOL (Test Isotope Separator On Line), which was used for the examinations of the decays of ^{17}Ne and ^{33}Ar. This mass separator, located at the TRIUMF cyclotron in Vancouver, Canada, ionizes and separates the reaction products that are created by the bombardment of liquid or solid targets with 500 MeV protons.

The results of several experimental investigations of the beta-delayed proton and alpha decays of the proton-rich nuclei; ^{31}Cl, ^{27}P, ^{28}P, ^{17}Ne and ^{33}Ar, are presented in the fourth section. The data are analyzed and interpreted revealing detailed spectroscopic information on their beta daughters, as well as providing a test of theoretical models. Additionally, the details of several search experiments to discover and identify ^{77}Zr are presented. This nucleus is the last member of the $A = 4n+1$, $T_z = -3/2$ series of beta-delayed proton emitters that can be studied with stable beams and stable targets without resorting to prohibitively small (HI,5n) reaction channels.

The fifth section of this thesis concludes by briefly summarizing the accomplishments achieved and results obtained, and indicating future experimental endeavors.

II. Theory

The discussion of the theoretical framework relevant to this thesis has two parts: a) a survey of topics pertaining to beta-delayed particle emission and b) a description of the charged-particle ion optics involved in upgrading the on-line mass analyzer, RAMA, to permit the experimental investigation of this phenomenom. Both of these topics are libraries in themselves and an attempt has been made to limit the discussion to those aspects directly relevant to the experiments performed and the equipment developed as described within this thesis.

II.A. Theoretical Aspects of the Nucleus and Radioactive Decay

Due to Coulomb repulsion, as one moves away from the valley of beta stability towards the proton drip line, the energy available for decay increases rapidly. This increase opens up exotic decay channels such as beta-delayed charged particle emission and direct proton emission. A nuclide is considered to exist if its lifetime is longer than 10^{-12} sec [Go 66]. Figures II-1a,b show the Chart of the Nuclides for $Z \leq 40$, $N \leq 52$ indicating the experimentally reached drip line as well as those nuclei with delayed particle decay branches. Which type of decay occurs is primarily dependent upon the energy available for decay. As the masses of many of these nuclei are unknown, accurate methods of prediction have been developed. Integral to these analyses is the concept of nuclear isospin, which is outlined in Sect. II.A.1.. Various nuclear mass models, relevant to drip-line nuclei, are presented in Sect. II.A.2., followed by a detailed description of beta decay in Sect. II.A.3., with the possible subsequent decay modes presented in Sect. II.A.4.. A discussion of direct ground state proton emission can be applied to the model presented in Sect. II.A.4.b., and a detailed review [Ho 88] covers this moderately rare decay mode.

II.A.1. Isospin

Heisenberg [He 32] introduced the concept of isospin by noting that neutrons and protons could be considered to be different states of the same particle, the nucleon, with isospin quantum number $T = 1/2$. Isospin arises from the charge independence of the nuclear strong force, namely that the forces between pairs of nucleons in the same state of relative motion are identical:

$$F_{pp} = F_{nn} = F_{np} \tag{2-1}$$

once the effect of the Coulomb force has been removed. The isospin projection (T_Z) of a proton is -1/2 while that of a neutron is +1/2. A nucleus with N neutrons and Z protons will have a ground state isospin configuration $T \geq |T_Z|$ with isospin projection

$T_Z = 1/2(N-Z)$.

A nuclear state with J^π, T can appear in a 2T+1 series of isobars. This T-multiplet of a given J^π state consists of the two extreme nuclei having $T = 1/2|N-Z|$ as the ground state and the middle nuclei having this "analog state" as an excited state. The excitation energy of these "isobaric analog states" (IAS) increases as (N-Z) decreases due to increases in the Coulomb interaction upon replacing a neutron with a proton. However, if neutron-proton mass differences and Coulomb energies are subtracted out, each member of a T-multiplet is degenerate in energy.

Support for charge independence comes from the near equality of nucleon-nucleon scattering lengths, a, and effective ranges, r_0, after correcting for the effects due to the Coulomb force. These results are tabulated in Table II-1 [Kr 87]. The scattering length is a measure of the strength of the interaction with a negative value indicating an unbound system. The large negative scattering lengths of Table II-1 are unfortunately very sensitive to the nuclear wave function ψ near $r = r_0$ and, hence, a small change in ψ can result in a large change in a. The difference between scattering lengths of the np and nn or pp system corresponds to only a very small difference between potentials (on the order of 1%).

Further evidence comes from the test of models developed to reflect certain characteristics of isospin, such as selection rules. One such test involves nuclear beta decay and superallowed transitions, to be discussed in Sect. II.A.2.b.i.. Briefly, all transitions between 0^+ analog states should have identical Fermi matrix elements, providing that isospin is a conserved quantum number. Eight superallowed $0^+ \rightarrow 0^+$ beta decays of nuclei ranging in mass from ^{14}O to ^{54}Co were examined [Ha 90]. After incorporating small amounts of charge and radiative corrections, it was determined that the ft values for these eight transitions are nearly equivalent with the average ft value of 3073.3±3.5 sec.

As mentioned above, the validity of isospin as a quantum number is a consequence of the charge independence of nuclear forces. However, it is known that there are direct and indirect effects that cause deviation from charge independence [He 66]. It should be noted that the size of these deviations is at most a few percent [Or 89], allowing the use of isospin as a reasonably conserved quantity.

The Coulomb repulsion between protons is the major contributor of direct effects. In reality, equation (2-1) cannot be achieved for it is impossible to "turn off" the Coulomb force at will. Since the Coulomb force is relatively weak compared to the nuclear force, it is possible to treat it as a perturbation [Jä 69]. The result is to shift the energy of the isobaric analog states relative to each other and to introduce small amounts of isospin mixing. The implication of isospin mixing in proton emission will be further discussed in Section IV.B. Other relatively minor sources of direct effects include magnetic interactions, the finite charge and magnetic moment distributions of the nucleons, and the neutron-proton mass difference.

Indirect effects are those that modify the nuclear force itself. The foremost is the consequence of the mass differences of the mesons exchanged between nucleons. The nn or pp system can only exchange the lighter π° pion, whereas the np system can also exchange a charged pion (π^{+} or π^{-}). The result is that the net strength of the np interaction is larger than that of the pp or nn interaction. Other indirect effects include corrections to the meson-nucleon coupling constants and the effects of the mixing of meson states of different isospin but of the same spin and parity. These all serve to make the pp interaction less attractive than the nn one [He 66].

II.A.2. Masses

A fundamental question within nuclear physics is the determination of the nuclear mass surface through both experimental procedures and theoretical development. A knowledge of nuclear masses permits the calculation of reaction Q-values and allows for an a priori assumption about the availablity of specific radioactive decay processes. Most mass models can be broken down and fitted into one of four general classes. These categories are: 1) semi-empirical or phenomenological models, 2) liquid-drop or droplet models, 3) models based on the shell model and 4) mass models based on mass relations. A compilation of eleven mass models is presented by Haustein [Ha 88b].

II.A.2.a. The Kelson-Garvey Mass Relationship

A successful method of estimating nuclear masses utilizes the two recursive relationships by Kelson and Garvey. The Garvey-Kelson (GK) relation [Ga 66] is valid for nuclei in which $N \geq Z$ or $N = Z =$ odd, while the Kelson-Garvey (KG) relation is applicable to nuclei with $Z > N$ and $T \geq 1$. Both relations are based on an independent-particle model of the nucleus where the nucleons move in a self-consistent field and each nucleon is fourfold degenerate. The operations of time reversal and isospin conjugation lead to each energy level being occupied by two neutrons and two protons with up and down spins. The two-body nuclear interaction is primarily absorbed into the single-particle Hartee-Fock energies, with the residual interaction occuring mainly between nucleons in the same level. If these interactions vary slowly and smoothly with mass number A, then this leads to the recursive relationship

$$M(Z-\Delta T, N+\Delta T) - M(Z,N) = \sum_{i=1}^{\Delta T}\left[M(Z-\Delta T-1+i, N+i) - M(Z-\Delta T+i, N-1+i)\right]. \tag{2-2}$$

Figure II-2a shows a heuristic proof while Figure II-2b shows the corresponding representation of the simplest form of equation (2-2). Figure II-2b shows a layout of the Chart of the Nuclides with the plusses and minuses indicating how that nuclide's mass should be evaluated.

The GK mass relation cannot be used to cross the N = Z line, so for nuclei in which Z > N and T > 1, the KG mass relation is used. It connects the proton-rich nucleus with its neutron-rich mirror through mass differences of the $T_Z = \pm 1/2$ nuclei. This relationship is based on the charge-symmetric character of the nuclear force with the mass difference between the mirror nuclei due solely to Coulomb energy effects. The mass $M(A,T_Z)$ of a nucleus with mass number A and isospin projection Tz can be found through the general relationship

$$M(A, T_Z=-T) - M(A, T_Z=+T) = \sum_{\substack{j=-(2T-1) \\ A+j=\mathrm{odd}}}^{+(2T-1)} \left[M\left(A+j, T_Z=-\frac{1}{2}\right) - M\left(A+j, T_Z=+\frac{1}{2}\right)\right]. \tag{2-3}$$

Figure II-3 shows a schematic example of equation (2-3) for a $T_Z = -3/2$ nucleus.

The use of equation (2-3) requires that the masses of the $T_Z = \pm 1/2$ nuclei are known; however, the ground state masses of these nuclei are known only up to ^{59}Zn on the proton rich side and ^{67}As on the neutron rich side [Au 93]. The mass of the $T_Z = +1/2$ nuclei with A > 67 can be determined from the GK mass relation with a Coulomb correction then applied to cross the N = Z line to give the $T_Z = -1/2$ nuclear ground state masses [Co 83 and Jä 84]. This method was used by Jänecke and Masson [Jä 88] with the results compared to 90 known mass excess values leading to a RMS deviation of 231 keV for nuclei with Z > N.

II.A.2.b. Coulomb Displacement Formula

A much more tractable procedure to connect isobaric analog levels in two neighboring nuclei is to use the Coulomb displacement energy formula [An 85]. The mass of each successive member of an isobaric multiplet is obtained [Co 75] from the equation

$$\Delta E_C = M_{Z>} - M_{Z<} + \Delta nH, \tag{2-4}$$

where, $M_{Z>}$, $M_{Z<}$ is the mass of the isobaric analog state in the higher Z nuclide and lower Z nuclide, respectively, and ΔnH is the neutron-hydrogen atom mass difference (782.3 keV).

The Coulomb displacement energy ΔE_C is given by

$$\Delta E_C = k_1\left(\frac{\overline{Z}}{A^{1/3}}\right) + k_2, \tag{2-5}$$

where, $\overline{Z}$ is the average atomic charge between pairs of the mass A nuclei and k_1 and k_2 are parameters that have been fitted to experimental data. For $3 \leq A \leq 45$: $k_1 = 1440.8$ keV, $k_2 = -1026.3$ keV [An 86] and for $44 \leq A \leq 239$: $k_1 = 1412$ keV, $k_2 = -861$ keV [An 88].

II.A.2.c. Isobaric Multiplet Mass Equation (IMME)

A final mass model to be discussed is the IMME which was first introduced by Wigner [Wi 57]. The degeneracy of the (2T+1) members of an isospin multiplet is broken by the charge-dependent coupling between nucleons, namely Coulomb interactions and spin-orbit coupling. These interactions can be treated as a perturbation H' to the charge-independent Hamiltonian H_{ci} and by the standard application of the Wigner-Eckart theorem to the eigenstates of H_{ci} leading to the expression

$$\left\langle \alpha T\, T_z \middle\| H' + H_{ci} \middle\| \alpha T\, T_z \right\rangle = a + bT_z + cT_z^2, \tag{2-6}$$

where, all nuclear quantum numbers aside from isospin are contained within α, and the coefficients a, b and c contain the scalar, vector and tensor components of the Coulomb energy, respectively. The IMME is more commonly expressed as

$$M(A,T,T_z) = a(A,T) + b(A,T)T_z + c(A,T)T_z^2. \tag{2-7}$$

Carrying out the perturbation calculation to second order leads to the additional terms dT_z^3 and eT_z^4, although there can only be 2T+1 coefficients for each value of T. The significance of non-zero d and e coefficients can be attributed to Coulomb repulsion in the proton-rich member spreading out the wavefunction, isospin mixing and charge-dependent many-body forces [An 85]. However, a significant fraction of each effect is taken up by the b and c coefficients [Be 79]. In general, the mass of the analog states can be successfully reproduced by consideration of the a, b and c coefficients only. Any d or e coefficients, if not zero, are of the order of 1-10 keV.

II.A.3. Beta Decay

Beta decay is the nuclear process moderated by the weak interaction, in which one type of nucleon is converted into the other accompanied by the emission of two leptons, a beta particle and either an antineutrino or a neutrino. Obviously, the exact process depends upon which side of the valley of beta stability the nuclide resides. On the neutron-rich side, a neutron is converted into a proton with the subsequent emission of an electron (β^-) and an antineutrino ($\bar{\nu}$). Q_{β^-}, the energy available for this mode of decay, is the energy equivalent of the mass difference between parent and daughter nuclides. β^+-decay involves the conversion of a bound proton into a bound neutron with the emission of a positron (β^+) and a neutrino (ν). The energy available for this decay, Q_{β^+} is the energy equivalent of the mass difference between parent and daughter nuclides minus the rest mass of two electrons.

Competing against β^+-decay is electron capture (EC) decay whereby an atomic electron is captured by the nucleus, combined with a proton to form a bound neutron and an emitted neutrino. In light nuclei with large $Q_{\beta+}$ values, the competition from EC-decay is insignificant for the following reasons. As Z decreases, the expectation value of finding an orbital electron within the nucleus decreases. Additionally, for a given Z, as the decay energy increases, the transition rate for β^+-decay increases more rapidly than the transition rate for EC-decay. Since the nuclei discussed in this thesis are light nuclei with rather large $Q_{\beta+}$ values, EC decay is insignificant and will not be further discussed.

II.A.3.a. Transition Rates

The decay probability per unit time is a result from time-independent perturbation theory. More specifically, it arises from the application of Fermi's Golden Rule #2 [Fe 50], which concerns transitions to a group of final states:

$$\lambda = \frac{2\pi}{\hbar}|W_{fi}|^2 \rho(E_f), \tag{2-8}$$

where, $\rho(E_f)$ is the density of final states and $|W_{fi}|^2$ is the interaction matrix element connecting initial and final states.

The minimum volume of phase space of any given state of the lepton is determined by the Heisenberg Uncertainty Principle [Fe 34]:

$$\Delta x \Delta y \Delta z \Delta p_x \Delta p_y \Delta p_z \approx h^3. \tag{2-9}$$

Additionally, the lepton is localized within a spatial volume, V, and momentum interval p to p + dp. The volume of a shell with radius, p, and thickness, dp, is given as $4\pi p^2 dp$. Then the number of final states is

$$dn = \frac{4\pi p^2 dp V}{h^3}. \tag{2-10}$$

Combining this for both emitted leptons, the density of final states in energy interval, dE_f, is

$$\rho(E_f) = \frac{dn}{dE_f} = \frac{16\pi^2 p_e^2 p_\nu^2 V^2 dp_e dp_\nu}{h^6 dE_f}. \tag{2-11}$$

The matrix element, W_{fi}, can be expressed as

$$W_{fi} = g\int \phi_e^* \phi_\nu^* \psi_f^* \hat{O} \psi_i d\Omega , \tag{2-12}$$

where, g, the Fermi coupling constant, is the strength of the interaction, ϕ_e^*, ϕ_ν^* are the complex conjugates of the lepton wavefunctions, ψ_i, ψ_f^* are the initial nuclear wavefunction and the complex conjugate of the final nuclear wavefunction, and $\hat{O}$ is the operator that converts one nucleon into the other.

The lepton wavefunctions can be expressed as plane waves normalized within the volume V:

$$\begin{aligned} \phi_e(r) &= \frac{1}{\sqrt{V}} e^{i\left(\frac{\vec{p}_e \cdot \vec{r}}{\hbar}\right)} \\ \phi_\nu(r) &= \frac{1}{\sqrt{V}} e^{i\left(\frac{\vec{p}_\nu \cdot \vec{r}}{\hbar}\right)}. \end{aligned} \tag{2-13}$$

Since the nuclear volume is small compared to the spatial volume for the emitted leptons, the wavefunctions can be expanded into a power series and only the first term considered:

$$\phi_\nu(r) = \frac{1}{\sqrt{V}}\left[1 + \frac{i\vec{p}_\nu \cdot \vec{r}}{\hbar} + \ldots\right] = \frac{1}{\sqrt{V}}. \tag{2-14}$$

Due to its charge, the beta particle's wavefunction is strongly affected by the Coulomb field of the nucleus and the orbital electrons. In the case of β^+-decay and relative to the hypothetical case of Z = 0, where the positron's wavefunction is well described as a plane wave, the Coulomb field of the nucleus tends to decrease the positron's density within the nuclear volume. Since the wavelength of the positron is large compared to the size of the nucleus, this effect is to change the probability density for the positron within the nuclear volume, while maintaining an approximately constant amplitude.

The wavefunction for the emitted positron can now be written as:

$$\phi_e(r) = \frac{1}{\sqrt{V}}\left[1 + \frac{i\vec{p}_e \cdot \vec{r}}{\hbar} + \ldots\right] \cdot F(Z,E)^{1/2} = \frac{F(Z,E)^{1/2}}{\sqrt{V}}, \tag{2-15}$$

where, F(Z,E), the Coulomb correction factor, is the ratio of electron density at the daughter nucleus to the density at infinity:

$$F(Z,E) = \frac{|\phi_e(0)|_Z^2}{|\phi_e(0)|^2}. \tag{2-16}$$

The main effect of F(Z,E), in the case of β^+-decay, is to accelerate the emitted positrons away from the nucleus and hence shift their energy spectrum away from the low-energy end. Substituting (2-14) and (2-15) into (2-12):

$$W_{fi} = \frac{g}{V} M_{fi} F^{1/2}(Z,E), \tag{2-17}$$

where, $M_{fi} = \langle \psi_f | \hat{O} | \psi_i \rangle$ is the nuclear matrix element.

Substituting (2-11) and (2-17) into (2-8), the decay probability per unit time is

$$\lambda = \frac{g^2}{2\pi^3 \hbar^7} |M_{fi}|^2 p_e^2 p_\nu^2 \frac{dp_e dp_\nu}{dE_f} F(Z,E). \tag{2-18}$$

The neutrino momentum, p_ν, can be rewritten in terms of E_f and the positron energy, E_e, (neglecting the small nuclear recoil energy):

$$E_f = E_e + p_\nu c \tag{2-19}$$

and

$$\frac{p_\nu^2 dp_\nu}{dE_f} = \frac{(E_f - E_e)^2}{c^3}. \tag{2-20}$$

Substituting (2-20) into (2-18) and integrating over all possible momenta gives the beta transition rate, λ

$$\lambda = \frac{g^2}{2\pi^3 \hbar^7 c^3} |M_{fi}|^2 \int_0^{p_{max}} F(Z,E)(E_f - E_e)^2 p_e^2 dp. \tag{2-21}$$

The integral is known as the Fermi integral, f(Z,E). Rewriting (2-21) in terms of the partial half-life gives the comparative half-life of the transition, ft,

$$ft = \frac{2\pi^3 \hbar^7 \ln 2}{g^2 m_e^5 c^4 |M_{fi}|^2} = \frac{4.7944 \times 10^{-5} \mathrm{MeV}^2\ \mathrm{fm}^6\ \mathrm{sec}}{g^2 |M_{fi}|^2}. \tag{2-22}$$

Beta decay half-lives range from ~10^{-2} sec to 10^{16} sec; therefore, it is easier to discuss ft values as the log ft.

II.A.3.b. Classification of Beta Decays

Beta decay transitions fall into two groups: allowed and forbidden. Allowed transitions are characterized by low ft values and are generally much faster since the emitted leptons carry off no orbital angular momentum ℓ, and there is no nuclear parity change ($\Delta\pi$ = no). In forbidden transitions, the leptons carry off angular momentum (one unit per degree of forbiddenness) and there is a possible change in nuclear parity dictated by

$$\Delta\pi = (-1)^{\ell}. \tag{2-23}$$

Table II-2 lists the selection rules for beta decay [Ra 73].

II.A.3.b.i. Allowed Decays

In allowed beta decay, the only change in nuclear spin (ΔI) results from the intrinsic spins of the emitted leptons. The intrinsic spin of each has a value ±1/2 and can be coupled in an anti-parallel singlet state or in a parallel triplet state. The former condition has $\Delta I = 0$ and is known as a Fermi (F), or vector, decay; the latter has $\Delta I = 0, \pm 1$ and is referred to as Gamow-Teller (GT), or axial vector, decay. The only exception is that $0^+ \rightarrow 0^+$ transitions cannot occur via GT decay. In addition, the isospin selection rules dictate that the change in isospin (ΔT) be $\Delta T = 0$ for a Fermi decay and $\Delta T = 0$ or 1 for a Gamow-Teller decay.

The comparative half-life for allowed transitions can be expressed as:

$$ft = \frac{4.7944 \times 10^{-5} \mathrm{MeV}^2\ \mathrm{fm}^6\ \mathrm{sec}}{g_V^2 |M_V|^2 + g_A^2 |M_A|^2}, \qquad (2\text{-}24)$$

where, M_V is the Fermi (vector) matrix element, M_A is the Gamow-Teller (axial vector) matrix element, g_V is the vector coupling constant, and g_A is the axial vector coupling constant.

A subset of allowed decays are the superallowed transitions. These take place between members of an isospin multiplet so they merely involve changing a proton into a neutron without changing its wavefunction. These decays are the fastest type of beta decay since there is excellent overlap between initial and final nuclear wavefunctions.

By examining several well known superallowed $0^+ \rightarrow 0^+$ decays, g_V can be experimentally determined since $M_A = 0$ and M_V can be calculated independently of any details of the nuclear wavefunctions involved, the only stipulation being that both states be pure isospin states. M_V can be expressed in terms of the isospin raising operator, τ_+, (for β^+-decay), or the lowering operator, τ_-, (for β^--decay),

$$\begin{aligned} M_V &= \left\langle I = 0^+, T, T_Z \middle| \tau \pm \middle| I = 0^+, T, T_Z \mp 1 \right\rangle \\ &= \sqrt{(T \mp T_Z)(T \pm T_Z + 1)} \end{aligned} \qquad (2\text{-}25)$$

for $J_{\mathrm{final}} - J_{\mathrm{initial}} = T_{\mathrm{final}} - T_{\mathrm{initial}} = 0$. Comparative half-life values were calculated in this manner using (2-25), as well as including corrections due to outer-radiative effects and charge-independence breaking effects [Ha 90]. From this, the effective vector coupling constant, g'_V, was determined to be

$$\frac{g'_V}{(\hbar c)^3} = (1.14939 \pm 0.00065) \times 10^{-5}\ \mathrm{GeV}^{-2}. \qquad (2\text{-}26)$$

The determination of the axial vector coupling constant is much more difficult due to the incomplete understanding of the matrix elements involved. From the measurement of the β-decay asymmetry of the free neutron, the ratio of the coupling constants was determined to be $|g_A/g_V| = 1.260 \pm 0.003$ [Kl 88].

The Gamow-Teller matrix element, M_A, can be written as a sum over all the nucleons (n) in the nucleus:

$$|M_A|^2 = \langle \psi_f | \sum^{n} \sigma(n) \cdot \tau_{\pm}(n) | \psi_i \rangle, \tag{2-27}$$

where, $\sigma(n)$ is the Pauli spin operator and $\tau_{\pm}(n)$ is the isospin raising or lowering operator for a given nucleon. The magnitude of $\tau_{\pm}(n)$ is dependent on the details of the nuclear wavefunctions involved. In the extreme single-particle limit, M_A can be calculated to an order of magnitude [Sh 74]. This method, however, is not accurate enough compared to experimental precision. Therefore, large-basis shell-model calculations have been performed that calculate matrix elements which are then compared to experiment. It has been observed that there is a quenching of the experimental GT strength compared to the calculated strength. In the p- and lower sd-shell nuclei, a quenching factor of 0.805 ± 0.035 was obtained [Wi 73], while in the upper sd shell and lower fp shell, factors of 0.58 ± 0.03 and 0.560 ± 0.027, respectively, were obtained [Br 85 and Mi 87].

Inserting (2-25) and (2-26) into (2-24) yields:

$$ft = \frac{6147 \pm 3 \ \text{sec}}{\left[T(T+1) - T_Z(T_Z \pm 1)\right] + (1.588 \pm 0.004)|M_A|^2} \tag{2-28}$$

for an allowed beta transition in which $T_f = T_i$.

II.A.3.b.ii. Forbidden Beta Transitions

As mentioned above, forbidden transitions result in a change in nuclear spin and/or a change in nuclear parity. They are forbidden in the sense that in the allowed approximation for the plane wave expansion of the emitted leptons, the nuclear matrix elements M_V and M_A are non zero only when the positron and neutrino carry off no orbital angular momentum. Therefore, if they do carry off angular momentum, the matrix elements must vanish and the decay cannot occur. In the plane wave expansion for ϕ_e and ϕ_ν ((2-14) and (2-15)), n additional terms, for each degree of forbiddenness, must be considered to take into account that the wavefunctions are not exactly constant over the nuclear volume. An additional influence arises from the intrinsic motion, v_n, of the nucleons inside the nucleus. This will give rise to an extra relativistic correction term to the matrix element of a magnitude v_n/c smaller than the uncorrected amount. Both of these effects serve to retard the beta decay transition rate [We 61].

II.A.4. Beta-Delayed Radioactivity

Following beta decay, the daughter nucleus can be left in an excited state which can subsequently emit one or more particles. As the nuclei discussed in this thesis are beta-delayed proton (βp) or beta-delayed alpha ($\beta\alpha$) emitters, only proton and alpha emission will be discussed. A recent review [Jo 95] covers other beta-delayed particle emission. There are well over a hundred known βp and $\beta\alpha$ emitters throughout the Chart of the Nuclides [Ha 88a]. The probability for the emission of a proton or alpha is dependent upon the energy available for decay, the Coulomb and centrifugal barriers, and the degree of overlap between initial and final wavefunctions. The general case of βp and $\beta\alpha$ emission is depicted in Figure II-4. The total decay energy available and the proton and alpha particle separation energies are marked as Q_{EC}, S_p and S_α, respectively.

Given the low density of states found in light nuclei, it is often possible to resolve individual transitions from measured particle spectra. The absolute intensity of a particular transition is given by

$$I_i = \left(I_{\beta^+}\right)\left(\frac{\Gamma_i}{\Gamma_T}\right), \qquad (2\text{-}29)$$

where, I_{β^+} is the intensity of the beta feeding to the emitting state and the subscripts i and T refer to either a proton or alpha and the total decay width expressed as the sum of all decay widths energetically permissible (in this case, $\Gamma_p + \Gamma_\alpha + \Gamma_\gamma$).

II.A.4.a. Gamma-Ray Transitions

In general, proton or alpha emission will occur much more rapidly than the competing gamma-ray emission channel. However, as the energy of the emitted proton or alpha decreases, the half-life for such a transition can increase to such a point that a gamma-ray transition will compete. An estimate of the lower limit of the half-life of a given gamma-ray transition has been derived by Weisskopf and Blatt [We 51 and Bl 52]. It is important to note that the half-life of an electromagnetic decay transition from an excited state will decrease if internal conversion also occurs. For an electric multipole transition of order L it is given as:

$$t_{1/2}(E) \approx \frac{0.645 \times 10^{-21}}{S}\left(\frac{140}{E_\gamma(\text{MeV})}\right)^{2L+1} A^{-\left(\frac{2L}{3}\right)} \text{sec}, \qquad (2\text{-}30)$$

and for magnetic multipole transitions it is given as:

$$t_{1/2}(M) \approx \frac{2.9 \times 10^{-21}}{S}\left(\frac{140}{E_\gamma(\text{MeV})}\right)^{2L+1} A^{-\left(\frac{2(L-1)}{3}\right)} \text{sec}. \qquad (2\text{-}31)$$

The statistical factor S is equal to:

$$S=\frac{2\left(1+\frac{1}{L}\right)}{\left[(2L+1)\ x\ (2L-1)\ x \ldots x\ 3\ x\ 1\ x\left(1+\frac{L}{3}\right)\right]^2}. \tag{2-32}$$

The selection rules, as well as the single-particle estimates of the gamma-ray half-lives are presented in Table II-3.

II.A.4.b. Proton and Alpha Transitions

The decay width for exit channel a, Γ_a, can be expressed as the product of the penetrability, $P_{a\ell}$, and the reduced width, $\gamma^2_{a\ell}$,

$$\Gamma_{a\ell}=2P_{a\ell}\left(\gamma^2_{a\ell}\right), \tag{2-33}$$

where, ℓ is the angular momentum of the emitted particle and chosen to be the lowest possible value that is consistent with $\Delta\pi=(-1)^{\ell}$. All the nuclear structure effects are contained in the $\gamma^2_{a\ell}$ term.

The penetrability can be calculated using the R-matrix formalism [La 58] considering the time-reversed process:

$$\begin{aligned} &p\ +\ (A-1, Z-1)\rightarrow(A,\ Z)\ \text{or}\\ &\alpha\ +\ (A-4, Z-2)\rightarrow(A,\ Z). \end{aligned} \tag{2-34}$$

The penetrability is given by:

$$P_{a\ell}=\frac{kR}{A^2_{a\ell}}, \tag{2-35}$$

where, k is the wave number of the emitted particle determined from the deBroglie relationship, $p=\hbar k$, in the center of mass system and R is the radius of the system, given as:

$$R=r_0\left(A_1^{1/3}+A_2^{1/3}\right). \tag{2-36}$$

The denominator of (2-35) is the penetration function and is expressed as:

$$A^2_{a\ell}=F^2_{a\ell}+G^2_{a\ell}, \tag{2-37}$$

where, $F_{a\ell}$ and $G_{a\ell}$ are the regular and irregular solutions to the Schrodinger equation for a Coulomb potential.

The reduced width, $\gamma^2_{a\ell}$, can be estimated from the Wigner sum-rule limit [Ma 68] and is expressed through the following:

$$\gamma^2_{a\ell}=\frac{3\,\hbar^2}{2\,\mu\,R^2}\Theta^2, \tag{2-38}$$

where, μ is the reduced mass and Θ^2 is a spectroscopic factor representing the probability of finding the emitted proton or alpha with the appropriate wavefunction at the nuclear surface.

Combining (2-33) and (2-38) and setting $\Theta^2 = 1$, the upper limit on the widths and the lower limit on the half-life of a proton or alpha emission are given as

$$\Gamma_{a\ell} = \frac{125.4 \, P_{a\ell}}{\mu R^2} \text{ MeV} \tag{2-39}$$

and

$$t = \tau \ln 2 = \frac{\hbar \ln 2 \, \mu R^2}{125.4 \, P_{a\ell}} \text{ sec.} \tag{2-40}$$

An example of penetrability calculations, using the code COCAGD [Se 73], is presented in Figure II-5. The plot concerns transitions from excited states in ^{24}Mg to the ground states of ^{20}Ne (for alpha emission) and ^{23}Na (for proton emission) following the beta decay of ^{24}Al [Ba 94]. The larger the excitation energy in ^{24}Mg, the greater the energy of the emitted particle. This illustrates the partial half-life's dependence on the energy and angular momentum of the emitted particle. The longer the partial half-life, the smaller the decay width which results in a decrease in the transition probability (unless it is the only channel open).

II.B. Charged-Particle Ion Optics

For purposes of discussion, a beam is defined as an ensemble of noninteracting particles, of charge q, moving more or less together and affected by the same external forces. This paraxial approximation greatly simplifies the mathematical treatment and is applicable to almost all beams. The beam consists of a collection of points each defined by the coordinate axes (x, y, z, p_x, p_y, p_z) within a volume of phase space. When discussing charged-particle beams, the x-coordinate is the radial or horizontal direction, the y-coordinate is the vertical direction and the z-coordinate is the axial direction along the beam axis. The magnetic rigidity, $B\rho$, is defined as

$$B\rho = \frac{p}{q}. \tag{2-41}$$

The beam consists of particles of different rigidities and the deviation, δ, of a particle's rigidity from that of a reference particle is expressed as

$$B\rho = (B\rho)_0 [1 + \delta], \tag{2-42}$$

where, $(B\rho)_0$ is the magnetic rigidity of a particle chosen to define the beam, referred to as the reference particle.

II.B.1. The Beam Ellipse

If the beam is not changing energy (monochromatic) and its transverse velocity is small compared to its axial velocity, then the angular dispersion in each plane is the ratio of transverse to axial momenta;

$$x' = \frac{p_x}{p_z} \text{ and } y' = \frac{p_y}{p_z}. \tag{2-43}$$

It is possible to represent the beam profile as independent ellipses in the (x, x') and the (y, y') planes. The area of this ellipse is the emittance defined as

$$\varepsilon_x = \frac{x \cdot x'}{\pi} \text{ and } \varepsilon_y = \frac{y \cdot y'}{\pi}. \tag{2-44}$$

The beam inside this ellipse is not uniformly dense, but rather has a Gaussian profile. In this case the fraction, f, of all ions within a beam profile can be related to the root mean square emittance, ε_{rms}, as [La 71]

$$f = 1 - \exp\left(\frac{-\varepsilon}{2\varepsilon_{rms}}\right), \tag{2-45}$$

with

$$\varepsilon_{xrms} = \left[\left(\overline{x^2}\,\overline{x'^2}\right) - \left(\overline{xx'}\right)^2\right]^{\frac{1}{2}} \tag{2-46}$$

and

$$\varepsilon_{yrms} = \left[\left(\overline{y^2}\,\overline{y'^2}\right) - \left(\overline{yy'}\right)^2\right]^{\frac{1}{2}}, \tag{2-47}$$

where the averages for x, y, x' and y' are weighted by the beam intensity. For a beam that is extracted parallel to the beam axis with energy, E_b, from a circular aperture with radius a, the rms emittance can be related to the ion source temperature T [Ho 89]

$$\varepsilon_{xrms} = \frac{a}{2}\left(\frac{kT}{2E_b}\right)^{\frac{1}{2}} = \varepsilon_{yrms}. \tag{2-48}$$

Breaking down the motion into three independent planes requires (through Liouville's theorem) that at any time t, the 2-dimensional phase space areas be conserved.

$$\iint d_x dp_x = \text{const}_x \; , \; \iint d_y dp_y = \text{const}_y \; , \; \iint d_z dp_z = \text{const}_z. \tag{2-49}$$

The implication being that the emittance in each plane must remain constant throughout the ion beam's entire trajectory.

II.B.2. Ion Motion In Magnetic And Electric Fields

There are two forces to be considered that influence the motion of a particle with charge q: namely, a Lorentz force from a static magnetic field (**B**) and a Coulomb force from an electrostatic field (**E**),

$$\begin{aligned}\vec{F}_B &= q\vec{v} \times \vec{B} \\ \vec{F}_E &= q \cdot \vec{E}.\end{aligned} \tag{2-50}$$

In both cases, the particle experiences a centripetal acceleration towards the center of a circle with a radius of curvature ρ

$$F_{B\text{ or }E} = \frac{mv^2}{\rho}. \tag{2-51}$$

Since both **B** and **E** are static fields, the force that the particle experiences is felt in only one plane, the bend plane. The path that this reference particle follows is defined as the central trajectory of the beam. The equations of motion for a particle in a static magnetic or electric field are derived in many texts [*e.g.*, Ba 66 and Ca 87] and only the results will presented here.

The equation of motion of the central trajectory are, to a first-order approximation, linear second-order differential equations. The solution in the bend plane consists of a linear combination of a sine-like function, a cosine-like function and a dispersion function: and in the non-bend plane, a linear combination of a sine-like function and a cosine-like function:

$$\begin{aligned}x(t) &= x_0C_x(t) + x'_0S_x(t) + \delta D_x(t) \\ y(t) &= y_0C_y(t) + y'_0S_y(t),\end{aligned} \tag{2-52}$$

where, x_0, x'_0, δ; and y_0, y'_0 are as defined above referring to the bend and the non-bend plane, respectively, $C_{x,y}$ and $S_{x,y}$ are the cosine-like and sine-like functions, and $D_x(t)$ is the dispersion function representing the separation of trajectories with different momenta as a result of the different radii of curvature that each experiences.

This solution can be represented as transfer matrices in both planes, R(x) and R(y), that can be used to describe the movement of a beam from an initial position at x_0 (y_0), x'_0 (y'_0) and δ_0 to a final position x (y), x' (y') and δ to a first-order approximation:

$$\begin{pmatrix} x \\ x' \\ \delta \end{pmatrix} = \begin{pmatrix} (x|x) & (x|x') & (x|\delta) \\ (x'|x) & (x'|x') & (x'|\delta) \\ 0 & 0 & 1 \end{pmatrix} \begin{pmatrix} x_0 \\ x'_0 \\ \delta_0 \end{pmatrix} \tag{2-53}$$

and

$$\begin{pmatrix} y \\ y' \end{pmatrix} = \begin{pmatrix} (y|y) & (y|y') \\ (y'|y) & (y'|y') \end{pmatrix} \begin{pmatrix} y_0 \\ y'_0 \end{pmatrix}, \tag{2-54}$$

where, the elements inside the matrix are the coefficients of the Taylor series expansion to the functions of (2-52).

This representation of transfer matrices is a powerful tool when designing beam lines. The calculation of solutions for ion optics starts with the creation of transfer matrices for each element along the beam line. Then starting from the end, the individual transfer matrices are multiplied together so as to generate a complete transfer matrix in each plane, $R_t(x)$ and $R_t(y)$. Included in the coefficients are the actual strengths of the optical elements being described. One needs to optimize these field strengths to suit the desired solution and there are four useful conditions that can be attained [Wo 87a]. The first is when $(x|x') = 0$. This describes a solution where the beam is initially at a point and is brought to a point focus at the end of the beam line (point-to-point focusing). The second is parallel-to-parallel focusing where the condition of $(x'|x) = 0$ is fulfilled. Initially the beam is traveling parallel ($x'_0 = 0$) and at the end it is still traveling parallel, although the size of the beam may be different. The final two conditions describe parallel-to-point and point-to-parallel focusing which occurs when $(x|x) = 0$ and $(x'|x') = 0$, respectively. The (y, y') plane can be similarly described.

The size of the envelope (in the x, x' plane) of the beam ellipse and the maximum angle of inclination of any trajectory within the beam can be determined from the matrix coefficients:

$$R_{xn} = \sqrt{(x|x)^2 x_0^2 + (x|x')^2 x_0'^2} \tag{2-55}$$

and

$$S_{xn} = \sqrt{(x'|x)^2 x_0^2 + (x'|x')^2 x_0'^2}, \tag{2-56}$$

where, R_{xn} and S_{xn} are the half-width and half-angle at $z = z_n$, respectively. R_{yn} and S_{yn} are also described in this manner.

After the beam has gone through a dispersive element such as a magnetic dipole, particles of different rigidity having undergone different deflections will be separated spatially on the focal plane. The dispersion, D_δ, is a measure of the dispersive strength of the dipole:

$$D_\delta = 2(x|\delta). \tag{2-57}$$

The rigidity resolving power, R_δ, is the reciprocal of the minimum distance between two trajectories that are on the focal plane that can still be separated:

$$R_\delta = -\frac{1}{\delta_{min}} = -\frac{(x|\delta)}{x_0(x|x) + x_0'(x|x')}. \tag{2-58}$$

Both (2-57) and (2-58) describe a homogeneous magnetic dipole with inclined edges which characterizes the main magnet in RAMA.

II.B.3. Aberrations

In deriving the equations of motion (2-52), only the first order terms of the Taylor series expansion were considered. However, for realistic beams, significant deviations from the first-order approximation are present, requiring the expansion to second- and higher-order terms. Generally, these deviations are only significant at focus points where the beam is constrained to a small cross section. As an extended treatment of aberrations is beyond the scope of this thesis, only generalizations will be presented. A more detailed treatment is provided in [Sz 88]. It is important to remember that in this discussion, only aberrations within the central trajectory are considered. Differences due to ions of a different mass give rise to a dispersion, $D\delta$, as defined in Sect. II.B.2.

Aberrations arise from several sources and can be grouped together as such. Chromatic aberrations are caused by an energy spread in the central trajectory. This is created by differences in initial velocities, as it is impossible for the ion source to produce a completely monochromatic beam. Also, scattering of the beam with itself, residual gas molecules or surfaces can change the velocity. Geometrical aberrations are those that involve differences in initial positions and angles of inclination within the central trajectory. These can be subgrouped by those in which the effect is due entirely to the initial angle (aperture aberration), to differences in initial position (image distortion) and those due to the combined effects of initial angle and position (mixed aberrations).

These aberrations are exacerbated by fringing fields of optical elements, multiple-order field effects due to imperfectly formed electrodes or pole faces and misalignments. The result is an image point constructed of a collection of individual ions arriving at a specific plane with different angles of inclination and different positions, blurring the focus. The full coordinate, to second order, is expressed as

$$\begin{aligned} x = {} & (x|x)x_0 + (x|x')x'_0 + (x|\delta)\delta_0 \\ & + (x|xx)x_0^2 + (x|xx')x_0x'_0 + (x|x\delta)x_0\delta_0 \\ & + (x|x'x')x'^2_0 + (x|x'\delta)x'_0\delta_0 + (x|\delta\delta)\delta_0^2 \\ & + (x|yy)y_0^2 + (x|yx')y_0x'_0 + (x|y'y')y'^2_0, \end{aligned} \tag{2-59}$$

in the x-direction, and as

$$\begin{aligned} y = {} & (y|y)y_0 + (y|y')y'_0 \\ & + (y|xy)x_0y_0 + (y|xy')x_0y'_0 + (y|x'y)x'_0y_0 \\ & + (y|x'y')x'_0y'_0 + (y|y\delta)y_0\delta_0 + (y|y'\delta)y'_0\delta_0 \end{aligned} \tag{2-60}$$

in the y-direction.

Concerning the RAMA system, the ultimate goal of its beam optics system is the size of the beam spot at the final focus points. As will be discussed in Sect. III.C.1.b., the initial source of the beam has angular dispersions x' and y', much larger than the corresponding beam size x and y. The only second-order geometrical aberrations that need to be considered are the aperature aberrations and the mixed aberrations. The correction of these effects can be accomplished by the use of magnetic sextupoles and edge sextupoles. Neither of these elements can affect the beam in first order, but only in second- and higher-order treatments.

II.C. Tables for Section II

Table II-1. Low energy nucleon-nucleon scattering parameters.

	SYSTEM		
	pp	nn	np*
Scattering Length, a (fm)	-17.1 ± 0.2	-16.6 ± 0.5	-23.715 ± 0.015
Effective Range, r_0 (fm)	2.84 ± 0.03	2.66 ± 0.15	2.73 ± 0.03

*The data for np scattering corresponds to results from the singlet state.

Table II-2. Beta Decay selection rules.

Type	ℓ	ΔI	$\Delta\pi$	Typical log ft
Superallowed	0	0	no	3
Allowed	0	0, 1	no	4 - 12
First Forbidden	1	0, 1, 2	yes	6 - 15
Second Forbidden	2	2, 3	no	11 - 18
Third Forbidden	3	3, 4	yes	17 - 19

Table II-3. Gamma-Ray transition selection rules.

Type	L	ΔI	$\Delta\Pi$	Partial half-life (sec)
E1	1	0, 1	yes	$5.7 \times 10^{-15} E^{-3} A^{-2/3}$
M1	1	0, 1	no	$2.2 \times 10^{-14} E^{-3}$
E2	2	0, 1, 2	no	$6.7 \times 10^{-9} E^{-5} A^{-4/3}$
M2	2	2	yes	$2.6 \times 10^{-8} E^{-5} A^{-2/3}$
E3	3	2, 3	yes	$1.2 \times 10^{-2} E^{-7} A^{-2}$
M3	3	3	no	$4.9 \times 10^{-2} E^{-7} A^{-4/3}$
E4	4	3, 4	no	$3.4 \times 10^{4} E^{-9} A^{-8/3}$
M4	4	4	yes	$1.3 \times 10^{5} E^{-9} A^{-2}$

II.D. Figures for Section II

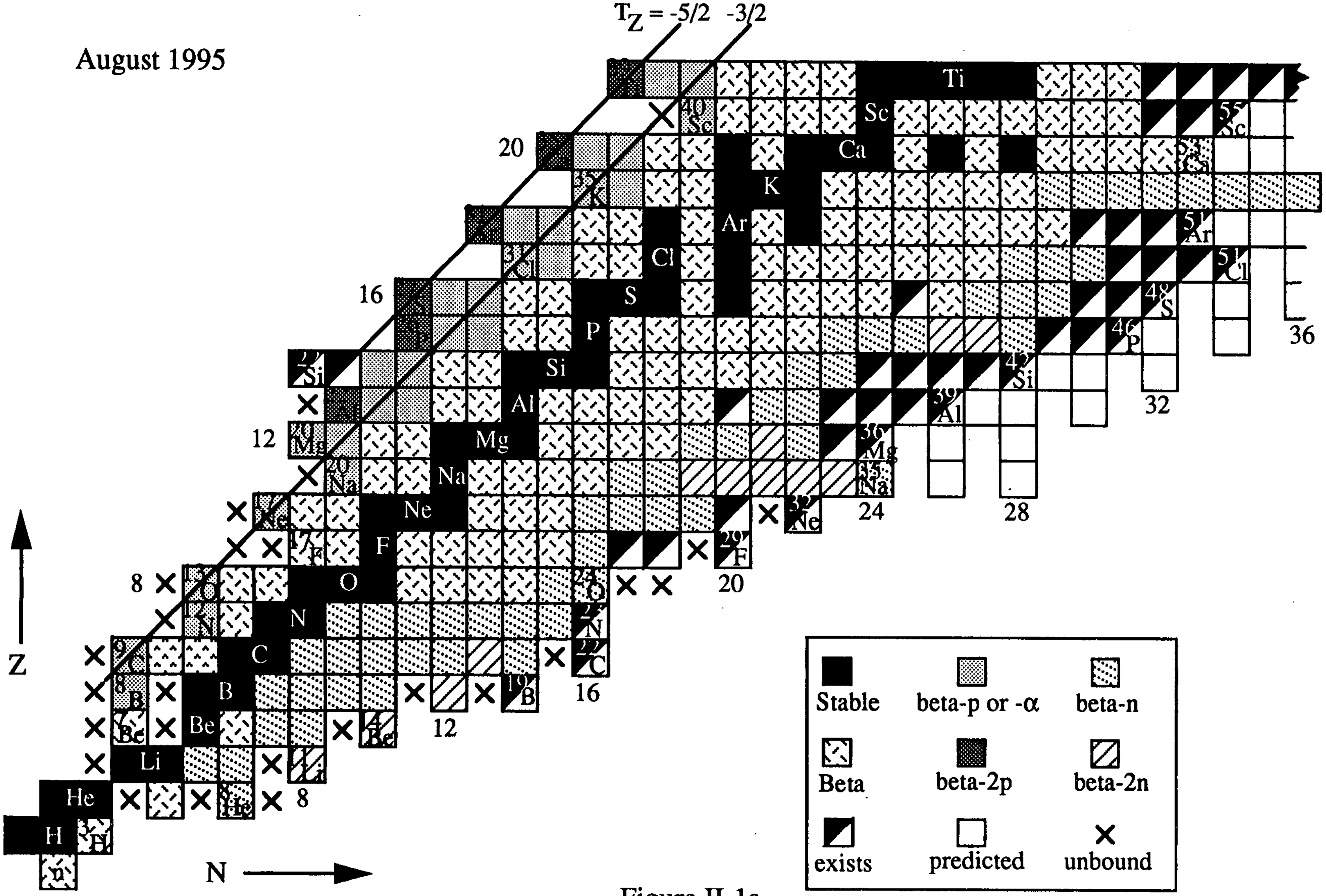

August 1995

Figure II-1a.

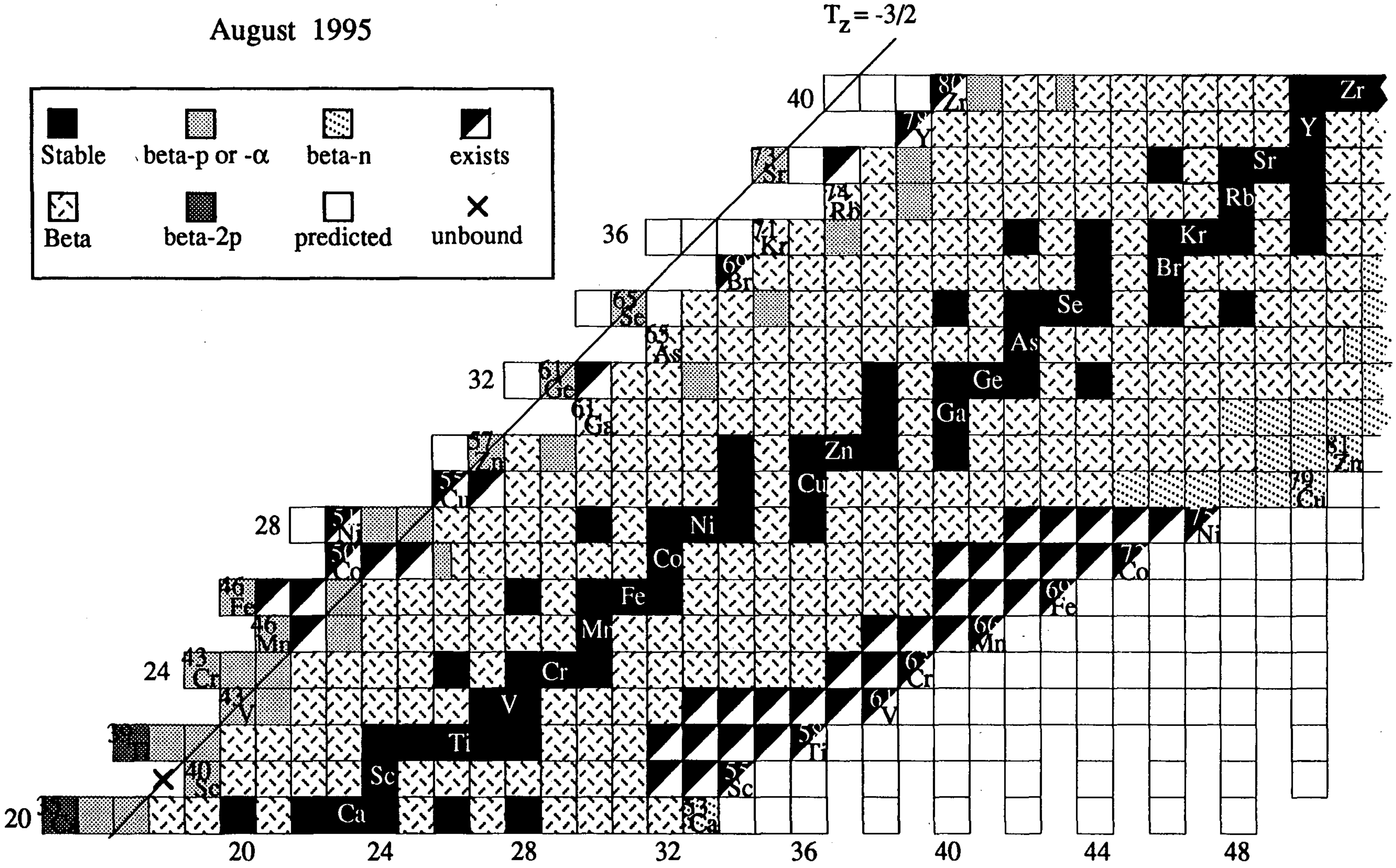
August 1995
Stable
beta-p or -α
beta-n
exists
Beta
beta-2p
predicted
unbound
Tz = -3/2
40
36
32
28
24
20
20
24
28
32
36
40
44
48
Zr
Y
Sr
Rb
Kr
Br
Se
As
Ge
Ga
Zn
Cu
Ni
Co
Fe
Mn
Cr
V
Ti
Sc
Ca
80Zr
77Y
74Rb
71Kr
69Br
65As
61Ge
61Ga
57Zn
55Cu
51Ni
50Co
46Fe
46Mn
43Cr
43V
40Sc
53Ca
55Sc
59Ti
61V
63Cr
66Mn
69Fe
72Co
75Ni
79Cu
81Zn

Figure II-1b.

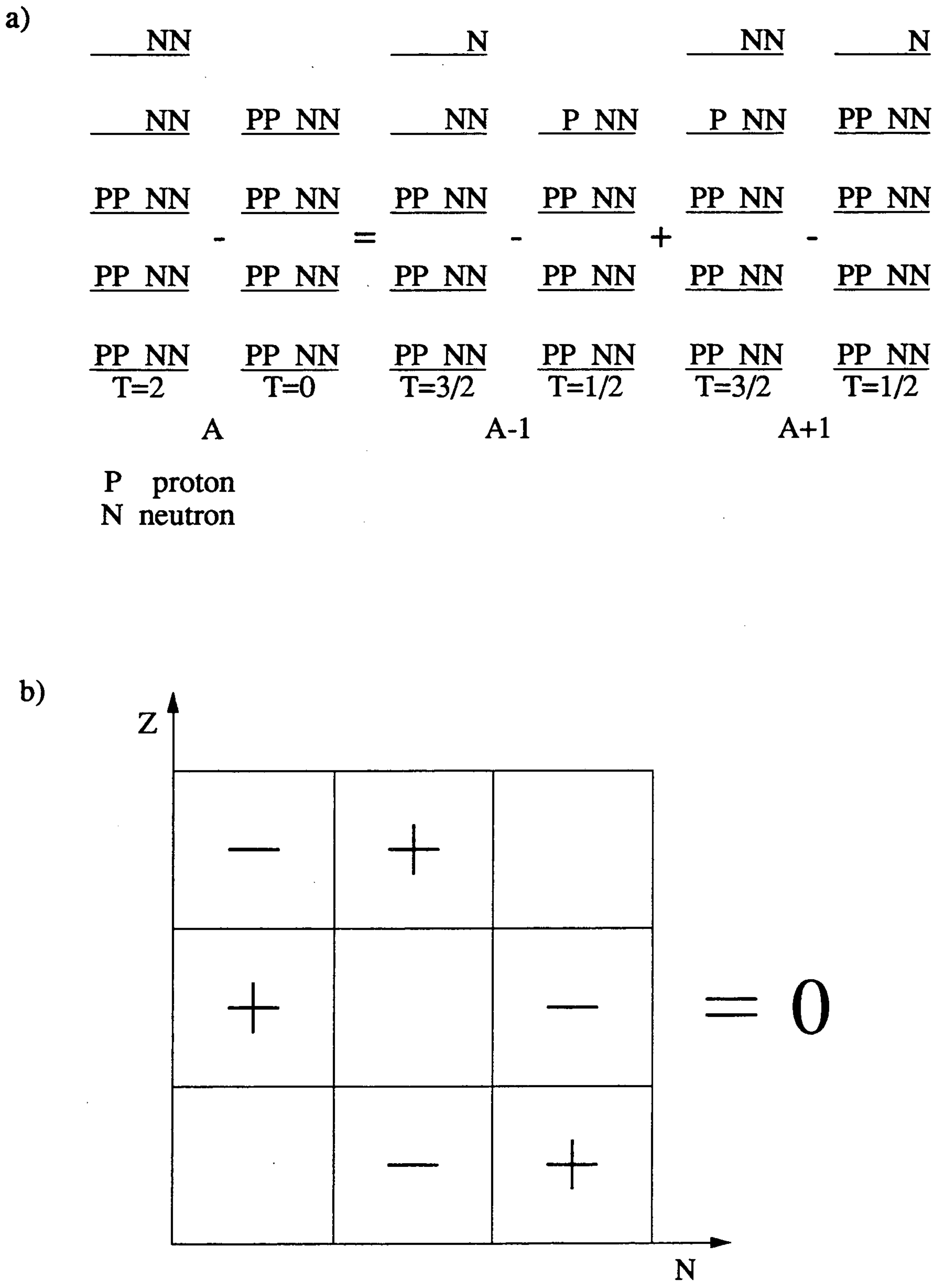
a)
NN
N
NN
N
NN
PP NN
NN
P NN
P NN
PP NN
PP NN
PP NN
PP NN
PP NN
PP NN
PP NN
-
=
-
+
-
PP NN
PP NN
PP NN
PP NN
PP NN
PP NN
PP NN
PP NN
PP NN
PP NN
PP NN
PP NN
T=2
T=0
T=3/2
T=1/2
T=3/2
T=1/2
A
A-1
A+1
P proton
N neutron
b)
Z
N
−
+
+
−
−
+
= 0

Figure II-2.

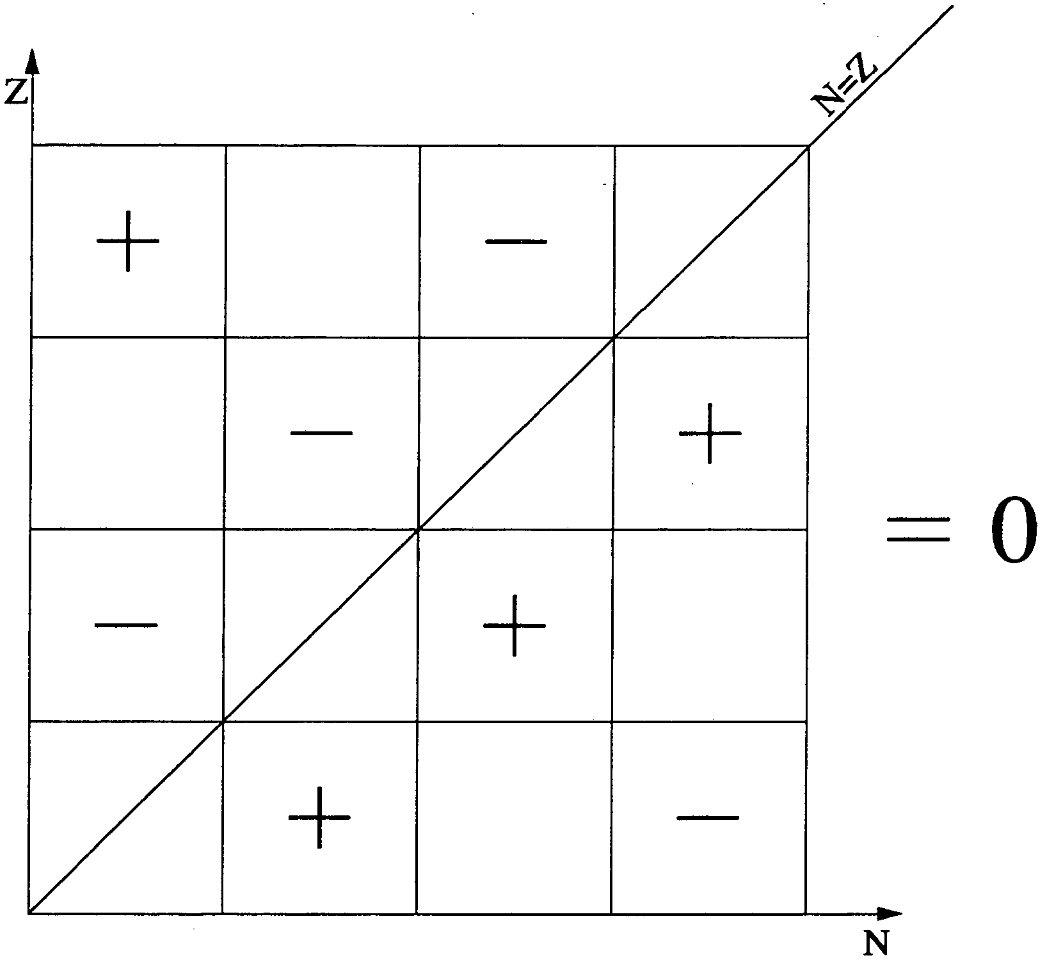

Figure II-3.

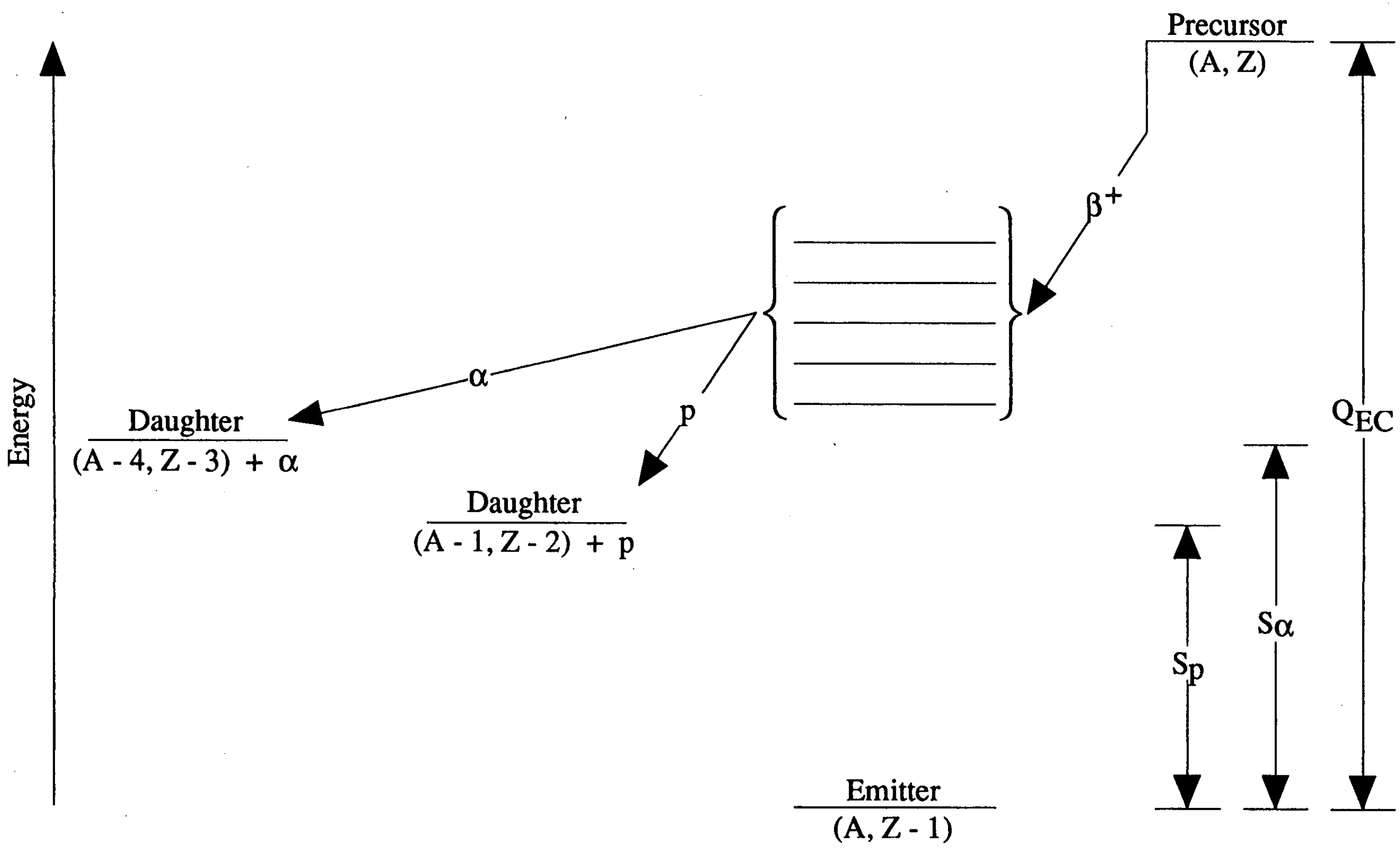
Precursor
(A, Z)
β+
α
p
Daughter
(A - 4, Z - 3) + α
Daughter
(A - 1, Z - 2) + p
Emitter
(A, Z - 1)
Energy
Q_{EC}
S_α
S_p

Figure II-4.

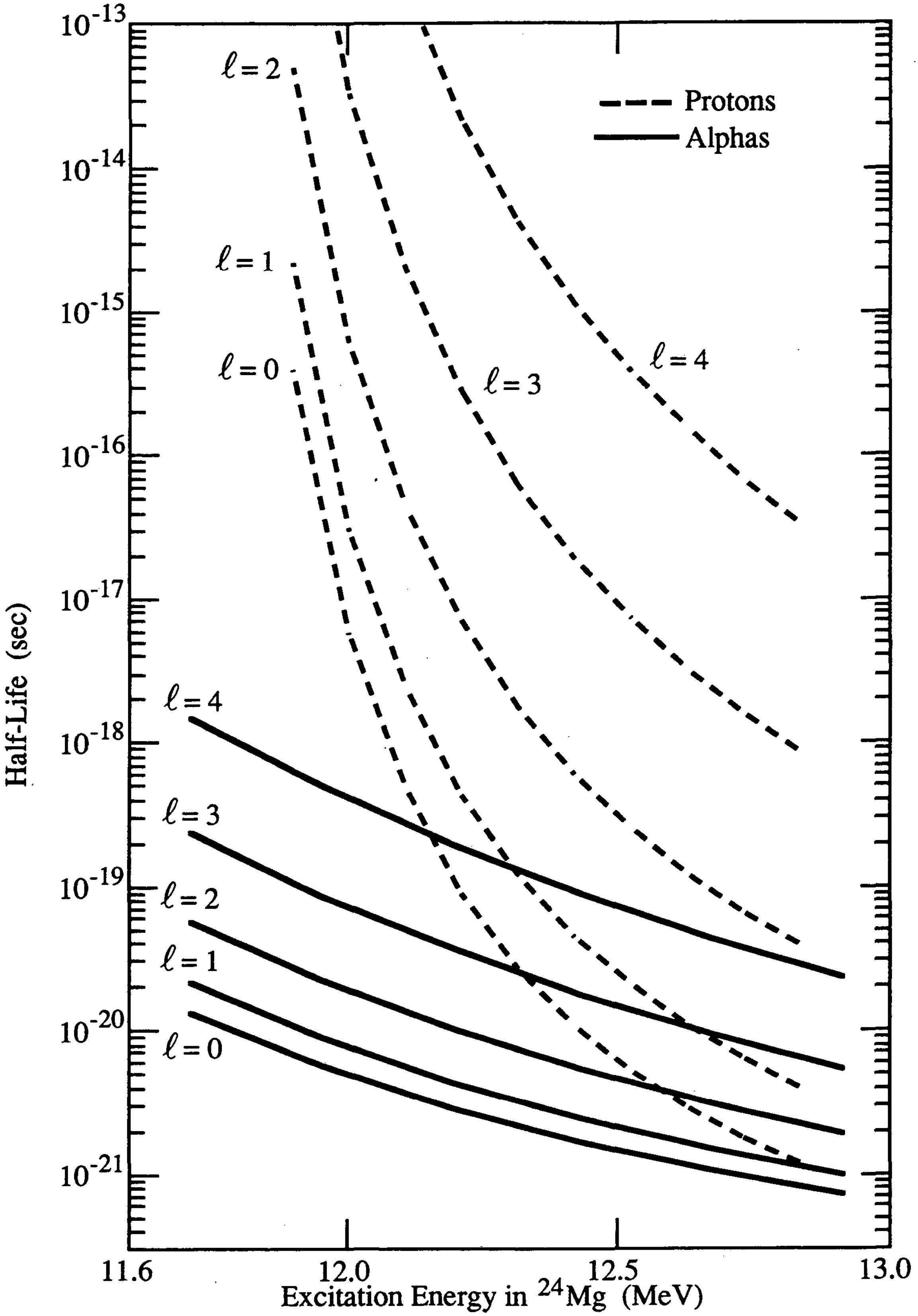

Protons
Alphas
$\ell = 2$
$\ell = 1$
$\ell = 0$
$\ell = 3$
$\ell = 4$
$\ell = 4$
$\ell = 3$
$\ell = 2$
$\ell = 1$
$\ell = 0$
10^{-13}
10^{-14}
10^{-15}
10^{-16}
10^{-17}
10^{-18}
10^{-19}
10^{-20}
10^{-21}
Half-Life (sec)
11.6
12.0
12.5
13.0
Excitation Energy in ^{24}Mg (MeV)

Figure II-5.

III. Experimental Apparatus

The experimental investigation of drip-line nuclei is hindered by short half-lives and diminishing cross sections. To surmount these severe limitations, our research group has developed several techniques. To overcome the short half-lives of these nuclei, we have developed a He-jet transport technique to rapidly transport activity from the target chamber either to a detector or to the ion source of RAMA. This method, as described in Sect. III.A., uses aerosols of potassium chloride in a helium carrier gas. Radioactive nuclei attach themselves to the clusters as the gas sweeps the target chamber and brings them to either detector or ion source. To overcome the low production rates, we take advantage of the fact that many of these nuclei are β-delayed charged-particle emitters. Thus it is possible to identify them based on this somewhat rare decay signature. To this end, we have developed detector telescopes, delineated in Sect. III.B., that enable us to identify and measure protons and alphas from the beta particles simultaneously and copiously produced. Another technique is to employ on-line mass separation. In this method, thermalized, neutral radioactive nuclei are ionized (usually to a +1 charge), extracted and accelerated. The ions are subsequently focused and separated based on their mass-to-charge ratio and then directed to a detector station. This technique has the additional advantage of being very fast. For a modest extraction voltage of 20 kV, a mass 20 ion can travel 400 meters in under 1 msec.

The experiments described in this thesis, with the exception of the ^{17}Ne and ^{33}Ar decay studies, were performed at the Ernest Orlando Lawrence Berkeley National Laboratory 88-Inch Cyclotron, using an electron cyclotron resonance (ECR) ion source [Cl 89a]. Reactions were carried out in Cave 2, labeled Exotic Nuclei in Figure III-1. Total beam transmission from the cyclotron exit to Cave 2 was 50-70%, with the upper end representative of light ions. The Recoil Atom Mass Analyzer, described in Sect. III.C., sits on the roof partially above Caves 1, 2, 3 and 5. The ^{17}Ne and ^{33}Ar decay studies were conducted at the TRIUMF cyclotron located in Vancouver, B.C., Canada, described in Sect. III-D. in conjunction with the TISOL facility.

III.A. Helium-jet

The He-jet recoil transport method has proven to be an effective means of rapidly removing radioactivity from high background production environments to low background counting stations. It is essentially chemically independent with the exception that the noble gases are not transported. Transport efficiencies as high as 90% can be achieved [Ma 69], although this number is very dependent on the geometry of a particular setup.

The He-jet transport system used for the experiments performed at LBNL is shown schematically in Figure III-2. The driving force for transport is the positive entropy change for the isothermal expansion of the helium gas from the high pressure target (supply) side to the vacuum at the exit. The vacuum is generated and maintained by a large capacity-high throughput roots blower (700-2400 liters/sec). If the pressure differential is great enough, then the gas flow through the capillary starts at subsonic speeds and obtains sonic velocity at the capillary exit [We 75]. Although the exact value is dependent on several parameters such as target chamber pressure, capillary diameter and length; the pressure at the capillary exit generally must be below 500 mtorr for the experimental setups described below. This is easily obtained with the roots blower. Gases other than helium such as H_2, N_2 and Ar have been studied but, for similar conditions to He, yields were lower and collection times were longer [Ma 69]. This longer time is due to the fact that the fastest the recoils can go is sonic velocity of the carrier gas and He has a higher sonic velocity than the heavier nitrogen and argon gases.

For successful transport, it is necessary that either the helium be cooled to liquid nitrogen temperatures [Äy 76] or there be impurities in the helium [Ma 74]. The exact nature of the impurity is not important as additives such as acetone, carbon tetrachloride, benzene, water, pump oil, chloride salts, methanol and ethylene glycol have all been used with success. The only requirement appears to be that the additive does not have such a low boiling point that it cannot form droplets at room temperature [Äy 74].

For He-jet studies performed by our research group, potassium chloride has been selectively used because of its small divergence upon exiting the capillary. This allows for a smaller skimmer orifice while not reducing the amount of radioactive nuclei entering the RAMA ion source. A study of the optical properties of an ethylene glycol loaded He-jet found that the aerosol beam was emitted in a cone of half-angle 4.5° from a straight 0.8 mm i.d. capillary [Hi 76]. However, it has been observed that the yield of radioactive nuclei drops by a factor of ~5 upon switching from KCl to ethylene glycol. This is due to the fact that the ethylene glycol aerosols tend to break apart before entering the RAMA ion source caused by its intense temperature at the entrance. To generate the aerosols, a tube furnace is used to heat KCl (mp 770°C) to approximately 600°C. At this temperature, the vapor pressure of KCl is ~5 mtorr and is increasing rapidly [Da 87]. The yield of transported radioactivity increases as the temperature of the KCl increases as more KCl is evolved from the reservoir in the furnace. However, the more KCl aerosols in the helium, the greater likelihood for blockages to occur in the capillary and also the quicker the skimmer hole of RAMA plugs up. As the temperature increases further, the yield of transported radioactivity begins to drop due to the greater formation of smaller mass clusters which are not as effectively transported as the larger mass clusters. If the temperature goes above 640°C, a KCl glass is formed, preventing further aerosol release.

For high vapor pressure liquid additives, the presence of intense ionizing radiation from the projectile beam is required to form high molecular weight (10^3-10^8 amu) clusters [Ju 71]. This presents another advantage to using chloride salts as opposed to ethylene glycol: since the clusters are already made, the choice of projectile beam is unimportant as it is not crucial to forming the necessary clusters. Radioactive nuclei, recoiling out of the target, are thermalized in the helium, attach themselves to the clusters and are subsequently transported along a capillary. Although the flow of the clusters through the capillary is laminar, it is very close to becoming turbulent. As the turbulence increases, the likelihood of clusters hitting (and sticking to) the walls and hence lost for transport increases. For this reason, care must be taken to ensure that the capillary is free of blockages and kinks. However, there is a Bernoulli force that returns off-axis clusters to the center region of the capillary [Wo 76]. This restoring force is proportional to the mass m of the clusters, their distance r from the capillary axis and the velocity v_0 of the gas with specific weight ρ:

$$F_B \approx m^{4/3} v_0^2 r^2 \rho. \tag{3-1}$$

The implication of (3-1) is that the restoring force is greatest for large clusters near the walls of the capillary.

Included in Figure III-2 is a schematic of the multiple target/multiple capillary He-jet target system used in these studies. The target chamber is pressurized with ~1.3 atm of He and is kept isolated from the high-vacuum beam line by two N_2 gas-cooled HAVAR [Ha 95] windows 0.023 mm thick. Short 1 mm i.d. capillaries transport the radioactivity to a header followed by the main capillary, exiting the system. This main capillary has a different i.d. depending on the requirements of each experiment. The typical helium flow rate is approximately 3-8 liters/min, depending on the length and the inner diameter of the main capillary. Also in Figure III-2 is a schematic of the single target/single capillary system. This setup is much faster than the multiple system due to the smaller sweepout volume, the lack of flow-limiting internal capillaries and the elimination of the capillary header. However, only one target can be used at a time, and so it is best utilized in the studies of very short-lived radionuclides.

III.B. Detectors

All the nuclei described herein were studied using gas ΔE-gas ΔE-silicon E detector telescopes. These detectors, along with the appropriate hardware and software gating techniques, are capable of identifying protons (down to ~200 keV) and alpha particles (down to ~400 keV) in the presence of a high beta background on an event-by-event basis. Many of these low-yield experiments involved the simultaneous production of delayed proton and delayed alpha emitters--sometimes from the same nucleus. So it was imperative that the detector system used be capable of distinguishing protons from alphas from beta particles. We were primarily interested in the low energy part of the particle spectrum, which is inaccessible with traditional silicon ΔE-silicon E telescopes.

The major limitation of Si ΔE-Si E detector telescopes is that in order to get particle identification, the ΔE detector has to be thin enough to allow the particle to pass through and still have enough energy to trigger the E detector. However, the thinner the Si wafer, the higher its capacitance and the higher the detector noise, resulting in worsening detector resolution. This has set the threshold for the lower limit of detectable proton energy to ~700 keV for event-by-event identification. Below ~700 keV, protons can only be identified from beta and alpha particles by examining how the peak shifts upon changing the thickness of the detector.

III.B.1. Construction

The main advantage that our gas ΔE-gas ΔE-silicon E detector telescopes has over traditional silicon ΔE-silicon E telescopes is the ability to identify low-energy protons and alphas on an event-by-event basis. This is accomplished by using Freon-14 (CF_4) gas as the differential energy loss medium. A schematic of this triples telescope is shown in Figure III-3. The gas region is subjected to an electric field supplied by biasing the center electrode grid to ~+600 V. The exact voltage is set during the on-line calibration conducted at the start of each experiment. This puts the gas operation at the upper part of the proportional mode, just below the Geiger-Müller region. This high electric field (~1500 V/cm) is necessary to provide the amplification required to separate and identify protons and alpha particles from beta particles.

There are two distinctive active gas volumes--defined from the center bias grid to each of the ground grids, from where charge holes created by the movement of electrons to the bias grid are collected and their signal is read. The grids themselves are constructed of 10 μm diameter, gold-coated tungsten wires arranged in a square 2-dimensional lattice. The gas is continuously flowing through the detector and is maintained at a constant pressure of 10-14 torr. The exact pressure is dependent upon the particular experiment and the detector version used. Isolating the gas region from the vacuum surrounding the detector telescope is a stretched 40-100 $\mu g/cm^2$ thick polypropylene window.

Several gases have been tested including Freon-14, isobutane, propane and P10 (a mixture of 90% argon and 10% methane). It was found that Freon-14 gave the best gain amplification for protons with the sharpest shaping time. It was also found to have the least sensitivity to high energy positrons and electrons [Mo 94].

The final element of the telescope is an ion-implanted silicon wafer 300 μm thick. Since the detector is situated close to the target chamber, the silicon crystal can be inflicted with severe radiation damage. The main visible result is an increase in the leakage current and a decrease in the energy resolution of the silicon detector. To minimize the effects of radiation damage, the detectors are cooled to between -10°C and -20°C with chilled ethanol. This also helps to suppress the electronic noise of the detector. Typical leakage currents are 0.1 μA after cooling.

Two configurations of detector telescopes were used in these experiments, a singles version and a six detector array. The singles version is shown schematically in Figure III-4. Each telescope is inside a hollow brass chamber 10 cm x 7.6 cm x 1.9 cm thick. Radioactivity was transported via a 1-1.5 mm i.d. capillary from the target chamber and deposited onto the edge of a slowly rotating wheel. Two detector telescopes, one above and the other below the wheel, viewed this spot, with each subtending a solid angle of 3% of 4π.

To increase the number of detectors without lowering the solid angle for any one detector, it became necessary to construct an array of detectors in a soccer ball-like configuration. This array, as depicted in the two schematic views of Figure III-5a,b, consists of 6 close-packed detector telescopes each subtending 4% of 4π. Activity is deposited on a moving tape at the center of the ball where it is viewed by 4 of the detectors. For this He-jet configuration, detectors 5 and 6 are not used because the tape drive blocks and severely limits their usefulness.

The full utilization of the detector ball can be realized when it is coupled to a mass separator. The tape drive is removed and the ion beam enters the detector ball from the opening left by the tape drive. Activity is deposited on a thin (20 μg/cm^2) carbon foil located directly in the center of the ball as depicted in Figure III-5c. Detectors 5 and 6 can now view the activity, increasing the solid angle to the maximum of 24% of 4π.

III.B.2. Counting Electronics and Data Acquisition

A block diagram of the electronics used in these experiments is shown in Figure III-6. Signals from each of the detectors were initially amplified with charge sensitive preamplifiers. The slow output signal from each gas detector was split and directed to a pair of high rate linear amplifiers, with the high gain amplifier (H. G. Amp) boosting the signal more than the low gain amplifier (L. G. Amp). This allowed for the simultaneous separation of protons and alphas from the beta particles without exceeding the range of the Analog-to-Digital Converters (ADCs). The slow outputs of each amplifier were sent to the ADCs which were part of a CAMAC data acquisition system. The fast outputs of the silicon detector amplifier and the gas filter high gain amplifier served as inputs to LeCroy octal discriminators where the thresholds were set to just above the noise. The signals were then stretched to 1 μsec and sent to a logic box. A coincidence was required between the filter gas ΔE detector and its corresponding silicon E detector in order to trigger a valid logic pulse. A master gate signal was generated whenever this coincidence was made for any one detector telescope and was used to strobe the ADCs in the CAMAC crate. The output of the ADCs was stored in a buffer in a MicroVax computer running a STARBURST system. The program CHAOS [Ra 91] recorded the data to 8mm magnetic tape, as well as performing the on-line data analysis and display.

A complication of operating detectors close to the cyclotron beam is the presence of prompt neutrons when the beam is on. This problem is most acute when utilizing light ion beams such as ^{3}He and protons. Fast neutrons will knock out protons in the polypropylene window and/or in the plastic construction materials of the detector ball whereupon they can generate valid signals and are indistinguishable from decay protons. For this reason, when running He-jet experiments using light ion beams, the cyclotron beam is pulsed and the electronics are enabled only when the beam is off. The cyclotron beam can be turned off by activating an electrostatic deflector located on the ECR injector line. The beam extracted from the ECR is at a 10 kV potential, and complete beam deflection can be achieved by applying a voltage of +700 Volts to one plate while keeping the other at ground. Cycling the voltage applied to the electrostatic field plates on or off requires only 2μs. The timing of the cyclotron beam and the electronics is controlled by a pair of gate generators. The first portion of the output pulse from the first gate generator is used to gate the electronics on at the logic box. The second portion serves as a start signal for the second gate generator, which controls the timing of the beam phase. In this manner, only those events recorded during the beam off phase are accepted into the computer. Each gate generator has an adjustable width with the total period controlled by a separate pulser so it is possible to have asymmetric electronics on, beam off/electronics off, beam on phases.

Selection of the pulsing structure is performed by considering the half-life of the nuclide of interest and the He-jet transit time. By assuming that the intensity of the cyclotron beam is constant when it is enabled, it is possible to generate a growth curve of the percentage of the number of product nuclei of interest present in front of the detectors at time t compared to the number present at time = infinity as a function of time that the beam is on. For $0 \leq t \leq$ beam on period, the percentage is defined as:

$$P_{\%} = 100\left(\frac{N(t)}{N(\infty)}\right), \tag{3-2}$$

with N(t) defined as:

$$N(t) = \frac{R\left(1 - e^{-\lambda\left(t - t_{transit}\right)}\right)}{\lambda}, \tag{3-3}$$

where, $t_{transit}$ is the He-jet transit time, λ is the decay constant of the nuclide of interest and R is its production rate.

For beam off $\leq t \leq$ total period, the curve is just the standard decay curve, keeping under consideration that the activity is still growing in for the amount of time equal to the He-jet transit time. The area under the decay curve can then be integrated and maximized with respect to the total pulsing period to give the ideal production and counting cycle. Figure III-7 shows a plot generated from a total period of 900 msec, consisting of a pulsing structure of a 570 ms of beam on, electronics off phase and a 330 ms beam off, electronics on phase with a helium-jet transit time of 200 ms. This timing structure maximizes the yield for a nuclide with a half-life of 260 ms.

The above procedure effectively eliminates events caused by knockout protons but not without a price. The main problem with running a pulsed beam is that one cannot collect as much data as is possible when utilizing an unpulsed cyclotron beam. For example, consider the above period wherein 63% of the time, the beam is on and the electronics are off, while 37% of the time, the beam is off and the electronics are on. Hence, during one period, one will only collect 23% (0.63 cyclotron duty cycle x 0.37 electronics enabled duty cycle) of the data that would have been generated and recorded if an unpulsed beam had been used during that period. Some gains can be made by increasing the beam intensity; however, it is not enough to offset this huge reduction in detectable activity, as the upper limit of acceptable beam intensity is determined by the counting rate in the silicon E detector. For this reason, pulsed beam experiments must be run for a longer time in order to collect enough statistics to make the results meaningful.

III.B.3. Calibration and Data Analysis

Detector calibrations were performed *in situ* using beta-delayed protons from the well known emitter, ^{25}Si, which is produced via the ^{24}Mg(^{3}He,2n)^{25}Si reaction with E(^{3}He) = 40 MeV [Ro 93]. ^{25}Si has many proton groups ranging from 387 keV to 5.405 MeV, making it an ideal source with which to calibrate our detectors.

Data analysis is performed by plotting the energy loss in each gas ΔE detector versus the energy deposition in the silicon E detector. Different types of particles (in this case: betas, protons and alphas) lose different amounts of energy in the ΔE detector and form bands corresponding to their mass M and charge Z based upon the relation:

$$\frac{dE}{dx} \propto \frac{MZ^2}{E}, \tag{3-4}$$

where, E is the total energy of the particle and dx is the path length in which the differential energy dE was lost. Since the gas detectors are operated at a relatively low pressure (10-12 torr), the amount of energy lost by a proton or alpha as it traverses the active region is generally small compared to the total energy of the particle. Thus energy losses in the gas are included implicitly in the energy calibration and the gas signals are used only for particle identification.

Figure III-8a,b shows two 2-dimensional ΔE vs.E plots of raw data recorded with one gas ΔE-gas ΔE-silicon E detector telescope during a typical 40 MeV ^{3}He + ^{nat}Mg calibration bombardment. A small uniform background has been subtracted from these plots to aid in the visualization of the data. A crude software gate can be drawn around the proton region in each plot. Backprojections are created by projecting those events that fall within the gate onto the other gas ΔE vs. silicon E plot. Figure III-8c,d shows two such backprojected spectra, with Fig. III-8c being a backprojection generated by drawing a gate around the protons in Fig. III-8b, and Fig. III-8d being a similar backprojection created from Fig. III-8a. It is clearly evident that the protons are well separated from the beta and alpha particles. A tighter proton gate can now be drawn around the protons in each plot, thus requiring a three-fold coincidence, and projected onto a 1-dimensional energy spectrum as shown in Figure III-9. As can be seen in Figure III-9, the betas have been completely suppressed and tests have demonstrated that less than one in a million beta events will fall into the software gates on both detectors [Mo 94]. Typical energy resolutions are 45 keV (FWHM) for the 387 keV and the 4091 keV proton groups.

Unfortunately, our method of incorporating energy losses into the final calibration is inaccurate when we extrapolate below the last known proton or alpha peak in the calibration spectrum. Although the response of the silicon detector is linear in energy, the differential energy loss of a particle as it passes through the various components of the detector telescope is not. Figure III-10 shows a plot of the total amount of energy lost for protons and alphas as they pass through a 60 μg/cm^2 polypropylene window, a 100 μg/cm^2 gas region and a 90 μg/cm^2 silicon detector deadlayer. This plot uses data tabulated in [In 93]. For valid low-energy proton calibrations below 387 keV, it becomes necessary to model the detector response. Using an external alpha source, the thickness of each component was measured separately. It was found that the silicon detector deadlayer is dependent on its temperature so those measurements were conducted on detectors chilled to the temperature that the experiment was performed. The gas density, also temperature dependent, was measured at operating temperature. As a test of the detector model, as well as to determine the silicon crystal response function, a separate experiment was conducted in which the proton groups in ^{25}Si were degraded. This was accomplished by placing known thicknesses of thin aluminum foils between the decaying source and the detector. The thicknesses were chosen such that the 387 keV proton group would be degraded stepwise down to below the low proton energy cutoff of the detector.

Once the low energy end of the silicon E detector calibration was determined, the differential energy losses were then calculated and folded back into the energy detected in the silicon detector to give the incident proton decay energy. We have successfully used this method to determine the energy of protons (223 ± 20 keV) emitted from the isobaric analog state following ^{23}Al β-decay [Ti 95].

The energy determination of possible low-energy alpha particles following the beta decay of ^{20}Na was performed in much the same way. In this case, known alpha groups from ^{20}Na [To 73] were used to set the initial calibration and the various detector thicknesses were separately measured and subsequently added back in to determine the incident alpha particle energy. This technique, as well as the calibration experiment, is described in more detail in Section III.C.2.c.iii. in reference to the ^{20}Na RAMA experiment.

III.C. Recoil Atom Mass Analyzer (RAMA)

The mass separation of nuclear reaction products provides a powerful technique in the study of nuclei far from stability. Mass separator systems for nuclear spectroscopic decay studies can fall under two very broad categories: recoil fragment mass analyzers (FMA) and on-line isotope separators (ISOL). Fragment mass analyzers take advantage of the forward emission cone of nuclear recoils emitted from (HI,xn) reactions. The primary beam is deflected while a most probable charge state of the energetic recoils is selected and mass separated as a secondary beam. The obvious advantage of this method is the speed, as the only delay time is the length of time it takes the recoil to travel through the target and mass separator. Additionally, with no ion source, it is chemically universal. However, only a few charge states out of the many possible can be selected at any one time, depending on the resolution of the bending magnet. A review by Enge [En 85] covers many more aspects of recoil separators than mentioned here.

In ISOL systems, the nuclear recoils are stopped or thermalized in either the target or the target region. They are then transported via such methods as a helium-jet, diffusion or a adsorption/desorption process to a mass separator. The nuclei are subsequently ionized, accelerated, mass separated and directed to a counting station for study. A variation of the ISOL technique is IGISOL (Ion Guide Isotope Separator On-Line) which uses helium to transport nuclear recoils directly to a post accelerator without the use of an ion source [Är 86]. In ultrapure helium, the ultimate charge state of any ion species is +1. The IGISOL technique though chemically universal, is currently hampered by low efficiencies for heavy mass recoils and the difficulties in obtaining ultrapure helium. A recent review [Ra 89] gives a more comprehensive description of ISOL systems.

The coupling of an ISOL system to a helium-jet, first proposed by Nitschke [Ni 70], is the principle on which RAMA was designed. As described in Section III.A., nuclear recoils are thermalized and attach themselves to high molecular weight clusters in the helium. A capillary transports the clusters to an evacuated chamber in which a skimmer system is used to remove the majority of the helium while allowing the heavier clusters/radioactivity to enter the ion source. Early results, using RAMA, were the identification of the A = 4n, T_Z = -2 series nuclei, ^{20}Mg and ^{24}Si, by the observation of beta-delayed protons from the IAS in the beta daughters [Mo 79a and Äy 79]. These results were used to complete the A = 20 and 24 isospin quintets, providing a stringent test of the isobaric multiplet mass equation [Äy 81]. Though further experimental studies were successfully completed, the system was limited by a low ion source efficiency and the inability to extract at voltages greater than 18 kV without breakdown of the main insulators. Additionally, the RAMA system was hampered by the relatively long transit time between the target and the ion source.

III.C.1. RAMA Upgrade, Phase I

The first phase of the planned RAMA upgrade was an overhaul of the ion source region. The overall goal was to improve ion source and extraction efficiency. With this in mind, it became necessary to redesign the ion source/extraction region with an emphasis on improving the vacuum pumping capabilities to allow for greater extraction voltages. Additionally, we wanted to improve on the extractors currently in use, as well as to redesign the ion source mounting system to facilitate ion source changes while maintaining system alignment.

Figure III-11 shows a schematic diagram of the redesigned ion source region. The design is such that the skimmer region, as well as the ion source operates at high voltage with extraction made to ground, as before. Systemic to a helium-jet is the copious amounts of helium entering the skimmer region which must be removed so as to minimize its effect on the vacuum within the optics region. This is readily accomplished by the use of a high capacity-large throughput (~2400 liters/sec) roots blower. With the roots blowers sitting at ground, it is necessary to use high voltage stepdown units. These units consist of several stages of screens acting as electron traps. Through a series connection of resistor chains through the screens, the voltage is lowered to ground without providing a continuous negative potential slope for discharge.

Owing to the laminar flow of the clusters/radioactivity in the He-jet, most of the radioactivity passes through the skimmer and enters the ion source while the largest fraction of helium is skimmed off at the skimmer box. Although dependent on several factors, including the size of the transfer capillary, the He-jet target chamber pressure and the capillary-skimmer distance, the pressure inside the skimmer box is typically 200-300 mtorr. The interstitial region between the skimmer and the ion source is pumped out by a second and smaller roots blower (and involves a second high voltage stepdown unit). Completing the vacuum components of the redesigned system is a 25 cm oil diffusion pump below the ion source box.

Typical operating pressures inside the ion source box are 10^{-5} torr while pressures in the optics region beyond the ion source box are in the 10^{-6} to 10^{-7} torr range. This represents a factor of at least ten in improvement in the vacuum over the previous RAMA ion source configuration. The obvious advantage to this is the monotonic increase in the mean free path between collisions with decreasing pressure. Collisions between the ion beam and residual gas molecules can result in charge exchange, neutralizing the ion. Elastic collisions will spread out the beam, distorting its Gaussian shape and affecting system resolution.

III.C.1.a. Ion Source and Extraction

Figure III-10 shows a schematic of the present RAMA ion source. This source is a version of a hot hollow cathode type ion source (HCIS), described by Sidenius [Si 70] and represents further modifications to earlier RAMA ion sources [Mo 80a, Mo 80b, Mo 81 and Bl 87]. This source is capable of ionizing many elements as long as the melting point of the filament is not exceeded. In this case, the limiting temperature is the melting point of the molybdenum components (mp = 2890 K). Since it is safe to operate the ion source to approximately 2000°C, yields for elements with higher melting points are often very low. Because of its small volume (~3 ml), the hold time of the source is short. Although dependent on the mass of the species of interest, as well as operating conditions such as the ion source temperature and the size of the emission slit, the delay time of the HCIS is on the order of milliseconds [Ki 81]. Additionally, its operation is very stable for long periods of time and once tuned, requires very little subsequent adjustment.

As evidenced by Figure III-12, the RAMA ion source has a relatively simple construction, thus facilitating filament changes. The ion source is constructed primarily of molybdenum (Mo), tantalum (Ta) and boron nitride (BN). Mo and Ta have similar high temperature properties with high melting points, high stiffness and low coefficients of expansion. Boron nitride is an excellent high temperature insulator that is extremely easy to machine. BN will not react with Ta at high temperatures, however, it will decompose if in contact with Mo at temperatures above 1500°C. Therefore, care must be taken to ensure that there is minimum contact between these two materials.

Electrons are generated by thermionic emission of a resistively-heated tungsten (mp = 3680 K) filament. The 0.76 mm tungsten filament [Ph 95] is annealed with potassium to make it pliant, since, to construct the filament, the wire must be rolled into a helix of 6-7 turns x 1.4 cm long. When the filament has heated up to a sufficient temperature, an arc is struck between the anode end cap and the end of the cathode, creating a plasma.

A simple definition of a plasma is that it is an essentially electrically neutral ensemble of electrons and positive ions which have equal densities and an isotropic velocity distribution [Se 71]. The intense electrical discharge produces a very dense medium of electrons and positive ions, which to first order, approximates a plasma. The plasma is supported by the addition of helium from either the main transport capillary or from a separate helium support gas line. In operations, it was found that sufficient quantities of helium entered the ion source so that no additional support gas was necessary.

Atoms entering the ion source are ionized predominantly via collisions with He ions in the plasma through the charge exchange reaction: $He^+ + A \text{ ---> } A^+ + He$. Losses of radioactivity in the ion source are generally to collisions between the neutral species and the wall. Several things can happen, but the two main loss mechanisms for solid elements are trapping due to condensation on a colder part of the ion source and a chemical reaction that results in the formation of a stable molecule with a low vapor pressure [Fr 73]. Of the two, the former is the more prevalent. The filament is a solenoid and based on typical operating conditions, a magnetic field of ~0.03 Tesla is created by running an electrical current through it. This magnetic field is sufficient to prevent any trapped ions from reentering the plasma. Upon disassembly after use, it was observed that the greatest concentration of radioactivity in the ion source was located on the inside walls of the tube surrounding the filament.

The situation for trapped ions is slightly different when the ion source is operated in the surface ionization mode. While activity stuck on the cathode cannot reenter the plasma, those that are attached to the anode cap can return to the plasma and subsequently extracted. In this case, the atom impinges on a wall, an outer electron from the atom is absorbed by the surface and the atom is ionized and released. This will only work if the first ionization potential of the atom is less than the surface's work function, effectively limiting this mechanism to the higher mass alkali metals.

Typical operating parameters for the RAMA ion source are 600 Watts of DC filament power with the arc potential at 220 Volts and 1.7 Amperes. The lifetime of the filament is greatly affected by the amount of current flowing through it. A filament will last for at least a day at 600 W but burns out after several hours at 750 W. It was found that changes in arc power made no difference in the amount of extracted beam current as long as the arc was maintained while increases in filament power would bring an increased yield. However, if the filament power was increased even further, the extracted yield would actually decrease. It appears that as the current through the filament increases, the magnetic field of the solenoid increases to such a point that it begins to squeeze out the electrons and ions and thus to extinguish the arc.

Ion beam extraction occurs when the plasma comes into connect with an electrode at a negative potential to the plasma. The potential drop is felt in a transition layer known as the sheath. If the electrode is sufficiently negative with respect to the plasma, a pure ion beam is extracted with all the electrons trapped inside the plasma region.

The ultimate limit of current density extracted in a space charge limit is given by the Child-Langmuir equation [Ch 11 and La 31]:

$$j = 1.72\left(\frac{q}{A}\right)^{1/2}\frac{U^{3/2}}{d} \quad \left(\mathrm{mA/cm^2}\right), \tag{3-5}$$

where, j is the current density, q is the charge state of the ion, A is the mass in amu, U is the extraction voltage in kV and d is the distance, in cm, between the ion source and extractor. Equation (3-5) represents an upper limit derived from two parallel plate electrodes. For typical RAMA operating parameters of a $^4He^+$ beam at 30 keV with a 2 cm extractor/ion source gap, j = 35 mA/cm^2. As evidenced by (3-5), a larger voltage will increase the amount of extracted beam. This was verified by observation when the yield of mass separated beam increased by more than a factor of 2 upon raising the extraction voltage from 20 kV to 30 kV. It appears that the larger voltage samples deeper into the plasma to extract greater quantities of beam. Although typical extraction currents are lower than this upper limit, they are large enough to cause significant detrimental space-charge effects in the extraction region. A 30 keV mass 4 beam will begin to experience noticeable space-charge effects at 50 μA [Wo 87b].

Without going into detailed mathematical models, which is done elsewhere [e.g., Fo 88 and Sz 88], space charge can be qualitatively described. Space-charge effects occur as a result of the ion density getting so large that ions begin to interact and repel one another. Motion in the transverse direction increases to a point that the paraxial ray approximation begins to break down. Additionally, the self field of the ions partially shields the ions from the effects of the applied external magnetic and electric fields. The main effect is to increase the beam divergence.

Based on a simple model of considering the beam to be a cylinder of charge and by examining the change in transverse momentum with respect to the axial momentum, and by comparing that to the beam divergence in the current = 0 limit, several general conclusions can be reached. As expected, space-charge effects worsen as more beam is squeezed into a smaller volume. Additionally, the space-charge effects are greater for slow-moving heavy ions (v^{-3} and $m^{1/2}$ dependence).

The best way to combat space charge is to have a source of negative charge carriers which can neutralize the excess beam. Free electrons can be created by collisions between the ion beam and the walls of the construction materials or between the ion beam and residual gas molecules. To prevent the electrons from streaming back to the ion source where they are quenched, it is advantageous to construct a potential well that traps the electrons in the vicinity of the extractors where the ion density is at its greatest. Such is the rationale for employing an accel-decel type extraction system. The first electrode serves as an accelerator for positive ions with the second (screening) electrode negatively biased at approximately 10% of the final extraction voltage. This creates the negative potential well which forms the electron trap. The RAMA extractor is actually an accel-decel-accel design with the third electrode at ground and the first electrode biased to a positive high voltage of approximately half the final beam voltage.

It was with this in mind that the RAMA extractor was designed. However, the full advantage of an accel-decel-accel type extractor can only be fully realized when used in conjunction with a high resolution mass separator. It had been proposed to add a high resolution dipole downstream of the main RAMA dipole. Although this proposed dipole is beyond the scope of the current upgrade, the RAMA optics system, when feasible, has been designed for such a future implementation. However, the current RAMA mass resolution does not fully warrant the use of an accel-decel-accel extractor. Therefore, in practice, we have been unable to fully implement and exploit the features of this type of extractor and, currently, beam extraction is made to ground via a one-step process.

A second feature of the extractors is a remote control unit. A moveable extraction system makes it possible to empirically determine the ideal gap between ion source and the first extraction electrode. If the gap is too large, then the beam has expanded to the point where only a small fraction has the necessary acceptance to enter the optics region. If the electrode is too close, then too much of the beam is extracted and space-charge effects will dominate, increasing the size of the beam beyond the acceptance of the optics [Ch 67]. Additionally, if the electrode is too close, there is the risk of sparking the high voltage, in which case all beam is lost. Ion source changes are facilitated by moving the extractors out of the way. The design of the ion source mounting is such that there is only one unique configuration in which the ion source can be mounted. In this manner, the ion source alignment with the capillary and the extractors is always maintained.

III.C.1.b. RAMA Optics

A schematic of the improved RAMA system is presented in Figure III-13. Radioactivity is transported from the target chamber via a 6 meter long polyethylene capillary to the skimmer region of RAMA. As described above, the helium is skimmed off, and neutrals are ionized, extracted and post accelerated to 30 keV. Immediately after extraction, an einzel lens is used to focus the ion beam through a small-diameter short (2.5 cm i.d. x 7.6 cm long) beam tube to the acceptance of the Wien filter magnet. The small-diameter beam tube serves to isolate the lower-vacuum ion source region from the substantially higher vacuum of the optics region.

This point focus at the entrance to the Wien filter serves as the virtual source for the RAMA optics. The Wien filter uses crossed magnetic and electric fields to function as a velocity selector. Its main purpose is to deflect and prevent the He^+ ions from entering into the optics region. Further details are presented below in the discussion of the second phase of the RAMA upgrade, as well as in ref [Mo 80a]. After the Wien filter, the beam is captured and focused through the main RAMA dipole to a point on the RAMA focal plane by an electrostatic quadrupole triplet. The triplet is operated in the DFD mode with the first and third quadrupole operated at the same voltage. By convention, the effect of each quadrupole to ion motion in the x-direction is designated D for a defocusing action and F for a focusing action. At low beam energies, electrostatic and magnetic focusing elements function equally well. However, due to the mass independence of the Coulomb force, electrostatic elements have the advantage in not requiring a retune upon changing the mass selection.

The main RAMA dipole is a surplus cyclotron beam bending magnet with entrance and exit angles of 11°, in which the central trajectory is bent 75.5° ($\rho = 0.6706$ m). The focus point is a pencil-like beam with a small magnification in the radial direction (Mx~0.5) and a larger magnification in the vertical direction (My~1.2). The initial beam is cylindrically symmetric with $x'_0 >> x_0$ and $y'_0 >> y_0$. Therefore, the most significant second-order terms in equations (2-59) and (2-60) are those in which x'_0 and y'_0 appear. To minimize these second-order aberrations, an upstream sextupole, along with edge sextupoles, are employed. Optics calculations also showed that the focal plane angle was rotated 61° to the ion trajectories. Therefore an exit sextupole was employed to rotate the focal plane back to 90° with respect to the axial (z) direction.

This intermediate focus point at the focal plane is useful for tuning the beam through the first half of the optics, as well as serving as a spot in which to place a silicon detector for radioactivity measurements. Off-line tests were performed using potassium transported via a He-jet from the KCl furnace. A measured mass scan was used to obtain a full width at one-tenth maximum (FWTM) mass resolution (M/ΔM) of 300. This is an improvement over the pre-upgrade mass resolution of 195 (FWTM) [Mo 80a]. A dispersion of 1.74 m was also calculated from the equation:

$$D = 2wR\left(\frac{B'}{\Delta B}\right), \tag{3-6}$$

where, D is the dispersion, R is the mass resolution, w is the measured distance, in meters, between adjacent masses at the focal plane, B' is the full magnetic field width at one-half the maximum intensity, and ΔB is the difference in magnetic field settings between mass m and m+1. This value agrees well with the calculated dispersion of 1.62 m obtained from the optics calculations.

Electrostatic deflection plates are used to bend the beam 10.7° and direct it to the shielded detector station (SDS) [Bl 87]. The SDS was constructed to provide a low background counting area. This was accomplished by assembling a platform with neutron and gamma shielding (water cans filled with a saturated solution of borax, paraffin boxes and low background lead bricks) approximately 8 meters downstream of the RAMA focal plane and several concrete wall thicknesses away from the cyclotron beam analyzing slits and the Cave 2 target. A second set of electrostatic quadrupole triplets operated in the DFF mode is used to capture and focus the beam for parallel transport, with an einzel lens utilized to squeeze the beam to a point focus at the center of the counting stations. Directing the beam to the 90° detector arm is easily accomplished with the utilization of horizontal deflection plates and a small electrostatic mirror. The deflection plates can be pulsed to permit a periodic flipping of the ion beam between counting stations which is useful in half-life measurements.

Off-line tests showed that the beam spot is fairly large at the focus point with $x \approx y \approx 0.64$ cm. This does not present a problem as long as detector dimensions are not exceeded. The off-line tests also demonstrated that ~90% of the beam at the focal plane is transported to the shielded detector station (SDS).

III.C.1.c. Tests with Radioactivity

Initial tests of the RAMA system were devoted to observation of alpha particle emitters in the rare earth region of the Periodic Table. These nuclei are easily produced in (HI,xn) reactions and have been previously observed with RAMA [Mo 79b]. Using beams of 125 MeV (mid target lab energy) $^{16}O^{5+}$ impinging on a ^{nat}Nd target, alpha particles from the decay of isotopes in the mass 150 region of erbium, holmium, dysprosium and terbium were observed. Mass separated samples were deposited on a thin (200-300 $\mu g/cm^2$) aluminum foil directly in front of a single ion-implanted Si detector at the focal plane of the main RAMA dipole. No attempt was made to quantify yields or to measure any spectroscopic information as the emphasis was on the mere observation of radioactivity.

These results are significant in that the high melting points of these elements require that the ion source be operating correctly. This includes the presence of a plasma in the region near the ion source exit aperture. Also, much of the early characterization of the RAMA ion source was conducted using the rare earth metals. Table III-1 lists the isotopes observed and Figure III-12 displays a typical spectrum obtained. The relatively poor detector resolution is a result of the alpha particle having to pass through the aluminum catcher foil and the use of an uncooled, neutron damaged silicon detector.

Quantitative tests were performed by measuring beta-delayed gamma-ray emission from proton-rich nuclei in the mass 20 and mass 60 region. These tests were conducted at the 0° detector arm by implanting activity onto an aluminum foil viewed by either one germanium gamma-ray detector at 0° or two Ge-γ detectors at ±90°. Table III-2 summarizes these results. Figure III-15 shows a beta-delayed gamma-ray spectrum from a mass 23 beam recorded at the SDS, while Figure III-16 shows a $\beta\gamma$ spectrum from a mass 65 sample, also recorded at the SDS.

The efficiency is defined as the ratio of decaying nuclei observed at the shielded detector station to the number produced during the bombardment time, T_b, and transported to the skimmer region:

$$\eta_{\mathrm{RAMA}} = \frac{(\text{counts observed})\left(\frac{1}{\eta_{\mathrm{det}}}\right)\left(\frac{1}{\text{Branching Ratio}}\right)}{\left(\frac{\mathrm{Inx}\sigma}{\lambda}\left(1-e^{-\lambda T_b}\right)\right)\left(e^{-\lambda t_{\mathrm{transit}}}\right)\left(\eta_{\mathrm{He-jet}}\right)}, \qquad (3\text{-}7)$$

where, in the numerator, detector efficiencies and branching ratios are folded into the number of counts observed. The denominator of equation (3-7) has the reaction equation multiplied by losses from decay in transit and losses due to the He-jet efficiency. The He-jet efficiency for these calculations is set at 50% while the transit time (t_{transit}) is between 100 ms and 300 ms depending on the particular He-jet target setup employed. The cross section, σ, is obtained from the statistical model, fusion-evaporation code ALICE [Bl 82]. Due to the uncertainties in these values, the RAMA efficiencies should not be taken as exact but rather as an order of magnitude indication of how well things are working.

Equation (3-7) represents the simplest case--in which the nuclei observed decaying are produced only through the nuclear bombardment reaction. Often the nucleus is produced via several methods: from the primary bombardment and from the decay of a parent nucleus that is produced during bombardment, as well as decay of the parent during transit. This is treated in many textbooks (e.g., [Fr 81]) with the result that the actual reaction rate is a summation of activity formed through the above methods.

Often, many tests were performed during a single experiment and it was impractical to put in a clean foil for each test. Subsequently, some of the events observed were due to the decay of nuclei implanted during the previous test. This was especially common with the longer lived activities and care had to be taken to correctly account for these "background" events.

All the nuclei reported in Table III-2 required a plasma for ionization with the exception of ^{24}Na, which can be ionized via surface ionization, although the efficiency that is reported is with the ion source in plasma mode. These results represent factors of 10-20 improvements over previous RAMA efficiencies.

III.C.1.d. Gallium-61 Decay Study

Upon demonstrating a relatively high yield for gallium (see Table III-2), we undertook an experiment to measure the beta-delayed gamma-ray emission of ^{61}Ga. This nuclide is the next incompletely characterized member of the A = 4n+1 series of the $T_z = -1/2$ nuclei. ^{61}Ga is an important nucleus in the rp process, whereby proton capture reactions compete with β^+ decay. In an extended rp process calculation of a type I x-ray burst, nucleosynthesis is thought to continue to the mass 100 region if ^{61}Ga and other nuclei near the drip line are sufficiently bound [Le 83].

^{61}Ga was recently identified [Mo 91] and a $t_{1/2} = 150 \pm 30$ msec half-life measured [Wi 93]. This result is consistent with systematics of the $T_z = -1/2$ nuclei in this region. However, no other spectroscopic data were obtained in these experiments. In the simple single particle shell model, the superallowed Fermi decay of ^{61}Ga involves the conversion of a $p_{3/2}$ proton into a $p_{3/2}$ neutron, corresponding to the ground state of ^{61}Zn. We would expect most of the β-decay strength to consist of this type of transition. One can calculate the Gamow-Teller matrix element for the allowed ground state to ground state transition. However, the known phenomenon of GT strength function quenching observed in other nuclei, could result in the beta decay proceeding through various low lying excited states in the beta daughter. In-beam gamma-ray spectroscopy shows that there are many excited states known in ^{61}Zn [Sc 89]. The first two reside at 88 keV and 124 keV above the ground state and have $J^\pi = 1/2^-$ and $5/2^-$, respectively. One goal of this experiment was the measurement of the extent of this quenching.

To produce ^{61}Ga, we used the ^{40}Ca(^{28}Si,αp2n)^{61}Ga reaction with 175 MeV out of the cyclotron (degraded to 130 MeV at target midpoint) ^{28}Si projectiles with a modified version of our multiple target/multiple capillary He-jet system to produce and transport radioactivity via a 6 m x 1.4 mm i.d. capillary to the RAMA skimmer region. Targets consisted of two ^{nat}Ca targets (2.8 mg/cm^2 and 0.7 mg/cm^2 thick). This reaction has an ALICE-predicted cross section of 240 μb.

It has been shown that improved He-jet transport efficiency can be expected as the number of exit tubes are increased [Mo 80b]. The tradeoff, however, is the longer holdup time in the system, due to the slower gas velocity in the small-diameter multiple capillaries that feed, via a header, into the single exit capillary. As a result, for a short-lived nucleus (e.g., ^{61}Ga), the overall efficiency would actually diminish. To partially remedy this problem, seven of the eleven exit tubes were blocked off so that the total transport time was reduced from ~200 ms to ~150 ms.

After ionization and acceleration, mass separated samples were deposited onto a moving tape at the SDS. The detector arrangement used for the experiment is shown in Figure III-16. Located at the 0° detector arm, there were two 28% coaxial Ge γ–detectors, at 180° to each other and 90° to the beam. On the same arm, there was also an intrinsic planar Ge detector to measure the beta spectrum. There was also a third Ge γ-detector located at the 90° detector arm. Although never used, its purpose was to perform any half-life measurements.

A major source of background in this experiment came from the production and separation of the other mass 61 nuclei, namely, ^{61}Zn ($t_{1/2}$ = 89.1 sec) and ^{61}Cu ($t_{1/2}$ = 3.41 h). ^{61}Zn and ^{61}Cu were made via the ^{40}Ca(^{28}Si,α2pn)^{61}Zn and ^{40}Ca(^{28}Si,α3p)^{61}Cu reactions and have ALICE-predicted cross sections 200 and 300 times greater than the production of ^{61}Ga, respectively. To filter out events from these two nuclei, we took advantage of the fact that ^{61}Zn has $E\left(\beta^+_{max}\right)$ = 4.38 MeV and ^{61}Cu has $E\left(\beta^+_{max}\right)$ = 1.22 MeV. Using the Jänecke-Masson mass formula [Jä 88], one predicts $E\left(\beta^+_{max}\right)$ = 8.18 MeV for ^{61}Ga. Therefore, it was possible to search for all gamma-rays in coincidence with β^+ particles with energy >5 MeV. Additionally, we built a slow-moving tape drive system. The RAMA beam was deposited onto an aluminized mylar tape (~1 meter long x 2.5 cm wide) moving at ~1 mm/sec to remove most of the ^{61}Zn and ^{61}Cu from the immediate vicinity of the detector before it could decay. The advantage of the presence of ^{61}Zn and ^{61}Cu is that the decay of both nuclei is well known, providing an internal calibration, as well as a convenient RAMA beam monitor.

Displayed in Figure III-18 is a spectrum recorded with one of the Ge-γ detectors with the major peaks labeled. As expected, the decays of the other mass 61 nuclei simultaneously deposited onto the tape dominate the spectrum. Upon gating on all betas with E > 5 MeV and removing background, no clear peaks are observed in either gamma-ray detector. This includes any excess 511 keV γ-rays from β^+ annihilation which would indicate a ground state to ground state transition.

While we observed that the cross section for the production of ^{61}Cu was consistent with the predictions of ALICE, the ^{61}Zn rate was down by a factor of 20 from the ALICE prediction. Therefore, the ^{61}Ga production cross section was down by at least a factor of 20 (and probably more than that) from the prediction. This systematic overprediction of the cross section by ALICE has also been observed in our studies of the A = 4n+1, T_z = -3/2 series of beta-delayed proton emitters. It was observed that ALICE would overpredict the production cross section by factors of 10-20 for drip-line nuclei in the mass 60 - 70 region [Ba 93b].

Based on the ALICE-predicted cross section of 240 μb and a 1% RAMA efficiency for gallium (measured at the beginning of the experiment), the deposition rate at the SDS should have been ~16 ^{61}Ga/sec. This assumes a He-jet transit time of 150 ms with 50% efficiency. Our inability to observe any ^{61}Ga decay was due to three problems: diminishing cross section, losses in transit from radioactive decay and use of older (and smaller) germanium detectors.

II.C.2. RAMA Upgrade, Phase II

The gallium-61 experiment proved that the first phase of the RAMA upgrade had been a success. We had improved the ion source efficiency, as well as the mass resolution of the main dipole. It also re-exposed the major weakness of the system: that of the long transit time between the production target and the skimmer. The relatively long transit time would continue to preclude experimental decay studies of nuclei with half-lives less than 200 ms. It was decided to undertake an upgrade to move the ion source region into Cave 2 to place it as close to the target as possible, thus minimizing the losses from radioactive decay in transit. The basic challenge would be a redesign of the optics system centered around the focus points at the magnet focal plane and at the SDS.

In addition, due to the close proximity of the ion source to the target, a remote handling system was also developed, to minimize radiation exposure to personnel when changing the ion source. This remote handling system consists of a motor, fully vacuum-interlocked, that retracts a bellows on the Cave 2 beam line. The beam line, which includes the RAMA He-jet target chamber and beam dump, is lowered via a hydraulic lift into a lead-lined sarcophagus. Finally, a shielded cover rolls over the top to fully enclose the target and beam dump region. All phases of this procedure are fully automatic with the control and monitoring performed outside the high radiation area.

III.C.2.a. Optics Calculations

Preliminary optics calculations were performed with the beam transport program LATTICE [St 89], operated in the lattice mode. LATTICE is a first-order code that uses matrix algebra to calculate and plot the propagation of a beam along a beamline. It also has an optimization routine to tune the beam to a specific desired focus at the end of the beam line. Because of its simplicity, LATTICE is extremely fast, allowing one to optimize beam line parameters quickly and accurately. The purpose of this exercise was to determine the feasibility of this project given the optical focusing elements available to us. For this reason, these calculations were performed only to the RAMA focal plane. Also, it was hoped that the current optics system from the entrance of the first quadrupole triplet to the RAMA focal plane could be left unperturbed.

Results of calculations using a 40 keV singly-charged mass 39 beam showed that with the addition of a quadrupole doublet, an einzel lens and a mirror, a focus could be achieved at the RAMA focal plane. A beam envelope with spot size halfwidths

$x = 1.5$ mm and $y = 5.0$ mm was realized. The other important feature of this solution is that it is very similar to the existing RAMA optics.

LATTICE does have some limitations. It is unable to calculate any effects above first order. From initial calculations when RAMA was first constructed, it was known that there were significant second-order effects that must be compensated. LATTICE is also unable to accurately treat certain beam line elements such as Wien filters and einzel lenses, both which play a crucial role in the RAMA beam line optics. In addition, while not presenting any real difficulties, the electrostatic quadrupoles had to be treated as magnetic quadrupoles and the resultant magnetic fields converted to electric fields.

Complete first- and second-order optics calculations were performed using the program COSY 5.0 [Be 87a]. COSY uses differential algebra techniques [Be 87b] to determine the coefficients of expansion of the Taylor series solution to the equation of motion of charged particles in a static electric or magnetic field [Be 89]. From this, transfer maps up to any order can be efficiently computed for any beam optics system. On a more practical note, COSY has the advantage over LATTICE in its ability to handle a fuller range of corpuscular optical elements up to any arbitrary order. As a check, the parameters determined from LATTICE were converted and used as input parameters in a COSY lattice with similar results.

Results from COSY calculations are presented as a beam trace in Figure III-19. The test particle beam is, as before, a 40 keV mass 39 beam. The size of the virtual source for the optics calculations is defined as the ion source exit aperture with the divergence defined from the geometric acceptance of the extractors. As before, the beam is cylindrically symmetric with $x'_0>>x_0$ and $y'_0>>y_0$. The beam is focused with two einzel lenses (EL1 and EL2) to a Wien filter (WF), which removes He^+ ions. An electrostatic quadrupole doublet (ED0), operating in DF mode, is used to capture and focus the beam through a 90° electrostatic mirror (EM1) to a virtual waist in front of the first electrostatic quadrupole triplet (EQ1). The optics calculations now begin to resemble the previous RAMA optics. The triplet, in DFD mode, is used to focus the beam through the main RAMA dipole to a point at the focal plane. The focus is a tall pencil-like beam with envelope halfwidths $x = 1.5$ mm and $y = 5.0$ mm, as calculated previously. A system dispersion of 1.85 m was also calculated. The entrance and exit sextupoles (SX1 and SX2) are employed to minimize the second-order aberrations in the beam spot. After a 10.7° deflection, the mass separated beam is focused and transported as a parallel beam by a second electrostatic quadrupole triplet operating in FDF mode. And, finally, a third einzel lens (EL3) is used to focus the beam to a point at the shielded detector station.

At this point, the beam envelope is nearly circular with halfwidths x = 1.2 mm and y = 1.5 mm. A small point focus was desired, because we planned to mount our detector ball at the SDS and deposit the RAMA beam onto a thin foil located in its center region. This foil has a length of 7.6 mm in the x-dimension and 12.6 mm in the y-dimension.

III.C.2.b. RAMA Optics

Figures III-20a-c provide a schematic diagram of the current RAMA system. Connecting the He-jet target to the skimmer region is an ~30 cm long x ~0.6 mm i.d. capillary. The transit time for this setup was measured by using the 40 MeV ^{3}He + ^{nat}Mg reaction with 20% ^{nat}Ne admixture and the single target/single capillary He-jet target setup. Radioactive recoils were transported along a 0.61 mm i.d. capillary and deposited onto a thin aluminum foil in front of a surface barrier silicon detector placed where the ion source is mounted. By gating on the 4.44 MeV alpha group in ^{20}Na, the transit time was measured to be 50 ms. This value is a good measure of the sweepout time of the target chamber since the transit time through the capillary should be much quicker than the time measured.

After ionization and extraction, the beam is focused by two einzel lens (one located in the ion source/extractor box in Figure III-20a, the other as shown in Figure III-20b) to a redesigned Wien filter. As before, the Wien filter is employed to remove He$^+$ ions. The redesign was necessary in order to increase the acceptance.

A Wien filter uses crossed magnetic and electric fields whereupon the forces acting on particles with charge q and a selected velocity v_0 are balanced out:

$$q\mathbf{E} - qv_0\mathbf{B} = 0. \tag{3-8}$$

Equation (3-8) is called the Wien condition. Particles of a different velocity v are deflected at an angle θ with

$$\theta = 2\sin^{-1}\left[\frac{LqE}{4U}\left(1-\frac{v}{v_0}\right)\right], \tag{3-9}$$

where, U is the energy of the ion, L is the effective length of the field, and E is the magnitude of the electric field. The physical geometry of the RAMA system required that the He$^+$ deflection angle be constrained between 6° and 12°. The maximum angle was chosen to prevent the deflected beam from striking the field plates while the minimum serves to prevent the beam from entering the rest of the optics system.

Field maps show that the magnetic field is fairly inhomogeneous in the region between the electric field plates and rapidly drops to zero outside the magnet yoke. As it is much easier to monitor and control the electric field, the Wien filter is operated by keeping the magnetic field constant and varying the electric field. The electric field will scale according to

$$\sqrt{\frac{m0}{m_1}}\ \mathbf{E_0} = \mathbf{E_1}, \qquad (3\text{-}10)$$

upon changing the mass selection from m_0 to m_1.

There are significant focusing effects from the Wien filter which was noticed when the yield of beam increased when the polarity of the first quadrupole was reversed. This focusing effect comes from the improper matching of the two fields in the fringing regions of the filter [Ka 90]. The doublet now runs in the DD mode with the first quadrupole barely turned on and the second quadrupole operated with a significantly higher electric field than called for by the calculations.

As depicted in Figure III-20b, bending the ion beam 90° is accomplished by an electrostatic mirror. The mirror was chosen over an electrostatic or magnetic dipole because of the limited space available. The electrostatic mirror is analogous to an optical mirror in that it reflects (or, in this case, deflects) and inverts the beam in the bend plane. It has no other effect on the beam optics. The mirror consists of a relatively (compared to beam dimensions) large (14 cm x 9 cm) high voltage plate separated by a 2 cm gap from a ground plane of equal dimensions. This ground plane is a frame with a 1-dimensional grid of 0.1 mm gold-coated tungsten wires spaced 3 mm apart stretched across it. This assembly is placed at 45° with respect to the beam axis such that the vertical and horizontal RAMA centerlines intersect at the center of the region between the high voltage anode and the ground grid. When voltage is applied to the anode, the beam travels through the ground grid and is bent 90° from the vertical center to the horizontal center of the RAMA dipole. The tilt angle of the mirror can be adjusted ±2.5° to fine tune the height of the beam to correct for any misalignments.

It was observed that two additional einzel lens were required between the mirror and the first quadrupole triplet. These were needed as it appeared that the beam was scraping the beam pipe in this long drift. Part of this problem was our inability to extract the beam at the full desired energy of 40 kV. This primarily was a result of the limitation on the mirror to hold more than 20 kV in the presence of the ion beam without breaking down. This breakdown was caused by the insufficient gap between the high voltage plate and the ground plane. A redesign of the mirror is currently in progress that will remove this restriction.

Since the remaining optics units to the focal plane were not disturbed, the beam is focused to a point with $y > x$. Figure III-21 shows a mass scan of a 25 keV mass 20 beam measured at the focal plane. The mass resolutions ($M/\Delta M$) quoted are comparable to the resolutions measured before the ion source move. From R_{FWHM}, a dispersion of 1.81 m is calculated, in agreement with results from COSY.

As shown in Figure III-20c, aside from moving the second quadrupole triplet and the last einzel lens, the optics of the SDS beamline are unchanged. The advantage to moving the quadrupole upstream is to focus the beam as soon as possible after the focal plane. COSY calculations show that the beam has a rather large divergence in the radial plane and for the desired parallel beam, the ultimate size after the quadrupole triplet is determined by how quickly it can be captured. With the last einzel lens, the beam is brought to a point focus at the shielded detector station.

III.C.2.c. Sodium-20 Experiment

The initial RAMA production experiment was to investigate a possible low-energy alpha emission following the beta decay of ^{20}Na, therefore, test runs were performed to check sodium yields. Figure III-21 shows one spectrum of ^{20}Na recorded at the focal plane. Using the single target/single capillary setup, ^{nat}Ne, which was mixed into the transport helium, was bombarded with 40 MeV ^{3}He to make ^{20}Na via the ^{20}Ne(^{3}He,3n)^{20}Na reaction. Radioactivity was transported along a 0.61 mm i.d. capillary to the RAMA ion source. After ionization, extraction to 25 keV and mass separation, mass 20 ions were deposited onto a thin aluminum foil in front of a silicon detector situated at the RAMA focal plane. Results from these test runs demonstrate an ~1% RAMA efficiency for sodium.

III.C.2.c.i. ^{20}Na Experimental Background

A low-energy peak had been observed during a series of experiments searching for low-energy protons from the IAS in ^{23}Al positron decay [Ti 95]. In these experiments, a 45 MeV proton beam impinged onto a ^{24}Mg target. Radioactive recoils were thermalized, transported via a helium-jet and deposited onto a tape located in the center of our low-energy detector ball (see Figure III-4). In the alpha region of the ΔE-E 2-dimensional spectra were alphas predominantly from the decays of ^{8}B (from carbon contaminants in the target) and ^{20}Na (from the ^{24}Mg(p,αn)^{20}Na reaction), as well as a small amount from ^{24}Al. Crude half-life measurements showed that this low-energy peak had a half-life consistent with ^{20}Na. Upon adding ^{20}Ne to our helium-jet to take advantage of the higher cross section for making ^{20}Na in the ^{20}Ne(p,n) reaction, this peak scaled with the production of ^{20}Na. A final indication was the disappearance of this peak when the proton bombarding energy was reduced to 20 MeV, which is below the ^{20}Na production threshold of 25.0 MeV. Despite this evidence, the question still remained as to whether this peak was from the decay of ^{20}Na, from the decay of another nucleus, or from a strange summing artifact of our detectors. A mass separated sample was needed to remove any ambiguities in the mass number, as well as to eliminate the high background count rate caused by the β-decay of other copiously and simultaneously produced nuclei closer to stability.

The βα decay of ^{20}Na was first reported by Torgerson et al. [To 73]. Approximately twenty percent of the time ^{20}Na decays to states in ^{20}Ne which subsequently decay by the emission of an alpha particle to the ground state of ^{16}O [Aj 87]. Because of the large amount of kinetic energy imparted to the recoiling ^{16}O nucleus, several experiments have been performed to determine $\beta-\nu-\alpha$ angular correlation coefficients [Cl 89b and Cl 83]. Such measurements provide a means in which to identify Fermi and Gamow-Teller components in nuclear β-decay and to test the validity of the conserved vector current hypothesis. The superallowed beta decay of the $J^\pi = 2^+$, T = 1 ^{20}Na ground state to the isobaric analog state in ^{20}Ne (E_X = 10.274 MeV) has a Gamow-Teller component since it is a $J \neq 0$ transition. As predicted by the conserved vector current hypothesis, the weak vector coupling constant, g_V', for this transition was determined to be in agreement with values deduced from J = 0 superallowed Fermi beta transitions [Cl 89b].

A partial decay scheme for ^{20}Na is depicted in Figure III-23. Shown are the alpha emitting states, as well as those states that could emit parity-conserving alpha particles with $\ell \leq 3$ to the ground state of ^{16}O. It is interesting to note that there are two states just above the alpha emission threshold: a 1^- state at 5.785 MeV and a 3^- state at 5.622 MeV excitation energy. Both states could be beta fed by a first forbidden beta transition followed by decay to the ground state of ^{16}O by emitting alpha particles with laboratory energies of 844 keV (ℓ = 1) and 714 keV (ℓ = 3), respectively. As a rough calibration indicated that the energy of this peak was ~700-850 keV, one of these states was considered to be the emitter. A comparison of half-lives for γ emission, assuming single particle motion, to the ^{20}Ne ground state to α emission to the ^{16}O ground state shows that the ℓ = 3, 714 keV alpha transition is ~4.5 orders of magnitude faster than the competing E3 gamma-ray to the ground state. However, the partial half-life of the ℓ = 1, 844 keV alpha particle is approximately equal to the competing E1 gamma transition to the ^{20}Ne ground state.

To produce ^{20}Na, a target system comprising five solid targets, (three of ^{24}Mg (~1 mg/cm^2) and two of ^{nat}Mg (~2 mg/cm^2)), as well as gaseous ^{20}Ne were bombarded with a 1-2 μA, 40 MeV proton beam. ^{20}Ne was mixed with the helium transport gas at an ~25% level to pressurize the multiple target/multiple capillary He-jet target chamber to 1.3 atm. The generation of ^{20}Na proceeded through the ^{20}Ne(p,n)^{20}Na and

$^{24}Mg(p,\alpha n)^{20}Na$ reactions. Radioactive recoils were thermalized and transported along a 0.61 mm i.d. stainless steel capillary to the skimmer region of RAMA. A 25 keV, mass separated ion beam was deposited onto an ~20 μg/cm^2 carbon foil located in the center of our low-energy detector ball. Figure III-24 shows a cutaway view of the detector setup. The detector was mounted onto the end of the 0° detector arm at the SDS. Beams of $^{20}Ne^+$ were used to tune the mass separator as well as to provide a convenient check on the RAMA stability.

III.C.2.c.ii. Results and Discussion

The sodium-20 deposition rate during this experiment was ~100 atoms/min. This rate was much lower than what was expected, for several reasons. The second quadrupole triplet was mistuned, resulting in improper optics along the shielded detector station beamline. This has been corrected by installing beam diagnostics in front of the 3° deflection plates. The diagnostic consists of three concentric copper rings with diameters 0-2.5 cm, 2.5-5 cm and 5-7.6 cm. Using these three "faraday cups", the quadrupole has now been correctly tuned so that 100% of the beam is confined to a 5 cm diameter. A second and much more serious effect was the diffusion of CF_4 from the detectors through the polypropylene entrance windows. Although the diffusion rate was small enough not to affect adversely the operation of the detector, it was large enough to affect the vacuum in the SDS region. The pressure increased by over 2 orders of magnitude upon flowing gas through the detector, causing the ion beam to blow up and lowering the amount hitting the carbon foil. To remedy this problem, a liquid nitrogen line trap has replaced the 0° detector arm of the SDS. This will trap the Freon-14 and preserve the vacuum except for the last 20 cm before the detector. Also, slots will be cut into the connection tube and a 15 cm oil-diffusion pump will be connected to the outer vacuum chamber, supplementing the roots blower. Finally, the detector ball will be redesigned to eliminate leaks to the backside of the detector which occur along the electrical feedthrough wires. These redesigns will allow the detector to be used in a high-vacuum environment.

Figure III-25 shows a summed alpha particle spectrum recorded with three of the gas ΔE-gas ΔE-silicon E detector telescopes. The two main peaks at 2.15 MeV (100%) and at 4.44 MeV (17.3%) are clearly visible, as well as a smaller peak just above the alpha particle detector threshold. The intensity of this peak is 4.5 ± 0.2% of the main 100% alpha group. Since this peak is below the range of an accurate calibration determined from the known ^{20}Na beta-delayed alpha groups, a separate experiment was performed to determine its energy.

III.C.2.c.iii. Detector Calibration

The detector calibration, as outlined in Section III.B.3., was performed independently of the main experiment. A beam of 40 MeV ^{3}He projectiles struck a helium/neon gaseous mixture as well as a single ^{nat}Mg target. Recoils were transported via the helium-jet and deposited onto an aluminum plate directly opposite the singles version of the gas ΔE-gas ΔE-silicon E detector telescope. Between the plate and the detector was a wheel which had 9 aluminum foil degraders, each of a different thickness, arrayed along the spokes. By rotating the wheel, we could observe the stepwise degradation of the ^{20}Na alpha peaks to below the detector threshold. For this experiment, aluminum foil degrader thicknesses between 0-1835 μg/cm^2 were used along with a detector telescope with a 44 μg/cm^2 polypropylene entrance window, a 66 μg/cm^2 Freon-14 gas thickness and a 58 μg/cm^2 silicon deadlayer. The thickness of each component had been previously measured off-line.

The generation of the calibration curve was performed in the following manner. Energy losses incurred by the undegraded alpha particles traversing the detector were calculated from the known thicknesses and the stopping power tables in ICRU Report 49 [In 93]. The dE/dx values in this energy range are well known so there should be little error associated with this calculation. Once calculated, a straight line relationship between energy deposited in the silicon crystal and channel number is determined. The incident energy of an unknown alpha peak can be obtained by first determining the energy deposited in the silicon detector. With the known detector component thicknesses, the energy losses through the detector can then be back calculated to arrive at an incident alpha energy.

As a test of this method and of the modeling of the detector, a comparison was made between experimental energy losses in the detector and predictions. Again, based on the known aluminum foil thicknesses and stopping powers, the energy of degraded alpha particles incident on the detector was calculated. This number was then compared to the measured energy deposited in the silicon crystal to determine the energy lost through the detector components. This curve is plotted in Figure III-26 for all data points recorded in this experiment. The experimental values agree with the predicted values down to ~1.5 MeV. Below this, while the curve generated from the experimental values has the predicted shape including the expected turnover around 1 MeV, the predictions tend to underestimate the energy loss through the detector. This underprediction is most likely due to nonlinearities associated with the detector electronics. The observation that the shapes of the two curves are similar implies that our modeling of the detector is accurate to at least 50 keV. Experiments are in preparation to measure the electronic nonlinearity function to improve upon this confidence limit.

Examples of data recorded during this detector calibration experiment are shown in Figure III-27a,b. Figure III-27a represents data in which no degrading foil was used, while Figure III-27b shows data in which a 1307 $\mu g/cm^2$ aluminum degrader was placed between the decaying source and the detector. One point in the calibration curve (Figure III-26) represents the low-energy peak in Figure III-27b, which arises from the 2.15 MeV alpha group, degraded to 695±17 keV. By back calculating the energy loss through the detector, the incident energy of the low-energy peak in Figure III-27a was determined to be 518±26 keV (in the lab). This energy is ~200 to 350 keV less than the energy of an alpha particle emitted from either state in ^{20}Ne under consideration. There are no known excited states in ^{20}Ne that could emit alpha particles within the required energy range to the ground state of ^{16}O.

The possibility that the alpha daughter state is an excited state in ^{16}O cannot be excluded. There are two possible energy and parity conserving transitions from excited states in ^{20}Ne leading to the third or fourth excited state in ^{16}O, as outlined in Table III-3. However, none of these possible emitter states are presently known to decay by alpha emission. It would be expected that their higher decay energy would favor a transition to the ground state over an excited state given such low angular momentum barriers to the transitions in question. The last column in Table III-3 is the calculated ratio of decay widths between an α transition to the ground state and the excited state in ^{16}O. As expected, the transition that leads to the ground state is favored by over 7 orders of magnitude. A parity violating transition can be ruled out as the 4.5% relative α intensity observed would require unrealistically high admixtures of positive parity states ($F^2 > 10^7$). As a comparison, the known parity non-conserving alpha transition following the beta decay of ^{16}N has a relative (to the main 1.77 MeV α group) intensity of $(3.8 \pm 0.7) \times 10^{-3}$% [Ne 74]. This indicates a mixing coefficient of $\sim 3 \times 10^{-15}$.

Figure III-28a-d shows 2-dimensional plots recorded in each of the gas ΔE vs. silicon E detector for the two runs shown in Figure III-27 (no degrader in Figure III-28a,b and 1307 $\mu g/cm^2$ degrader in Figure III-28c,d). These plots are backprojected spectra in which beta particles and protons have been gated out. Evident in each spectra are alpha particles from ^{20}Na and ^{8}B (the cluster of points just below the main 2.15 MeV alpha group in Figure III-28a,b). The lines drawn on each spectrum represent the predicted shape of the differential energy loss for alpha particles. It is interesting to note that while the degraded 2.15 MeV alpha group falls inside the expected position in both gas ΔE-silicon E plots, the low-energy peak in Figure III-28a,b does not.

These results lead us to conclude that the low energy peak is not an alpha particle, but rather it is an ^{16}O recoil entering the detector telescope (and stopping in the second gas ΔE detector) in coincidence with a beta particle traversing the telescope and triggering the silicon E detector. This conclusion had been initially rejected because it was believed that the polypropylene entrance windows would stop any ^{16}O recoils. However, extrapolated data from the stopping power tables of Northcliffe and Schilling [No 70] show that while the recoils can penetrate the window, they are stopped in either the gas region or in the silicon deadlayer. Further we can ascertain that it is the 537 keV ^{16}O recoil associated with the 2.15 MeV alpha transition that we are observing as it loses just enough energy in both ΔE gas detectors to make it appear at first glance to be an alpha particle. In contrast, the 1.11 MeV ^{16}O recoil from the 4.44 MeV alpha transition loses too much energy in each gas detector, which puts each signal beyond the range of the ADC. Finally, the shape and centroid of the low-energy peak are almost identical to the beta spectrum, further reinforcing our conclusion.

III.D. TISOL Facility

The TISOL (Test Isotope Separator On-Line) is an ISOL-based mass separator located at TRIUMF in Vancouver, B. C., Canada [Ox 87]. The TRIUMF Cyclotron is a 6-sector isochronous cyclotron capable of accelerating H^- ions to 520 MeV. Extraction from the cyclotron is achieved by intercepting the primary beam with a thin carbon foil to generate beams of positively charged protons up to 10 μA for delivery to the Proton Hall. The TISOL facility, located in the Proton Hall on beamline 4A, uses spallation or fission/fragmentation reactions on targets of solids or liquids heated up to 2500°C. Figure III-29 shows a schematic layout of the TISOL facility [Au 92].

For the experiments described in this thesis that were performed at TRIUMF, a Na loaded zeolite target was employed. Zeolites are a class of three-dimensional polysilicates in which SiO_4/AlO_4 tetrahedra molecules are interconnected to form highly symmetrical structures called cuboctahedra [Bu 89]. These structures act as "molecular sieves" as they contain large cavities in which cations such as Ca^+, Na^+ and K^+ can be trapped. The 13X zeolite ($NaAlSiO_4$) target used in the TISOL experiments has a 1.2 nm cavity which can hold 17-19 Ar, N_2 or O_2 molecules at low temperatures. As the target is heated, these molecules are released as the "sieve" regenerates [Do 92].

Atoms and molecules diffuse out of the target through a small transfer tube and enter into an ECR ion source [Do 90]. Positive singly-charged atomic and molecular ions are extracted at 12 keV, and mass separated through a 90° vertical magnetic dipole

($\rho = 1.25$ m). The ions are then focused electrostatically to a point at one of three experimental stations. Typical full width at one half maximum mass resolutions, ($M/\Delta M$), are 1000-3000 depending on the setting of the resolution analyzing slits.

III.E. Tables for Section III

Table 3-1. Rare earth alpha emitters observed at the RAMA Focal Plane using the 125 MeV ^{16}O + ^{nat}Nd reaction.

Element	Melting Point (K)	Isotope[a)]	Half-life	Alpha Energy (MeV)
Terbium	1630	^{151}Tb^{g}	17.61 h	3.409
Dysprosium	1682	^{151}Dy	17 m	4.067
		^{152}Dy	2.37 h	3.629
		^{153}Dy	6.3 h	3.456
Holmium	1743	^{151}Ho (hs)	35.2 s	4.517
		^{151}Ho (ls)	47 s	4.607
		^{152}Ho (hs)	50 s	4.453
		^{152}Ho (ls)	2.4 m	4.387
		^{153}Ho (hs)	2.0 m	3.91
		^{153}Ho (ls)	9.3 m	4.01

a) The high spin and low spin isomers of the holmium isotopes are designated by the symbols (hs) and (ls), respectively.

Table 3-2. RAMA efficiencies for some selected nuclei.

Nucleus	Half-Life	Melting Point (K)	Reaction	η_{Rama} (%)
^{23}Mg	11.32 s	922	^{24}Mg(p,pn)^{23}Mg	0.01[a)]
^{24}Na	14.96 h	371	$^{25(26)}$Mg(p,2p(2pn))^{24}Na	0.3[a)]
^{61}Cu	3.35 h	1358	^{40}Ca(^{28}Si,α3p)^{61}Cu	0.3
^{61}Zn	1.485 m	693	^{40}Ca(^{28}Si,α2pn)^{61}Zn	0.1[a)]
^{63}Zn	38.5 m	693	^{40}Ca(^{28}Si,4pn)^{63}Zn	0.9
^{65}Ga	15.2 m	303	^{58}Ni(^{16}O,2αn)^{65}Ga	3.8
^{67}Ge	19.0 m	1210	^{58}Ni(^{16}O,αp2n)^{67}Ge	0.2

a) RAMA efficiency was not optimized.

Table 3-3. Possible low energy (518±26 keV) alpha transitions to excited states in ^{16}O following the beta decay of ^{20}Na.

Emitter State in ^{20}Ne E_{ex}; J^{π}	Final State in ^{16}O E_{ex}; J^{π}	E_{α}^{lab}(keV) ; ℓ	$\frac{\Gamma_{gs}^{\alpha}}{\Gamma_{ex}^{\alpha}}$
12.327; 2^+	6.917; 2^+	544 ; 0	3.4E+07
12.472; 2^+	7.117; 1^-	500 ; 1	3.1E+08

III.F. Figures for Section III

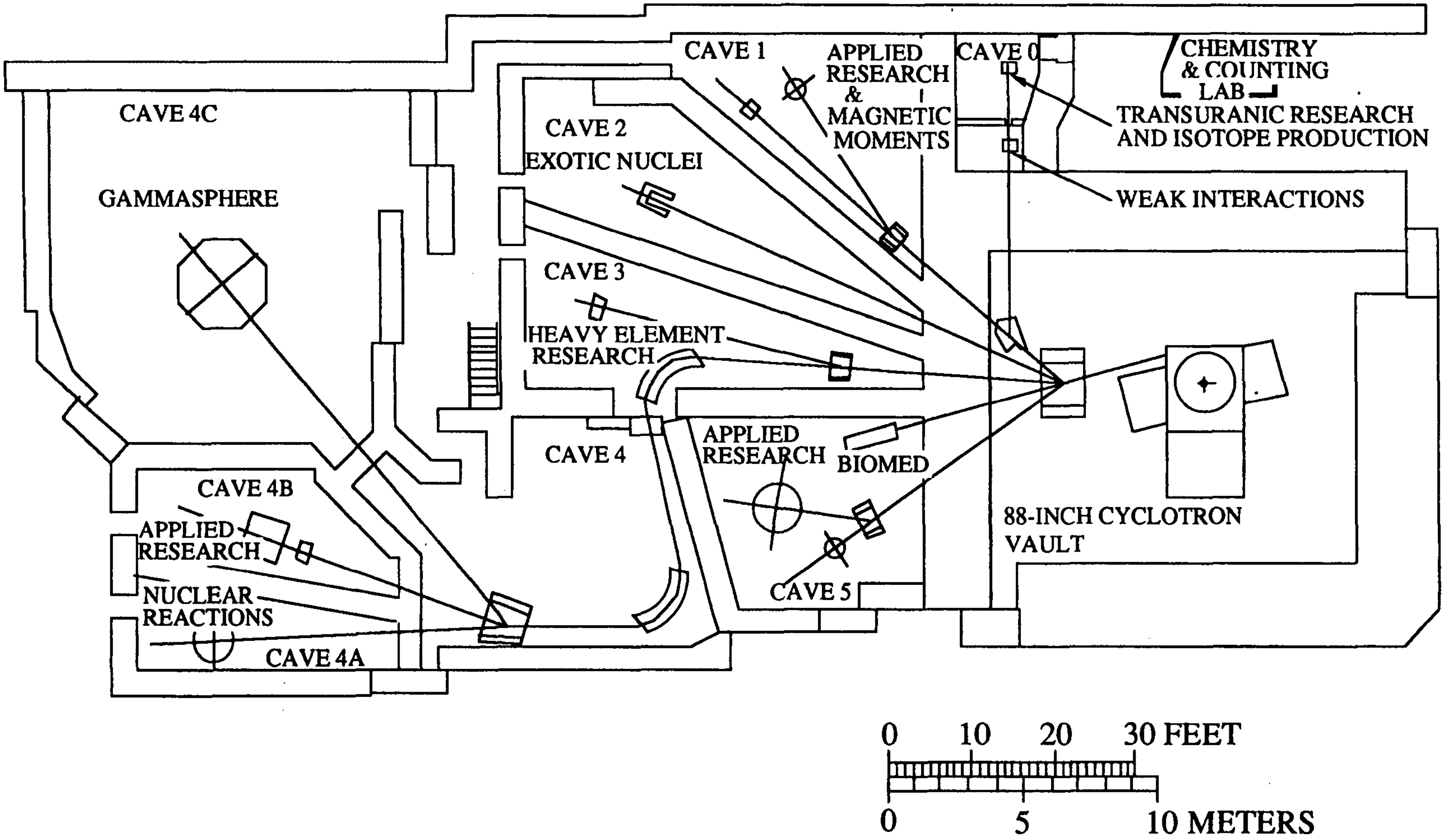

88-INCH CYCLOTRON FACILITY

Figure III-1.

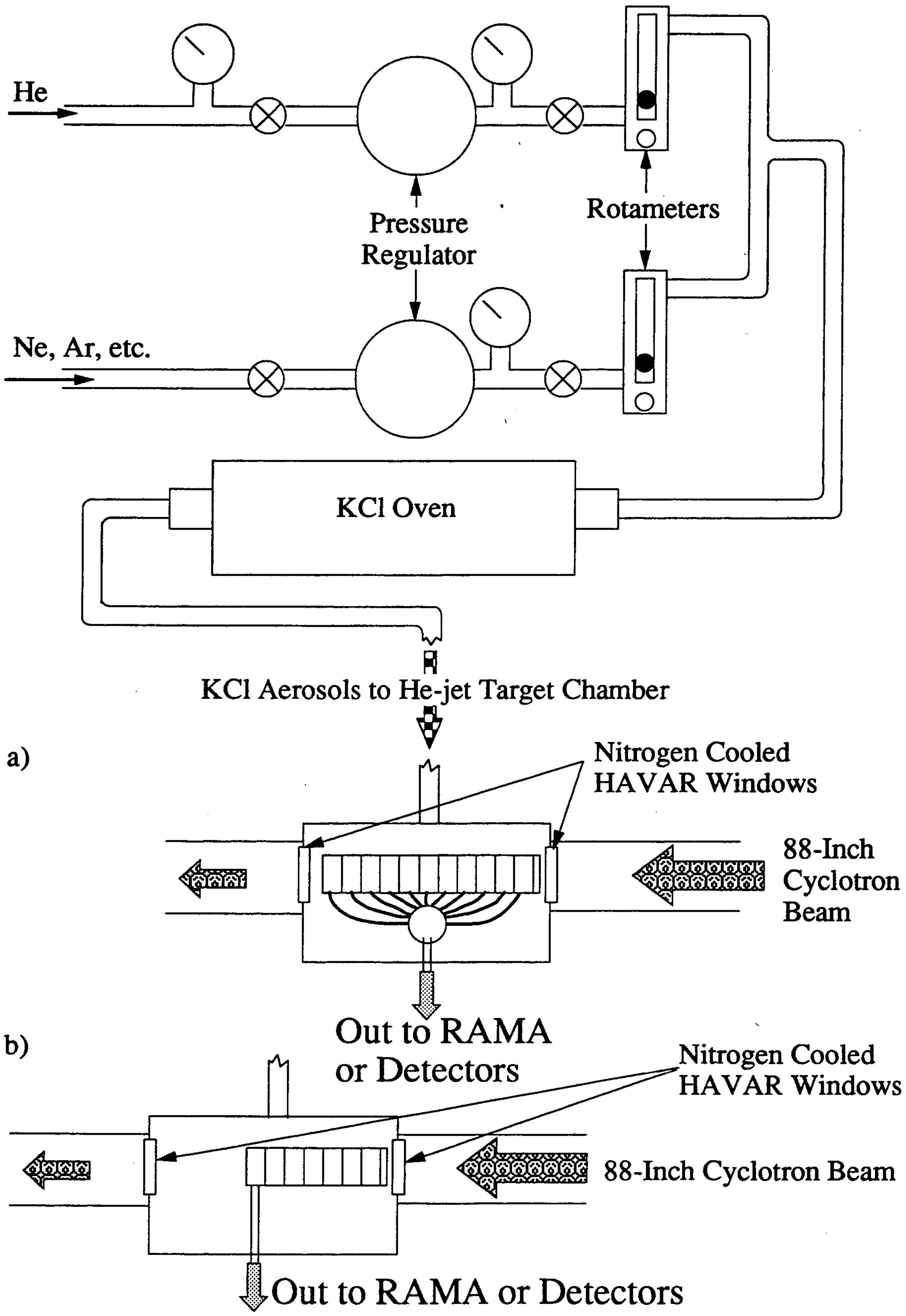
He
Ne, Ar, etc.
Pressure
Regulator
Rotameters
KCl Oven
KCl Aerosols to He-jet Target Chamber
a)
Nitrogen Cooled
HAVAR Windows
88-Inch
Cyclotron
Beam
Out to RAMA
or Detectors
b)
Nitrogen Cooled
HAVAR Windows
88-Inch Cyclotron Beam
Out to RAMA or Detectors

Figure III-2.

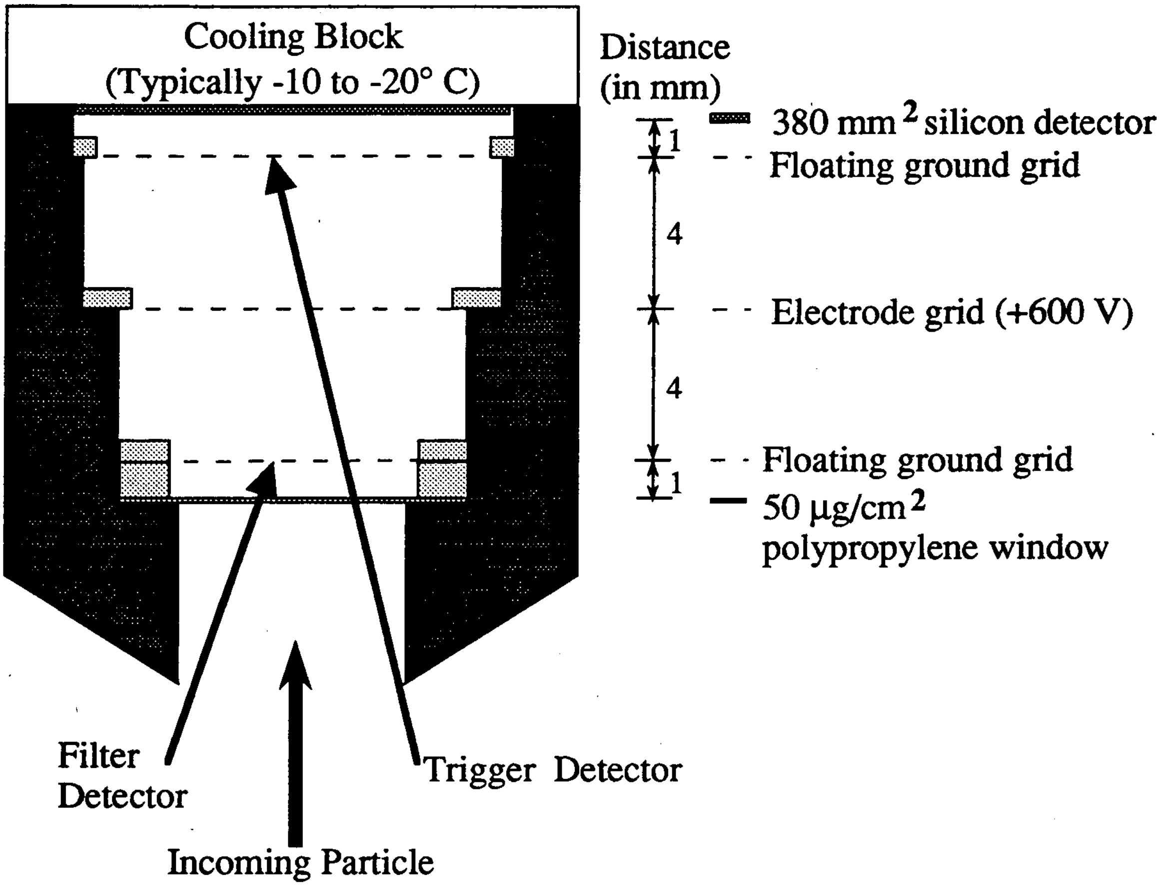
Cooling Block
(Typically -10 to -20° C)
Distance
(in mm)
1
4
4
1
380 mm² silicon detector
Floating ground grid
Electrode grid (+600 V)
Floating ground grid
50 µg/cm² polypropylene window
Filter Detector
Trigger Detector
Incoming Particle

Figure III-3.

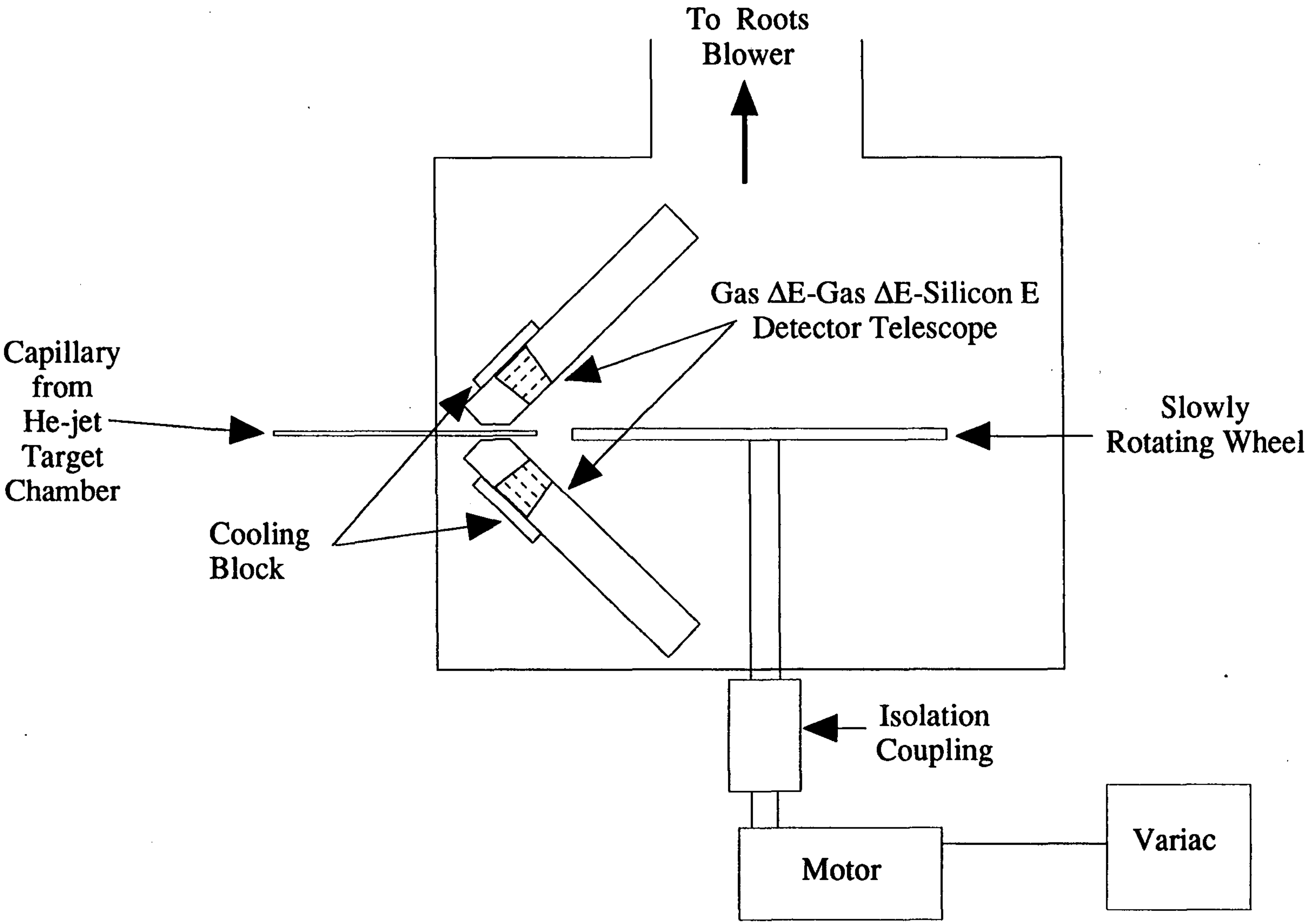
To Roots Blower
Gas ΔE-Gas ΔE-Silicon E Detector Telescope
Capillary from He-jet Target Chamber
Slowly Rotating Wheel
Cooling Block
Isolation Coupling
Variac
Motor

Figure III-4.

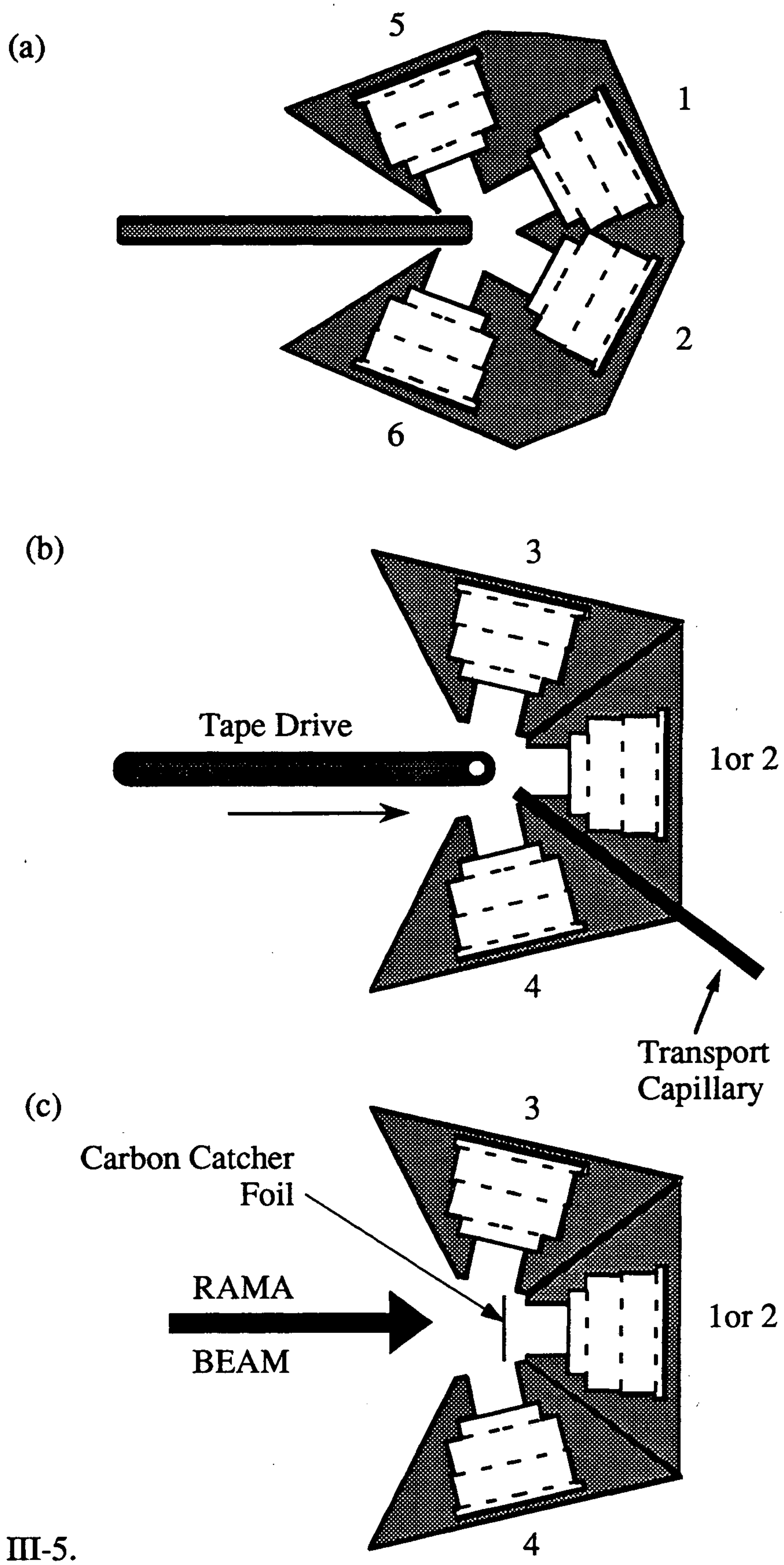
(a)
5
1
2
6
(b)
3
Tape Drive
1or 2
4
Transport Capillary
(c)
3
Carbon Catcher Foil
RAMA
BEAM
1or 2
4

Figure III-5.

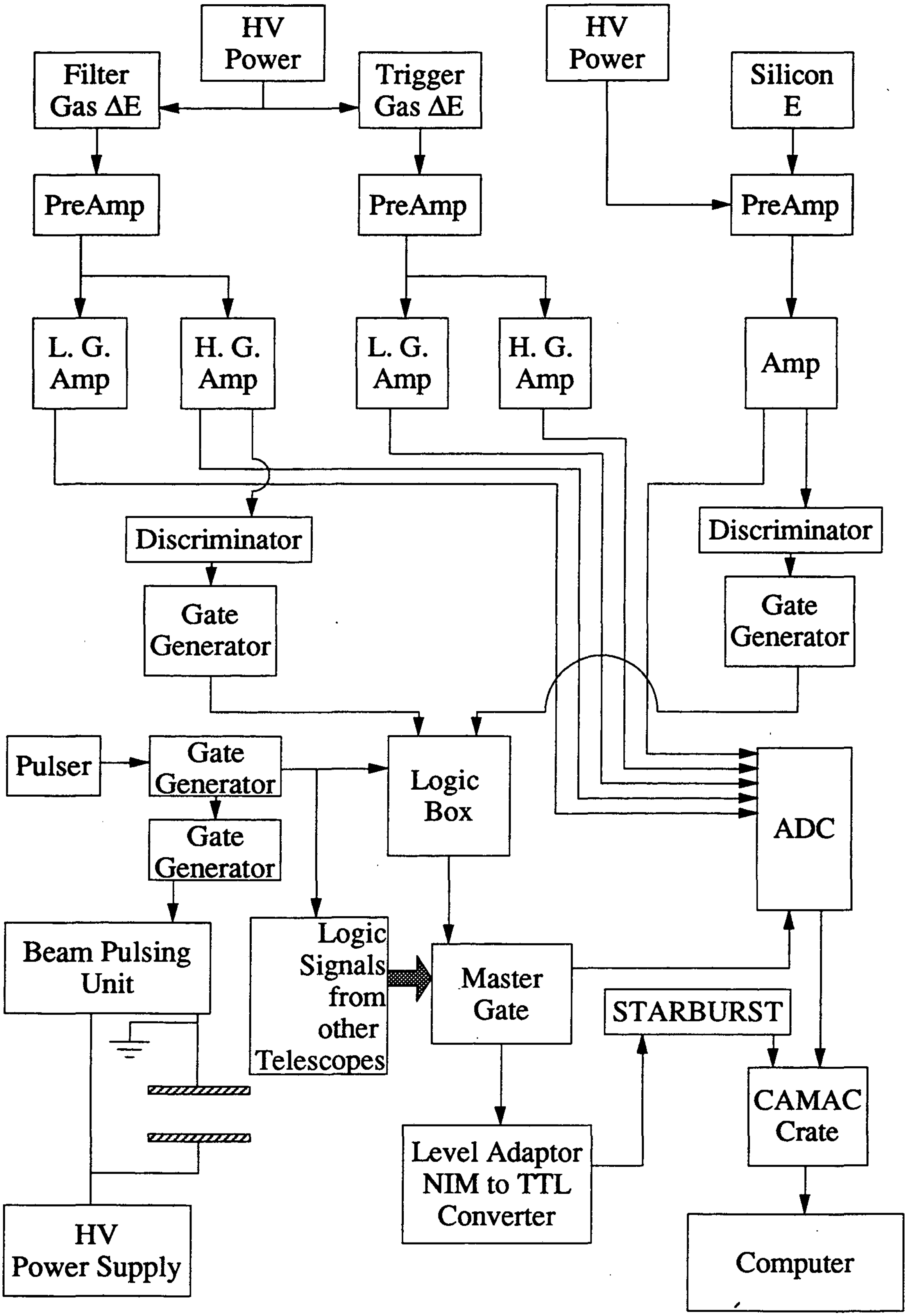
HV Power
Filter Gas ΔE
Trigger Gas ΔE
HV Power
Silicon E
PreAmp
PreAmp
PreAmp
L. G. Amp
H. G. Amp
L. G. Amp
H. G. Amp
Amp
Discriminator
Discriminator
Gate Generator
Gate Generator
Pulser
Gate Generator
Gate Generator
Logic Box
ADC
Beam Pulsing Unit
Logic Signals from other Telescopes
Master Gate
STARBURST
CAMAC Crate
Level Adaptor NIM to TTL Converter
HV Power Supply
Computer

Figure III-6.

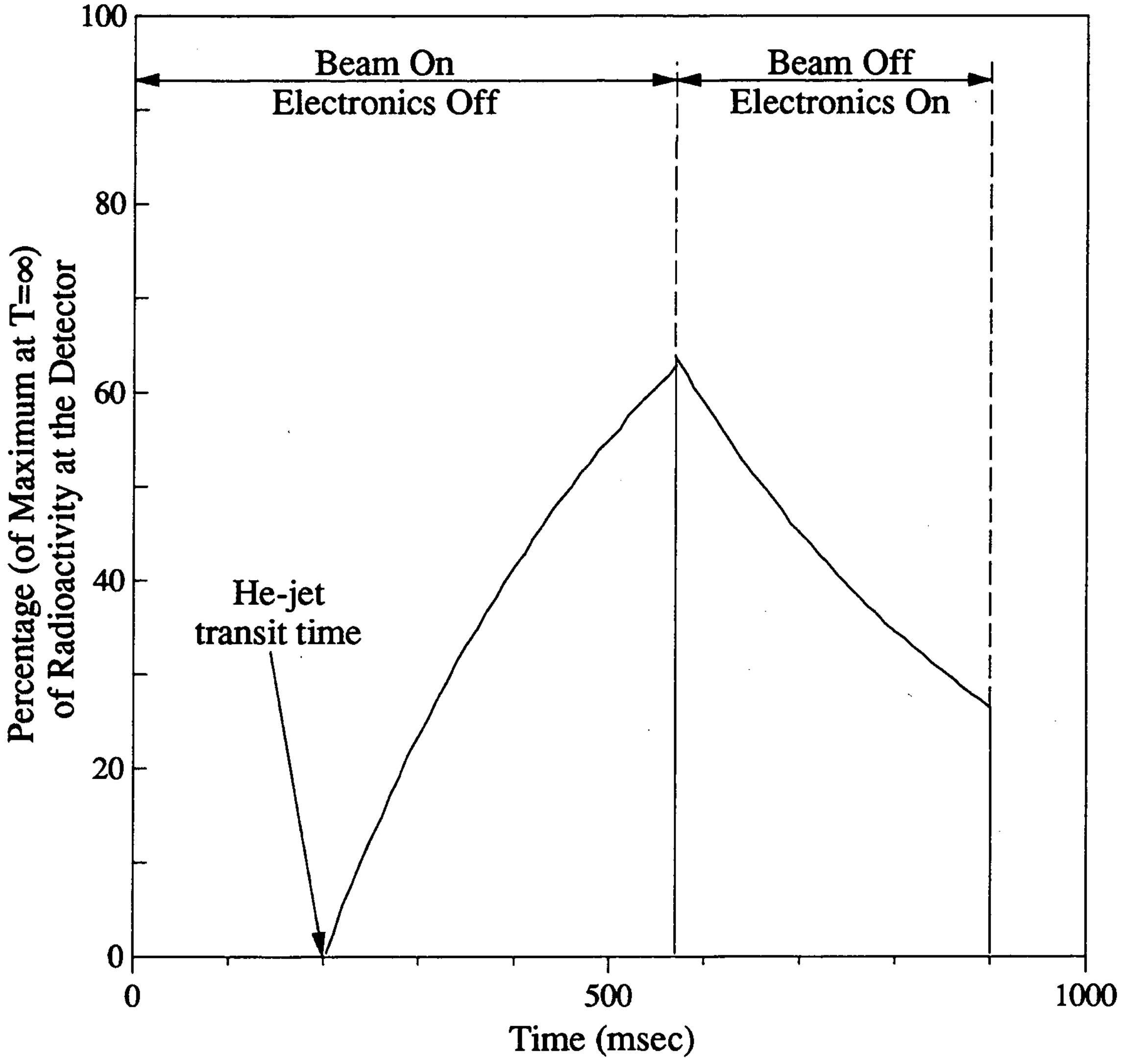
Beam On
Electronics Off
Beam Off
Electronics On
He-jet
transit time
Percentage (of Maximum at T=∞)
of Radioactivity at the Detector
100
80
60
40
20
0
0
500
1000
Time (msec)

Figure III-7.

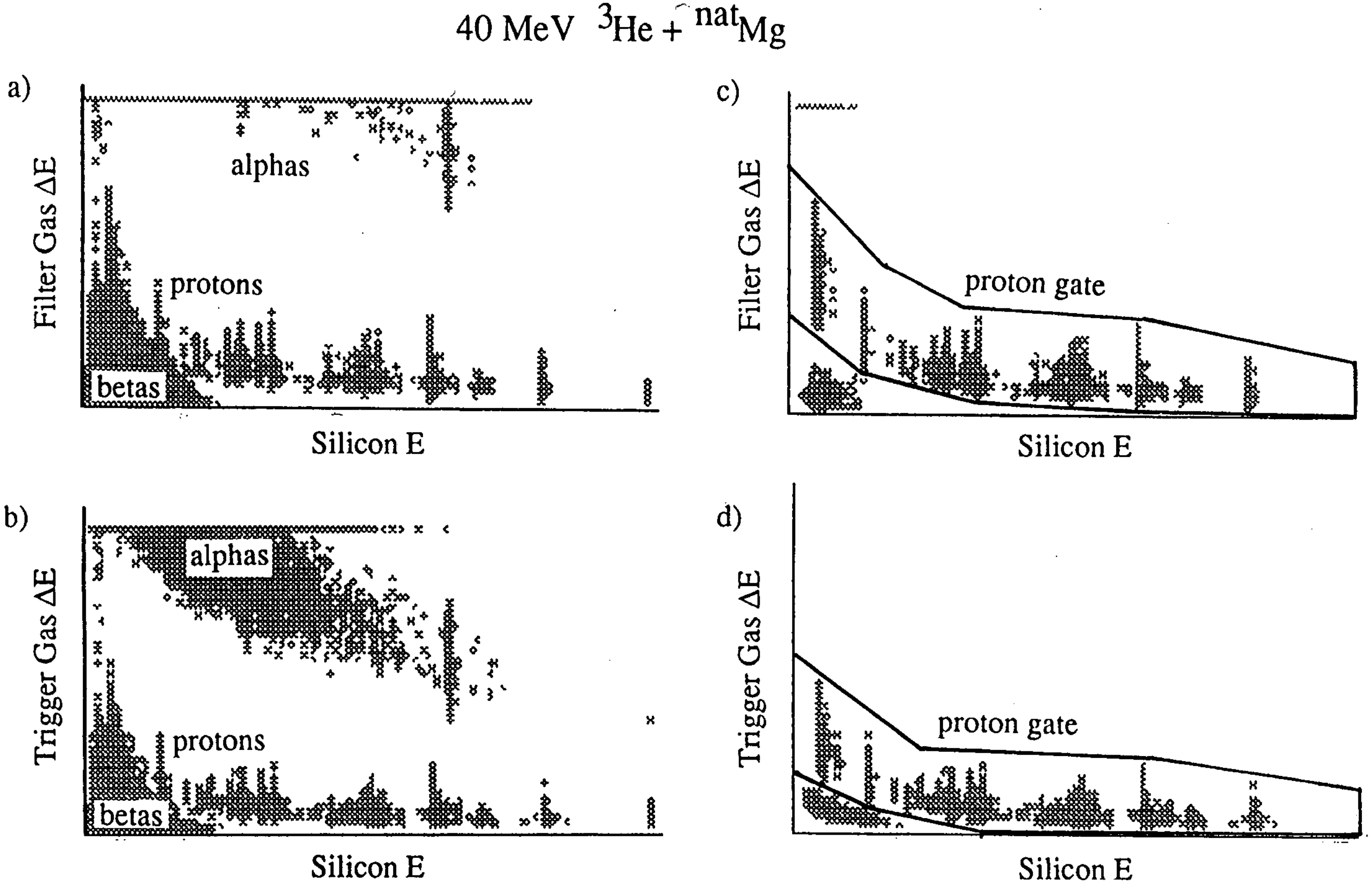
40 MeV ^{3}He + ^{nat}Mg
a)
Filter Gas ΔE
alphas
protons
betas
Silicon E
b)
Trigger Gas ΔE
alphas
protons
betas
Silicon E
c)
Filter Gas ΔE
proton gate
Silicon E
d)
Trigger Gas ΔE
proton gate
Silicon E

Figure III-8.

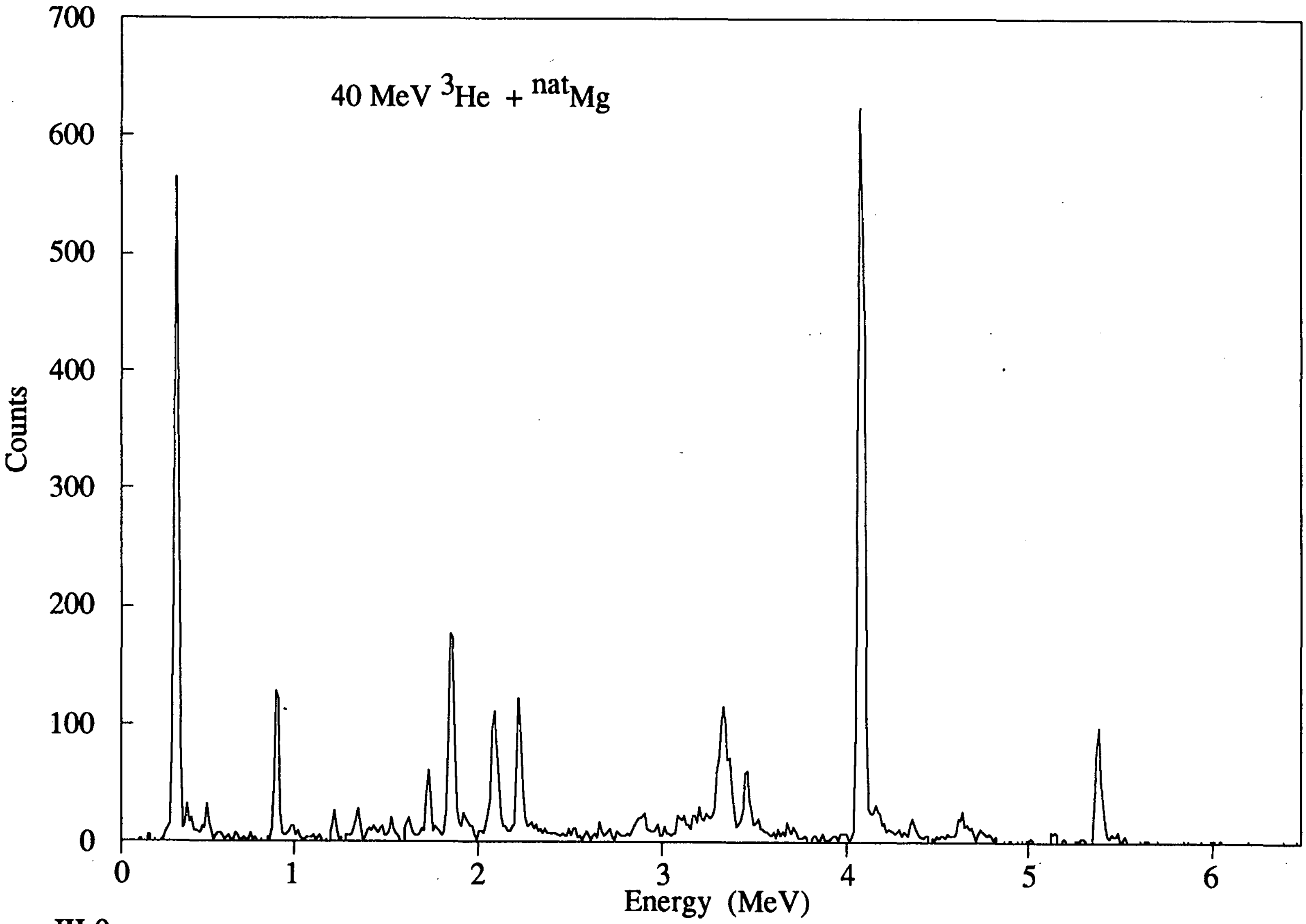
40 MeV 3He + natMg
Counts
0
100
200
300
400
500
600
700
Energy (MeV)
0
1
2
3
4
5
6

Figure III-9.

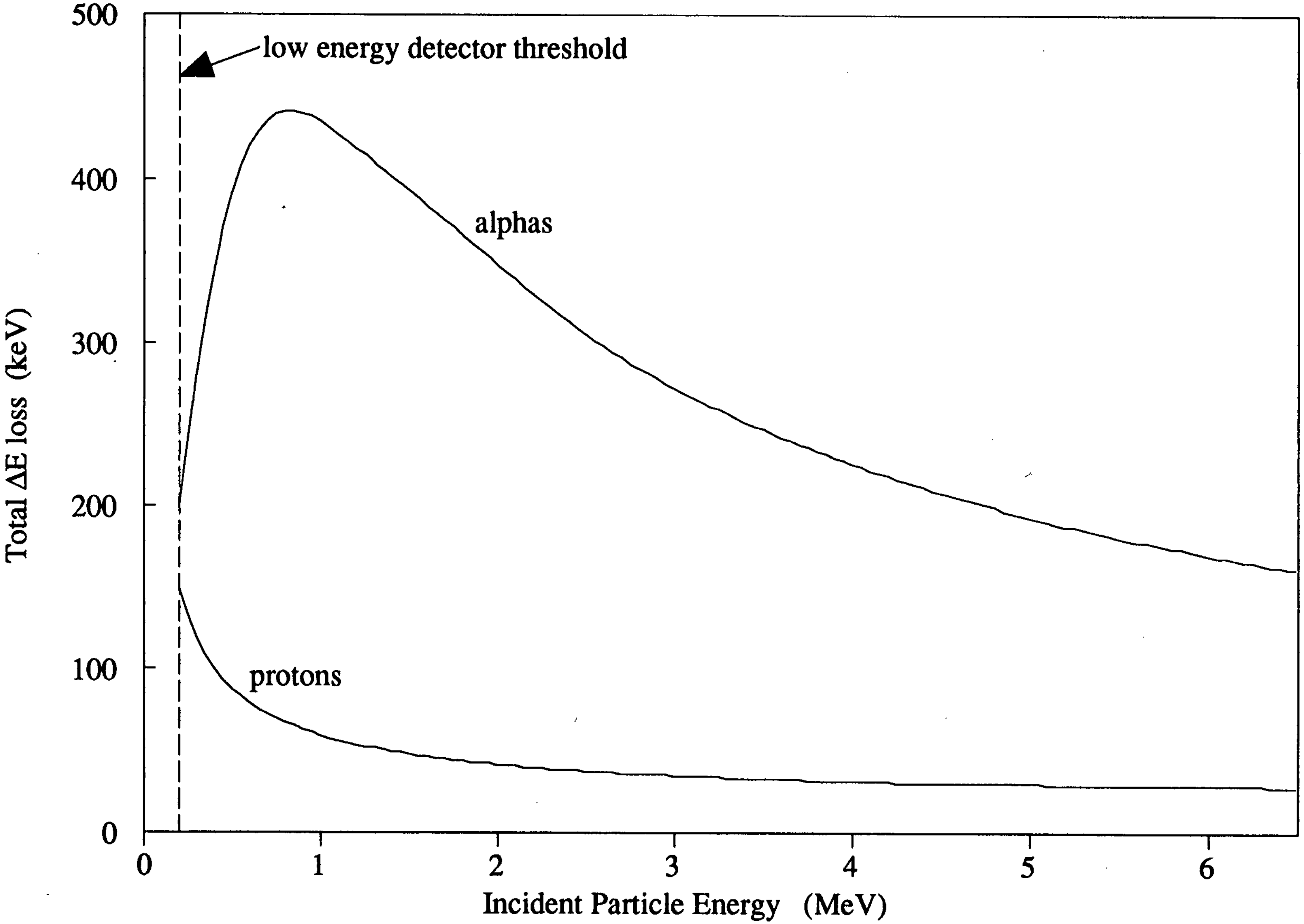

Figure III-10.

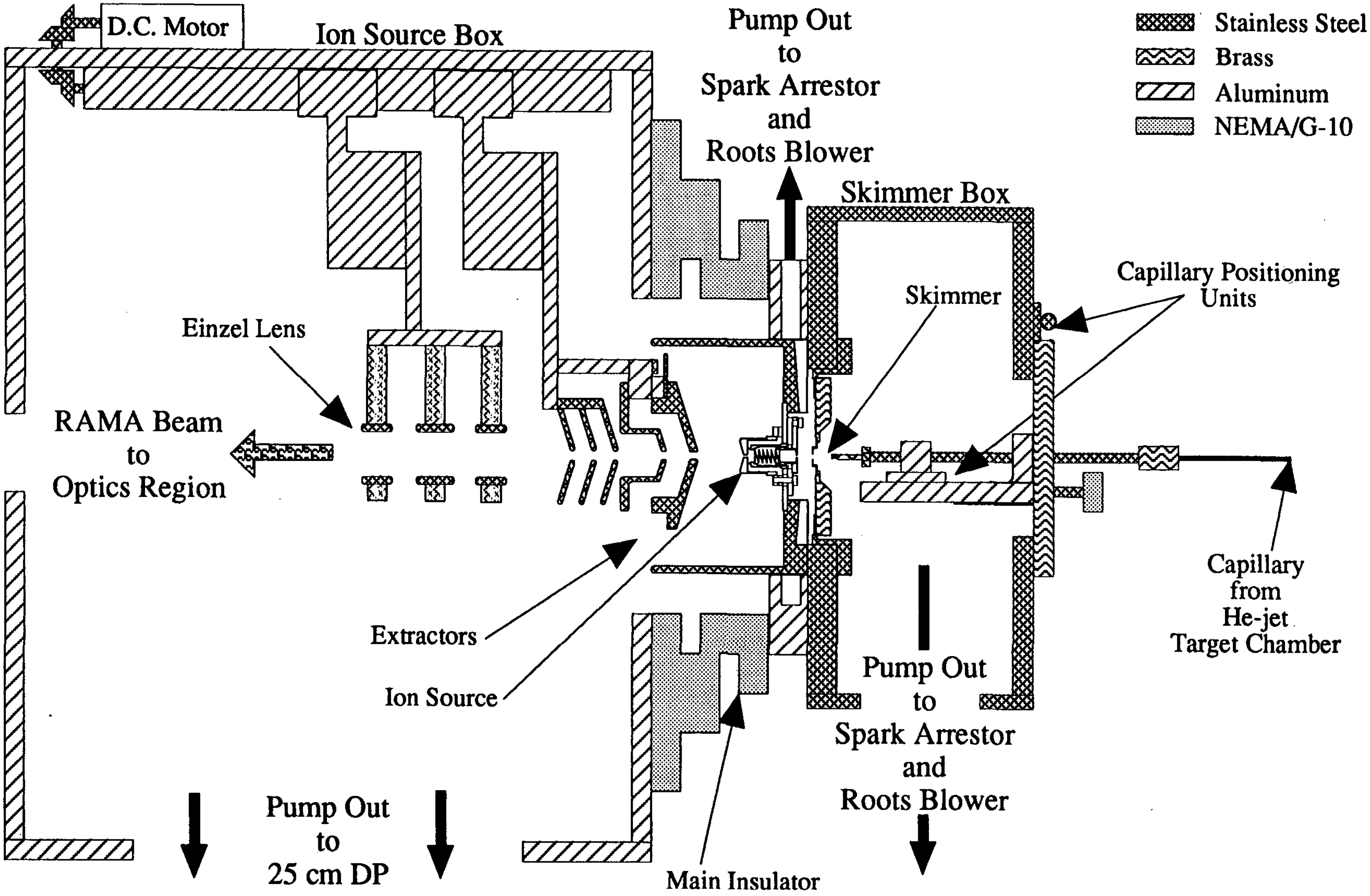

Figure III-11.

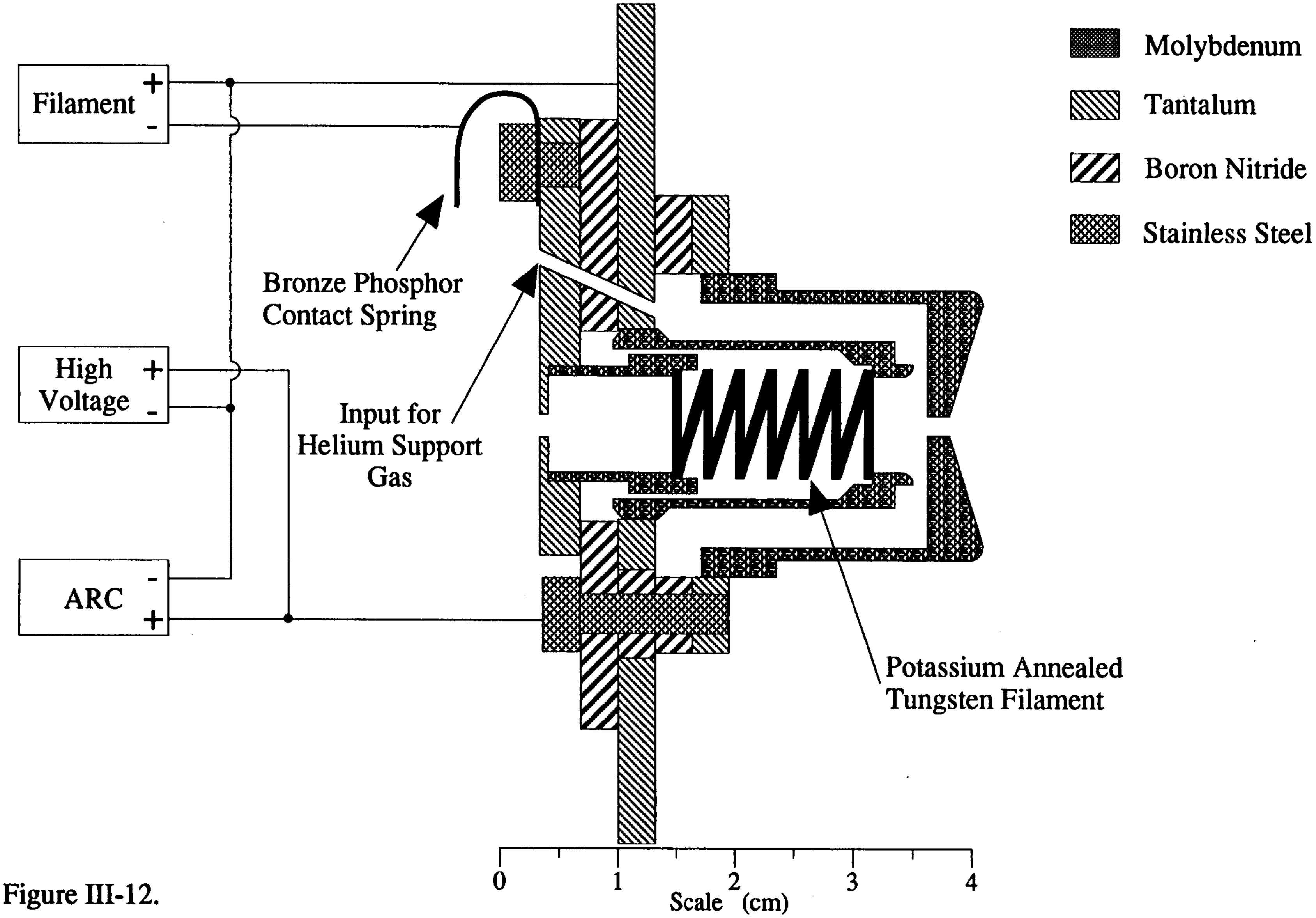

Figure III-12.

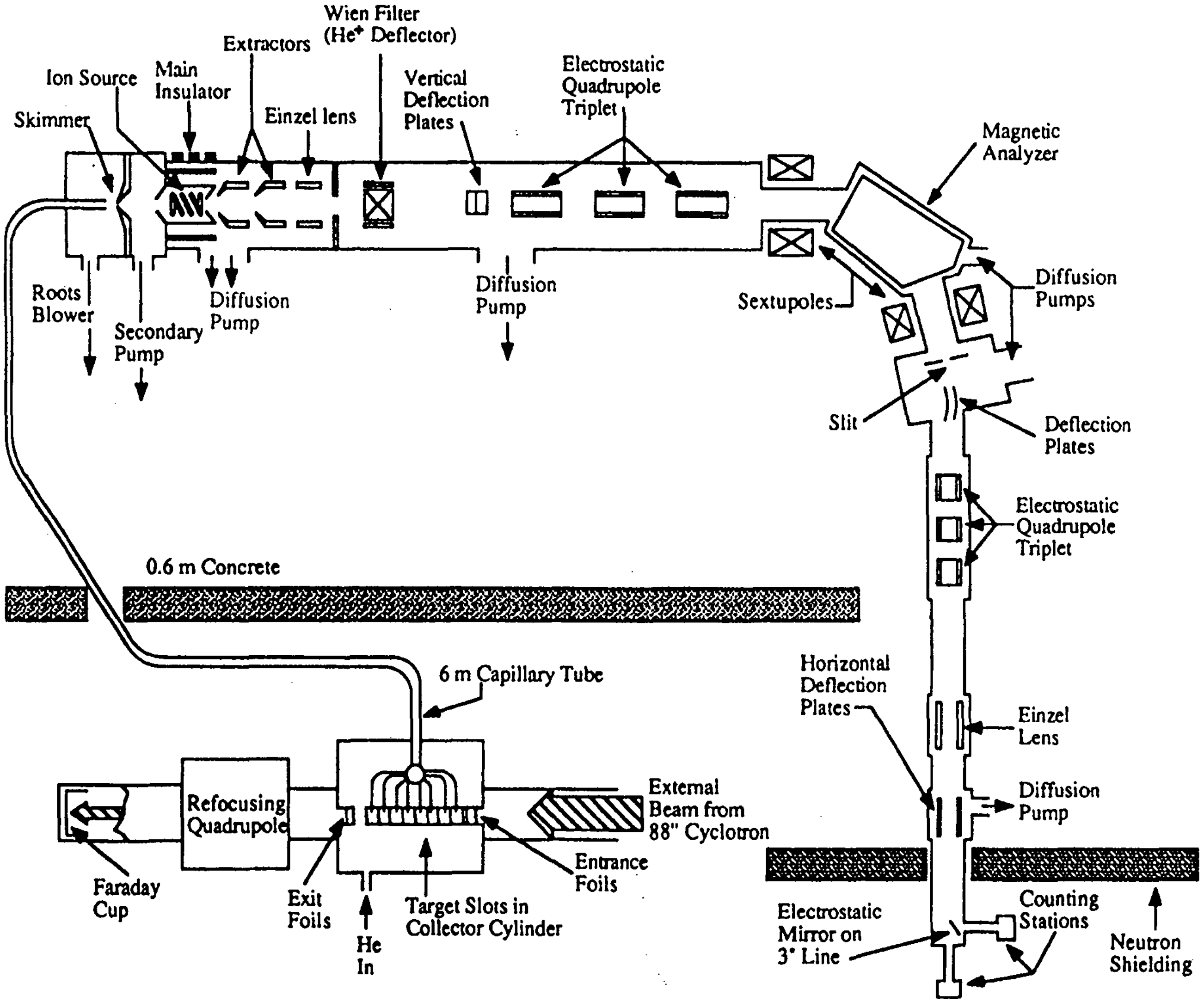

Figure III-13.

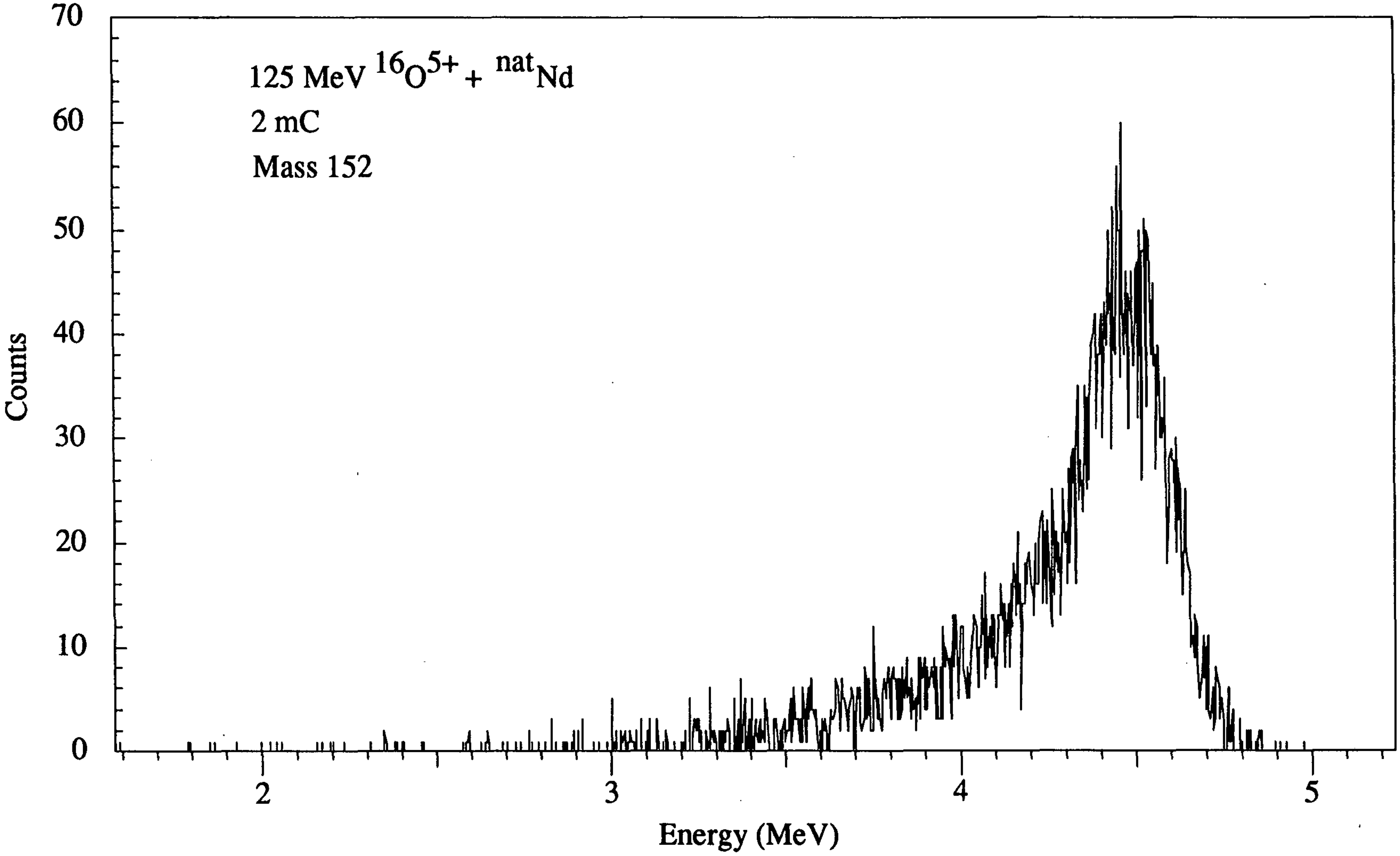

Figure III-14.

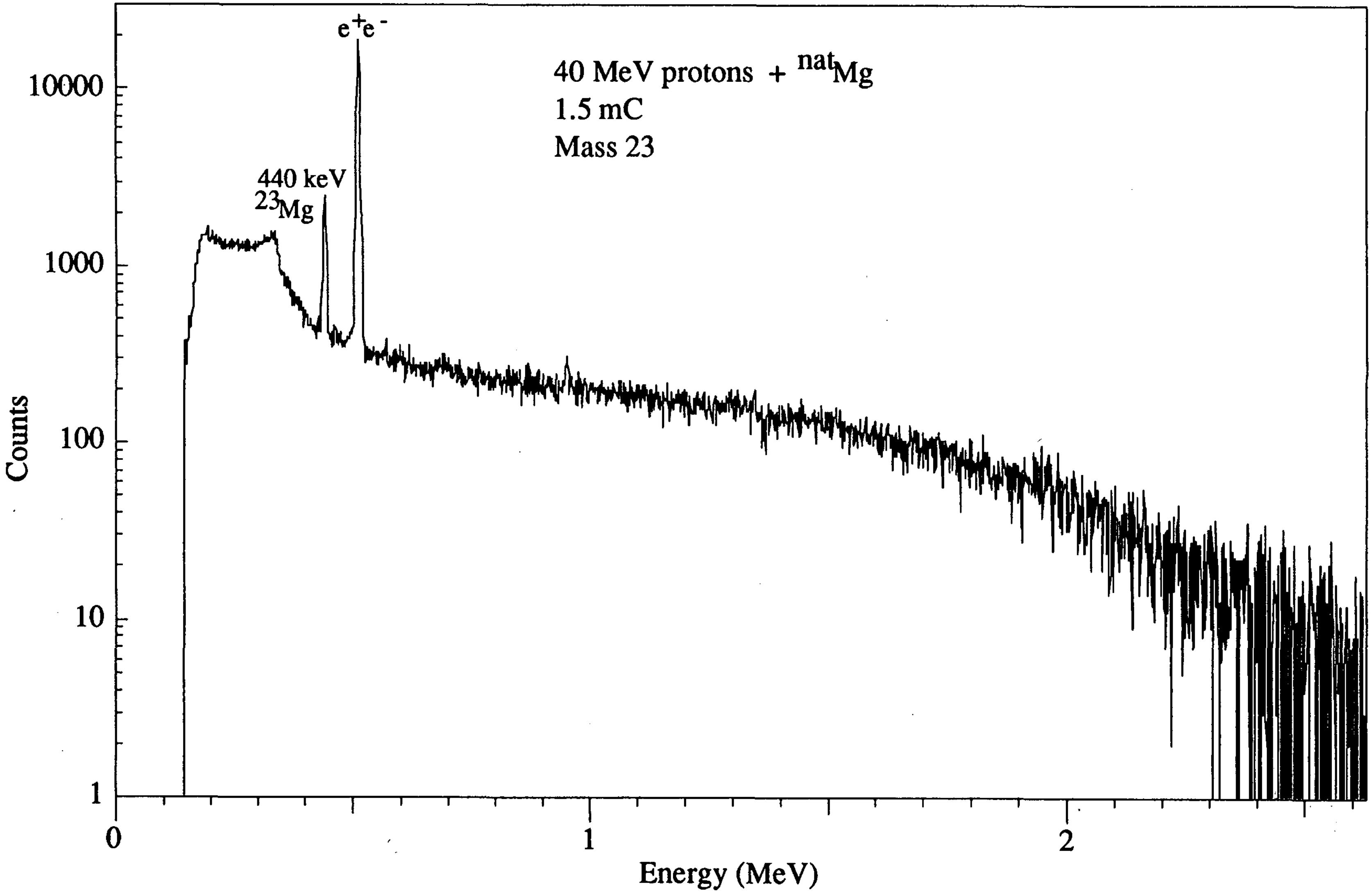

Figure III-15.

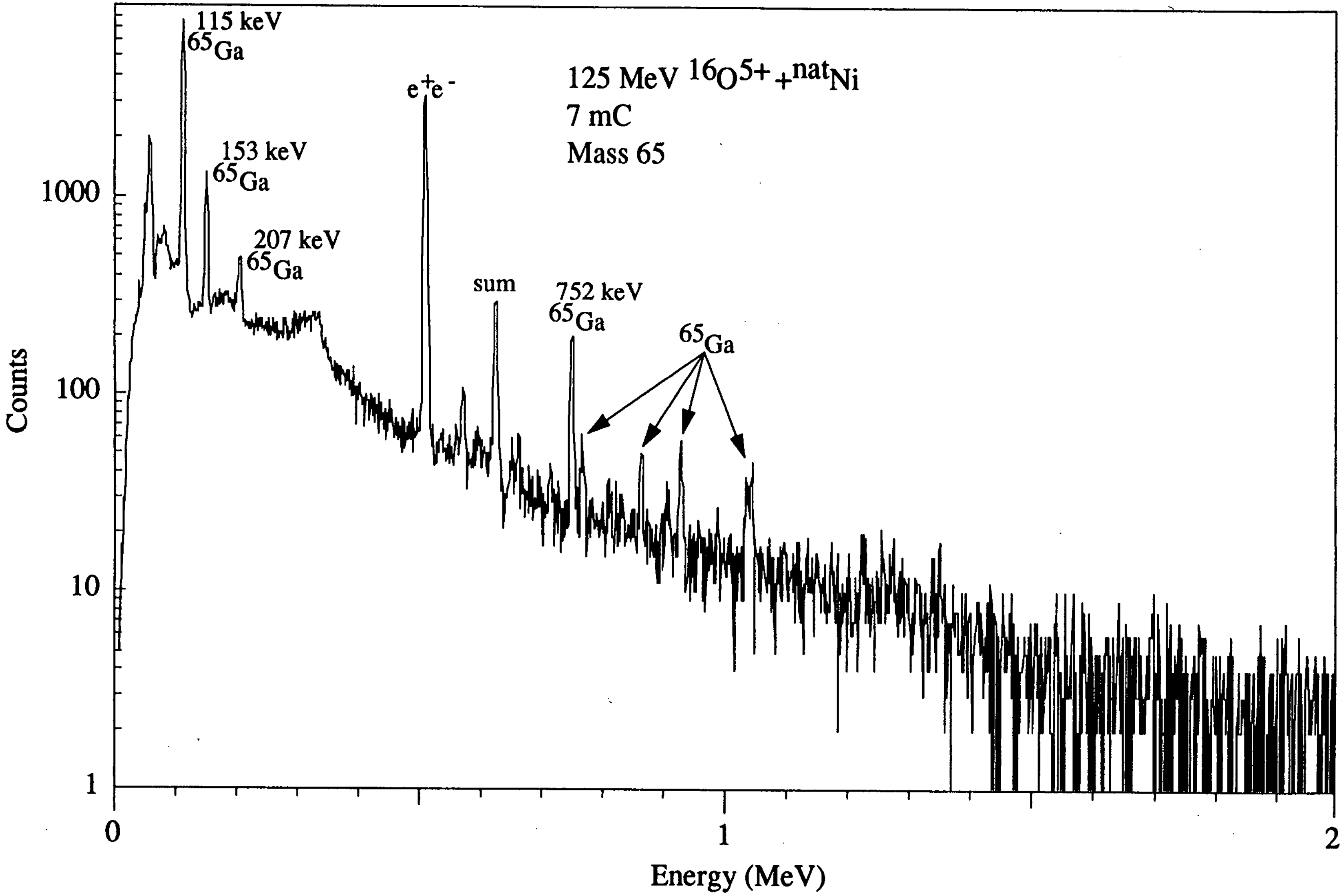

Figure III-16.

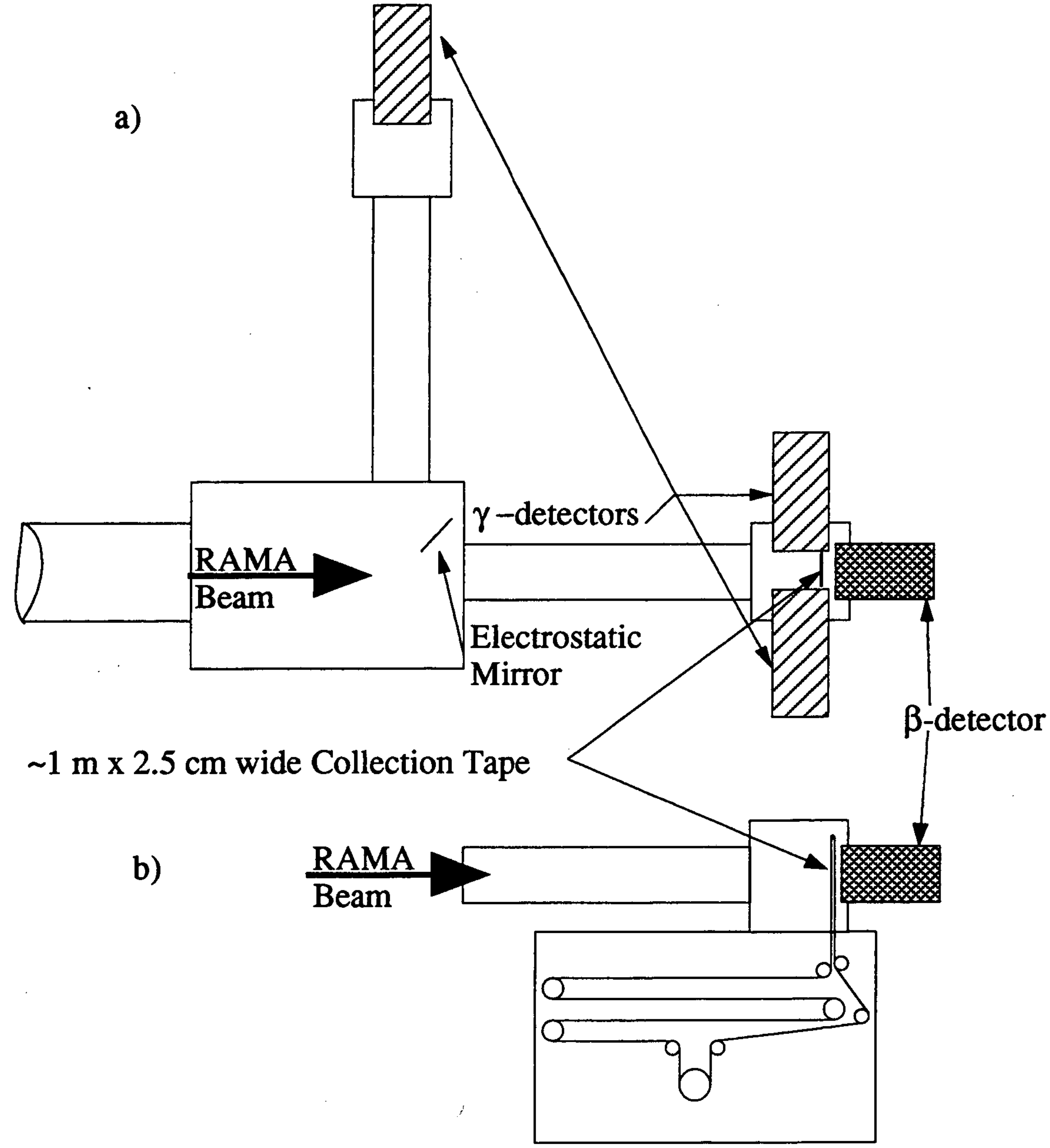

Figure III-17.

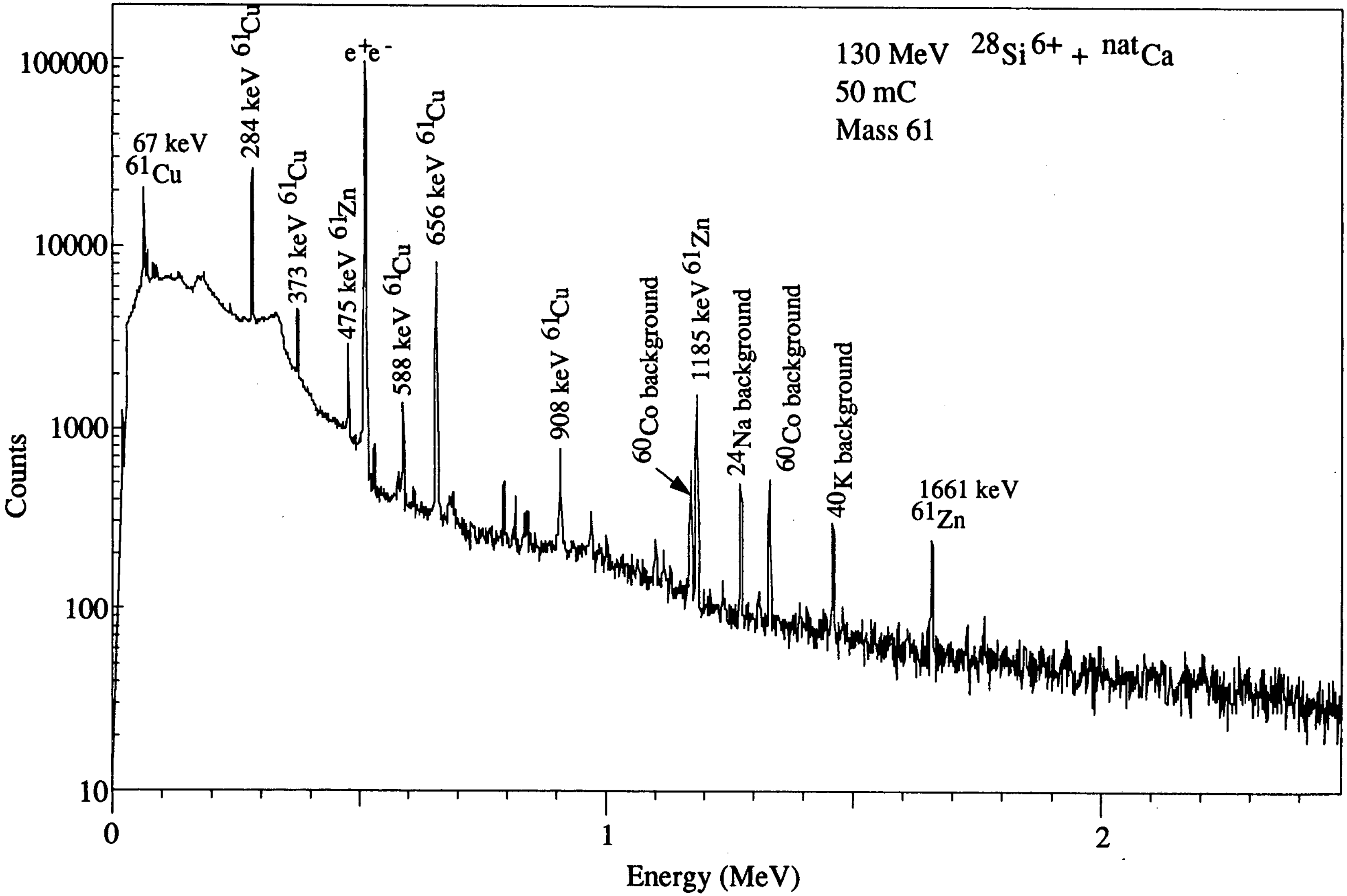

Figure III-18.

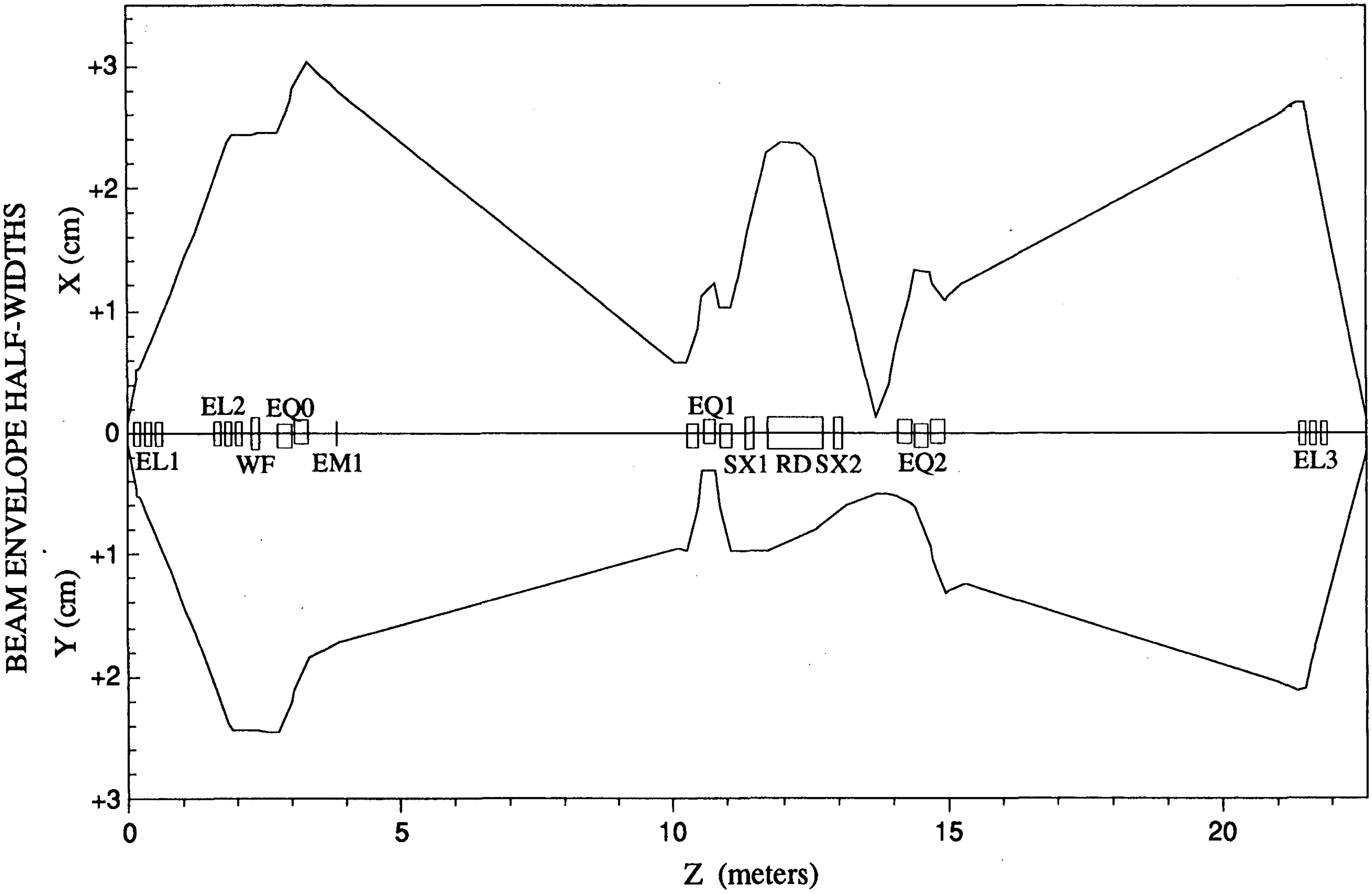

Figure III-19.

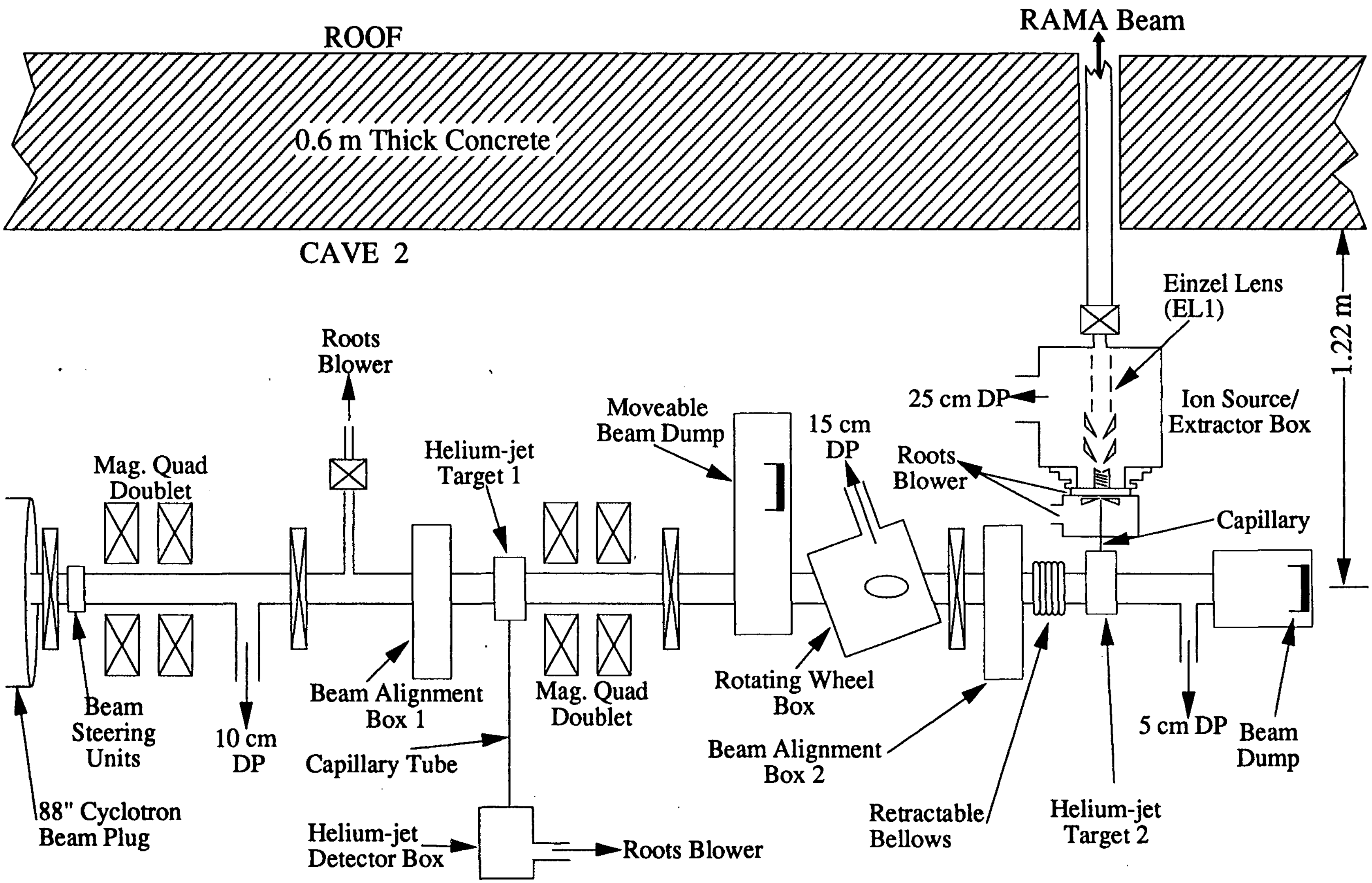

Figure III-20a.

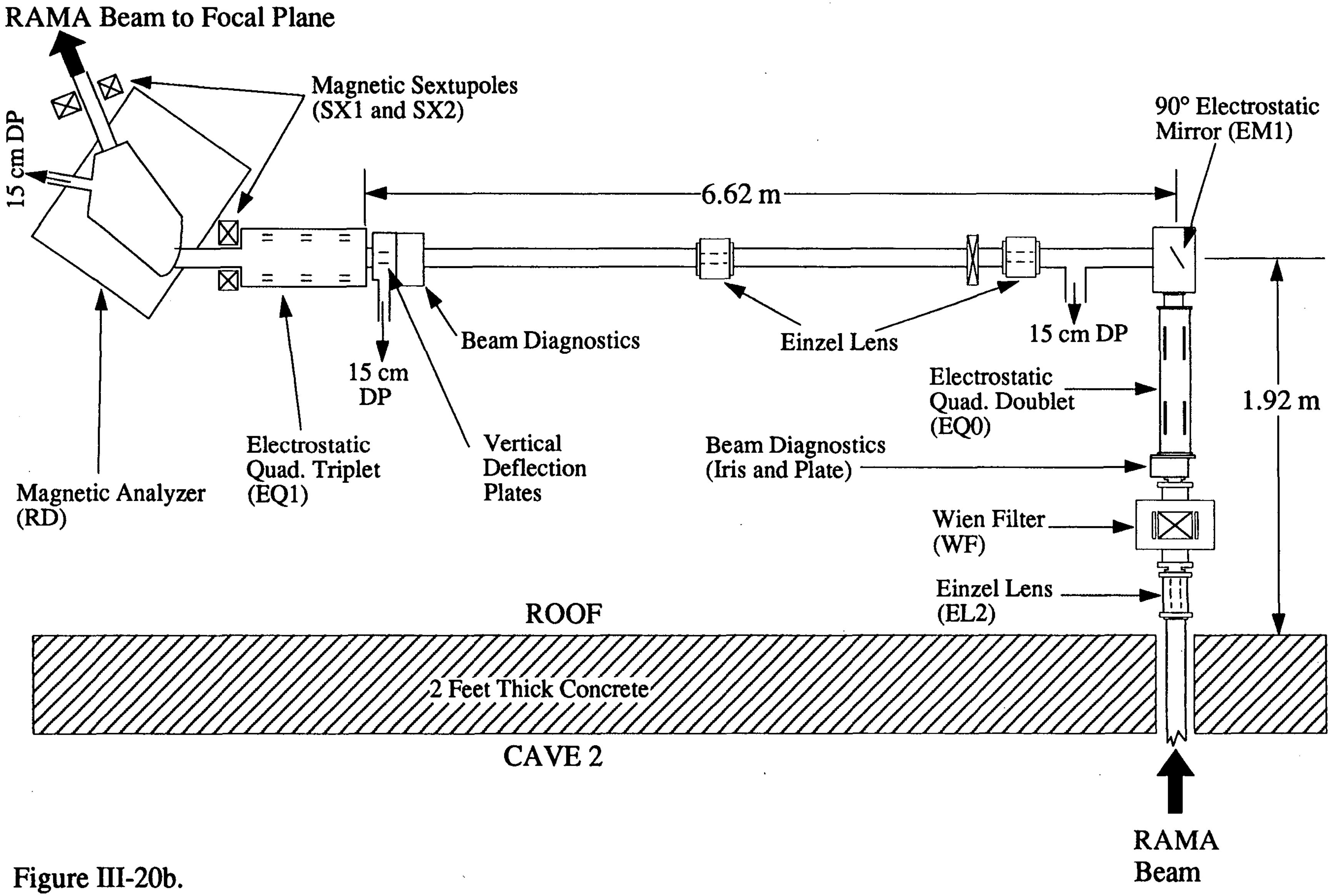

Figure III-20b.

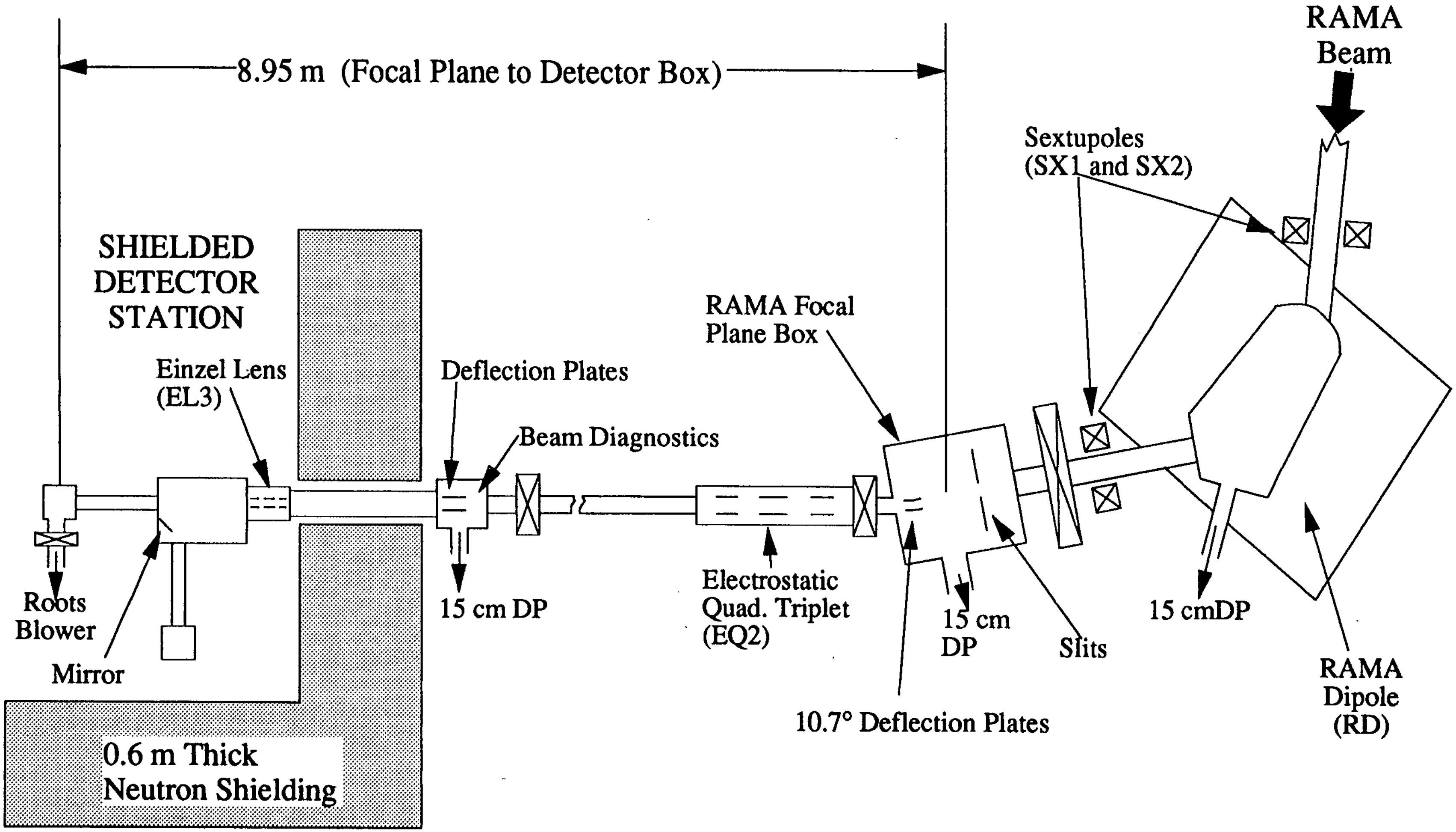

Figure III-20c.

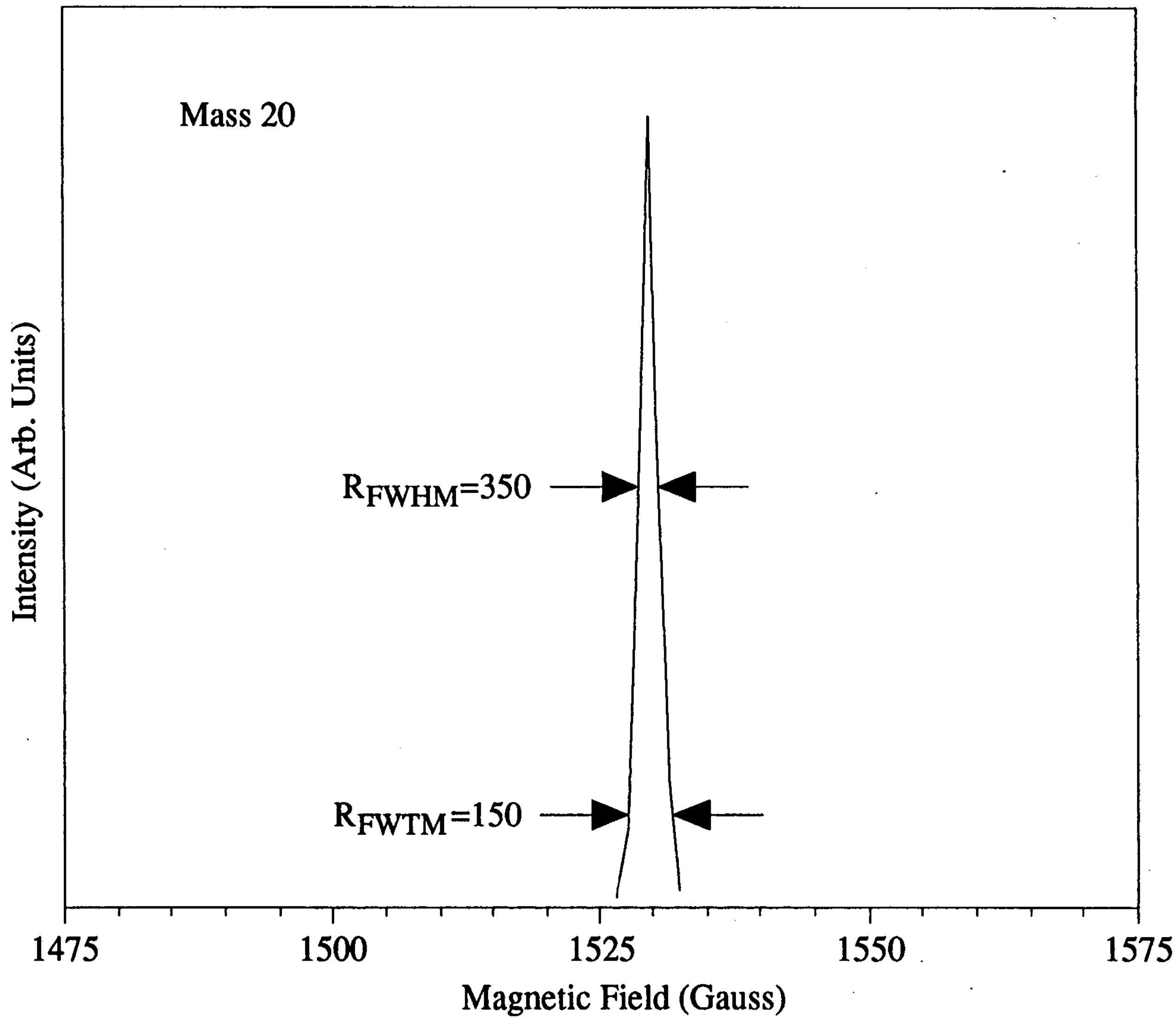

Figure III-21.

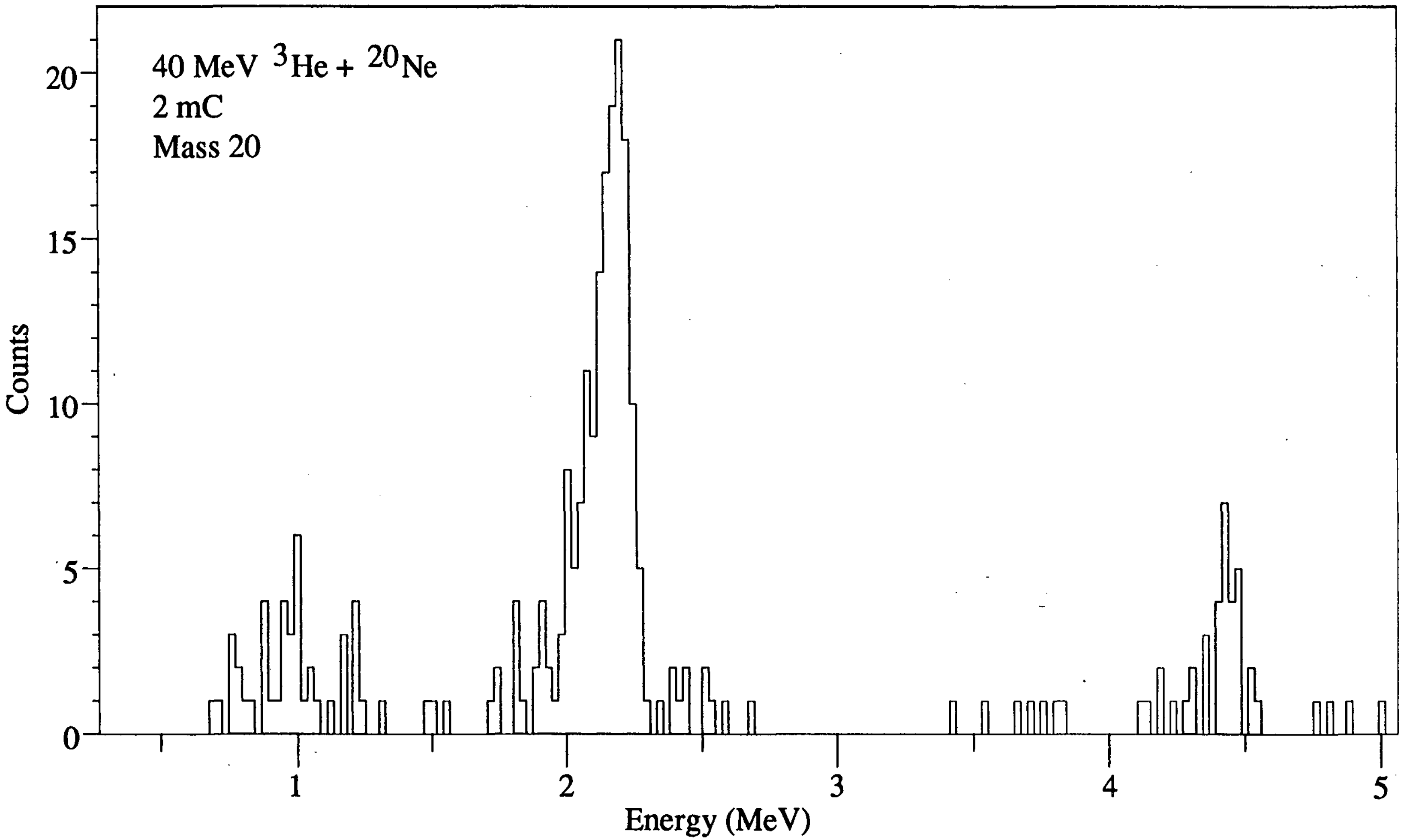

Figure III-22.

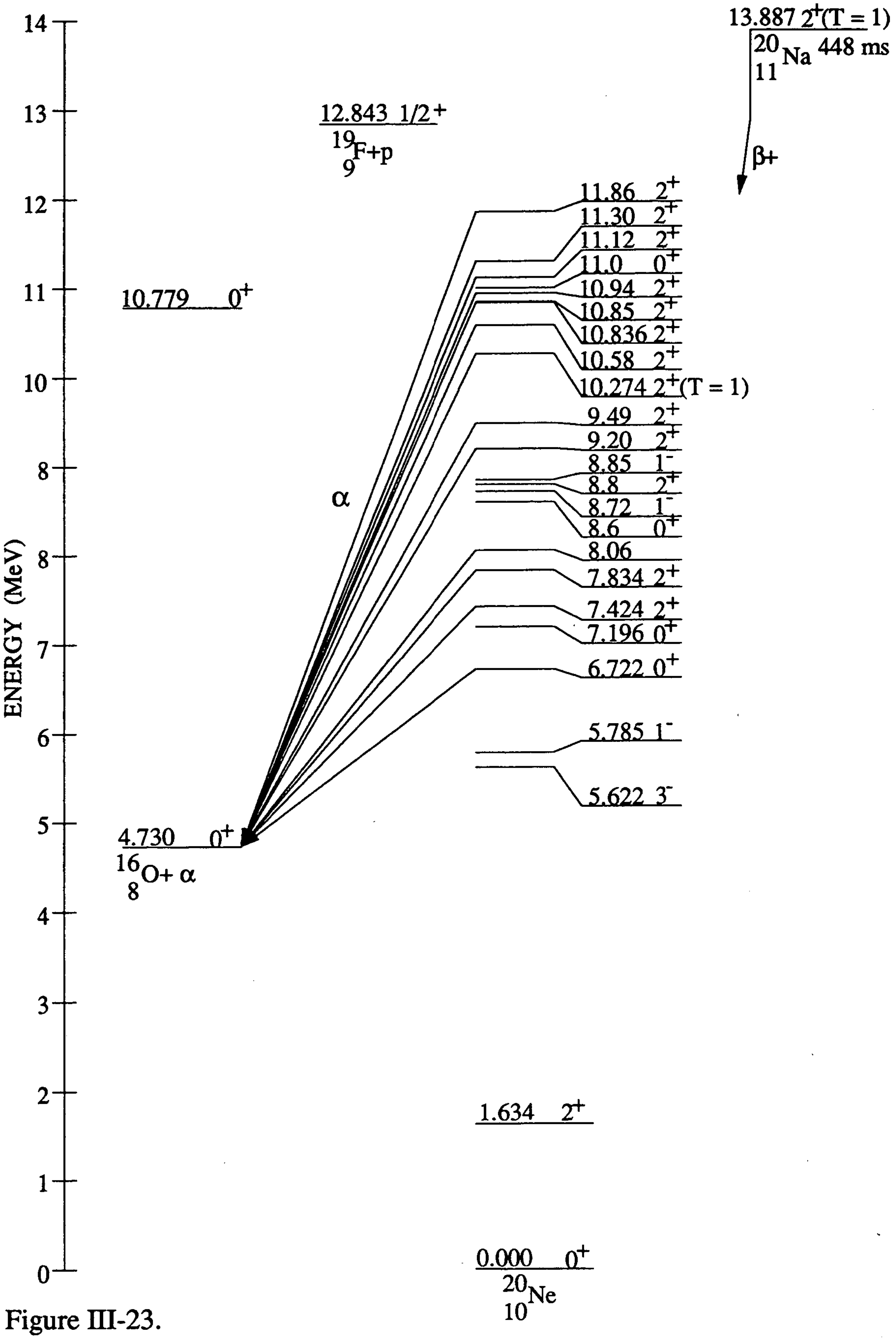

Figure III-23.

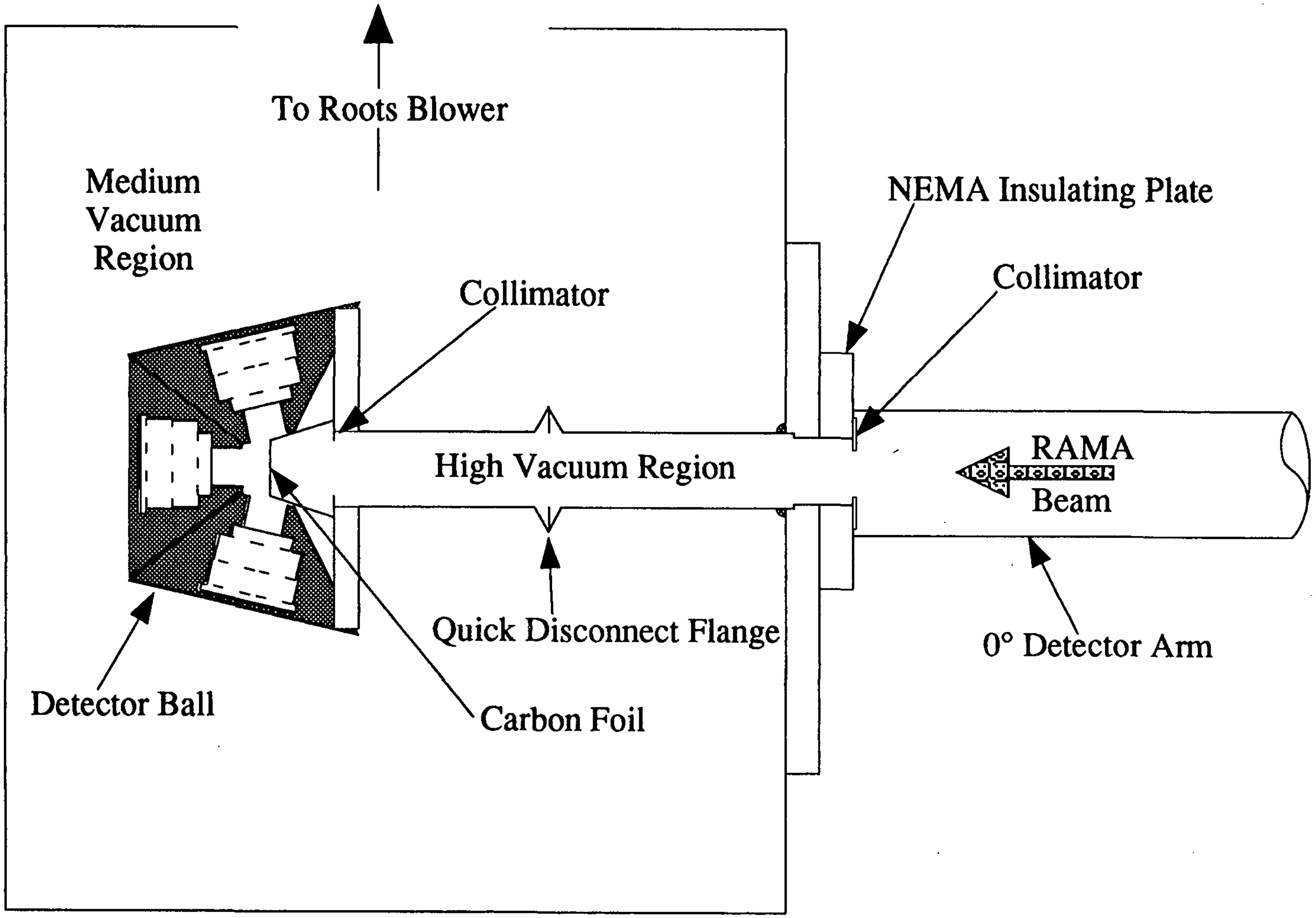

Figure III-24.

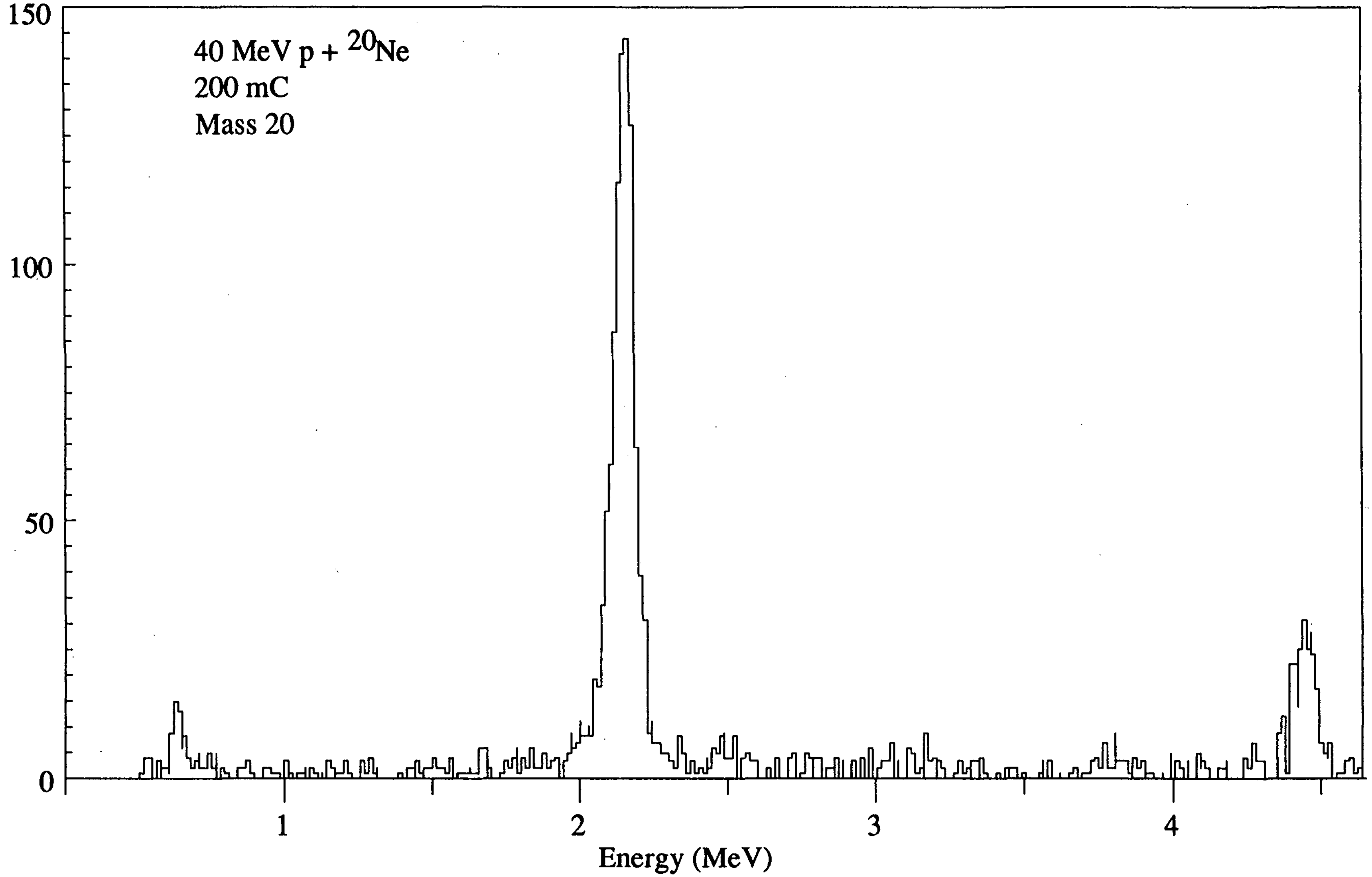

Figure III-25.

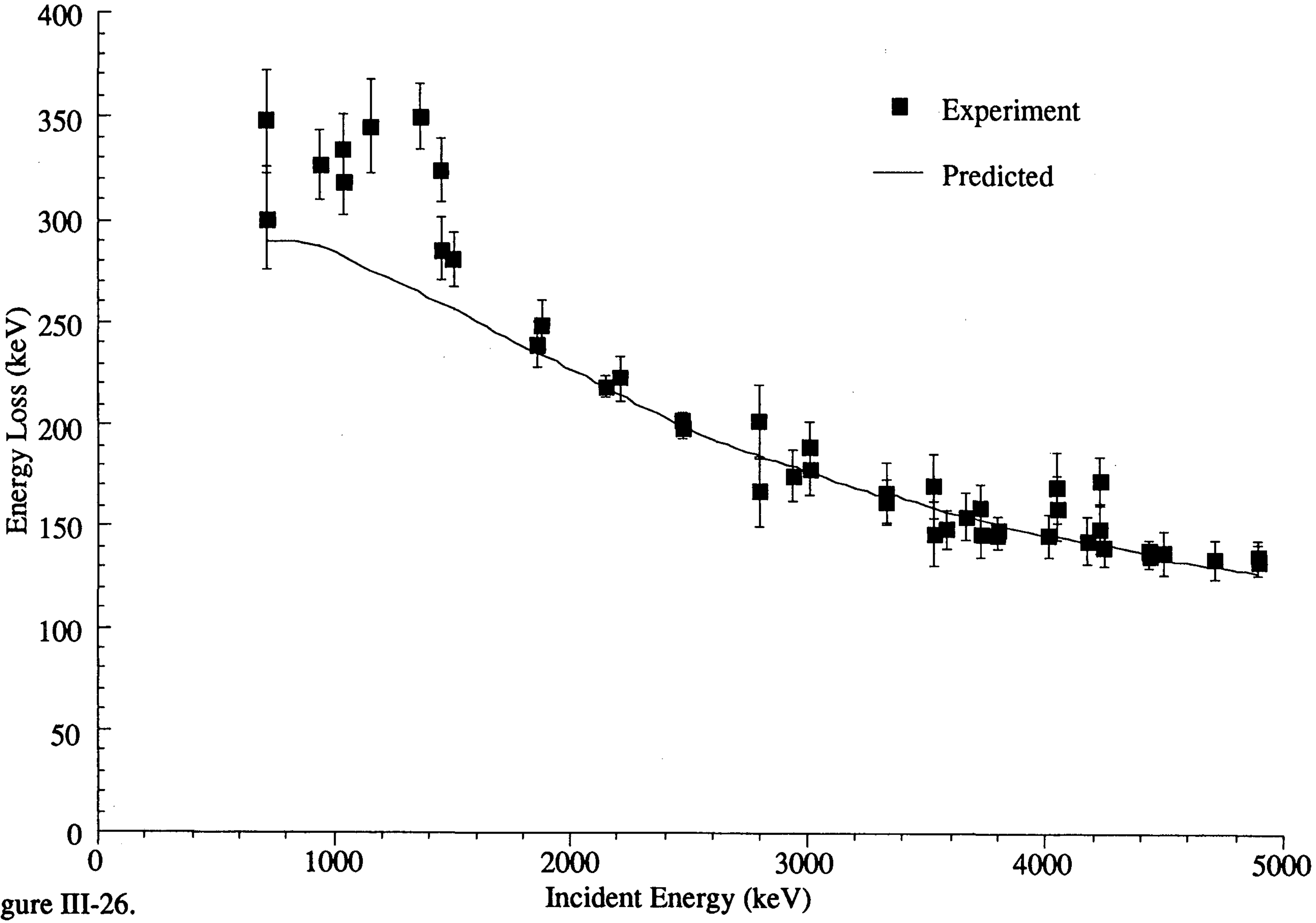

Figure III-26.

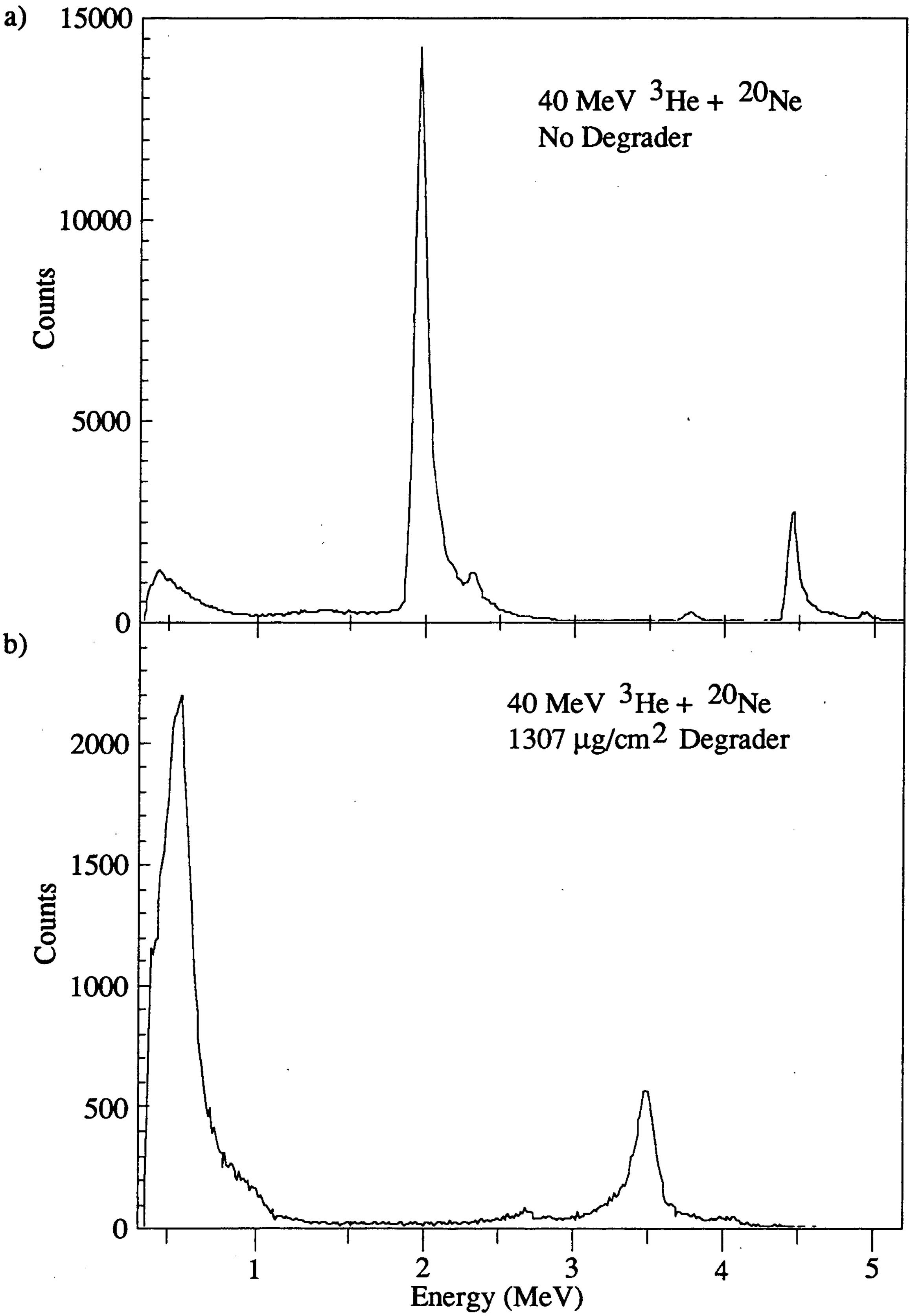

Figure III-27.

40 MeV $^{3}He + {}^{nat}Ne$

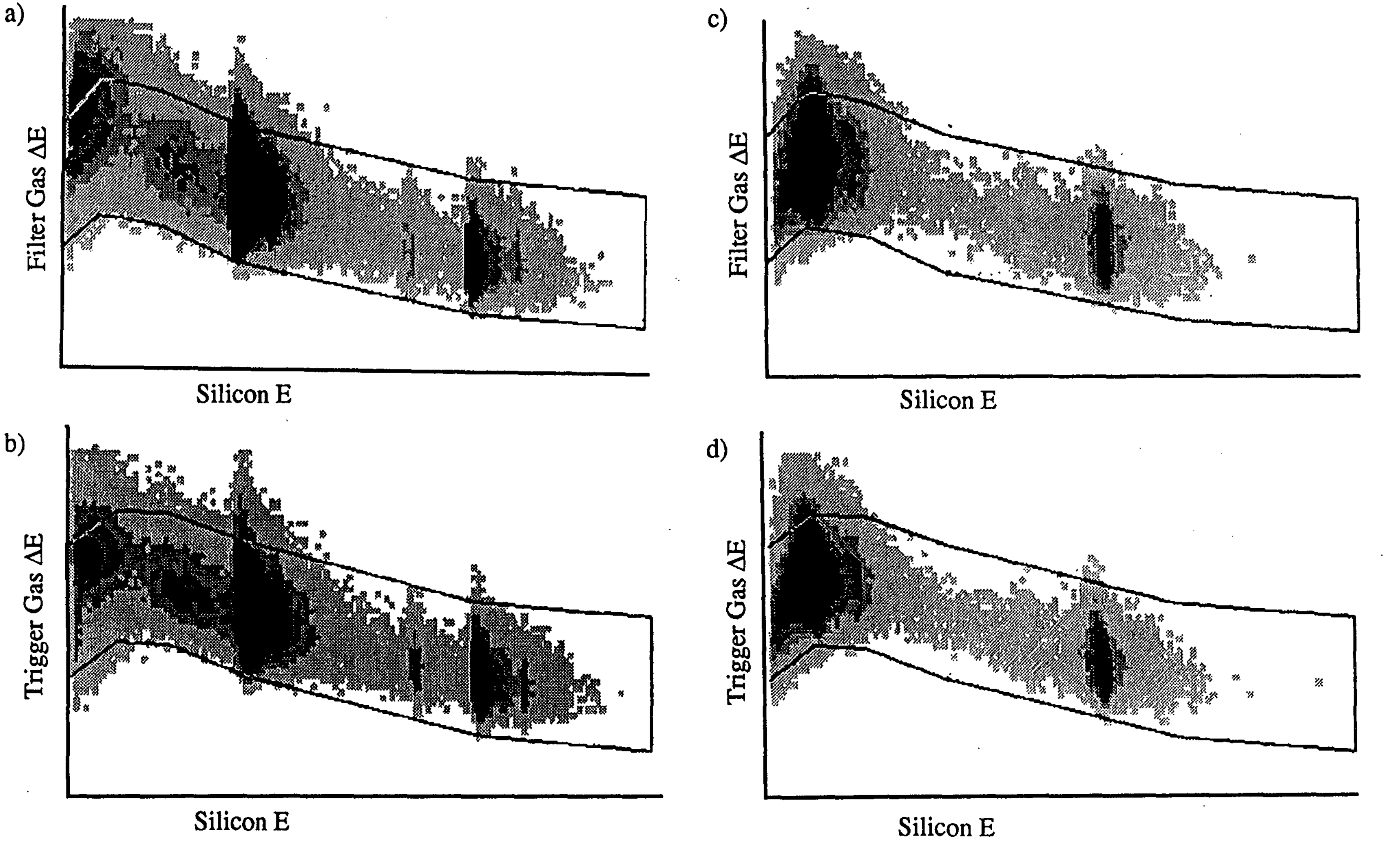

Figure III-28.

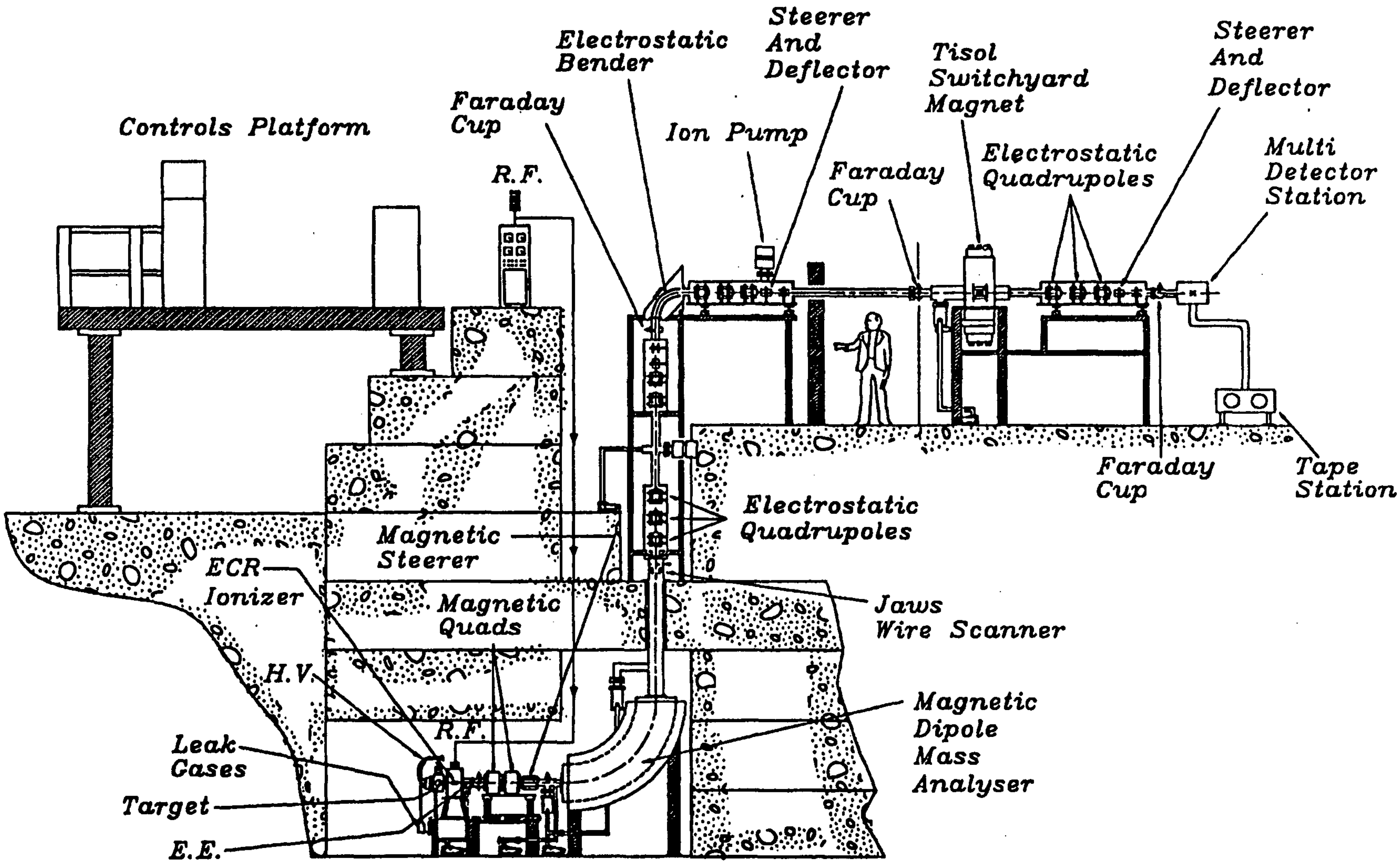

Figure III-29.

IV. Experimental Results and Discussion

IV.A. The Beta-Delayed Proton Decays of ^{31}Cl and ^{27}P

IV.A.1. Introduction

The decays of the A = 4n+3, $T_z = -3/2$ series nuclei, ^{31}Cl and ^{27}P, offer an opportunity to study beta transition strengths up to high excitation energy in their beta daughters. This series of nuclei, in which the decays of four members have been investigated (^{23}Al [Ti 95 and Go 72], ^{27}P [Äy 85], ^{31}Cl [Äy 85, Äy 83 and Äy 82] and ^{35}K[Ew 80]) are all characterized by high Q_{EC} values and exhibit beta-delayed proton branches. These nuclei are made in relatively high yields by (p,2n) reactions; however, as is often the case with proton drip-line nuclei, their experimental investigation is hampered by their short half-lives and by the decays of the simultaneously and copiously produced nuclei closer to stability. As demonstrated in the previous chapter, our group has developed fast detection techniques that exploit the beta-delayed charged-particle decay features of proton drip line nuclei.

The beta decays of light proton-rich nuclei are characterized by two general features. The first is a superallowed Fermi transition to the isobaric analog state in the beta daughter. However, of the experimentally investigated members of the A = 4n+3 series, only ^{23}Al and ^{31}Cl have isobaric analog states in their beta daughters that are predicted to be unbound to proton emission. While proton emission from the IAS in ^{23}Mg following the beta decay of ^{23}Al was recently observed [Ti 95], the decay of the IAS in the beta daughter of ^{31}Cl remains unobserved, primarily due to the fact that it is unbound by only 150 keV. Barrier penetration calculations reveal that, for the ^{31}Cl case, gamma-ray emission is favored over proton emission by over five orders of magnitude for the de-excitation of the IAS. In this case, beta-feeding to the IAS would best be investigated through delayed gamma emission. However, such an endeavor would require mass separation and techniques for effectively ionizing chlorine atoms have not yet been developed by our research group.

The other feature consists of Gamow-Teller transitions to states both below and above the IAS. The low-lying states are often bound to proton emission and hence inaccessible to study without some means of mass separation. However, the states above the IAS are, in general, open to proton emission. This cluster of states represents the tail of the Gamow-Teller giant resonance observed in (p,n) reactions [Be 81 and Go 81].

A full space $d_{5/2}$-$s_{1/2}$-$d_{3/2}$ shell model was used to generate wavefunctions [Wi 84] for the T = 3/2 ground states of the A = 31 and A = 27 parents and all possible daughter states within the beta decay energy window. From these wavefunctions, values of the Gamow-Teller matrix elements for each beta decay transition were determined. Gamow-Teller strength B(GT) is related to ft values through the following relation

$$\mathrm{ft} = \frac{6147\ \mathrm{sec}}{\mathrm{B(F)} + \mathrm{B(GT)}}, \qquad (4\text{-}1)$$

as described in Section II.A.3. These shell model calculations [Wi 83, Br 83 and Br 85] predict that a significant fraction of beta decay transitions should populate the states that make up the tail of the GT giant resonance; the study of ^{31}Cl and ^{27}P with their large beta decay energies ($Q_{EC}(^{31}\mathrm{Cl}) = 11.98$ MeV and $Q_{EC}(^{27}\mathrm{P}) = 11.63$ MeV) are suitable nuclei in which to sample deeper into the GT resonance.

The previous most extensive experimental investigation on the decays of ^{31}Cl and ^{27}P was performed by our research group in 1985 [Äy 85]. In that study, only protons between 700 keV and 2700 keV could be observed with a detector resolution of 75 keV for protons. Additionally, delayed proton emission from the simultaneously produced $T_z = -1$ isotopes ^{32}Cl and ^{28}P were present in the proton spectra of ^{31}Cl and ^{27}P, respectively. With our low energy proton gas ΔE-gas ΔE-silicon E detector telescopes, which can detect and identify protons down to ~200 keV with ~40 keV resolution, we undertook a study to improve upon our earlier results.

IV.A.2. ^{31}Cl Experimental

^{31}Cl was produced through the ^{32}S(p,2n)^{31}Cl reaction by bombarding five 2 mg/cm^2 thick ZnS targets, each mounted on a 1.7 mg/cm^2 thick aluminum disk, with a beam of 45 MeV protons. The beam intensity throughout the bombardment was typically 3 μA. The multiple target/multiple capillary He-jet setup (see Figure III-2a) was employed for this experiment. Radioactive recoils, upon clearing the target, were thermalized and attached to KCl aerosols in a He-jet and transported along short 1 mm i.d. capillaries to a main header. They were then subsequently transported along a 1.8 m long x 1.4 mm i.d. capillary to the counting station. The total delay time of the system was estimated to be 200 ms. The detector setup, as depicted schematically in Figure III-4, consisted of two gas ΔE-gas ΔE-silicon E detector telescopes arranged to view the He-jet deposition spot on the edge of a slowly rotating wheel. The proton detector calibration was performed by using delayed protons from ^{25}Si [Ro 93], produced during a 40 MeV ^{3}He bombardment on ^{nat}Mg via the ^{24}Mg(^{3}He,2n)^{25}Si reaction. This calibration was conducted immediately before the main production run.

To avoid the detection of knockout proton events caused by prompt neutrons impinging on hydrogen-containing materials in or near the detector, the beam and counting electronics were pulsed. The effect of beam pulsing on counting statistics was described in Section III.B.2. Based on the known ^{31}Cl half-life of 150 ± 25 ms [Äy 82], a total cycle that consisted of a 330 ms beam on, electronics off phase and a 410 ms beam off, electronics on phase was selected to maximize the yield of ^{31}Cl.

IV.A.3. ^{31}Cl Results and Discussion

Figure IV-1 shows a gated proton spectrum resulting from a 220 mC bombardment of 45 MeV protons on ZnS. The main ^{31}Cl and ^{32}Cl proton groups have been labeled. The proton assignments for ^{32}Cl were made based on the previous work of Honkanen et al., [Ho 79a], while the ^{31}Cl proton assignments were made based on the works of Äystö et al., [Äy 82] and [Äy 85]. In addition to protons from ^{31}Cl and ^{32}Cl, there is a significant amount of delayed protons from ^{25}Si, produced from the aluminum backing disks through the ^{27}Al(p,3n)^{25}Si reaction with a Q_{value} of -37.9 MeV. Nuclei made from the Al can escape the target and enter the He-jet through holes and tears in the ZnS layer. ^{25}Si is a well known beta-delayed proton emitter [Ro 93] and Figure IV-2 shows a delayed proton spectrum resulting from a 40 MeV ^{3}He beam bombardment on five 2 mg/cm^{2} ^{nat}Mg targets recorded during the detector calibration phase of this experiment. Another known beta-delayed proton emitter is ^{24}Al, which could be made from the aluminum backing disks through the ^{27}Al(p,p3n)^{24}Al reaction. However, the Q_{value} of this reaction is -41.4 MeV, which is very near the 45 MeV proton bombarding energy. While ^{24}Al could be made, the production cross section would be expected to be very small and with a 1.2 x 10^{-5} βp branching ratio [Ba 94], any possible contribution from ^{24}Al to the proton spectrum of Figure IV-1 can be ignored.

Because of the significant ^{25}Si contribution, only the 762 keV proton peak from ^{32}Cl could be cleanly observed. An estimate of the ^{32}Cl contribution to the 986/991 keV proton peak was made by consideration of the number of events in the 762 keV proton peak and the fact that this group is 46±10% of the main 100% proton group at 991 keV [Ho 79a]. Based on the observed events above the proton background at 762 keV, 60% of the observed events at 991/986 keV are delayed protons from the decay of ^{31}Cl.

Using the known intensities for ^{25}Si beta-delayed proton groups [Ro 93], and the observed intensity of the 905 keV proton group as a reference point, the amount of ^{25}Si contributing to each peak seen in Figure IV-1 was determined. It was found that other than those from ^{25}Si, there were no other significant proton groups ($I_p \geq 1\%$) above the 1524 keV proton group. Additionally, there were no indications of the 1173 keV and 845 keV proton group at the most probable level reported by [Äy 85]. However, the reported intensities of these two groups was 3±2% each and the present results put the maximum intensity at 1%. The current results, as well as the results of [Äy 85] are presented in Table IV-1.

The discrepancies between our current and the previous work can be attributed to the presence of ^{25}Si in both data sets. Both experiments utilized the same ZnS targets, however, in their case, with the targets being newer, there were probably less noticeable cracks and holes in the ZnS. Consequently the level of ^{25}Si contamination was much less in the previous experiment. That experiment employed an 8.3 μm silicon ΔE, a 68 μm silicon E detector telescope, followed by a 200 μm E_{reject} detector. The reject counter served to eliminate protons above 2.7 MeV, as well as to eliminate positron associated events. The low-proton energy cutoff was slightly below 700 keV. The overall detector resolution for protons was 75 keV. Hence, they were unable to observe the full ^{25}Si beta-delayed proton spectrum.

Thus, the proton groups in Table IV-1 in which the relative intensities are listed at ≤1% are, in order of increasing energy, most likely the 905 keV, 1215 keV, 1727 keV, 1848 keV, 2082 keV and 2219 keV beta-delayed proton groups in ^{25}Si, with the possibility that they result from the decay of ^{31}Cl excluded at the 99% confidence level.

An estimate of the βp branching ratio can be made by comparing the yields of ^{31}Cl protons to ^{32}Cl protons and by using the predicted ALICE code [Bl 82] cross section for ^{31}Cl with the ^{32}Cl production cross section inferred from the data of [Äy 85]. This leads to a total 3×10^{-3} branching ratio to proton emitting states in ^{31}S and a log ft value of 4.7 for the 7138 keV excited state. These results are obviously different than the results of [Äy 85] which is to be expected owing to their overestimation of the βp branching ratio due to their (unknowing) ^{25}Si contamination. A partial decay scheme of ^{31}Cl is presented in Figure IV-3. The solid lines indicate those transitions observed in the current experiment. The spin and parity of ^{31}Cl is taken from its mirror ^{31}Si. Proton emitting states in ^{31}S, fed by allowed beta decay, de-excite to the ^{30}P ground state with the emission of either an $\ell = 0$ or an $\ell = 2$ proton. The excited state spectrum of ^{31}S has been measured through ^{29}Si(^{3}He,n)^{31}S reactions [Da 75] and several of their observed states have energies that are consistent with the levels observed in the present work. The 17% beta branch to the isobaric analog state at 6.277 MeV was estimated by assuming a log ft = 3.3 for the superallowed Fermi transition.

Log ft values of 4.7 and 5.3 were calculated for the beta decay transitions leading to the 7.14 MeV and 7.69 MeV states in ^{31}S, respectively. These values indicate allowed beta decays which result in $\Delta J = 0, \pm 1$, with no change in parity. The Gamow-Teller strength B(GT) was then calculated using equation (4-1). For these calculations, isospin mixing, which would give rise to a non-zero B(F), is assumed to be insignificant within the level of precision. The summation of B(GT) within each 250 keV energy bin based on experimental data, as well as the results of theoretical calculations are presented as histograms in Figure IV-4. The observable experimental window ranges from approximately 300 keV above the proton separation energy, Sp, to $2m_ec^2$ below the Q_{EC}.

It is interesting to note that only a small portion of the total predicted strength is observed. However, only small amounts of beta feeding to excited states above 8.5 MeV excitation would lead to B(GT) values that are on the order of the theoretical predictions. The present experiment, because of the severe ^{25}Si contamination, is sensitive to beta branches above 2 x 10^{-3}%, assuming that once populated, proton emission to the ground state is the dominant decay mode. However, such a small decay branch could account for an appreciable amount of Gamow-Teller strength.

IV.A.4. ^{27}P Experimental

The experimental conditions for the study of ^{27}P were almost identical to the setup used in the study of ^{31}Cl. Five 6 mg/cm^2 ^{nat}Si targets were bombarded with 28 MeV and 45 MeV protons to produce ^{28}P and ^{27}P through the ^{28}Si(p,n)^{28}P and ^{28}Si(p,2n)^{27}P reactions, respectively. Radioactive recoils were transported and deposited onto the edge of a slowly rotating wheel via our multiple target/multiple capillary He-jet system which employed a 1.8 m long x 1.5 mm i.d. stainless steel capillary as the main transport line. The detector setup was the same for this experiment as for the ^{31}Cl study. It used two gas ΔE-gas ΔE-silicon E detector telescopes arranged to view the edge of the wheel, with each detector subtending a solid angle that was 3.5% of 4π.

As before, beam pulsing was employed to eliminate the detection of protons induced by fast neutrons with a cycle that consisted of a 500 ms beam on, electronics off phase and a 400 ms beam off, electronics on phase. As the half-lives of the two nuclei of interest are very nearly identical (260 ± 80 ms [Äy 85] and 270.3 ± 0.5 ms [En 90] for ^{27}P and ^{28}P, respectively), the same pulsing structure was used for each bombardment. The proton beam current was kept at ~2 μA on target in order to keep the count rate in the silicon counters below 50 kHz during the beam off phase.

Proton detector calibrations were performed by using beta-delayed protons from ^{25}Si, which was produced in a separate bombardment, via the ^{27}Al(p,3n)^{25}Si reaction at E_p = 45 MeV. Additional proton calibrants came from the known beta-delayed protons of ^{28}P [Ho 79a]. The beta-delayed alpha particles from ^{28}P were used for determining the alpha particle calibration. Typical detector resolutions were 30 keV for protons and 65 keV for alpha particles.

IV.A.5. ^{27}P Results and Discussion

A spectrum of beta-delayed protons recorded during a 290 mC bombardment of 28 MeV protons on ^{nat}Si targets is presented in Figure IV-5. The bombarding energy was chosen to be below the ^{27}P production threshold of 30.7 MeV. The six observed proton groups, labeled $p_1 ... p_6$, correspond to the proton groups from ^{28}P, observed by [Ho 79a], while proton group p_7, at 1444 keV, is a new transition. This is a relatively weak group with an intensity that is 1.7% of the main proton group at 680 keV (p_2). Based on energy considerations, we assign this group as a transition from the 13.095 MeV excited state in ^{28}Si to the ^{27}Al ground state.

A spectrum of beta-delayed alphas from ^{28}P recorded concurrently with the proton spectrum is presented in Figure IV-6. The labeled peaks all originate from ^{28}P, as reported previously by [Ho 79a]. While we observe the nine most intense alpha particle groups, the weakest, at 1668 keV, was not observed. This group was reported by [Ho 79a] to be 6.8 ± 3.9 % of the most intense alpha group (α_6) at 2105 keV. Thus our level of statistics and poorer alpha particle detector resolution (65 keV versus 20 keV reported by [Ho 79a]) could have prevented us from positively identifying this transition.

Total βp and $\beta\alpha$ branches were determined by [Ho 79a] by comparing the yield of each individual proton group, as well as the yield of each individual alpha group, to the yield of the 1.778 MeV γ-ray line which is associated with 95.5% of all ^{28}P beta decays [En 90]. ^{28}P βp and $\beta\alpha$ branches of $(13\pm4) \times 10^{-6}$ and $(8.6\pm2.5) \times 10^{-6}$, respectively, were determined by those authors. A 1.5 ± 0.6 $\beta p/\beta\alpha$ ratio can be inferred from their results and this compares favorably to the 1.4 ± 0.4 ratio of delayed protons to delayed alphas as determined from the present results. The energies, as well as the intensities, of the ^{28}P delayed charged particle groups are presented in Table IV-2. Figure IV-7 depicts a ^{28}P partial decay scheme. The beta feeding to each state was determined based on the present yield of charged particles with total βp and $\beta\alpha$ branches of 13×10^{-6} and 8.6×10^{-6}, respectively, as determined by [Ho 79a].

The delayed protons recorded during a 240 mC bombardment of 45 MeV protons on the same silicon targets as the 28 MeV proton bombardment is presented in Figure IV-8. In addition to the peaks observed in the preceding bombardment, four additional proton groups, labeled $p_1 ... p_4$, have been assigned to the beta-delayed proton emission of ^{27}P. Protons groups p_3 and p_4, with energies of 731 keV and 1324 keV, were previously observed by [Äy 85], while p_2, at 610 keV, is a new transition. Our evidence for also assigning proton group p_1, with laboratory energy 459 keV, to ^{27}P comes from comparing the yields of ^{28}P at 28 MeV and 45 MeV bombarding energies and observing a surplus of events at the higher bombarding energy from what would be expected if this peak were purely a result of the decay of ^{28}P. The results are summarized in Table IV-3.

The alpha particle spectrum, which is not shown, recorded at the 45 MeV proton bombarding energy is dominated by the alpha continuum from the decay of ^{8}B [Aj 88], as well as alpha groups from the decays of ^{20}Na [To 73] and ^{24}Al [Ho 79b]. ^{8}B was produced from carbon contaminants in the target, while ^{20}Na and ^{24}Al were produced via ^{28}Si(p,2αn)^{20}Na and ^{28}Si(p,αn)^{24}Al reactions with Q_{values} of -36.0 MeV and -24.6 MeV, respectively. No other alpha groups were discernible.

Based on the previous results of [Äy 85], energy considerations and barrier penetration calculations, these proton groups all result from the decay of ^{27}Si excited states to the 0^+ isomeric state in ^{26}Al, which lies 228 keV above the 5^+ ^{26}Al ground state. Additionally, the log ft values for the ^{27}P beta decay feeding to these states were calculated to be between 4.8 and 6.1, indicating an allowed character. The J^π of the ^{27}P ground state, taken from its mirror, ^{27}Mg, is $1/2^+$. Thus allowed beta decay would populate either $1/2^+$ or $3/2^+$ states. Barrier penetration calculations also show that the $\ell = 2$ proton transitions to the 0^+ isomeric state are favored by over three orders of magnitude over possible $\ell = 4$ proton transitions to the 5^+ ground state.

A partial decay scheme for ^{27}P is presented in Figure IV-9. The ^{27}P beta branch to proton emitting states in ^{27}Si was calculated by first determining the effective ^{28}P production cross section at 45 MeV. This was accomplished by comparing the yields of ^{28}P at the two bombarding energies and by using the ^{28}P production cross section at 28 MeV as given by the ALICE code. The calculated ^{28}P effective production cross section at 45 MeV, along with the ALICE-predicted cross section for ^{27}P at 45 MeV, were used in comparing the yields of the two phosphorus nuclides at the higher bombarding energy to estimate a 0.07% βp branch of ^{27}P. Taking the ^{27}P half life of 260 ms, a log ft of 4.8 was calculated for the beta feeding to the 8.445 MeV state. The 15% beta decay branch to the lowest T = 3/2 isobaric analog state in ^{27}Si at 6.626 MeV excitation was calculated assuming a log ft value of 3.30.

As in the analysis of the ^{31}Cl data, the Gamow-Teller strength of each decay was calculated by assuming that the Fermi component B(F) was negligibly small. The results are presented as a histogram in Figure IV-10 where the Gamow-Teller strength has been sorted into 250 keV bins. The results of the shell model calculations described in the Introduction are presented in the top half of Figure IV-10 for comparison. Our observable energy window ranges from approximately 500 keV above the proton separation energy, S_p, to 1022 keV below the Q_{EC}.

IV.A.6. Conclusions

Returning to Figures IV-4 and IV-10, some further remarks are warranted. The top half of each plot shows the results of shell model calculations described earlier, using ^{31}Cl and ^{27}P predicted half-lives of 159 ms and 215 ms, respectively. The calculated B(GT) values shown have been multiplied by a 0.60 quenching factor [Br 85], which has been observed in comparision of theoretical calculations and medium energy (p,n) experiments. Most of the GT strength is found between 7 and 10 MeV excitation in the beta daughter. A comparision of the theoretical calculations for the two nuclei reveals that ^{31}Cl GT decay is spread out over many more states in the beta daughter than ^{27}P GT beta decay. The $3/2^+$ predicted ^{31}Cl ground state J^π allows for Gamow-Teller decay to access states with spin-parities of $1/2^+$, $3/2^+$ and $5/2^+$ in ^{31}S, while GT decay of the $J^\pi = 1/2^+$ predicted ^{27}P ground state restricts the ^{27}Si final state spins and parities to $1/2^+$ and $3/2^+$.

In the case of ^{31}Cl, ~60% of the calculated strength was accessible to observation through delayed proton emission. As depicted in Figure IV-4, we were able to positively identify a portion of the expected strength within this decay energy window. However, concerning the unobserved strength, the decay branches are too weak for us to see. As mentioned earlier, the presence of significant amounts of ^{25}Si precluded us from making a sensitive analysis of the data set. A further investigation would be necessary to remove any ambiguities in the proton spectrum shown in Figure IV-1.

In the case of ^{27}P, ~25% of the total predicted strength was expected to fall within our detection energy window, and in referring to Figure IV-10, we identified a portion of the summed strength that was predicted to fall between 8 and 11 MeV. Inspection of Figure IV-8 indicates the presence of a continuum of protons underneath the most intense proton peaks. The amount of ^{24}Al ,which was produced at this bombarding energy, present in this spectrum can be inferred from the intensity of the 1.982 MeV α group and the measured $\beta p/\beta\alpha$ branching ratio of $(4.7 \pm 0.2) \times 10^{-2}$ [Ba 94]. An analysis of the delayed alpha spectrum recorded at 45 MeV indicates that ~10% of the continuum under the proton peaks (which is centered at ~750 keV) in Figure IV-8 resulted from the decay of ^{24}Al. It is clear that while delayed protons from ^{24}Al represent a component, they are not the only contibutor to this proton "background". Thus it is possible that this continuum of protons could account for some of the missing strength between 8 and 9 MeV excitation.

Above 9 MeV in ^{27}Si excitation energy, diminishingly small proton branches are required to produce B(GT) values of the order predicted. In Figure IV-10, consider the predicted strengths at $E^*(^{27}\mathrm{Si}) \approx 9.88$ and 10.38 MeV. Such states, if populated, could decay through the emission of protons with lab energies of ~2.1 and ~2.6 MeV, respectively, to the 0^+ isomeric state in ^{26}Al. Based on the level of statistics in Figure IV-8, there would only need to be ~19 events and <1 event at these two energies to produce a GT strength of 0.1 for each (respective) state. Such small proton branches are below the sensitivity of the current experiment.

IV.B. The Beta-Delayed Proton Decays of ^{17}Ne and ^{33}Ar

IV.B.1. Introduction

Our experimental investigation on the decays of ^{17}Ne and ^{33}Ar are indirectly the result of an experiment we performed at the TISOL mass separator at TRIUMF (see Section III.D. and references therein) to examine the beta-delayed two proton emission of ^{31}Ar. As these nuclei are noble gases, they cannot be effectively transported via a He-jet. However, the TISOL facility relies on diffusion out of the target as the main transport mechanism, and therefore does not require the radioactivity to stick to high molecular weight clusters, as required for the He-jet technique. Recently, there have been several papers published by Borge et al. concerning the beta-delayed proton decays of ^{17}Ne [Bo 88] and ^{33}Ar [Bo 87] in which there were several discrepancies on peak energies, intensities and assignments with the results published by Hardy et al. [Ha 71]. Schardt and Riisager [Sc 93] measured the beta-delayed proton spectrum of ^{33}Ar as part of their investigation into beta-neutrino recoil broadening as a probe of the weak interaction. They reported several proton group intensities that are in disagreement with earlier results. Using a mass separated beam and our low energy gas ΔE-gas ΔE-silicon E detector telescopes, which would give us six independent measurements, we wanted to resolve these differences.

^{17}Ne and ^{33}Ar are both well known members of the $T_Z = -3/2$, $A = 4n+1$ series of beta-delayed proton emitters. ^{17}Ne was first identified experimentally at McGill University by Barton et al. [Ba 63] through the observation of delayed protons following the bombardment of a LiF target with 95 MeV protons. Later work of [Mp 64], [Ha 65a], [Es 67], [Ha 71] and [Bo 88] have observed additional beta-delayed proton groups. Approximately one year later, Reeder et al [Re 64] reported on the discovery of ^{33}Ar, also through the observation of beta-delayed proton groups. Additional protons following the beta-decay of ^{33}Ar were reported by [Po 66], [Ha 71] and [Bo 87].

The β^+-decays of these two nuclei, as is true for most of the known members of this series (^{9}C [Aj 88] and ^{13}O [Aj 86a] being the two exceptions), consist, in part, of a superallowed transition between the $T = T_Z = -3/2$ ground state and the lowest $T = 3/2$ state in the $T_Z = -1/2$ beta daughter, followed by isospin forbidden proton emission to either the ground state and/or excited states in the proton daughter. Assuming that the final state in the $T_Z = 0$ proton daughter is a pure isospin state, then small admixtures of other isospin states in the emitter nucleus are necessary for that proton emission to occur.

The extent of isospin mixing between the $T = 3/2$ analog state and $T = 1/2$ states can be treated by second-order perturbation theory. The amount of isospin purity a^2 of the $T = 3/2$ state is given by [Bl 73]:

$$a^2 = \frac{\left|\langle T=3/2, T_Z=-1/2 \middle| H_{CD} \middle| T=1/2, T_Z=-1/2\rangle\right|^2}{\left(E_{3/2}-E_{1/2}\right)^2}, \tag{4-1}$$

where, H_{CD} is the charge dependent Hamiltonian and E_T is the excitation energy of the state with isospin T. The final state wavefunction can be expressed as the superposition of the two isospin states:

$$\Psi_f = a\left|\psi_f^a(J_f;T=3/2)\right\rangle + b\left|\psi_f^b(J_f;T=1/2)\right\rangle, \tag{4-2}$$

where, $a^2 + b^2 = 1$. Applying the isospin raising operator to connect the initial and final states, the value of the Fermi matrix element, M_V, becomes

$$M_V = a\left(\sqrt{(T-T_Z)(T+T_Z+1))}\right) \tag{4-3}$$

and finally, inserting (4-3) into equation (2-28) yields

$$ft = \frac{6147 \text{ sec}}{3a^2 + (1.588)|M_A|^2} \tag{4-4}$$

for a superallowed beta transition between $T = 3/2$ states.

The isospin purity of the IAS can be determined by the experimental observation of beta-delayed particle decay branches. Recalling equations (2-16) and (2-21) the statistical rate function f of an allowed beta transition can be calculated by integrating the Fermi function F(Z,E) over all values of positron energy:

$$f = R\int_1^{W_0} F(Z,W)W(W^2-1)^{1/2}(W_0-W)^2dW, \tag{4-5}$$

where, R is a relativistic correction (~2% for Z = 9 and ~6% for Z = 17), W is the positron energy in units of m_ec^2 and F(Z,W) is the nonrelativistic limit of the Fermi function, given as:

$$F(Z,W)=\frac{-2\pi Ze^2}{\hbar v\left(1-\exp\left(\frac{2\pi Ze^2}{\hbar v}\right)\right)}, \qquad (4\text{-}6)$$

where, Z is the atomic number of the daughter nucleus and v is the velocity of the positron far from the nucleus. With the partial half-life measured from the absolute intensities of the emitted particles, a log ft for the beta-feeding to that state can be determined, and compared to that calculated from equation (4-4).

IV.B.2. Experimental

Radioactive secondary beams of ^{17}Ne and ^{33}Ar were generated at the TISOL facility described in Section III.D. 500 MeV proton beams of 1 μA intensity bombarded a calcium-loaded zeolite target. Radioactive atoms and molecules, diffusing out of the target were ionized in the TISOL ECR ion source. They were then accelerated, mass separated and deposited onto a thin carbon foil located in the center of our six detector telescope array depicted in Figure III-5c. As mentioned in the introduction, the main motivation of this experiment at TRIUMF was the investigation of the beta-delayed two proton decay of ^{31}Ar. Consequently, experimental conditions were optimized for the study of ^{31}Ar, while β-delayed protons from the decays of ^{17}Ne and ^{33}Ar (as well as ^{32}Ar [Bj 85]) were used for purposes of determining system efficiencies and proton detector calibration curves. Alpha particle calibrations were determined using beta-delayed alpha particles from the decays of ^{17}N [Do 94] and ^{18}N [Zh 89]. These nuclei were bonded with the stable isotopes of nitrogen and oxygen and extracted as the singly-charged molecular ions, N_2^+ and NO^+ at the m = 31, 32 and 33 mass positions.

The three element detector telescope (as described in Sect. III-B.) consisted of two ~60 μg/cm^2 thick ΔE gas regions followed by a 600 μm thick silicon E detector. Isolating the gas region from the high vacuum environment was an ~50 μg/cm^2 thick polypropylene window. This gave an effective detection region from ~300 keV to ~9 MeV for protons. The detector resolution, as will be discussed in Section IV.B.4, was determined to be 35 keV for protons.

IV.B.3. ^{17}Ne Results and Discussion

A gated proton spectrum collected and summed from five of the detector telescopes at the mass 17 setting is presented in Figure IV-11. The ^{17}Ne deposition rate on the carbon foil during this 75 minute bombardment was ~2200 atoms/min. Because of the low statistics, only the relatively strong proton groups are marked. As mentioned above, the detector did not cover the entire energy window available for proton emission. However, from previous work [Aj 86b], it is known that those undetectable protons ($E_p > 9$ MeV) account for a very small portion of the total beta strength. In addition to observing the groups seen by Hardy et al. [Ha 71] and Borge et al. [Bo 88], a new low energy proton peak (peak 1 in Figure IV-11) with $E_{lab} = 686$ keV, corresponding to the transition from the 8436 keV state in ^{17}F to the 7117 keV state in ^{16}O, has been identified. Note that this proton energy is below the low energy thresholds of each of the previous ^{17}Ne decay works mentioned above.

As evidenced by Figure IV-11, the proton peaks are relatively broad with a measured FWHM of 112 keV for the main 4591 keV proton group. This broadening is the result of inherent detector resolutions, proton emission from a moving source (which is greatest for light mass nuclei with large beta-decay energies) and the width of the 5488 keV emitter state in ^{17}F. In general, the particle emitting states in ^{17}F are broad [Aj 86b] and the 68 keV width of this state is indicative of the natural widths of these states (with the exception of the IAS at 11193 keV, whose width is 200 eV).

Shown in Figure IV-12 is a summed alpha particle spectrum recorded at the same time as Figure IV-11. The peak shown has a laboratory energy of 1725 keV and corresponds to the known alpha transition from the 8075 keV state in ^{17}F to the ^{13}N ground state. No other alpha groups can clearly be distinguished, although the possibility of the presence of much weaker alpha transitions cannot be excluded.

Table IV-4 summarizes the proton and alpha transitions marked in Figures IV-11 and IV-12. Our results are in excellent agreement with the data of [Ha 71]. Our agreement with [Bo 88], however, is not as good. However, the proton and alpha energies reported in [Bo 88] are often inconsistent with the assignment given, casting doubt on their understanding of their detection system. Also, note that this later work has misassigned the 2166 keV proton group as a transition between a state at 10.0 MeV in ^{17}F to the 7.12 MeV state in ^{16}O.

Table IV-5 tabulates the ^{17}Ne beta-delayed charged particle intensities. Again, our results are in agreement with [Ha 71], with the exception of particle emission from the 8436 keV state in ^{17}F. Their lower value can be explained by their inability to detect the proton transitions leading to the 6917 keV and 7117 keV ^{16}O final states. This can be verified by adding in the relevant particle intensities from the present work to their data.

However, such a correction is not sufficient to explain the discrepancy between the present work and the results presented by [Bo 88]. In their work, protons and alpha particles are identified on a peak-by-peak basis by comparing the energy shifts of the peaks within the spectra taken with silicon counters of different thicknesses. Two of the alpha particle groups observed have energies that correspond to proton transitions from the 8436 keV state in ^{17}F to the ground state and first excited state of ^{16}O. While not doubting the assignments, their inability to separate protons from alpha particles on an event-by-event basis has probably resulted in the improper determination of the contribution of the alpha particle's intensity to the total peak.

[Bo 88] interprets the proton spectrum differently and reports that the ^{17}F state at 8825 keV is unobserved. To account for the observed protons that [Ha 71] attributes to the transition between this state and the 6052 keV state in ^{16}O, a new state in ^{17}F at 10030(50) keV is proposed that decays to the 7117 keV state in ^{16}O. The other transition from this state (8825 —> gs) reported here and by [Ha 71] is attributed to a proton transition from a state in ^{17}F at 8.2 MeV to the ^{16}O ground state. We have adopted the earlier assignments as the energetics of the proton peaks are consistent with the work of [Ha 71] and not with the assignments made by [Bo 88].

A partial decay scheme for ^{17}Ne is presented in Figure IV-13. Shown are those β-delayed charged particle transitions observed in the present work, as well as those observed by [Ha 71]. The branching ratios were calculated based on the present work for those transitions described in Table IV-5, with the values for the less intense transitions and/or those proton transitions above our energy detection window taken from [Ha 71]. The branching ratio to the first excited state was recently measured to be $1.65 \pm 0.16\%$ with a log ft = 6.37 [Bo 93]. The β^+-decay branch to the ^{17}F ground state, which is a second forbidden beta transition, was determined by comparison to the mirror ^{17}N decay, and the value reported by [Ha 71] is used here. Total βp and βα branching ratios of 96.2% and 1.7% were determined.

The log ft for each transition was then calculated via equations (4-5) and (4-6). The ^{17}Ne mass excess was taken to be 14.529 MeV with respect to the ^{17}F ground state and its half-life is 109±1 msec. The results are also presented in Figure IV-13. The results presented in Figure IV-13 are in quantitative agreement with the work of [Ha 71]. The calculation of the isospin purity of the T = 3/2, 11.193 MeV state using the value of the Gamow-Teller matrix element used by [Ha 71], ($|M_A|^2 = 0.11$), leads to a value that is consistent with 100%. This result, while in agreement with the result reported by [Ha 71] (a^2 >95%), is not really an improvement over the previous results due to the present experiment's inability to observe the entire spectrum of decays from the isobaric analog state.

IV.B.4. ^{33}Ar Results and Discussion

The average ^{33}Ar deposition rate from TISOL on the center foil at the mass 33 setting was ~350 atoms/min. Figure IV-14 shows a summed gated proton spectrum recorded from all six detector telescopes during this portion of the experiment. All proton groups with $E_p \leq 6$ MeV described by Hardy et al. [Ha 71], Borge et al. [Bo 87] and Schardt et al. [Sc 93] are observed. The prominent groups ($I_p \geq 8‰$ of the main 1000‰ group at 3167 keV) are marked and listed in Table IV-6. With the exception of peak 1, all marked peaks result from transitions from ^{33}Cl excited states to the ground state of ^{32}S, with peak 6, at $E_p = 3167$ keV, corresponding to the decay from the lowest $T = 3/2$ state in ^{33}Cl. The FWHM of the 1000‰ peak at 3167 keV is 42 keV. A 115 ± 15 eV width of this state is known [En 90] and the effects of beta-neutrino line broadening have been calculated to be 22.9 keV [Sc 93]. From this, a 35 keV detector resolution can be determined.

The mass 33 alpha spectrum primarily shows alpha particles from the decay of ^{17}N which is present in the mass 33 beam as the $^{17}N^{16}O^{+}$ molecular ion. Although the ^{17}N beta-delayed alphas could be obscuring an extremely weak ^{33}Ar $\beta\alpha$ group, it is unlikely as the alpha particle separation energy to the ^{29}P ground state is 6.478 MeV with a total decay energy window of 4.124 MeV. Proton emission from these states above the alpha particle separation energy would be expected to be favored over alpha emission. Additionally, less than 1% of the known total beta-decay branch goes to states in ^{33}Cl above 6.478 MeV.

The measured proton energies and intensities are listed in Table IV-6. All the proton peaks listed, with the exception of peak 1, result from transitions between ^{33}Cl excited states and the ^{32}S ground state. Peak 1 is a proton transition that connects the 5866 keV excited state in ^{33}Cl to the first excited state in ^{32}S at 2230 keV excitation. The excitation energy in ^{33}Cl for those transitions going to the ^{32}S ground state can be obtained by the formula :

$$E^{*}_{\mathrm{keV}} = 2277 + 1.031\left(E_{p}^{\mathrm{lab}}\right). \qquad (4\text{-}7)$$

Our results concerning the intensities, with the exception of peak 7, are in agreement with the work of [Ha 71]. Discrepancies exist between our work and the results presented by [Bo 87] for peaks 1, 2, 4 and 9. [Bo 87] reports a peak at 1697 ± 6 keV of 1.5 ± 0.1‰ relative intensity. Such a peak may exist as a shoulder on peak 2; however, our data do not verify this transition. Two major discrepancies exist between the current work and [Sc 93], as evidenced by Table IV-6. Their reported intensities for the 3347 keV and the 3418 keV proton groups are significantly less than that reported here and by [Ha 71] and [Bo 87]. As a complete proton spectrum is not given in [Sc 93], it is unclear as to the nature of this large discrepancy.

A partial decay scheme for ^{33}Ar is shown in Figure IV-15. The beta decay branch to each state listed was determined from the present results and from the intensity values reported by [Ha 71] for those transitions not reported in Table IV-6. An estimate of the beta branching to the ^{33}Cl ground state was made by examining the decay of the mirror, ^{33}P, which β^--decays 100% of the time to the ^{33}S ground state with a log $ft^- = 5.02$. The log ft^+ for the corresponding ^{33}Ar(gs)—>^{33}Cl(gs) transition can be calculated by the following relation [Es 71]:

$$\frac{ft^+}{ft^-} - 1 = C\left[Q_{EC} - Q_{\beta^-}\right], \tag{4-8}$$

where, C is a constant equal to ~5.2E-03 MeV^{-1}. Using (4-5) to calculate the statistical rate function f, a 17.5% β^+ branch to the ^{33}Cl ground state was estimated. The γ-ray data of [Ha 71] showed that the γ-ray intensity was 1.42 times the total proton intensity which, combined with the above result, gives a βp branch of 34.1 ± 4.5%.

Table IV-6 accounts for at least 97% of all proton decays, which implies that the IAS—>^{32}S(gs) proton transition (E_p = 3167 keV) is 80% of all proton transitions with a beta feeding branch of 27.3%. A transition from the IAS to the first excited state in ^{32}S at 2.230 MeV is energetically allowed with the emission of a ℓ=2, 1.006 MeV (lab) proton. However, comparison of the corresponding proton decay widths, Γ_p, indicates that the transition to the ^{32}S ground state is favored by ~3 orders of magnitude over the decay to the first excited state. There is no indication of a 1 MeV proton of this intensity in Figure IV-14.

A log ft = 3.33 for the β^+ transition to the IAS in ^{33}Cl was calculated using a ^{33}Ar mass excess of 11.624 MeV relative to the ^{33}Cl ground state and a half-life of 174 msec. Combining this with the value for $|M_A|^2 = 0.28$ [Ha 65b], the isospin purity of the IAS was determined to be 81%, in perfect agreement with the results of [Ha 71]. However, based on a line-shape calculation of the 3167 keV proton group recorded by [Sc 93], an upper limit of $|M_A|^2 < 0.018$ was determined. This value results in an isospin purity of 95%. which is close to the result obtained in the limit that $|M_A|^2 = 0$ (a^2 = 96%). The implications of isospin mixing with neighboring T = 1/2 states has been previously discussed by [Ha 71] and [Es 71]. Analysis of the four levels near the IAS suggests that each has a 1-2% T = 3/2 character. As those authors pointed out, this is of the right order to account for the strength missing from the IAS.

Examination of the low energy (E_p<1 MeV) part of the spectrum of Figure IV-14 reveals some semblance of structure. There are several excited states in ^{33}Cl which could emit protons in this energy region either to the ground state or to excited states in ^{32}S. Based on the arguments presented below and with the level of statistics presented in Figure IV-14, the possibility that this structure is due to proton emission from these excited states is taken with some reservation.

The possibility that proton transitions connect excited states in both ^{33}Cl and ^{32}S can be rejected for several reasons. First, one would expect that for a ^{33}Cl(E*)—>^{32}S(E*) transition, the corresponding transition to the ^{32}S ground state would also be observed. Examination of the known proton transitions indicates that five of the ^{33}Cl excited states fit this latter criterion. However, the proton groups emitted from these states to the ^{32}S ground state have intensities between 0.3 and 2.3‰ of the main (1000‰) proton group. Comparisons of proton decay widths between transitions to the ground state and transitions to excited states show that the former are favored by at least 2.5 orders of magnitude for the best case (^{33}Cl(5.450)—>^{32}S(2.230)), with the other four ^{33}Cl(E*)—>^{32}S(E*) transitions favored by ~5 orders of magnitude over the corresponding ^{33}Cl(E*)—>^{32}S(gs) transition. The data shown in Figure IV-14 are not sensitive to such small proton intensities.

Of the three possible excited states in ^{33}Cl which can energetically emit protons with $0.5<E_p<1$ MeV, to the ^{32}S ground state, two would be beta fed by second forbidden beta transitions (^{33}Cl(E*) = 2.839 and 2.975 MeV) while the other (^{33}Cl(E*) = 2.846 MeV) would be beta fed by a first forbidden beta transition. Additionally, only the state at 2.975 MeV would be expected to have proton emission compete favorably with γ-ray de-excitation. The βγ spectrum of ^{33}Ar, measured by both [Ha 71] and [Bo 87], shows no γ-ray lines from any of these excited states. Any transition from the 2.975 MeV state in ^{33}Cl to the ^{32}S ground state would be accompanied by the emission of an $\ell=4$, 682 keV (lab) proton. Although there is tentative evidence of a possible weak proton group near E_p = 700 keV, with a relative proton intensity I_p < 0.5‰, it is not conclusive. Further investigation is necessary to confirm this result.

IV.C. Search for the Beta-Delayed Proton Decay of ^{77}Zr

IV.C.1. Background

In recent years, our group has measured the decays of ^{61}Ge [Ho 87], ^{65}Se [Ba 93a] and ^{73}Sr [Ba 93c] through the observation of delayed protons emitted from the isobaric analog state in the beta daughters. The above nuclei are the heaviest members of the A = 4n+1, T_z = -3/2 series of nuclei studied to date with ^{77}Zr being the next member of this series that remains uncharacterized. All members of this series from ^{9}C to ^{73}Sr, with the exception of ^{69}Kr (which has not yet been observed), are known to be beta-delayed proton emitters with decay branches ranging from 11 to 100% [Ha 88a]. These heaviest members have all been produced via (HI,3n) fusion-evaporation reactions using stable Z = N beams and targets. Because of the lack of stable Z = N beams and targets above calcium, ^{77}Zr represents the last member of this series that can be effectively produced via this method without the use of radioactive beams and/or targets.

The importance of studying these drip line nuclei is that they provide an extreme test of nuclear mass models. ^{77}Zr is 13 neutrons away from the closest stable zirconium isotope and 3 neutrons away from the next lightest isotope observed to date, ^{80}Zr [Li 87]. Nuclei in this region are known to be strongly deformed due to shell effects caused by a gap in the single particle level sequence near N = Z = 38 [Li 90]. In order for a particular nuclear mass model to accurately predict the mass of ^{77}Zr, it must account for this deformation.

Presented in Figure IV-16 is a chart of predictions made by six of the mass models presented in the 1986-1987 Atomic Mass Predictions [Ha 88b] for the center of mass energy of protons emitted from the IAS in the emitter to the $T_Z = 0$ daughter ground state versus the precursor nuclide, ^{61}Ge to ^{77}Zr. Also presented is the experimentally observed decay energy (corrected for center-of-mass). The proton energy predictions are calculated by using the Coulomb displacement formula (Sect. II.A.2.b.) to connect the predicted precursor ground state mass to the isobaric analog state mass in the emitter nuclide and comparing this energy level to the calculated proton separation energy to the predicted proton daughter ground state mass.

As evidenced by Fig. IV-16, the mass models agree within 250 keV at ^{61}Ge, but rapidly begin to diverge, so that by ^{77}Zr, they cover a range greater than 1500 keV. Also evident is that as one moves away from stability, the three recursive-type relations (Jänecke-Masson, Masson-Jänecke and Comay-Kelson-Zidon) better predict the proton energies than the global parameter models (Möller-Nix, Möller et al. and Tachibana et al.). This suggests the ability of these models to better reflect local changes in the nuclear mass surface. The observation of protons following the beta decay of ^{77}Zr would serve to determine if this trend continues.

IV.C.2. Experimental and Discussion

To produce ^{77}Zr, a separated isotope ^{40}Ca target (1.9 mg/cm^2 thick) was bombarded with a 160 MeV (mid-target lab energy) ^{40}Ca^{11+} beam from the 88-Inch Cyclotron utilizing the ^{40}Ca(^{40}Ca,3n)^{77}Zr reaction and our single target/single capillary He-jet target system (Figure III-2b). Because of the power deposition on the HAVAR entrance foils, the beam current was restricted to 30 particle nA. Any more than this beam intensity would result in the foils overheating and rupturing. Recoils were thermalized in a KCl loaded He-jet, transported via a 1.07 mm id capillary and deposited onto a moving tape in the center of our gas ΔE-gas ΔE-silicon E detector telescope array (Figure III-5a,b). During a 30 mC bombardment, we observed beta-delayed protons from ^{65}Se and ^{73}Sr which are produced via the ^{40}Ca(^{40}Ca,3α3n)^{65}Se and ^{40}Ca(^{40}Ca,α3n)^{73}Sr reaction channels. We also observed several protons at a lab energy around 4.2 MeV. This is significant in that, referring to Figure IV-16, three of the mass predictions calculate a proton lab energy that is within 200 keV of this energy.

Since the yields of nuclei produced via (^{40}Ca,xα3n) reactions were higher than desired, the experiment was repeated using a ^{40}Ca^{11+} beam with a mid-target energy of 147 MeV. In a 70 mC bombardment, the yields of ^{65}Se and ^{73}Sr dropped considerably, as expected. Additionally, the previously seen proton group at 4.2 MeV was also observed.

Before making the assignment of this proton group to the decay of ^{77}Zr, a third bombardment was performed. This experiment used the same setup and 1.9 mg/cm^2 ^{40}Ca target, but a 145 MeV (mid-target lab energy) ^{36}Ar^{8+} beam was employed. The non observation of protons near 4.2 MeV would imply that the source of these protons is from a nuclide with $39 \leq Z \leq 40$. Unfortunately, a 50 mC bombardment showed evidence for a weak proton group at approximately 4.2 MeV, indicating that the source is fully or partially from a $Z \leq 38$ beta-delayed proton emitter.

Using the nomographs in references [Mo 51] and [Ve 66], a beta decay branching ratio of ~45% to the lowest T = 3/2 state in ^{77}Y is estimated by the assumption of a log ft = 3.3 [Ha 66] for the superallowed beta decay and through the Coulomb displacement formula calculation of the maximum kinetic energy of 10.45 MeV for the emitted beta particles. A half-life of 10 msec, taken from the gross theory of beta decay [Ta 73], is assumed for this calculation. A He-jet efficiency of 5% with a transit time of 30 msec for the single target/single capillary setup was measured for germanium [Ho 87] and is taken to be the same for zirconium. The ALICE predicted cross section for the ^{40}Ca(^{40}Ca,3n)^{77}Zr reaction at beam energies of 140-160 MeV is ~100 nb. Based on these parameters, as well as an effective target thickness of 0.95 mg/cm^2 and detector geometries, we should have observed approximately 11 and 26 delayed proton events following the beta decay of ^{77}Zr in each of the first two ^{40}Ca bombardments, respectively.

Noting the above, a shorter half-life or a smaller production cross section than expected could explain the lack of an unambiguous observation of ^{77}Zr. If the half life is much shorter than the transit time of our He-jet system, then there will be significant losses due to radioactive decay in transit. As mentioned previously, the ALICE predicted cross section for the ^{40}Ca(^{40}Ca,3n)^{77}Zr reaction at beam energies of 140-160 MeV is ~100 nb. The ALICE predicted peak cross sections for the reactions used to produce the three most recently discovered members of the A = 4n+1, T_z = -3/2 series nuclei, ^{61}Ge, ^{65}Sr and ^{73}Sr are 670 nb (^{40}Ca(^{24}Mg,3n)^{61}Ge), 540 nb (^{40}Ca(^{28}Si,3n)^{65}Se) and 250 nb (^{40}Ca(^{36}Ar,3n)^{73}Sr) at beam energies of approximately 4.2 MeV/nucleon, each. It was observed that ALICE had overpredicted the cross section for the production of these three nuclei at their respective bombarding energies by factors of 10-20. If a similar situation exists for ^{77}Zr, then its production cross section could be as low as 5 nb, with a corresponding drop in the yield of ^{77}Zr beta-delayed protons.

Aside from the possibility of a shorter than expected half-life, and/or a significantly reduced production cross section, preventing our observation of ^{77}Zr, the possibility that there was a lower mass delayed proton emitter masking the ^{77}Zr group cannot be discounted. Any of these effects would have been sufficient to prevent our unambiguous identification of beta-delayed protons from ^{77}Zr.

IV.D. Tables for Section IV

Table IV-1. ^{31}Cl beta-delayed proton groups.

	Relative Proton Intensity		
E_p (keV)$^{a)}$	This Work	[Äy 85]	$E^*(^{31}S)^{b)}$
845 ± 30	≤ 1	3 ± 2	
986 ± 10	100$^{c)}$	100 ± 2$^{c)}$	7138 ± 8
1173 ± 30	≤ 1	3 ± 2	
1524 ± 15	11 ± 5	23 ± 6	7691 ± 12
1695 ± 20	≤ 1	10 ± 3	
1827 ± 20	≤ 1	13 ± 4	
2113 ± 30	≤ 1	7 ± 3	
2204 ± 30	≤ 1	6 ± 3	

a) Laboratory energy.

b) Based on the ^{30}P + proton separation energy of 6127 ± 2 keV.

c) Defined.

Table IV-2. ^{28}P beta-delayed charged particle groups.

			Relative Intensity	
Peak a)	Particle Energy b)	E*(^{28}Si) c)	This Work	[Ho 79a]
p1	468±10	12.071	6.0±1.0	12 ± 6
p2	680± 7	12.291	100 d)	100 d)
p3	826± 7	12.443	5.6±1.0	11 ± 6
p4	956± 5	12.577	56.0±3.8	50 ±21
p5	1087±10	12.713	4.1±0.8	6.1± 3.5
p6	1269± 5	12.902	17.6±1.8	23 ± 9
p7	1444±12	13.083±12	1.7±0.5	≤6
α1	1312± 5	11.516	25 ±3	24 ±10
α2	1434± 5	11.659	79 ±6	74 ±28
α3	1668± 5	11.932	≤3	6.8± 3.9
α4	1789± 5	12.073	15 ±4	15 ± 7
α5	1976± 5	12.291	14 ±5	14 ± 7
α6	2105± 5	12.441	100 d)	100 d)
α7	2200± 5	12.552	23 ±6	20 ± 9
α8	2351± 5	12.728	6 ±2	5.8± 3.5
α9	2497± 5	12.899	13 ±3	12 ± 6
α10	2665± 7	13.095	3 ±1	4.5± 2.5

a) Refer to Figure IV-5 for protons (p_1...p_7) and to Figure IV-6 for alphas (α_1...α_{10}).

b) Energies are reported in keV in the lab. system with proton groups p_1 through p_6 taken from [Ho79a] and proton group p_7 from this work.

c) Based on 11.586 MeV proton separation energy to the ground state of ^{27}Al and on 9.986 MeV alpha particle separation energy to the ground state of ^{24}Mg.

d) Defined.

Table IV-3. ^{27}P beta-delayed proton groups.

Peak[a)]	E_p[b)]	$E^*(^{27}Si)$[c)]	Relative Intensity This Work	Relative Intensity [Äy 85]
p1	459±14	8165±14	7±3	
p2	610±11	8321±11	92±4	
p3	731±10	8445±10	100[d)]	100[d)]
p4	1323±17	9065±17	5±2	6±3

a) Refer to Figure IV-7.

b) Energies are reported in keV in the lab. system.

c) Based on 7.692 MeV proton separation energy to the 0^+ isomeric state in ^{26}Al.

d) Defined.

Table IV-4. ^{17}Ne Beta-Delayed Charged Particle Energies. The first column peak number refers to Figure IV-11 in the case of protons and Figure IV-12 in the case of alpha particles.

Peak	^{17}F —> ^{16}O	E_p (calc)$^{a)}$	E_p measured this work	E_p measured [Ha 71]	E_p measured [Bo 88]
1	8436 —> 7117	676	686(15)		
2	8436 —> 6917	865	868(15)		844(10)
3	8075 —> 6052	1339	1349(10)	1349(25)	1312(10)
4	8436 —> 6052	1678	1681(10)	1666(30)	1651(5)
5	8825 —> 6052	2044	203715)	2035(35)	2039(10)$^{c)}$
6	4609 —> gs	3772	3767(10)	3772(15)	3763(4)
7	11193 —> 6131	4198	4193(10)	4194(10)	4192(4)
8	5488 —> gs	4598	4591(10)	4591(10)	4593(4)
9	6037 —> gs	5115	5114(10)	5115(10)	5115(4)
10	8075 —> gs	7032	7025(10)	7031(10)	7021(5)
11	8436 —> gs	7372	7370(10)	7373(10)	7370(5)
12	8825 —> gs	7738	7744(15)	7744(30)	
	^{17}F —> ^{13}N	E_α (calc)$^{b)}$	E_α measured this work		
	8075 —> gs	1726	1726(15)		1653(21)$^{d)}$

All energies are reported in keV in the center-of-mass system.

a) p + ^{16}O separation energy = 600 keV.

b) α + ^{13}N separation energy = 5819 keV.

c) This peak is misassigned in [Bo 88] to a transition between a state at 10.0 MeV in ^{17}F to the 7.12 MeV state in ^{16}O.

d) This value represents an average of measurements reported by the authors.

Table IV-5. ^{17}Ne Beta-delayed Charged Particle Intensities . The percentage values are given relative to the 5488 ---> gs transition.

^{17}F	^{16}O Final States				^{13}N Final State	Summed Strength (%)		
Initial State	gs	6052	6917	7117	gs	This work	[Ha 71]a)	[Bo 88]
4609	29.8	----	----	----	----	29.8(2.0)	30.1(1.3)	27.96(0.30)
5488	100b)	----	----	----	----	100b)	100b)	100b)
6037	20	----	----	----	----	20.0(3.0)	19.7(0.4)	13.2(0.4)
8075	8.2	3.1	----	----	3.2	14.5(2.5)	12.6(0.2)	12.3(1.5)
8436	2.0	9.2	4.6	1.2	----	17.0(3.0)	12.04(0.02)	6.8(0.3)
8825	<0.5	2.3	----	----	----	2.5(1.5)	3.52(0.11)	----

All energies are quoted in keV.

a) Values from [Ha 71] do not include alpha particle transitions.

b) Defined.

Table IV-6. ^{33}Ar Beta-delayed Proton Intensities. The peak number refers to the designations made in Figure IV-14.

		Relative Proton Intensity (‰)			
Peak	E_p a)	This Work	[Ha 71]	[Bo 87]	[Sc 93]
1	1321±20	8.9 ± 1	8.6 ± 3.6	6.2 ± 0.3	5.8 ± 0.1
2	1643±10	15.2 ± 2	15.1 ± 0.7	11.1 ± 0.3	12.6 ± 0.2
3	1781±10	14.6 ± 2	16.0 ± 0.7	14.0 ± 0.3	14.8 ± 0.2
4	2096±10	95.0 ± 5	93.9 ± 1.9	76.5 ± 0.7	76.4 ± 0.5
5	2478±10	11.7 ± 3	11.7 ± 0.6	10.7 ± 0.3	11.4 ± 0.2
6	3167± 5	1000 b)	1000 b)	1000 b)	1000 b)
7	3347±10	30.0 ± 8	20.7 ± 0.8	24.4 ± 1.3	1.0 ± 0.2
8	3481±20	16.5 ± 4	13.8 ± 0.6	13.4 ± 1.3	<0.2
9	3850±15	21.0 ± 3	21.9 ± 0.8	26.1 ± 0.7	23.1 ± 0.2
10	5033±10	9.0 ± 3	10.9 ± 0.5	10.7 ± 0.3	7.0 ± 0.2

a) Energy in keV in the lab. system.

b) Defined.

IV.E. Figures for Section IV

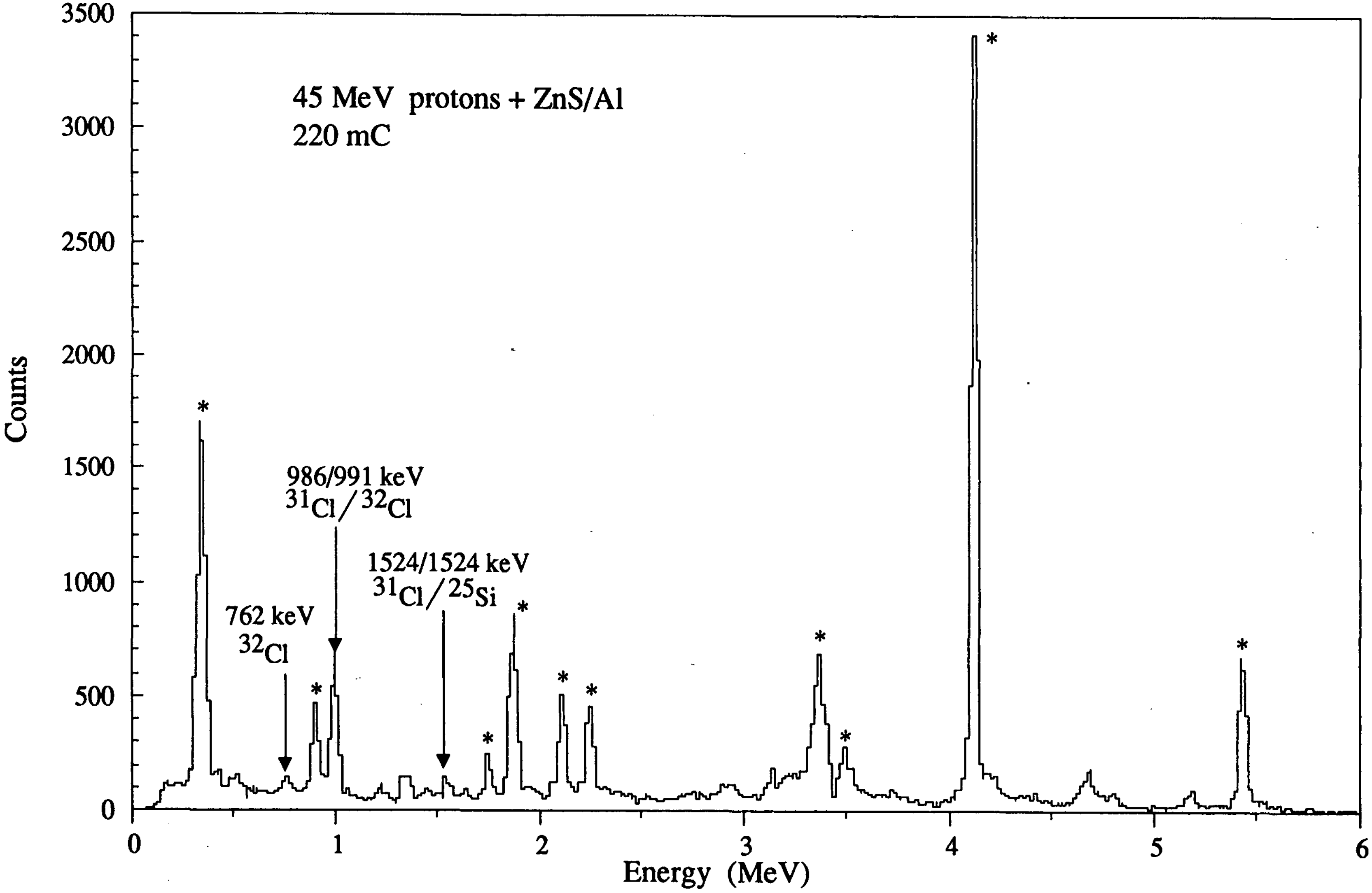
45 MeV protons + ZnS/Al
220 mC
Counts
Energy (MeV)
0
500
1000
1500
2000
2500
3000
3500
0
1
2
3
4
5
6
762 keV
^{32}Cl
986/991 keV
^{31}Cl/^{32}Cl
1524/1524 keV
^{31}Cl/^{25}Si
*

Figure IV-1.

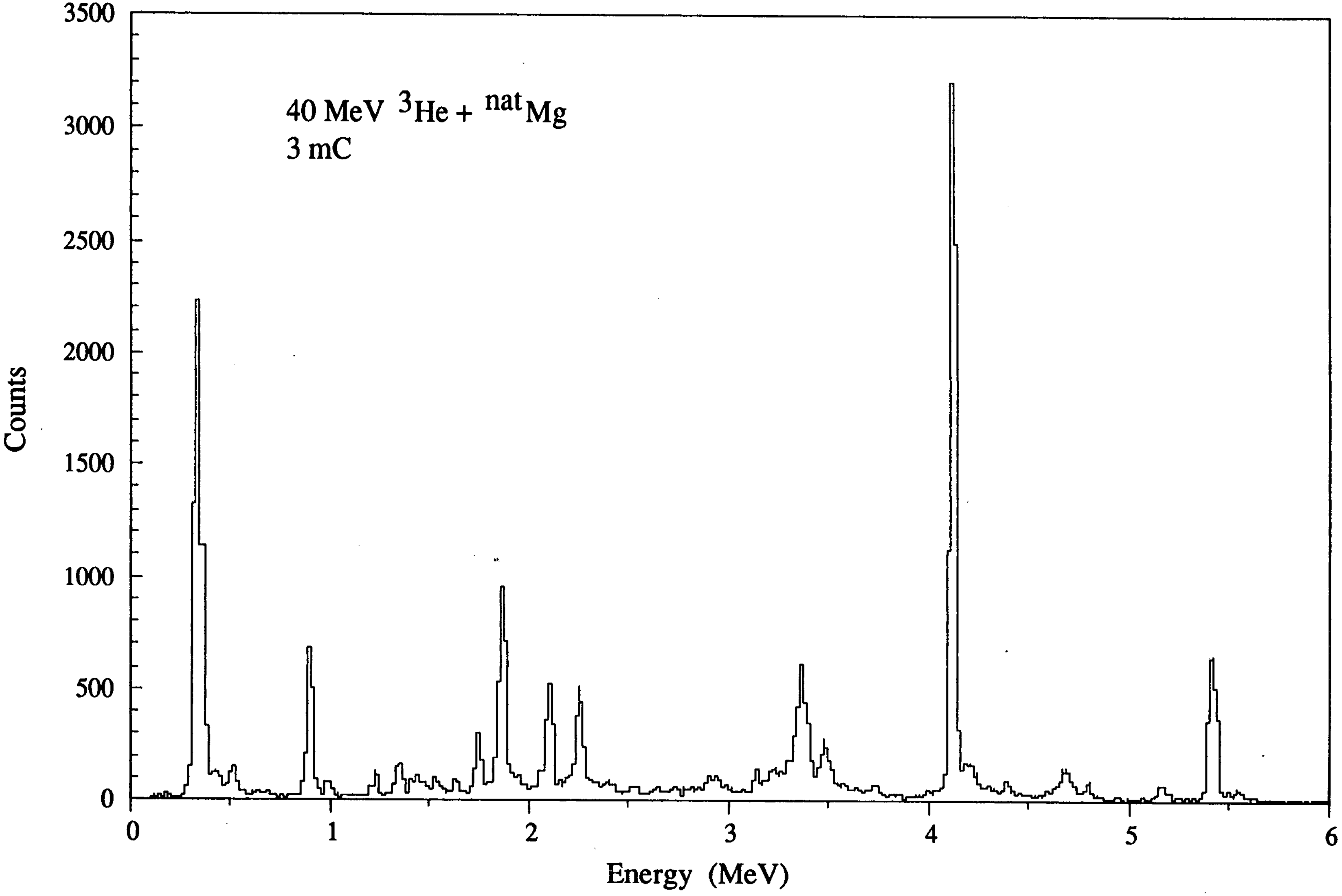
40 MeV ^{3}He + ^{nat}Mg
3 mC
Counts
3500
3000
2500
2000
1500
1000
500
0
Energy (MeV)
0
1
2
3
4
5
6

Figure IV-2.

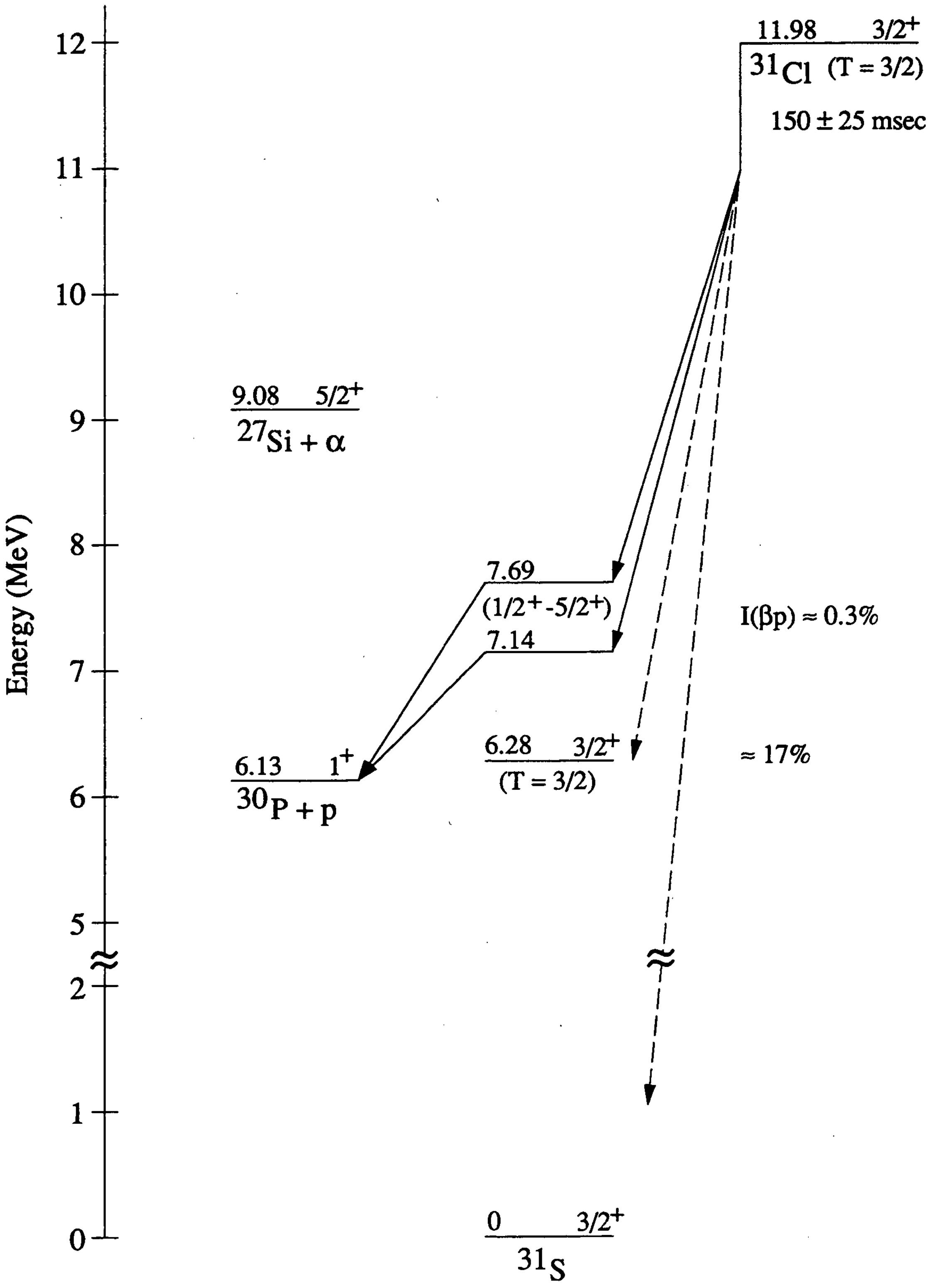

Energy (MeV)
12
11
10
9
8
7
6
5
2
1
0
11.98 3/2+
31Cl (T = 3/2)
150 ± 25 msec
9.08 5/2+
27Si + α
7.69
(1/2+-5/2+)
7.14
I(βp) ≈ 0.3%
6.13 1+
30P + p
6.28 3/2+
(T = 3/2)
≈ 17%
0 3/2+
31S

Figure IV-3.

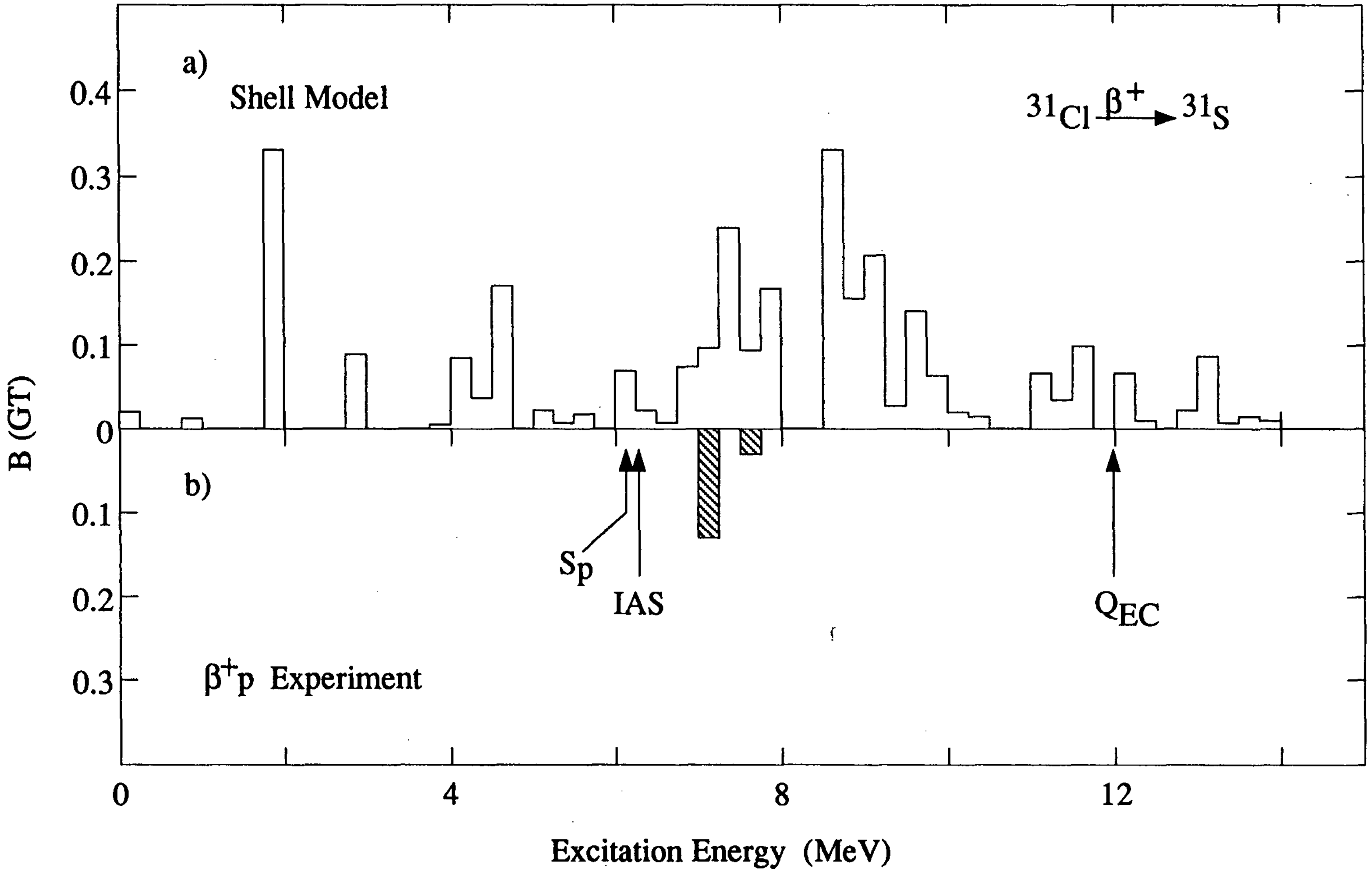
a)
Shell Model
$^{31}Cl \xrightarrow{\beta^+} {}^{31}S$
b)
β^+p Experiment
S_p
IAS
Q_{EC}
B (GT)
0.4
0.3
0.2
0.1
0
0.1
0.2
0.3
0
4
8
12
Excitation Energy (MeV)

Figure IV-4.

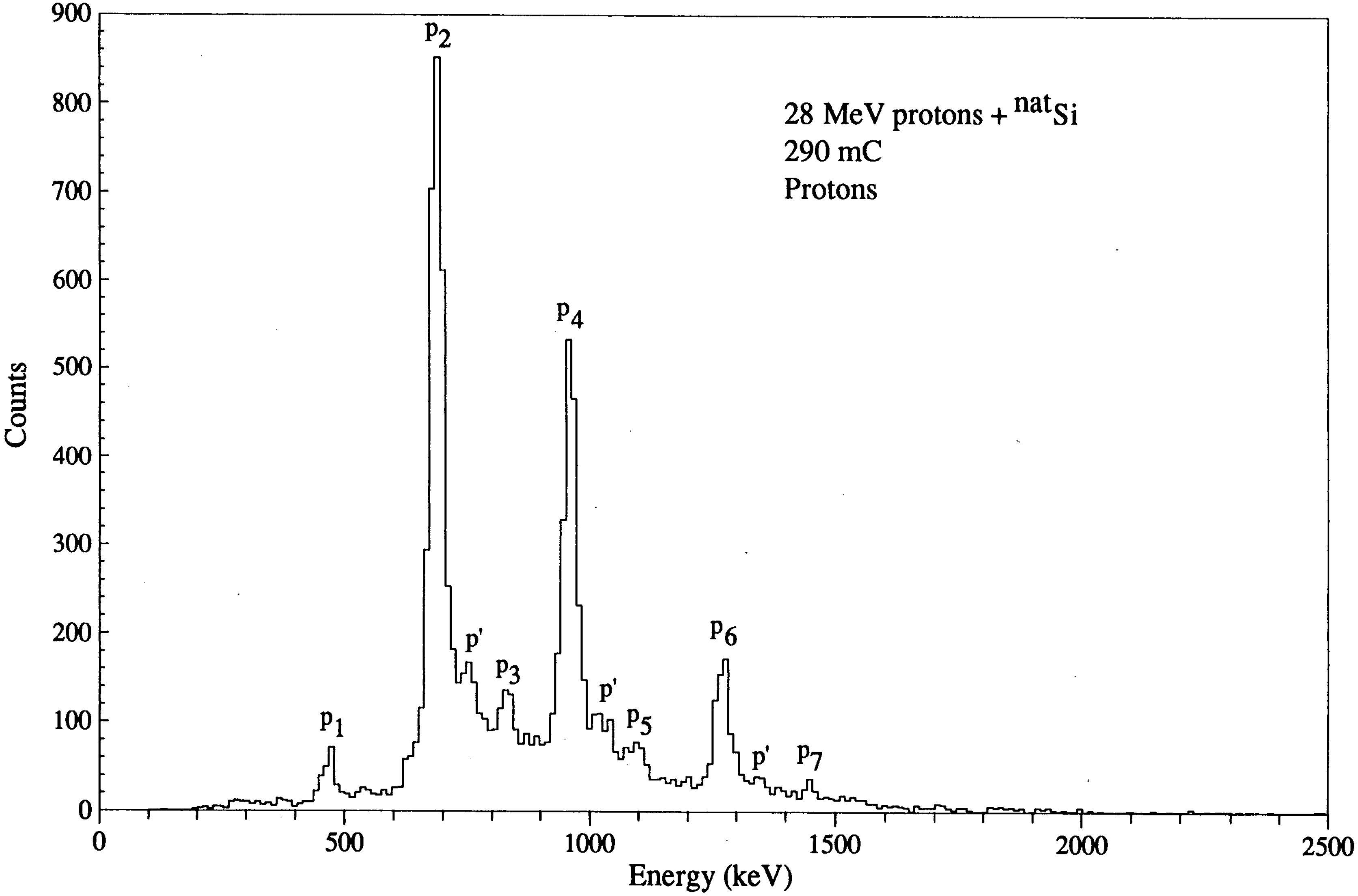
28 MeV protons + ^{nat}Si
290 mC
Protons
p_1
p_2
p'
p_3
p_4
p'
p_5
p_6
p'
p_7
Counts
0
100
200
300
400
500
600
700
800
900
Energy (keV)
0
500
1000
1500
2000
2500

Figure IV-5.

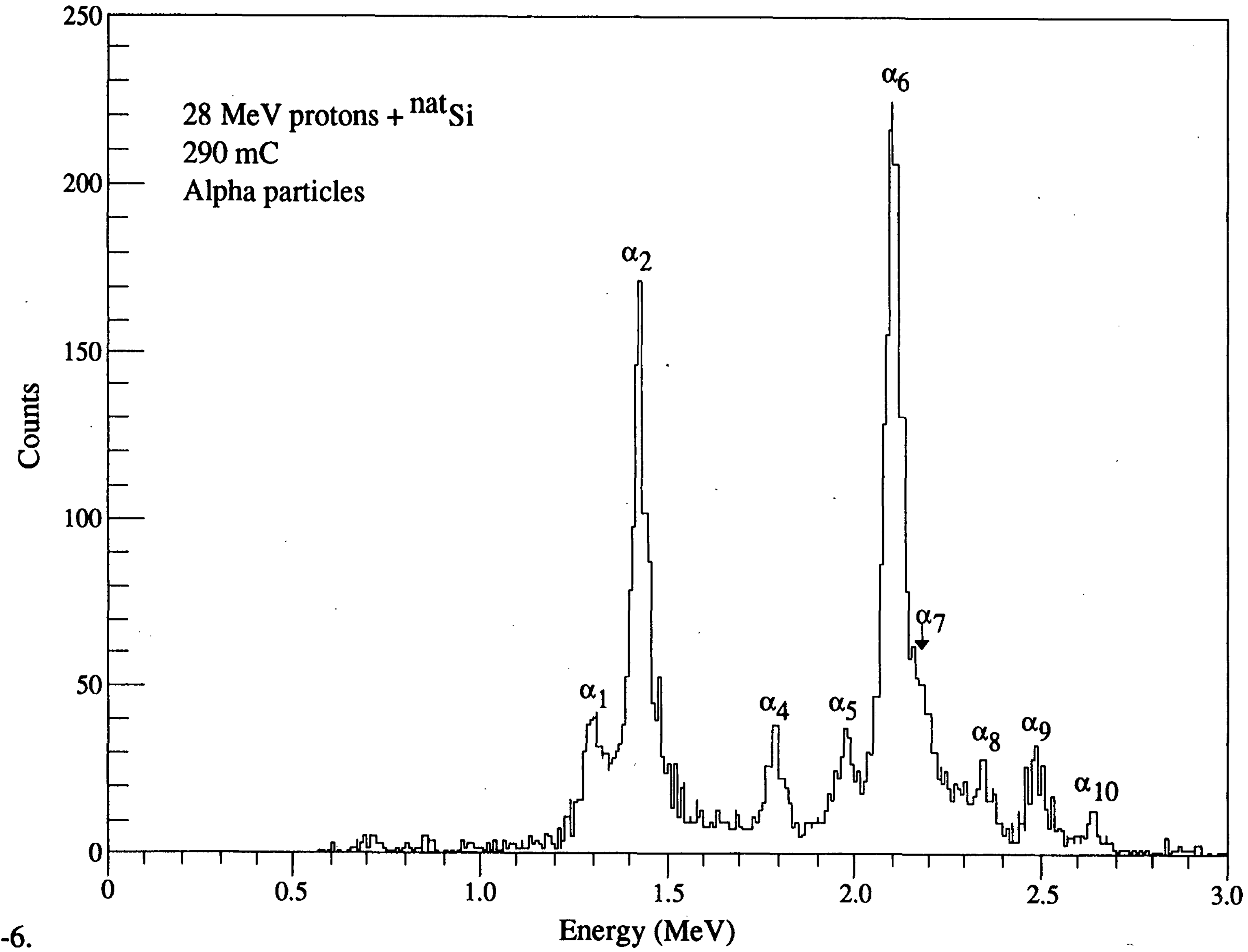
28 MeV protons + ^{nat}Si
290 mC
Alpha particles
Counts
Energy (MeV)
0
50
100
150
200
250
0
0.5
1.0
1.5
2.0
2.5
3.0
α_1
α_2
α_4
α_5
α_6
α_7
α_8
α_9
α_{10}

Figure IV-6.

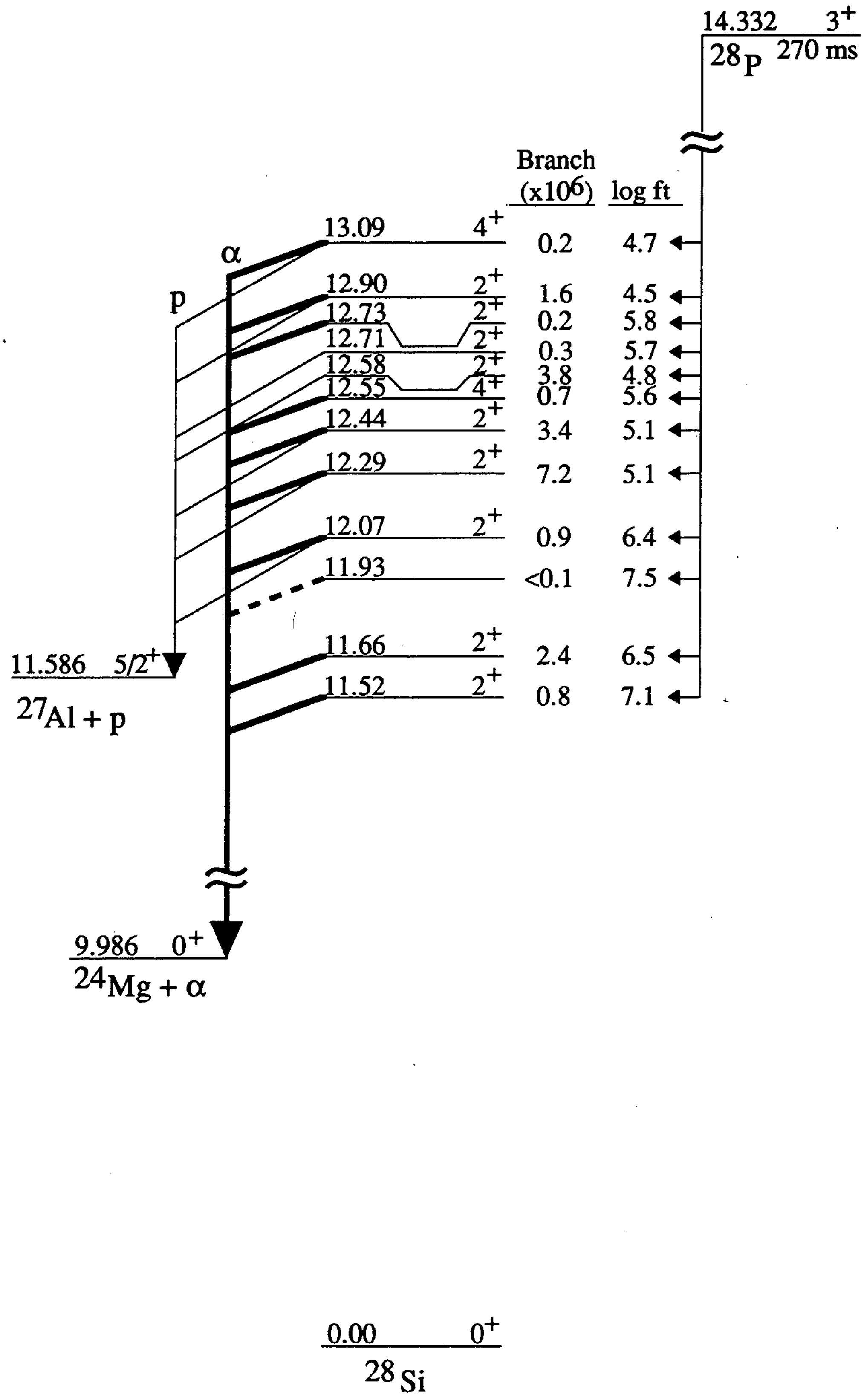
14.332 3+
28P 270 ms
Branch (x10^6)
log ft
13.09 4+ 0.2 4.7
12.90 2+ 1.6 4.5
12.73 2+ 0.2 5.8
12.71 2+ 0.3 5.7
12.58 2+ 3.8 4.8
12.55 4+ 0.7 5.6
12.44 2+ 3.4 5.1
12.29 2+ 7.2 5.1
12.07 2+ 0.9 6.4
11.93 <0.1 7.5
11.66 2+ 2.4 6.5
11.52 2+ 0.8 7.1
α
p
11.586 5/2+
27Al + p
9.986 0+
24Mg + α
0.00 0+
28Si

Figure IV-7.

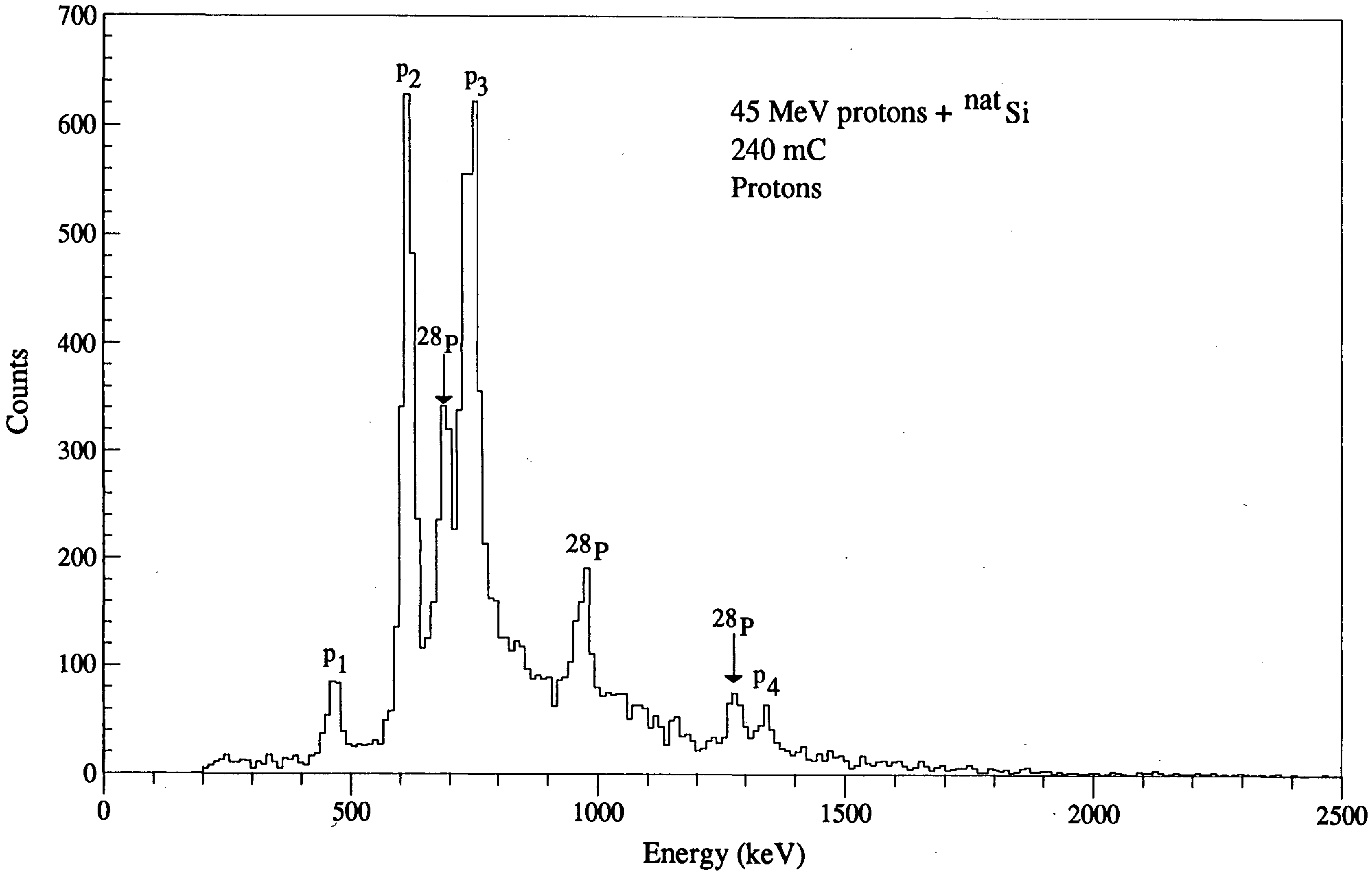
45 MeV protons + ^{nat}Si
240 mC
Protons
p_2
p_3
^{28}P
^{28}P
^{28}P
p_1
p_4
Counts
0
100
200
300
400
500
600
700
Energy (keV)
0
500
1000
1500
2000
2500

Figure IV-8.

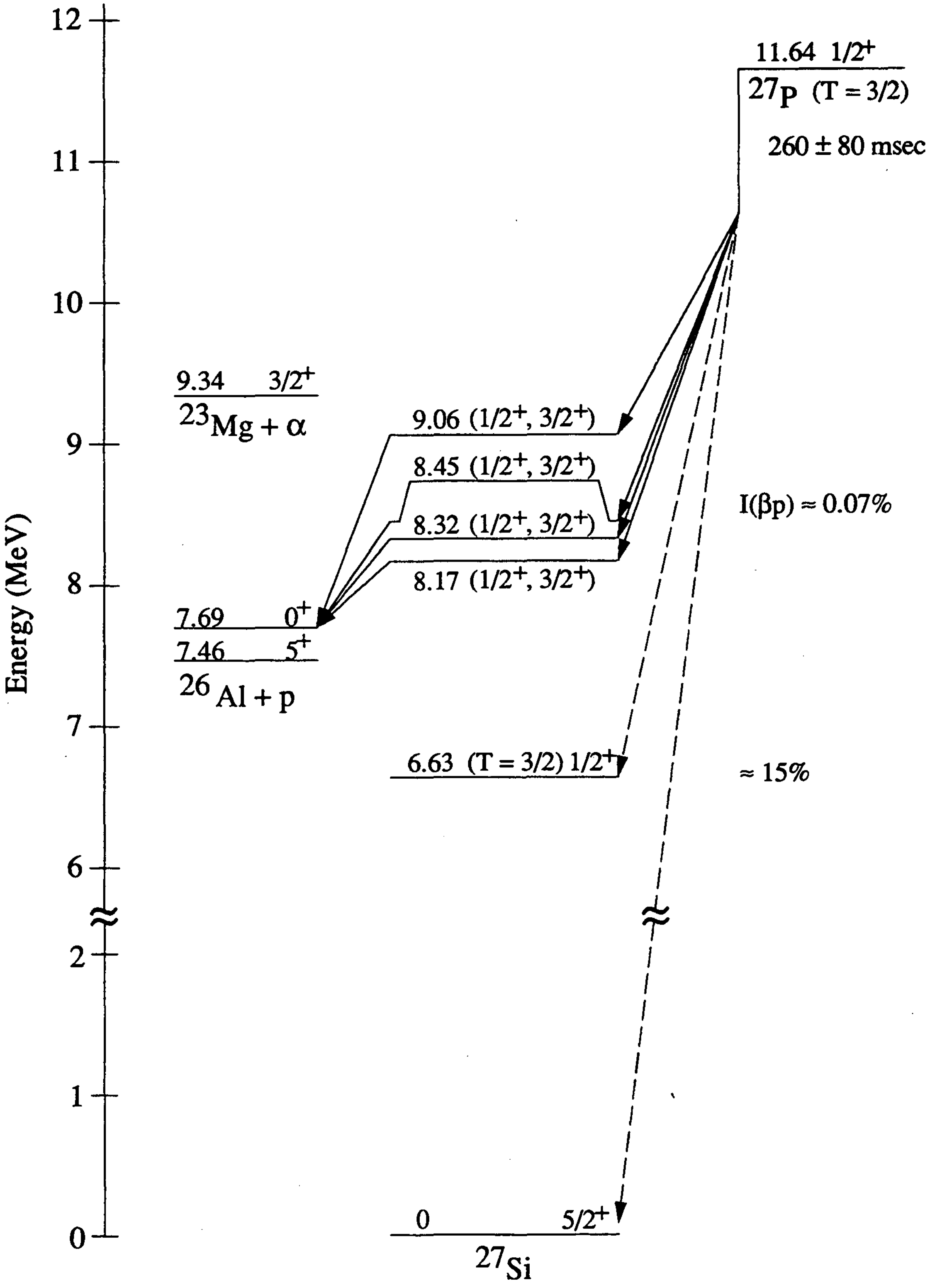

Energy (MeV)
12
11
10
9
8
7
6
2
1
0
9.34 3/2+
23Mg + α
7.69 0+
7.46 5+
26 Al + p
9.06 (1/2+, 3/2+)
8.45 (1/2+, 3/2+)
8.32 (1/2+, 3/2+)
8.17 (1/2+, 3/2+)
6.63 (T = 3/2) 1/2+
0 5/2+
27Si
11.64 1/2+
27P (T = 3/2)
260 ± 80 msec
I(βp) ≈ 0.07%
≈ 15%

Figure IV-9.

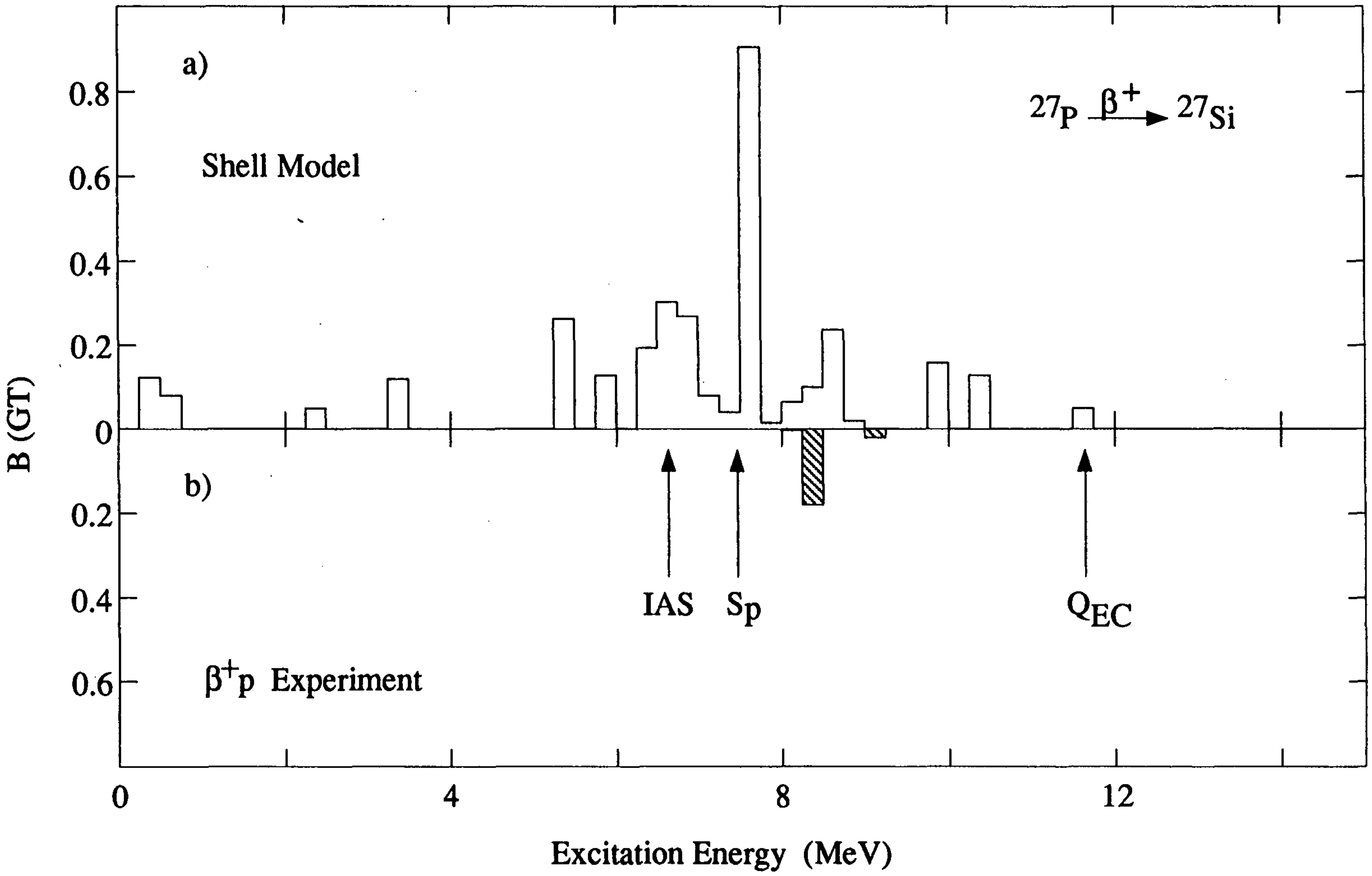
a)
Shell Model
$^{27}P \xrightarrow{\beta^+} {}^{27}Si$
b)
β^+p Experiment
IAS
Sp
Q_{EC}
B (GT)
0.8
0.6
0.4
0.2
0
0.2
0.4
0.6
0
4
8
12
Excitation Energy (MeV)

Figure IV-10.

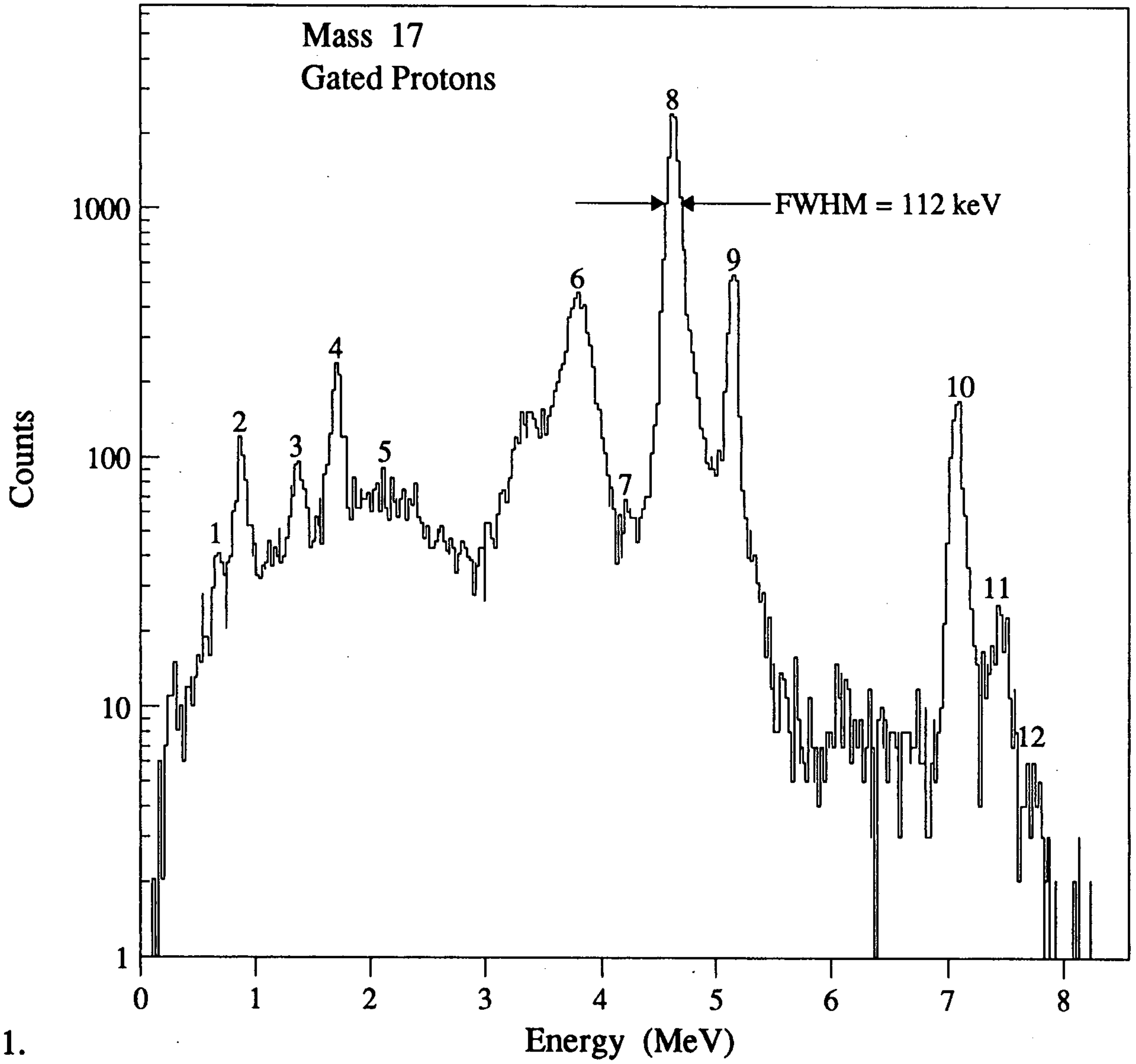
Mass 17
Gated Protons
FWHM = 112 keV
1
2
3
4
5
6
7
8
9
10
11
12
Counts
1
10
100
1000
0
1
2
3
4
5
6
7
8
Energy (MeV)

Figure IV-11.

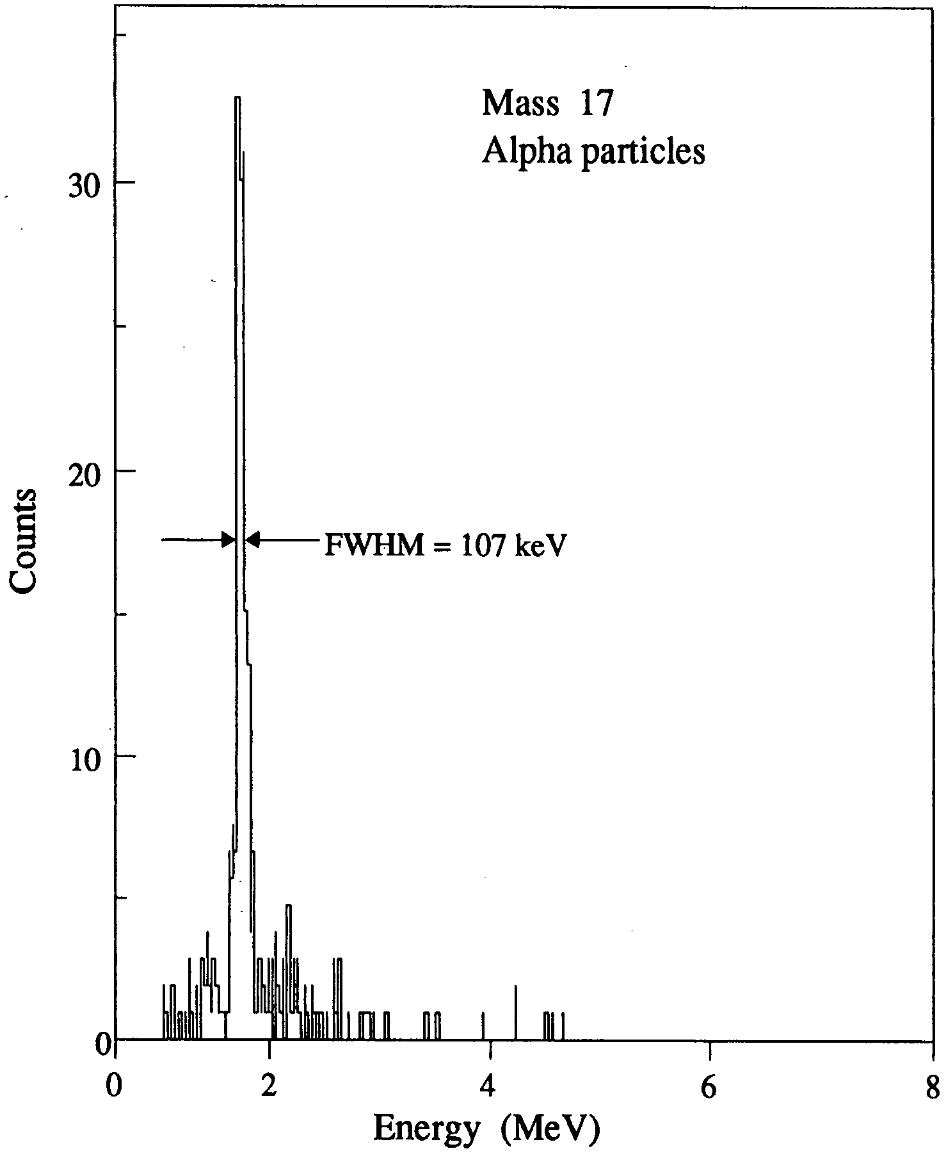
Mass 17
Alpha particles
FWHM = 107 keV
Counts
0
10
20
30
0
2
4
6
8
Energy (MeV)

Figure IV-12.

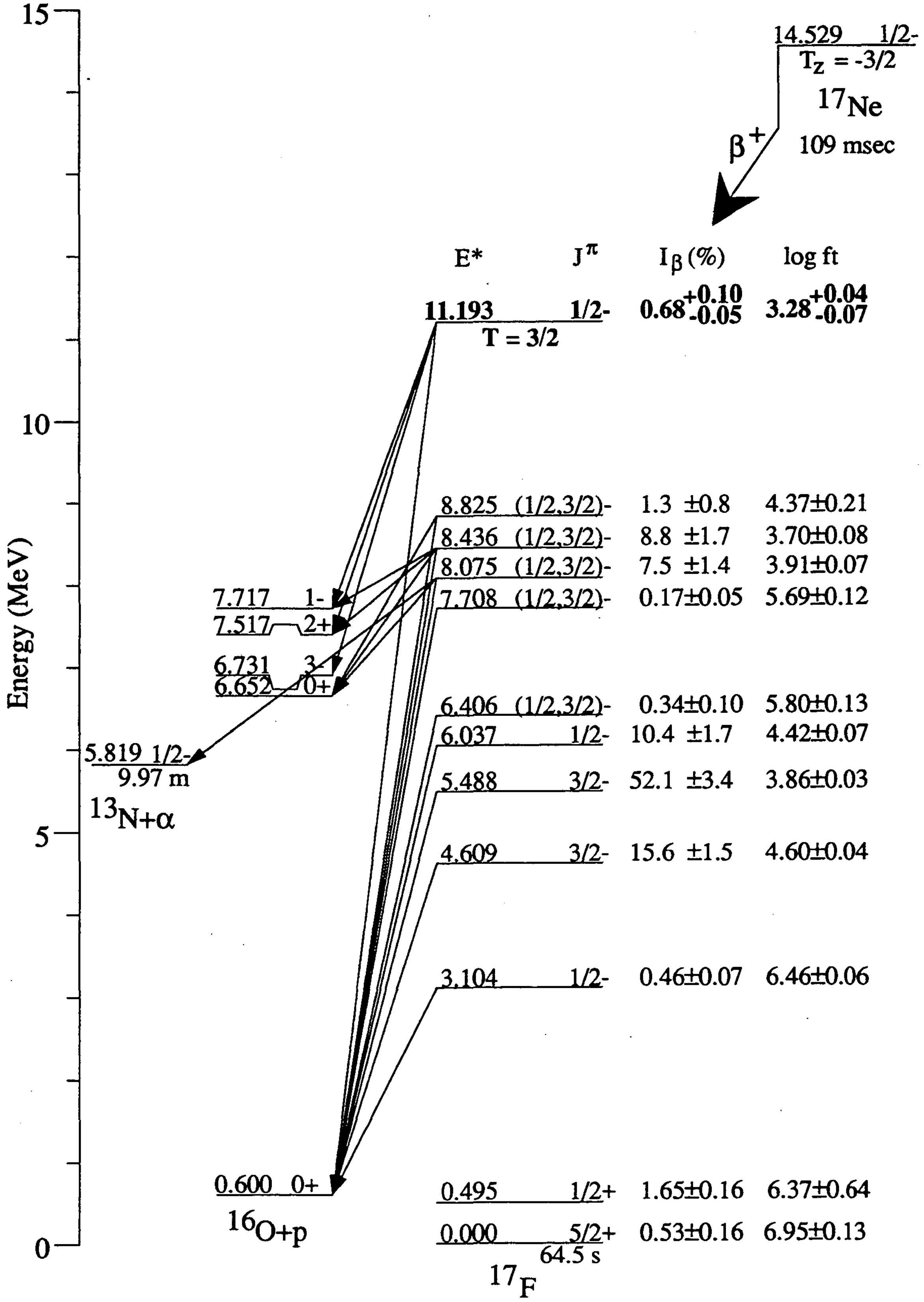

E*	J^π	I_β (%)	log ft
11.193	1/2-	$0.68^{+0.10}_{-0.05}$	$3.28^{+0.04}_{-0.07}$
8.825	(1/2,3/2)-	1.3 ±0.8	4.37±0.21
8.436	(1/2,3/2)-	8.8 ±1.7	3.70±0.08
8.075	(1/2,3/2)-	7.5 ±1.4	3.91±0.07
7.708	(1/2,3/2)-	0.17±0.05	5.69±0.12
6.406	(1/2,3/2)-	0.34±0.10	5.80±0.13
6.037	1/2-	10.4 ±1.7	4.42±0.07
5.488	3/2-	52.1 ±3.4	3.86±0.03
4.609	3/2-	15.6 ±1.5	4.60±0.04
3.104	1/2-	0.46±0.07	6.46±0.06
0.495	1/2+	1.65±0.16	6.37±0.64
0.000	5/2+	0.53±0.16	6.95±0.13

Figure IV-13.

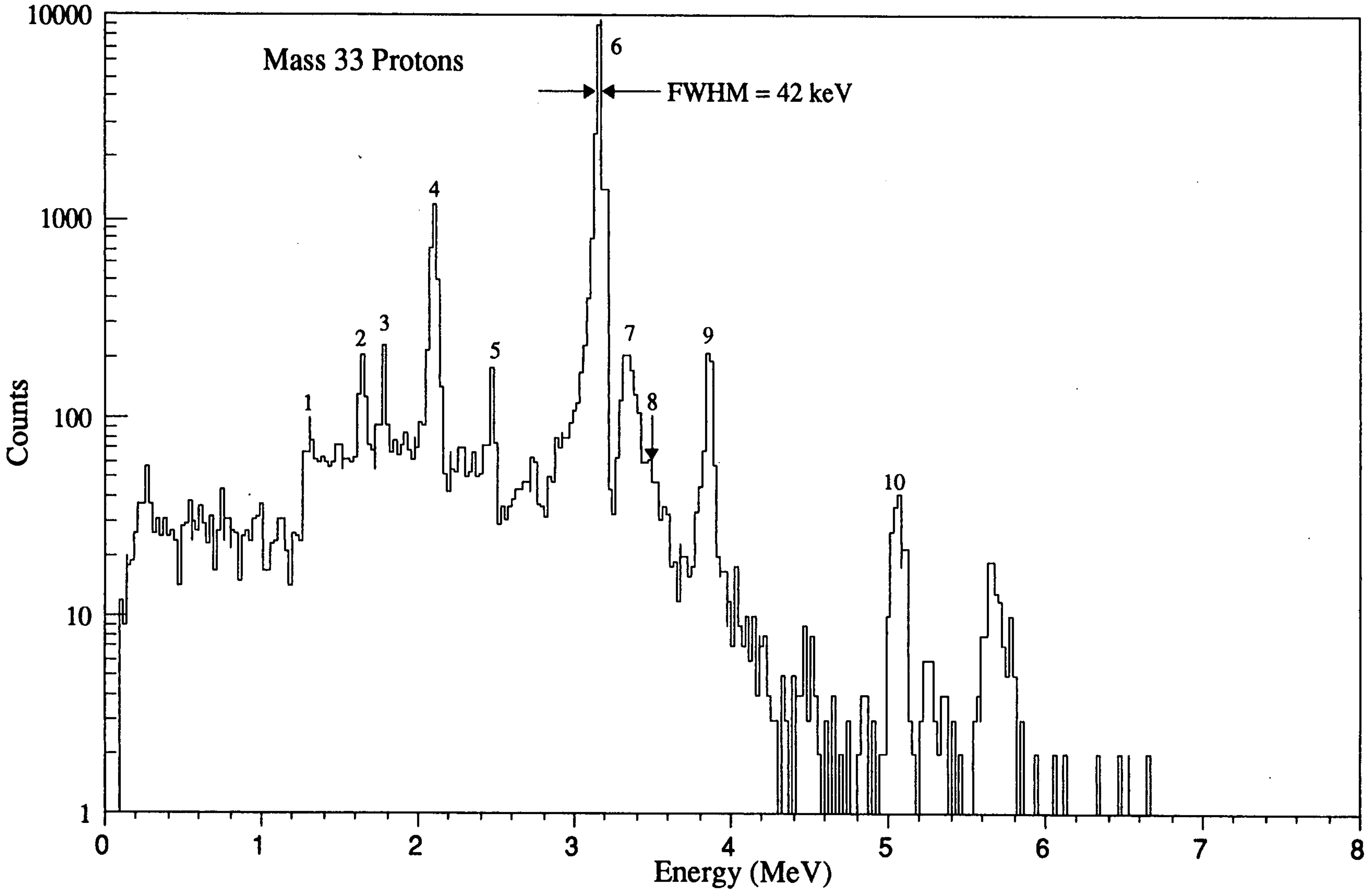
Mass 33 Protons
FWHM = 42 keV
1
2
3
4
5
6
7
8
9
10
Counts
10000
1000
100
10
1
Energy (MeV)
0
1
2
3
4
5
6
7
8

Figure IV-14.

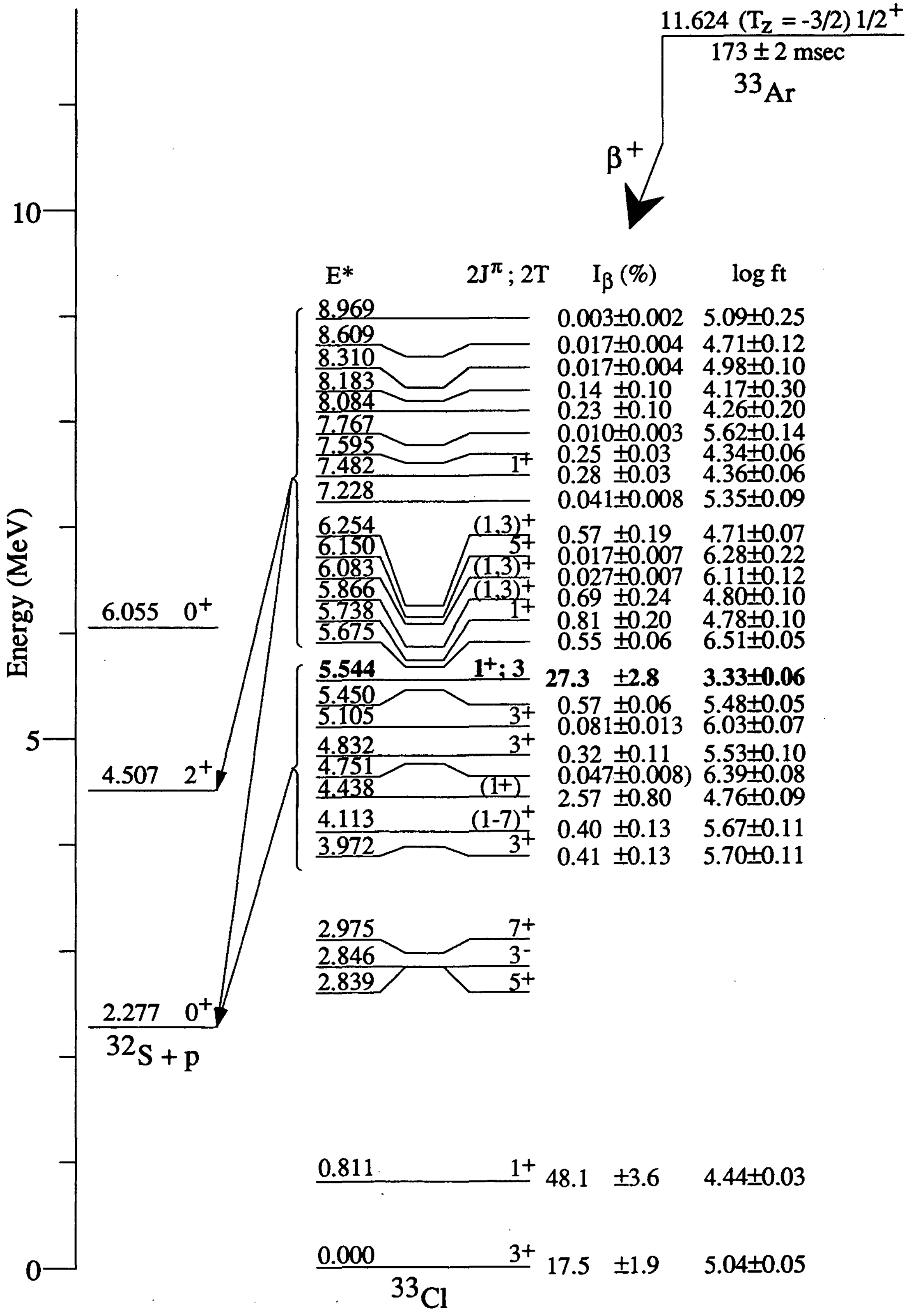
11.624 (T_z = -3/2) 1/2$^+$
173 ± 2 msec
^{33}Ar
β$^+$
Energy (MeV)
0
5
10
6.055 0$^+$
4.507 2$^+$
2.277 0$^+$
^{32}S + p
E*
2J$^\pi$; 2T
I_β (%)
log ft
8.969 0.003±0.002 5.09±0.25
8.609 0.017±0.004 4.71±0.12
8.310 0.017±0.004 4.98±0.10
8.183 0.14 ±0.10 4.17±0.30
8.084 0.23 ±0.10 4.26±0.20
7.767 0.010±0.003 5.62±0.14
7.595 0.25 ±0.03 4.34±0.06
7.482 1$^+$ 0.28 ±0.03 4.36±0.06
7.228 0.041±0.008 5.35±0.09
6.254 (1,3)$^+$ 0.57 ±0.19 4.71±0.07
6.150 5$^+$ 0.017±0.007 6.28±0.22
6.083 (1,3)$^+$ 0.027±0.007 6.11±0.12
5.866 (1,3)$^+$ 0.69 ±0.24 4.80±0.10
5.738 1$^+$ 0.81 ±0.20 4.78±0.10
5.675 0.55 ±0.06 6.51±0.05
5.544 1$^+$; 3 27.3 ±2.8 3.33±0.06
5.450 0.57 ±0.06 5.48±0.05
5.105 3$^+$ 0.081±0.013 6.03±0.07
4.832 3$^+$ 0.32 ±0.11 5.53±0.10
4.751 0.047±0.008) 6.39±0.08
4.438 (1+) 2.57 ±0.80 4.76±0.09
4.113 (1-7)$^+$ 0.40 ±0.13 5.67±0.11
3.972 3$^+$ 0.41 ±0.13 5.70±0.11
2.975 7$^+$
2.846 3$^-$
2.839 5$^+$
0.811 1$^+$ 48.1 ±3.6 4.44±0.03
0.000 3$^+$ 17.5 ±1.9 5.04±0.05
^{33}Cl

Figure IV-15.

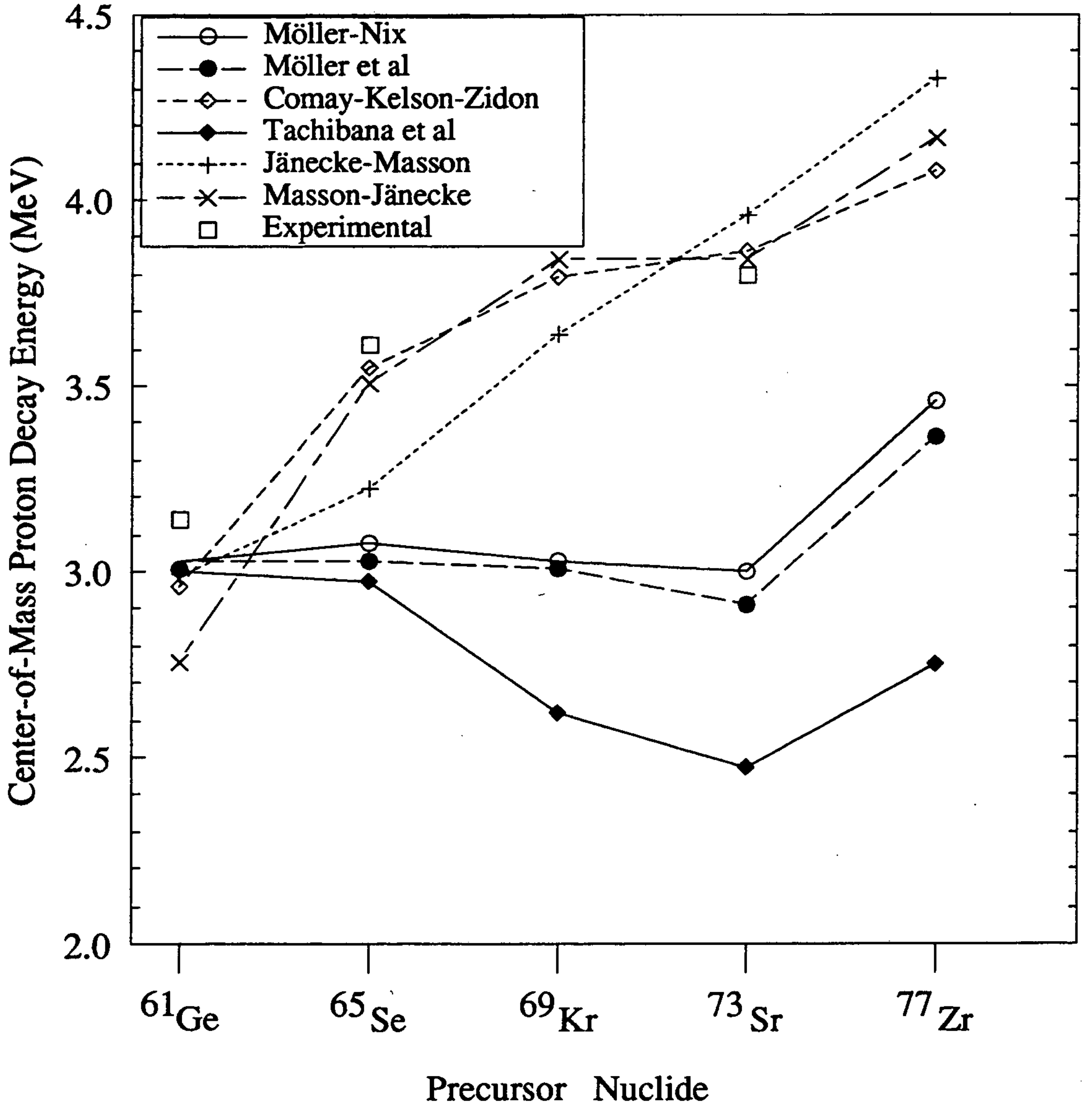
Möller-Nix
Möller et al
Comay-Kelson-Zidon
Tachibana et al
Jänecke-Masson
Masson-Jänecke
Experimental
Center-of-Mass Proton Decay Energy (MeV)
4.5
4.0
3.5
3.0
2.5
2.0
⁶¹Ge
⁶⁵Se
⁶⁹Kr
⁷³Sr
⁷⁷Zr
Precursor Nuclide

Figure IV-16.

V. Summary and Conclusions

Several experimental techniques have been used to investigate the decays of proton-rich nuclei. As these nuclides tend to have short half-lives, a rapid He-jet system was used to transport radioactivity away from the production chamber to either a detector station or a mass separator. The detectors used exploited the beta-delayed charged particle decay characteristics of these nuclides and allowed us to study nuclei made in minuscule yields in the presence of the extremely high background created by the decays of other simultaneously produced nuclei. The detectors consisted of one or more gas ΔE-gas ΔE-silicon E triples telescopes that took advantage of the different amount of differential energy loss of each type of particle (betas, alphas or protons) incurred upon passing through each gas region. These detectors were capable of identifying protons down to ~200 keV and alphas down to ~400 keV on an event-by-event basis.

Several improvements to the He-jet coupled, on-line mass separator, RAMA, have been implemented. Through a redesign of the ion source/extraction region, the RAMA system efficiencies have been enhanced by factors of 10-20 over previous RAMA efficiencies. By placing the ion source/extraction region as close as possible to the production chamber, the transit time to the ion source has been minimized. This removed the relatively long transit times (>200 ms) that had been a severe limitation to using RAMA to study short-lived nuclides.

We have used the above techniques in tandem to determine the nature of a low energy charged particle emitted following the beta decay of ^{20}Na. We had observed, during our investigation into low energy proton emission from the IAS in ^{23}Mg, a peak that appeared to be a low energy alpha particle. Altough this peak scaled with the production of ^{20}Na, a mass separated beam was necessary for confirmation. Using RAMA, as well as a separate detector calibration experiment, we were able to ascertain that this peak was not an alpha particle but rather was the ^{16}O recoil (accompanying alpha emission from ^{20}Ne excited states) in coincidence with a beta particle which had fired both the silicon detector and one of the gas detectors, hence opening the computer.

The decays of several proton-rich sd shell nuclei were also investigated. Beams of 45 MeV protons, bombarding ZnS targets, were used to examine the beta-delayed proton decay of ^{31}Cl. It was revealed that the unexpected presence of ^{25}Si, made from the aluminum target backings, in the data of [Äy 85] had caused those authors to misassign several transitions in the decay of ^{31}Cl. Based on the ^{32}Cl yield at 28 MeV, inferred from the data of [Äy 85], the beta-delayed proton branch of ^{31}Cl was estimated to be 0.3%.

Beams of 28 MeV and 45 MeV protons impinging on targets of natural silicon were used to study the beta-delayed charged-particle decays of ^{28}P and ^{27}P, respectively. The delayed proton spectrum at 28 MeV showed all the ^{28}P beta-delayed proton groups described by [Ho 79a], as well as a new proton group at 1444 ± 12 keV. The intensity of this peak was 1.7 ± 0.5 % of the main 100% proton group at 680 keV. The alpha particle spectrum that was recorded at the same time as the proton spectrum showed most of the alpha peaks described by [Ho 79a]. The exception was that the least intense alpha peak reported by [Ho 79a] could not be observed. However, our upper limit was determined to be within the error limits reported by those authors. We were also able to improve upon the limits of the relative particle intensities.

The spectrum of delayed protons recorded at 45 MeV showed, in addition to ^{28}P proton peaks and the ^{27}P proton peaks described by [Äy 85], two new lower energy proton peaks. The two new peaks have energies of 459 ± 14 keV and 610 ± 11 keV with intensities of 7 ± 3 % and 92 ± 4 % of the main 100% peak at 731 keV, respectively, and involve transitions between excited states in the ^{27}Si beta-daughter to the 0^+ isomer in ^{26}Al. Based on the yields of ^{28}P at 28 MeV and ^{27}P at 45 MeV, a beta-delayed proton branch of 0.07% was estimated.

The Gamow-Teller component of the preceding beta decay of each proton transition observed from the emitter state, either ^{31}S (for ^{31}Cl decay) or ^{27}Si (for ^{27}P decay), was compared to results obtained by shell model calculations. While a portion of the predicted strength was positively identified, it was not possible to discern the complete beta decay strength because certain states were very weakly populated. The decays of these states could involve the emission of protons with intensities that are below the current level of statistics.

Using the TISOL mass separator at TRIUMF and our low energy proton detector ball, the beta-delayed charged-particle decays of ^{17}Ne and ^{33}Ar were investigated. In the case of ^{17}Ne, a proton group with energy 729 ± 15 keV was observed here for the first time. This group was assigned to the transition from the 8436 keV excited state in ^{17}F to the 7117 keV excited state in ^{16}O. Additionally, it was shown that the energies and intensities of the observed proton groups were in better agreement with the earlier work of [Ha 71] than with the results presented by [Bo 88]. The delayed proton spectra recorded at the mass 33 setting of TISOL revealed the beta-delayed proton groups of ^{33}Ar. The results of the current work on ^{33}Ar were again shown to be in better agreement with the work of [Ha 71] rather than with the results of [Bo 87] and [Sc 93].

The isospin purity of the lowest T = 3/2 state in the ^{17}Ne and ^{33}Ar beta daughters, ^{17}F and ^{33}Cl, was determined based on the results of the current work and the work of [Ha 71]. For the IAS in ^{17}F, an isospin purity consistent with 100% was calculated. A 95% isospin purity of the IAS in ^{33}Cl was calculated using the GT matrix element as given by the experimental results of [Sc 93]. This value was close to the purity expected in the limit that the GT matrix element was zero. A previous analysis had indicated that four levels near the IAS each have a 1-2% T = 3/2 character which would account for the missing Fermi strength from the IAS.

A search for the beta-delayed proton decay of ^{77}Zr was performed. This nucleus is the final member of the $T_z = -3/2$, A = 4n + 1 series of beta-delayed proton emitting nuclei that could be effectively studied without the use of radioactive beams and/or targets. The observation of delayed protons from the IAS in the beta daughter would serve to provide a test of various mass models. The predictions of the proton energy made by several mass models begin to diverge at ^{61}Ge (a lighter mass member of this series), and by ^{77}Zr, differ by more than 1500 keV. It had been previously observed that the recursive type mass relations had better predicted the energies of emitted protons following the beta decay of the last two discovered members of this series, ^{65}Se and ^{73}Sr, than had the global parameter type models and it would be instructive to see if this trend would continue.

In attempting to produce ^{77}Zr, two ^{40}Ca bombarding energies of 160 MeV and 147 MeV were used on ^{40}Ca targets. In both experiments a proton peak at ~4.2 MeV was observed. However, a proton group, also at 4.2 MeV, was observed following a 145 MeV ^{36}Ar bombardment of a ^{40}Ca target. The results of this control experiment indicate that this peak was all or partially from the decay of a $Z \leq 38$ beta-delayed proton emitter. Several conclusions were drawn concerning the lack of an unambiguous observation of ^{77}Zr. If the half-life was shorter than the He-jet transit time, then there would be significant losses due to radioactive decay in transit. Also, the predicted cross section could be smaller than expected, as well as the possibility that the decay of a lighter mass nuclide was obscuring the ^{77}Zr group. Any one (or a combination) of these effects would have been sufficient to prevent the observation of ^{77}Zr.

In conclusion, the effectiveness of mass separation combined with the use of low energy particle identification detector telescopes has been demonstrated to be a powerful tool in the experimental investigation of the decays of proton rich nuclei far from the valley of beta stability. Future work will be involved in the development of ion source techniques so that mass separated samples of ^{31}Cl and ^{27}P may be prepared. This will allow the study of the complete beta decays of these nuclides as it will then be possible to examine the gamma de-excitation, as well as the proton emission, of the daughter states. Based on our preliminary results from the search for ^{77}Zr, it is clear that in order to detect ^{77}Zr, its effective yield must somehow be enhanced over the production of other beta-delayed proton emitters. This might be accomplished through the use of mass separation and/or radioactive beams or targets.

VI. References

Aj 86a F. Ajzenberg-Selove, Nucl. Phys. **A449**, 1 (1986).

Aj 86b F. Ajzenberg-Selove, Nucl. Phys. **A460**, 1 (1986).

Aj 87 F. Ajzenberg-Selove, Nucl. Phys. **A475**, 1 (1987).

Aj 88 F. Ajzenberg-Selove, Nucl. Phys. **A490**, 1 (1988).

An 85 M. S. Antony, J. Britz, J. B. Bueb and A. Pape, At. Data Nucl. Data Tables **33**, 447 (1985).

An 88 M. S. Antony, J. Britz and A. Pape, At. Data Nucl. Data Tables **40**, 9 (1988).

Är 86 J. Ärje, J. Äystö, H. Hyvönen, P. Taskinen, V. Koponen, J. Honkanen, K. Valli, A. Hautojärvi and K. Vierinen, Nucl. Instr. Meth. **A249**, 431 (1986).

Au 92 J. M. D'Auria, L. Buchmann, M. Dombsky, P. McNeely, G. Roy, H. Sprenger and J. Vincent, Nucl. Instr. Meth. **B70**, 75 (1992).

Au 93 G. Audi and A. H. Wapstra, Nucl. Phys. **A565**, 1 (1993).

Äy 74 J. Äystö, P. Puumalainen and K. Valli, Nucl. Instr. Meth. **115**, 65 (1974).

Äy 76 J. Äystö, V. Rantala, K. Valli, S. Hillebrand, M. Kortelahti, K. Eskola and T. Raunemaa, Nucl. Instr. Meth. **139**, 325 (1976).

Äy 79 J. Äystö, D. M. Moltz, M. D. Cable, R. D. VonDincklage, R. F. Parry, J. M. Wouters, and J. Cerny, Phys. Lett. **82B**, 43 (1979).

Äy 81 J. Äystö, M. D. Cable, R. F. Parry, J. M. Wouters, D. M. Moltz and J. Cerny, Phys. Rev. **C23**, 879 (1981).

Äy 82 J. Äystö, J. Honkanen, K. Vierinen, A. Hautojärvi, K. Eskola and S. Messelt, Phys. Lett. **110B**, 437 (1982).

Äy 83 J. Äystö, P. Taskinen, K. Eskola, K. Vierinen and S. Messelt, Phys. Scrip. **T5**, 193 (1983).

Äy 85 J. Äystö, X. J. Xu, D. M. Moltz, J. E. Reiff, Joseph Cerny and B. H. Wildenthal, Phys. Rev. **C32**, 1700 (1985).

Äy 89 J. Äystö and Joseph Cerny, in *Treatise on Heavy-Ion Science,* Vol. 8, D.A. Bromley, ed., (Plenum Press, New York, 1989), p. 207.

Ba 63 R. Barton, R. McPherson, R. E. Bell, W. R. Frisken, W. T. Link and R. B. Moore, Can. J. Phys. **41**, 2007 (1963).

Ba 66 A. P. Banford, The Transport of Charged Particle Beams, (E. & F. N. Spon Ltd., London, 1966).

Ba 93a J. C. Batchelder, D. M. Moltz, T. J. Ognibene, M. W. Rowe and Joseph Cerny, Phys. Rev. **C47**, 2038 (1993).

Ba 93b J. C. Batchelder, Ph.D. Thesis. Lawrence Berkeley Laboratory Report # LBL-34999 (University of California, Berkeley Report # UC-414), unpublished (1993).

Ba 93c J. C. Batchelder, D. M. Moltz, T. J. Ognibene, M. W. Rowe R. J. Tighe, and Joseph Cerny, Phys. Rev. **C48**, 2593 (1993).

Ba 94 J. C. Batchelder, R. J. Tighe, D. M. Moltz, T. J. Ognibene, M. W. Rowe and Joseph Cerny, Phys. Rev. **C50**, 1807 (1994).

Be 79 W. Benenson and E. Kashy, Rev. Mod. Phys. **51**, 527 (1979).

Be 81 G. F. Bertsch, Nucl. Phys. **A354**, 157c (1981).

Be 87a M. Berz, H. C. Hoffman and H. Wollnik, Nucl. Instr. Meth. **A258**, 402 (1987).

Be 87b M. Berz, Nucl. Instr. Meth **A258**, 431 (1987).

Be 89 M. Berz, Part. Accel. **24**, 109 (1989).

Bj 88 T. Björnstad, M. J. G. Borge, P. Dessagne, R. D. Von Dincklage, G. T. Ewan, P. G. Hansen, A. Huck, B. Jonson, G. Klotz, A. Knipper, P. O. Larsson, G. Nyman, H. L. Ravn, C. Richard-Serre, K. Riisager, D. Schardt, G. Walter and the ISOLDE Collaboration, Nucl. Phys. **A443**, 283 (1985).

Bl 52 J. M. Blatt and V. F. Weisskopf, Theoretical Nuclear Physics, (Wiley, New York, 1952).

Bl 73 R. J. Blin-Stoyle, Fundamental Interactions and the Nucleus, (North-Holland/American Elsevier, New York, 1973) p. 68.

Bl 82 M. Blann and J. Birplinghoff, LLNL report UCID-19614, unpublished (1982).

Bl 87 F. B. Blönnigen, D. M. Moltz, T. F. Lang, W. F. Knoll, X. Xu, M. A. C. Hotchkis, J. E. Reiff and J. Cerny, Nucl. Instr. Meth. **B26**, 328 (1987).

Bo 87 M. J. G. Borge, P. Dessagne, G. T. Ewan, P. G. Hansen, A. Huck, B. Jonson, G. Klotz, A. Knipper, S. Mattsson, G. Nyman, C. Richard-Serre, K. Riisager, G. Walter and the ISOLDE Collaboration, Phys. Scrip. **36**, 218 (1987).

Bo 88 M. J. G. Borge, H. Cronberg, M. Cronqvist, H. Gabelmann, P. G. Hansen, L. Johannsen, B. Jonson, S. Mattsson, G. Nyman, A. Richter, K. Riisager, O. Tengblad and M. Tomaselli, Nucl. Phys. **A490**, 287 (1988).

Bo 93 M. J. G. Borge, J. Deding, P. G. Hansen, B. Jonson, G. Martínez Pinedo, P. Møller, G. Nyman, A. Poves, A. Richter, K. Riisager, O. Tengblad and the ISOLDE Collaboration, Phys. Lett. **B317**, 25 (1993).

Br 83 B. A. Brown and B. H. Wildenthal, Phys. Rev. **C28**, 2397 (1983).

Br 85 B. A. Brown and B. H. Wildenthal, At. Data and Nucl. Data Tables **33**, 347 (1985).

Bu 89 I. S. Butler and J. F. Harrod, Inorganic Chemistry, (Benjamin/Cummings Publishing Co., Inc., Redwood City, CA, USA, 1989) p. 481.

Ca 87 D. C. Carey, The Optics of Charged Particle Beams, (Harwood, Switzerland, 1987).

Ch 11 C. D. Child, Phy. Rev. (Ser. 1) **32**, 492 (1911).

Ch 67 I. Chavet and R. Bernas, Nucl. Instr. Meth. **47**, 77 (1967).

Cl 83 E. T. H. Clifford, J. C. Hardy, H. Schmeing, R. E. Azuma, H. C. Evans, T. Faestermann, E. Hagberg, K. P. Jackson, V. T. Koslowsky, V. J. Schrewe, K. S. Sharma and I. S. Towner, Phys. Rev. Lett. **50**, 23 (1983).

Cl 89a D. J. Clark and C. M. Lyneis, in Proceedings of the Twelfth International Conference on Cyclotrons and Their Applications, B. Martin and K. Ziegler, ed.,(World Scientific Publishing Co., Berlin, 1989) p. 170.

Cl 89b E. T. H. Clifford, E. Hagberg, J. C. Hardy, H. Schmeing, R. E. Azuma, H. C. Evans, V. T. Koslowsky, V. J. Schrewe, K. S. Sharma and I. S. Towner, Nucl. Phys. **A493**, 293 (1989).

Co 75 W. J. Courtney and J. D. Fox, At. Data Nucl. Data Tables **15**, 141 (1975).

Co 83 E. Comay and J. Jänecke, Nucl. Phys. **A410**, 103 (1983).

Da 75 J. M. Davidson, D. A. Hutcheon, D. R. Gill, T. Taylor, D. M. Sheppard and W. C. Olsen, Nucl,Phys. **A240**, 253 (1975).

Da 87 T. E. Daubert, R. P. Danner, H. M. Sibul and C. C. Stebbins, Physical and Thermodynamic Properties of Pure Chemicals Data Compilation, (Taylor & Francis, Washington, D.C., 1987).

Dé 89 C. Détraz and D. J. Vieira, Annu. Rev. Nucl. Part. Sci. **39**, 407 (1989)

Do 90 M. Dombsky, J. M. D'Auria, L. Buchmann, H. Sprenger, J. Vincent, P. McNeely and G. Roy, Nucl. Instr. Meth. **A295**, 291 (1990).

Do 92 M. Dombsky, L. Buchmann, J. M. D'Auria, P. McNeely, G. Roy, H. Sprenger and J. Vincent, Nucl. Instr. Meth. **B70**, 125 (1992).

Do 94 M. Dombsky, L. Buchmann, J. M. D'Auria, U. Giesen, K. P. Jackson, J. D. King, E. Korkmaz, R. G. Korteling, P. McNeely, J. Powell, G. Roy, M. Trinczek and J. Vincent, Phys. Rev. **C49**, 1867 (1994).

En 85 H. A. Enge, in *Treatise on Heavy-Ion Science,* Vol. 7, D.A. Bromley, ed., (Plenum Press, New York, 1985), p. 403.

En 90 P. M. Endt, Nucl. Phys. **A521**, 1 (1990).

Es 67 R. A. Esterlund, R. McPherson, A. M. Poskanzer and P. L. Reeder, Phys. Rev. **156**, 1094 (1967).

Es 71 J. E. Esterl, Ph.D. Thesis. Lawrence Radiation Laboratory Report # UCRL-20480, unpublished (1971).

Ew 80 G. T. Ewan, E. Hagberg, J. C. Hardy, B. Jonson, S. Mattson, P. Tidemand-Petersson and I. S. Towner, Nucl. Phys. **A343**, 109 (1980).

Fe 34 E. Fermi, Z. Physik **88**, 61 (1934).

Fe 50 E. Fermi, Nuclear Physics. Revised Edition, notes compiled by J. Orear, A. H. Rosenfeld and R. A. Schlutter, (University of Chicago Press, Chicago, 1950).

Fo 88 A. T. Forrester, Large Ion Beams: Fundamentals of Generation And Propagation, (John Wiley & Sons, New York, 1988).

Fr 73 J. H. Freeman and G. Sidenius, Nucl. Instr. Meth. **107**, 477 (1973).

Fr 81 G. Friedlander, J. W. Kennedy, E. S. Macias, J. M. Miller, Nuclear And Radiochemistry 3rd Edition, (John Wiley & Sons, New York, 1981) p. 200.

Ga 66 G. T. Garvey and I. Kelson, Phys. Rev. Lett. **16**, 197 (1966).

Go 66 V. I. Goldanskii, Annu. Rev. Nucl. Sci. **16**, 1 (1966).

Go 72 R. A. Gough, R. G. Sextro, Joseph Cerny, Phys. Rev. Lett. **28**, 510 (1972).

Go 81 C. D. Goodman, Comments Nucl. Part. Phys. **10**, 117 (1981).

Ha 65a J. C. Hardy and R. E. Bell, Can. J. Phys. **43**, 1671 (1965).

Ha 65b J. C. Hardy and B. Margolis, Phys. Lett. **15**, 276 (1965).

Ha 71 J. C. Hardy, J. E. Esterl, R. G. Sextro and Joseph Cerny, Phys. Rev. **C3**, 700 (1971).

Ha 88a J. C. Hardy and E. Hagberg, in *Particle Emission from Nuclei*, Vol 3, M. Ivascu and D. Poenaru, eds., (CRC Press, Boca Raton, Fl, 1988) p. 99.

Ha 88b P. Haustein, special editor, At. Data Nucl. Data Tables **39**, 185 (1988).

Ha 90 J. C. Hardy, I. S. Towner, V. T. Koslowsky, E. Hagberg and H. Schmeing, Nuc. Phys. **A509**, 429 (1990).

Ha 95 HAVAR is a trade name for an alloy composed primarily of Co (42.0%), Cr (20.0%), Fe (19.9%), Ni (12.5%), Mn (1.6%), Mo (2.2%) and W (2.7%), along with small amounts (<0.2%) of C, Si, P and S. It has a density of 8.3 g/cm^3. It is manufactured by Hamilton Precision Metals, a division of HMW Industries Inc., Lancaster, PA 17604.

He 32 W. Heisenberg, Z. Phys. **77**, 1 (1932).

He 66 E. M. Henley, in *Isobaric Spin in Nuclear Physics*, Proceedings of the Conference on Isobaric Spin in Nuclear Physics, J. D. Fox and D. Robson, eds., (Academic Press, New York, 1966), p. 3.

Hi 76 W. J. Hiller and W. D. Schmidt-Ott, Nucl. Instr. Meth. **139**, 331 (1976).

Ho 79a J. Honkanen, M. Kortelathi, K. Valli, K. Eskola, A. Hautojärvi and K. Vierinen, Nucl. Phys. **A330**, 429 (1979).

Ho 79b J.Honkanen, M. Kortelahti, J. Äystö, K. Eskola and A. Hautojärvi, Phys. Scripta **19**, 239 (1979).

Ho 87 M. A. C. Hotchkis, J. E. Reiff, D. J. Vieira, F. Blönnigen, T. F. Lang, D. M. Moltz, X. Xu and Joseph Cerny, Phys. Rev. **C35**, 315 (1987).

Ho 88 S. Hofmann, in *Particle Emission from Nuclei*, Vol 2, M. Ivascu and D. Poenaru, eds., (CRC Press, Boca Raton, Fl, 1988) p. 25.

Ho 89 A. J. T. Holmes, in *The Physics and Technology of Ion Sources*, I. G. Brown, ed., (John Wiley & Sons, Inc., 1989), p. 53.

In 93 International Commission on Radiation Units and Measurements, Stopping Powers and Ranges for Protons and Alpha Particles, ICRU Report 49, (Bethesda, MD, 1993).

Jä 69 J. Jänecke, in *Isospin in Nuclear Physics*, D. H. Wilkinson, ed., (North-Holland Publishing, Amsterdam, 1966), p. 297.

Jä 84 J. Jänecke and E. Comay, Phys. Lett. **140B**, 1 (1984).

Jä 88 J. Jänecke and P. J. Masson, At. Data Nucl. Data Tables **39**, 265 (1988).

Jo 95 B. Jonson and G. Nyman, to be published in *Handbook of Nuclear Decay Modes*, (CRC Press, Boca Raton).

Ju 71 H. Junglas, R. D. MacFarlane and Y. Fares, Phys. Rev. Lett. **27**, 556 (1971).

Ka 90 M. Kato and K. Tsuno, Nucl. Instr. Meth. **A298**, 296 (1990).

Ke 66 I. Kelson and G. T. Garvey, Phys. Lett. **23**, 689 (1966).

Ki 81 R. Kirchner, K. H. Burkard, W. Hüller and O. Klepper, Nucl. Instr. Meth. **186**, 295 (1981).

Kl 88 E. Klemt, P. Bopp, L. Hornig, J. Last, S. J. Freedman, D. Dubbers and O. Schärpf, Z. Phys. **C37**, 179 (1988).

Kr 87 K. S. Krane, Introductory Nuclear Physics, (John Wiley & Sons, Inc., New York, 1987) p. 99 and 102.

La 31 I. Langmuir and K. T. Compton, Rev. Mod. Phys. **3**, 251 (1931).

La 58 A. M. Lane and R. G. Thomas, Rev. Mod. Phys. **30**, 257 (1958).

La 71 P. Lapostolle, IEEE Trans. Nucl. Sci. **NS-18**, 1101 (1971).

Le 83 W. H. G. Lewin and P. C. Joss, in *Accretion Driven Stellar X-Ray Sources*, W. Lewin and E. van den Heuel, editors, (Cambridge Univ. Press, Cambridge, 1983) p.41.

Li 87 C. J. Lister, M. Campbell, A. A. Chishti, W. Gelletly, L. Goettig, R. Moscrop, B. J. Varley, A. N. James, T. Morrison, H. G. Price, J. Simpson, K. Connell and O. Skeppstedt, Phys. Rev. Lett. **59**, 1270 (1987).

Li 90 C. J. Lister, P. J. Ennis, A. A. Chishti, B. J. Varley, W. Gelletly, H. G. Price and A. N. James, Phys. Rev. **C42**, R1191 (1990).

Ma 68 J. B. Marion and F. C. Young, Nuclear Reaction Analysis: Graphs and Tables, (North-Holland Publishing, Amsterdam, 1968), p. 84-86.

Ma 69 R. D. MacFarlane, R. A. Gough, N. S. Oakey and D. F. Torgerson, Nucl. Instr. Meth. **73**, 285 (1969).

Ma 74 R. D. MacFarlane and W. C. McHarris, in *Nuclear Spectroscopy and Reactions Part A*, J. Cerny, ed., (Academic Press, New York, 1974), p. 243.

Mi 87 H. Miyatake, K. Ogawa, T. Shinozuka and M. Fujioka, Nuc. Phys. **A470**, 328 (1987).

Mo 51 S. A. Moszkowski, Phys. Rev. **82**, 35 (1951).

Mo 79a D. M. Moltz, J. Äystö, M. D. Cable, R. D. VonDincklage, R. F. Parry, J. M. Wouters, and J. Cerny, Phys. Rev. Lett. **42**, 43 (1979).

Mo 79b D. M. Moltz, Ph. D. Thesis, Lawrence Berkeley Laboratory Report # LBL-9718, unpublished (1979).

Mo 80a D. M. Moltz, R. A. Gough, M. S. Zisman, D. J. Vieira, H. C. Evans and J. Cerny, Nucl. Instr. Meth. **172**, 507 (1980).

Mo 80b D. M. Moltz, J. M. Wouters, J. Äystö, M. D. Cable, R. F. Parry, R. D. VonDincklage and J. Cerny, Nucl. Instr. Meth. **172**, 519 (1980).

Mo 81 D. M. Moltz, J. Äystö, M. D. Cable, R. F. Parry, J. M. Wouters, P. E. Haustein and J. Cerny, Nucl. Instr. Meth. **186**, 141 (1981).

Mo 88 D. M. Moltz and Joseph Cerny, in *Particle Emission from Nuclei*, Vol 3, M. Ivascu and D. Poenaru, eds., (CRC Press, Boca Raton, Fl, 1988) p. 133.

Mo 91 M. F. Mohar, D. Bazin, W. Benenson, D. J. Morrissey, N. A. Orr, B. M. Sherrill, D. Swan, J. A. Winger, A. C. Mueller and D. Guillemaud-Mueller, Phys. Rev. Lett. **66**, 1571 (1991).

Mo 94 D. M. Moltz, J. D. Robertson, J. C. Batchelder and Joseph Cerny, Nucl. Instr. Meth. **A349**, 210 (1994).

Mp 64 R. McPherson, J. C. Hardy and R. E. Bell, Phys. Lett. **11**, 65 (1964).

Mu 93 A. C. Mueller and B. M. Sherrill, Annu. Rev. Nucl. Part. Sci. **43**, 529 (1993).

Ne 74 K. Neubeck, H. Schober and H. Wäffler, Phys. Rev. **C10**, 320 (1974).

Ni 70 J. M. Nitschke, in Proceedings of the International Conference on the Properties of Nuclei Far From Stability, (Leysin, 1970), CERN Report 70-30, (1970), p. 153.

No 70 L. C. Northcliffe and R. F. Schilling, Nucl. Data Tables **A7**, 233 (1970).

Or 89 W. E. Ormand and B. A. Brown, Phys. Rev. Lett. **62**, 866 (1989).

Ox 87 K. Oxorn, J. E. Crawford, H. Dautet, J. K. P. Lee, R. B. Moore, L. Nikkinen, L. Buchmann, J. M. D'Auria, R. Kokke, A. J. Otter, H. Sprenger and J. Vincent, Nucl. Instr. Meth. **B26**, 143 (1987).

Ph 95 Tungsten filament is manufactured by Philips Elmet, Lewiston, ME 04240, Composition: 99.95% W, 0.01% K, 0.04% other (Si, Al, C, Mo, O, Ni, Fe, Na, Cr, Cu).

Po 66 A. M. Poskanzer, R. McPherson, R. A. Esterlund and P. L. Reeder, Phys. Rev. **152**, 995 (1966).

Ra 73 S. Raman and N. B. Gove, Phys. Rev. **C7**, 1995 (1973).

Ra 89 H. L. Ravn and B. W. Allardyce, in *Treatise on Heavy-Ion Science,* Vol. 8, D.A. Bromley, ed., (Plenum Press, New York, 1989), p. 363.

Ra 91 W. Rathbun, Lawrence Berkeley Laboratory Report #LBL-29734 (1991) unpublished.

Re 64 P. L. Reeder, A. M. Poskanzer and R. A. Esterlund, Phys. Rev. Lett. **13**, 767 (1964).

Ro 92 E. Roeckl, Rep. Prog. Phys. **55**, 1661 (1992).

Ro 93 J. D. Robertson, D. M. Moltz, T. F. Lang, J. E. Reiff, J. Cerny and B. H. Wildenthal, Phys. Rev. **C47**, 1455 (1993).

Sc 89 R. B. Schubank, J. A. Cameron and V. P. Janzen, Phys. Rev. **C40**, 2310 (1989).

Sc 93 D. Schardt and K. Riisager, Z. Phys. **A345**, 265 (1993).

Se 71 A. Septier, in Proceedings of the Symposium on Ion Sources and Formation of Ion Beams, Th. J. M. Sluyters, ed., (Upton, NY, 1971), p. 63.

Se 73 Computer program writted by R. Sextro.

Sh 74 A. deShalit and H. Feshbach, Theoretical Nuclear Physics Volume I: Nuclear Structure, (John Wiley & Sons, Inc., New York, 1987) p.787.

Si 70 G. Sidenius, in Proceedings of the International Conference on Electromagnetic Isotope Separators and the Techniques of Their Applications, H. Wagner and W. Walcher, eds., (Marburg, FRG,1970), p. 423.

St 89 Program writted by J. Staples, LBL (1989).

Sz 88 M. Szilágyi, Electron and Ion Optics, (Plenum Press, New York, 1988) p. 497.

Ta 73 K. Takahashi, M. Yamada and T. Kondoh, At. Data Nucl. Data Tables **12**, 101 (1973).

Ti 95 R. J. Tighe, J. C. Batchelder, D. M. Moltz, T. J. Ognibene, M. W. Rowe, J. Cerny and B. A. Brown, Phys. Rev. **C52**, R2298 (1995).

To 73 D. F. Torgerson, K. Wien, Y. Fares, N. S. Oakey, R. D. MacFarlane and W. A. Lanford, Phys. Rev. **C8**, 161 (1973).

Ve 66 R. I. Verrall, J. C. Hardy and R. E. Bell, Nucl. Instr. Meth. **42**, 258 (1966).

We 51 V. F. Weisskopf, Phys. Rev. **83**, 1073 (1951).

We 61 H. A. Weidenmüller, Rev. Mod. Phys. **33**, 574 (1961).

We 75 C. Weiffenbach, S. C. Gujrathi, J. K. P. Lee and A. Houdayer, Nucl. Instr. Meth. **125**, 245 (1975).

Wi 57 E. P. Wigner, Proceedings of the Robert A. Welch Foundation Conferences on Chemical Research, W. O. Milligan, ed., (Robert A Welch Foundation, Housten, TX, 1957) Vol. 1, p. 67.

Wi 73 D. H. Wilkinson, Nuc. Phys. **A209**, 470 (1973).

Wi 83 B. H. Wildenthal, M. S. Curtin and B. A. Brown, Phys. Rev.**C28**, 1343 (1983).

Wi 84 B. H. Wildenthal, Prog. Part. Nucl. Phys. **11**, 5 (1984).

Wi 93 J. A. Winger, D. P. Bazin, W. Benenson, G. M. Crawley, D. J. Morrissey, N. A. Orr, R. Pfaff, B. M. Sherrill, M. Steiner, M. Thoennessen, S. J. Yennello and B. M. Young, Phys. Lett. B. **209**, 214 (1993).

Wo 76 H. Wollnik, Nucl. Instr. Meth. **139**, 311 (1976).

Wo 87a H. Wollnik, Optics of Charged Particles, (Academic Press Inc., Orlando, Fl, 1987).

Wo 87b H. Wollnik, Nucl. Instr. Meth. **A258**, 289 (1987).

Zh 89 Z. Zhao, M. Gai, B. J. Lund, S. L. Rugari, D. Mikolas, B. A. Brown, J. A. Nolen, Jr. and M. Samuel, Phys. Rev. **C39**, 1985 (1989).

ERNEST ORLANDO LAWRENCE BERKELEY NATIONAL LABORATORY
ONE CYCLOTRON ROAD | BERKELEY, CALIFORNIA 94720

Prepared for the U.S. Department of Energy under Contract No. DE-AC03-76SF00098